

NON - INVASIVE METHODS FOR *IN SITU* ASSESSING AND MONITORING OF THE  
VULNERABILITY OF ROCK ART MONUMENTS

ELIZABETH BEMAND

A thesis submitted in partial fulfilment of the requirements of Nottingham Trent University  
for the degree of Doctor of Philosophy

September 2015

## **Abstract**

Rock art monuments provide a link to our ancient cultural pasts, they possess seeming permanence but are sensitive to their environment. The increasing emphasis on non-destructive testing and demand for thorough characterisation of cultural heritage material *in situ* requires the development of advanced diagnostic methods, providing the motivation for this work on the application of optical coherence tomography, hyperspectral imaging and nuclear magnetic resonance to rock art panels. Optical coherence tomography is shown to be an effective method to determine the grain size distribution and hydraulic conductivity of historic sandstone *in situ*. Studies were performed on historic sandstone headstones to demonstrate the relationship between the hydraulic conductivity of sandstone and the type and severity of weathering features present. A study of rock art panels *in situ* is given, to characterise the host rock and provide quantitative assessment of the vulnerability of the panels to weathering processes. The relative impact of natural weathering and anthropogenic damage is shown and a comparison between the characteristic of a proxy sample and the rock art panel itself is provided to highlight the importance of non-destructive in-situ methods for the monitoring and assessing of the vulnerability of rock art monuments. Hyperspectral imaging is demonstrated as an effective technique to determine the presence of moisture in stone, while nuclear magnetic resonance measurements show limitations for use *in situ* in open air locations.

*In memory of the love and support of my parents*

*Paul James Bemand*

*22<sup>nd</sup> July 1948 – 28<sup>th</sup> June 2013*

*Valerie Bemand*

*26<sup>th</sup> March 1950 – 2<sup>nd</sup> July 2013*

## **Acknowledgements**

I would like to acknowledge the support I have received from my supervisors Haida Liang and Martin Bencsik.

Assistance with field work from Sammy Cheung and Andrei Lucien from Nottingham Trent University

My introduction to rock art by Sebastian Payne from English Heritage

Mercury porosimetry data provided by Matthew Hall and Nottingham University

Micro-CT imaging provided by Andrew Ramsay at Nikon Metrology

This collaborative research project is jointly funded by the UK Arts and Humanities Research Council and the Engineering and Physical Sciences Research Council through the Science and Heritage Programme ([www.heritagescience.ac.uk](http://www.heritagescience.ac.uk)), and English Heritage.

## Contents

<b>1</b>	
<b>Introduction .....</b>	<b>8</b>
1.1 Background and motivation	
1.1 Review of methods	
1.2a Rebound measurements	
1.2b Drilling resistance measurements	
1.2c Ultrasound measurements	
1.2d Electrical resistance measurements	
1.1e Capillary uptake tests	
1.3 Thesis objective	
<b>2 Optical Coherence Tomography imaging of the subsurface structure of sandstone...20</b>	
2.1 Introduction	
2.2 Materials and methods	
Image acquisition	
2.3.2 Imaging protocol	
2.4 Image Analysis	
2.5 Summary	
<b>3. Optical Coherence Tomography measurement of Hydraulic Conductivity.....46</b>	
3.1 Introduction	
3.2 Materials and methods	
3.2.1 Samples	
3.2.2 Measurement Procedure	
3.3 Results and Discussion	
<b>4. Hyperspectral Imaging for remote moisture monitoring.....64</b>	
4.1 Introduction	
4.2 Instrument	
4.3 Results and Discussion	
4.4 Conclusions	
4.5 Further work – application of the technique to painted caves and grottoes	
<b>5 Nuclear Magnetic Resonance investigation of porosity.....79</b>	

5.1 Introduction	
5.2 Materials and methods	
5.2.1 Instrument	
5.2.2 Sintered Discs	
5.2.3 Sandstone	
5.3 Considerations for in-situ measurements	
5.4 Comparison with other techniques	
5.4.1 X-ray micro-computed tomography	
5.4.2 Mercury Intrusion Porosimetry	
5.5 Summary	
<b>6 Studies of historic stone in-situ.....</b>	<b>99</b>
6.1 Sandstone headstones at Nottingham General Cemetery	
6.1a BG1873	
6.1b GC1876	
6.1c JG1873	
6.1d WW1881	
6.1e AF1875	
6.1f WS1887	
6.1g HB1877	
6.1h AT1850	
6.1i WK1884	
6.2 Derbyshire standing stones at Barbrook I and Gardom's edge	
6.2a Barbrook I stone circle	
6.2b Gardom's edge monolith	
6.3 Northumberland rock art panels	
6.3a Chatton Park	
6.3b Roughting Linn	
6.4 Discussion	
<b>7 Conclusions.....</b>	<b>257</b>

7.1 Future work

List of Publications .....269

## **Chapter 1 Introduction**

### **1.1 Background and motivation**

The modification of stone surfaces has spanned the entirety of human existence [1] and remains when other material evidence is lost. Prehistoric rock art is a unique source of knowledge that has the potential to transform our understanding of the lives of our ancestors and how they adapted to and changed their environment. Such remains often form significant features in our surroundings, but are also valuable as a resource for research, education, leisure and tourism and for their influence of identity and spirit of place. Rock art monuments provide a link to our ancient cultural pasts; they possess seeming permanence but are sensitive to their environment.

Since 1979 many rock art sites have been protected as Scheduled Monuments under the Ancient Monuments and Archaeological Areas Act [2]. Rapid changes due to anthropogenic land use and climactic variation will cause damage and decay over time.

Rock art in Northumberland has been comprehensively described on Web Access to Rock Art: the Beckensall Archive of Northumberland Rock Art [3], the website ERA England's rock art [4] and the independent society 'the megalithic portal' [5] and in books such as British Prehistoric Rock Art by Stan Beckensall [6]

Cultural heritage stone conservation more commonly occurs in the built environment subject to urban conditions rather than erosion in the natural environment [7]. The bulk of stone conservation research has been on structures rather than landforms and needs to be adapted for outcrops that have been modified by humans.

Artificial weathering for durability testing of building materials is unavoidably reductionist and cannot replicate the potential for the synergistic and antagonistic behaviour of weathering processes in the natural environment [8].

A key problem in cultural resource management is identifying those artefacts in need of immediate conservation by generating clear data for decision makers. It is essential to measure the extent, severity and monitor the rate of decay over time [9].

## **1.2 Review of methods**

Knowledge of the characteristics of the host rock is vital to inform decisions to ameliorate the impact of decay processes, delaying the inevitable progression of paedogenesis. Effective diagnosis of present conditions is the first step towards conservation which can then be followed by intervention or conservation measures.

Diagnostic mapping of weathering provides a context and description of measurement locations for *in situ* methods. Methods to investigate stone weathering *in situ* rely on proxy measurements; methods that measure stone characteristics considered to either indicate a vulnerability to weathering processes or those that change due to the action of weathering. Reviewed in this chapter are methods for measuring the strength and mechanical properties such as the rebound and drilling resistance of the stone and ultrasonic velocity measurements. Also reviewed are methods used to evaluate the presence and transport of water within the stone such as electrical resistance and capillary uptake measurements. The methods reviewed all require contact and are micro destructive or require the application of adhesive or other medium to the surface of the stone.

Structural maps provide the investigation with the means for determining the types, arrangement and distribution of macroscopic fabric elements, these are important for the properties of the material and they represent a way of creating a critical weathering inventory and macroscopic description in order to quantify and stage decay [10, 11].

The detailed registration of weathering forms are made by monument mapping by which spatial distributions of fabric and damage characteristics are mapped and schematically represented in order to contextualize in-situ measurements and sampling locations, to assist in merging the results from a suite of techniques at different scales.

Current measurement techniques will be discussed, including the difficulties of applying them to open-air rock art sites in-situ or for continuous monitoring. The increasing emphasis on non-destructive testing and the demand for thorough characterization of materials in-situ requires the development of advanced diagnostic methods [12].

In-situ methods such as drilling resistance measurements and rebound hammer have been used to monitor rock hardness as a measure of weathering state for sandstone cultural heritage alongside laboratory methods requiring sampling such as mercury intrusion porosimetry (MIP).

Various different durability estimators have been proposed linking between strength and longevity of stone; measurements of strength by ultrasonic wave velocity, hardness, drilling resistance which can be performed at open-air sites *in situ*.

### **1.2a Rebound measurements**

Rebound hammer or Schmidt hammer has become a common tool for assessing the mechanical strength of stone in situ [13]. It was originally developed by E. Schmidt for non-destructive in situ testing of concrete. It is used in geomorphological and cultural heritage investigations to provide a measure of rock hardness from rebound characteristics of rock surfaces [14]. The rebound distance of a controlled impact perpendicular to the surface is measured by the instrument. There are various models commercially available that do not necessarily provide comparable results. Hardness can be a measure of weathering in some cases but the relationship with weathering is not simple, some processes can lead to surface hardening while others cause

progressive softening of the rock surface. It should be used with caution on cultural heritage materials; a test strike should be performed on an inconspicuous area to avoid chipping or marking damage to the surface under investigation. Measurements are sensitive to rock fabric and surface texture and moisture content and the size and mass of the block, it is not suitable for small blocks and can break small blocks on impact. The technique has some issues with operator variance and at present there is no standardized procedure for testing and is best used as a relative measure of weathering.

### **1.2b Drilling resistance measurements**

Drilling resistance measurements techniques initially developed in 1908 for the testing of construction materials [15]. It is a portable micro-destructive technique that has been used for in-situ hardness measurements of stone and other construction materials for cultural heritage applications. Small diameter (3-5 mm) drill bits are used to make the technique micro-destructive but as a result of the small sample size multiple measurements may be required to be representative of heterogeneous natural materials. Drilling depths of 10 mm are used to give depth profiles in order to investigate weathering fronts within the stone surface and the penetration of consolidation treatments. Calibration tests need to be performed both before use and at regular intervals during the working life of drill bits to characterise the variability between drill bits and wear effects from repeated use. The presence of moisture can also affect drilling measurements by causing packing effects from dust accumulation in the drill hole which can cause increased resistance results. While micro-destructive, the technique is potentially damaging and may cause disintegration to the material around the drilling hole. Drilling resistance measurements can provide depth resolved profiles of material hardness but the destructive nature of the technique restricts its use and it cannot be used to survey a monument or for continuous monitoring.

### **1.2c Ultrasonic velocity measurements**

Measurement is made of the velocity of compressional waves through a material, from the time taken for ultrasonic waves to pass through a material, from a transmitter to a receiver both held in contact with a coupling medium between the transducer and material surface. The greater the density of the stone the faster the ultrasonic waves move through it [16 - 19], the lower velocity in air enables the detection of voids in the material due to cracks or fissures and can indicate structural disintegration within the material. Stone with high ultrasonic wave velocity tends to have a longer durability [16, 17]. If possible the velocity measured is transmitted through the material to get a direct measurement; if not, measurements can be performed at the surface giving an indirect measurement from ultrasonic waves back-reflected by cracks or sedimentary structures such as bedding planes in the material. Measurements are dependent on the rock fabric and are affected by discontinuities within the material and can be used topographically [18] to map discontinuities. Measurements can be made parallel and perpendicular to bedding plane or other sedimentary structures to detect anisotropy. The ratio between measurements can be used to create an anisotropy index. Irregular surfaces can make measurements difficult depending on the shape and size of the transducer. The presence of moisture can also influence the velocity of ultrasonic waves through the stone [19]. The technique can be unreliable for assessing the condition of the stone directly below the surface but it has been used extensively in conjunction with drilling resistance measurements to link surface softening with weakening of the stone interior. While the technique is considered non-destructive, the application of Vaseline [31] or organic gel [17] at the interface between the transducer and the material to provide an effective contact with the surface limits its use for cultural heritage applications.

### **1.2d Electrical resistance measurements**

Measuring the resistance between two points attached or tapped in to the surface of the object, the technique is based on the concept that the electrical resistance of a material will decrease when water is present. It is an indirect method; the signal measured does not come from the water but from the conductance of the material, which is affected by the presence of water as well as various other factors and can be modified significantly by the presence of dissolved contaminants in the water. Resistivity will be further decreased by the presence of ions in the water giving a falsely high water content result. The measurement can identify moisture difference in the material between measurements but variation in the presence of salts can cause inconsistency between measurements of the same material. There are various simple but invasive techniques that involve installing different probes into the artefact such as metal screws or wooden dowels, which may influence measurements by their material properties. A non-destructive method using conductive self-adhesive pads has been developed avoiding the destructive practice of drilling and attaching nails into the rock surface making it suitable for use on cultural heritage materials [18, 19, 20]. The technique allows estimation of moisture distributions within porous stone, the quantitative estimation of water content from resistivity measurement is less reliable because of the potentially disruptive influence of dissolved salts. Calibration is problematic due to unknown salt content composition and distribution, so it is not easy to measure absolute water content values.

### **1.2e Capillary uptake tests**

Water absorption tube testing is an in-situ method used to evaluate the water absorption of a porous material. When a water column is applied to a porous material, the water penetrates the material. The water volume absorbed after a definite time is a characteristic of the material and may be decreased by surface incrustation and increased by structural disintegration. It depends

on the porosity and capillary properties of the material as well as its initial saturation level and can provide an indirect measurement of pore characteristics. The method is used in building construction and conservation to test materials and evaluate hydrophobic treatments. An open cylindrical body (tube / pipe) is attached horizontally or vertically to the surface being measured and filled with a set volume of water. Standard measurement time is an hour requiring the attachment medium to be adhesive enough to hold the pipe in place over that time frame. A compromise must be made between potential damage to the surface from the attachment medium and the equipment staying in place. It is not suitable for severely deteriorated surfaces as it may not adhere and risks granular loss from the surface. The method can also have difficulties with the pipes leaking or falling off during experiments but can give useful results and is cheap and relatively easy to perform.

It is necessary to move on from micro-destructive techniques towards non-destructive testing methods that can be used portably in the open-air locations of artefacts removing the need to remove samples or rely on proxy materials to measure characteristic such as porosity and pore size distribution.

The increasing emphasis on non-destructive testing and the demand for thorough characterization of materials in-situ requires the development of advanced diagnostic methods providing the motivation for this work.

### **1.3 Thesis Objective**

**The aim of this project is to develop non-invasive in-situ methods for assessing and monitoring the surface and subsurface conditions of rock art panels.**

**Optical Coherence Tomography, Nuclear Magnetic Resonance and Hyperspectral imaging are applied to monitor and assess the vulnerability of rock art monuments in-situ.**

The objective of the study is the development of techniques to apply non-destructive methods to replace current micro destructive techniques and to further enable the quantitative assessment of stone characteristics and vulnerability to weathering *in situ* without the need for sampling or reliance on proxy samples.

### **Optical Coherence Tomography**

Optical Coherence Tomography (OCT) is a 3D imaging technique that relies on the detection of light scattered-back from the sample, it was designed for non-invasive examination of the interior of the eye and the subsurface structure of biological tissues [24].

The OCT uses a near infrared light source and detector array with which it registers the back-scattered light, measuring the travel time using interference between light that has interacted with the sample and a reference beam to produce ‘virtual’ cross-sectional images of the surface and subsurface non-invasively. It is a non-destructive method using low intensity light at a safe working distance (>1 cm), so examination can be performed anywhere on the panel or repeated over time for monitoring purposes.

### **Hyperspectral imaging**

Spectroscopy is the study of light as a function of wavelength that has been reflected or emitted from a material. The wavelength dependence of absorption processes allows us to derive information about its composition from its reflected light using a detector and a means of wavelength selection. Imaging spectroscopy is a means of obtaining a spectrum at each position

in a large array of spatial positions so that any one spectral wavelength can be used to make a recognizable image.

Absorption bands are detectable in the spectrum of materials caused by the presence of specific chemical bonds [25], water is a strong infrared absorber producing diagnostic spectral features. Near infrared hyperspectral imaging can be used for the identification and mapping of the presence of water by spectral feature analysis to quantitatively monitor the spatial variation of water through the surface and subsurface of the panel.

## **NMR**

Nuclear Magnetic Resonance has widespread use in many areas of science and technology most familiarly in medicine for MRI (Magnetic Resonance Imaging) biomedical purposes. Mobile single sided NMR is based on the principles of unilateral inside out NMR (where the sample is placed outside the magnet) initially developed to travel down bore holes for the purpose of well logging [26]. Oil industry analysis of NMR signals provides information about the fluids in the porous network of the surrounding rock matrix.

NMR signal is produced by applying a series of radio-frequency pulses to a sample within the polarizing magnetic field which are absorbed and re-emitted by hydrogen nuclei. This enables the spatially resolved detection of a hydrogen containing fluid (e.g. water H<sub>2</sub>O) within the sample which translate to the fluid filled porosity of the material.

In Chapter 2, Optical Coherence Tomography imaging of the subsurface structure of sandstone, an imaging protocol is presented followed by image analysis to determine the representative grain size of sandstones from three-dimensional OCT volumetric scans. Chapter 3: OCT measurement of hydraulic conductivity, describes the application of OCT to detect the ingress of water into sandstone with measurement of the wetting front velocity of water through the

sandstone material which gives the hydraulic conductivity of the material. In Chapter 4, hyperspectral imaging for remote moisture monitoring, the application of hyperspectral imaging to the remote detection of moisture in materials is presented with a method of spectral feature analysis to determine water content. Chapter 5: NMR measurement of porosity, investigates the possibility of using NMR to produce depth resolved measurements of porosity in-situ is investigated and the results compared with those from Micro-CT imaging and mercury intrusion porosimetry. In Chapter 6 the methods developed for *in situ* investigations are applied to historic stones and rock art panels. Chapter 7 summarises the findings of the work and future projects resulting from it.

## References

- 1 P. Bahn. The Cambridge illustrated history of prehistoric art. Cambridge. Cambridge University Press. (1998)
- 2 Ancient Monuments and Archaeological Areas Act 1979  
<http://www.legislation.gov.uk/ukpga/1979/46>
- 3 <http://rockart.ncl.ac.uk/>
- 4 <http://archaeologydataservice.ac.uk/era/>
- 5 <http://www.megalithic.co.uk/>
- 6 S. Beckensall. British Prehistoric Rock Art. Tempus Publishing Ltd. (2002)
- 7 G.A. Pope, T.C. Meierding, T.R. Paradise. Geomorphology's role in the study of weathering of cultural stone.
- 8 A. V. Turkington, T.R. Paradise, Sandstone weathering: a century of research and innovation. *Geomorphology*, 67, 229-253. (2005)

- 9 E.Doehne, C.A. Price, Stone Conservation an Overview of Current Research. (Getty Conservation Institute 2010), Chap.1.
- 10 P.A.Warke, J.M. Curran, A.V. Turkington, B.J. Smith. Condition assessment for building stone conservation: a staging system approach. *Building and Environment*. 38, 1113-1123. (2003)
- 11 B.J. Smith, R. Prikryl. Diagnosing decay: the value of medical analogy in understanding the weathering of building stones. *Geological Society of London, Special Publications*, 271, 1-8. (2007)
- 12 Torok, R.Prikryl, "Current Methods and Future Trends in testing, durability analyses and provenance studies of natural stones used in historical monuments" , *Engineering Geology* 115 138-142 (2010)
- 13 H. Viles, A. Goudie, S. Grab, J. Lalley, "The use of Schmidt Hammer and Equotip for rock hardness assessment in geomorphology and heritage science: a comparative analysis" *Earth Surface Processes and Landforms* 36,320-333 (2011)
- 14 G. Pope. "Weathering of Petroglyphs: direct assessment and implications for dating methods," *Antiquity* 74, 833-843, (2000)
- 15 M. Pamplona, M. Kocher, R. Snethlage, L. Aires Barros, "Drilling resistance: overview and outlook". *Zeitschrift der Deutschen Gesellschaft für Geowissenschaften* 158, 665-676 (2007)
- 16 G. Vasconcelos, P.B. Lourenco, C.A.S. Alves, J. Pamplona, " Ultrasonic evaluation of the physical and mechanical properties of granites" *Ultrasonics* 48, 453-466 (2008)
- 17 M.P. Saez, J. Rodriguez-Gordillo. Structural anisotropy in Marcel marble (Spain) by ultrasonic, x-rd XRD and optical microscopy methods. *Construction and Building Materials*. 23, 2121-2126. (2009)

- 18 S. Siegesmund, T. Kracke, J. Ruedrich, R. Schwarzburg. "Jewish cemetery in Hamburg Altona (Germany): State of marble deterioration and provenance". *Engineering Geology* 115, 200-208 (2010)
- 19 S.Kahraman. "The correlations between the saturated and dry P-wave velocity of rocks" *Ultrasonics* 46, 341-348 (2007)
- 20 G. Barbera, G. Barone, P. Mazzoleni, A. Scandurra. "Laboratory measurement of ultrasound velocity during accelerated aging tests: Implication for the determination of limestone durability". *Construction and Building Materials* 36, 977-983 (2012)
- 21 L.Mol, H.A. Viles. "Goelectric investigations into sandstone moisture regimes: Implications for rock weathering and the deterioration of San Rock Art in the Golden Gate Reserve, South Africa ". *Geomorphology* 118, 280-287 (2012)
- 22 O. Sass, H.A. Viles. "Wetting and drying of masonry walls: 2D-resistivity monitoring of driving rain experiments on historic stonework in Oxford, UK". *Journal of Applied Geophysics* 70, 72-83 (2010)
- 23 N. A. Cutler, H.A. Viles, S. Ahmad, S. McCabe, B.J. Smith. Algal 'greening' of stone heritage structures. *Science of the Total Environment*. 442, 152-164. (2013)
- 24 D. Huang, E. A. Swanson, C. P. Lin, J. S. Schuman, W. G. Stinson, W. Chang, M. R. Hee, T. Flotte, K. Gregory, C. A. Puliafito, J. G. Fujimoto, "Optical coherence tomography," *Science*, 254, 1178-1181 (1991).
- 25 Clark, R. N., 1999. Chapter 1: Spectroscopy of Rocks and Minerals, and Principles of Spectroscopy, in *Manual of Remote Sensing, Volume 3, Remote Sensing for the Earth Sciences*, (A.N. Rencz, ed.) John Wiley and Sons, New York, p 3- 58.
- 26 Kleinberg, R. L., 2002. Well Logging, *Encyclopaedia of Nuclear Magnetic Resonance*, John Wiley & Sons, 4960-4968.

## **2. Optical Coherence Tomography imaging of the subsurface structure of sandstone**

### **2.1 Introduction**

The first stage of studying cultural heritage materials is often to characterise their material properties. The petrographic properties of sandstone influence mechanical properties and so the vulnerability to weathering [1, 2].

Analysis of the grain size distribution of sandstone is carried out routinely at cultural heritage sites [2, 3, 4, 5, 6] to characterise the material properties of the stone such as the range of grain sizes, the mean and standard deviation. Some studies have found a correlation between the grain size distribution and mechanical properties of stone [1, 2, 7]. A smaller mean grain size may correlate with higher strength and a larger mean grain size may indicate that the stone is less well sorted.

Conventional methods to determine the grain size distribution of sandstone require the removal of samples from the site and subsequent sample preparation before analysis in a laboratory.

The standard method of particle size analysis by sieving requires the disaggregation of samples which can be difficult and time consuming through chemical or mechanical means. Petrographic studies to determine the grain size by image analysis of petrographic thin sections also requires extensive sample preparation.

Previous studies of rock art panels have relied on the collection of proxy samples from the same horizon but distanced from the rock art panels themselves. In the case of Roughting Linn, one of the best examples of rock art, there is nowhere to collect a representative sample from, because it is the only outcrop present [8].

The development of a non-invasive method to determine grain size distributions would enable measurements over different areas of an outcrop rather than relying on small samples to be

representative or the use of a proxy material. It would also enable measurements of the rock art motifs themselves to determine any effect on the subsurface structure due to their formation and to be repeated on the same point of the outcrop to monitor changes over time due to weathering processes.

OCT is a fast scanning Michelson interferometer that can measure backscattered light at each depth position within the sample to produce “virtual” cross sectional images of the surface and subsurface non-invasively. It was designed for non-invasive examination of the interior of the eye and the subsurface structure of biological tissues [9].

In biomedical applications optical coherence tomography has been used to produce non-invasive “optical biopsies” of human tissues in vivo in order to limit sampling and ensure samples are representative. It has also been used for the non-invasive imaging for paintings and archaeological objects to produce cross-sectional images of the subsurface structure in order to reduce sampling and enable examination on any are of the object [10-15] and has been used to investigate changes in scattering properties of a geological material (jade) due to natural and artificial aging [16, 17].

In the case of sandstone, optical coherence tomography can be used to produce virtual cross sections of the subsurface structure and can be used as an “optical thin section” to detect and characterise the grain size distribution in-situ without the need for sampling.

## **2.2 Materials and methods**

The instrument used is a portable Thorlabs OCP930R with a light source operating at a central wavelength of 930 nm and a full width half-maximum (FWHM) bandwidth of 100 nm. The axial resolution is 6.5  $\mu\text{m}$  in air and the lateral resolution is 9  $\mu\text{m}$ . The OCT probe consists of the Michelson interferometer and an objective lens with a numerical aperture of 0.06. A

scanning mirror within the OCT probe enables rapid scanning in the transverse direction. The OCT is a Fourier domain OCT where the reference mirror is stationary and the interference signal is collected as a function of wavelength through a spectrometer [18]. The interference spectrum is then resampled into uniform  $k$  space, tapered with a Hann window and Fourier transformed to obtain a depth resolved structure of the sample. The pixel intensity at a point in the image corresponds to the strength of the backscattered light from that point inside the object. The spectral interference pattern detected by the probe at each position contains information about the depth resolved structure of the sample in its spectral frequency content, which is recovered by Fourier transform for each depth scan. The structures within the material are visualised due to different optical scattering properties and when a series of adjacent depth scans are displayed form a ‘virtual cross-section’ image into the material.

The instrument has been used for the in situ examination of paintings and cultural heritage materials [14].

The probe is attached to a motorized micrometre linear stage, to obtain an image cube as the stage scans in the transverse y-direction perpendicular to the x-range of the scan.

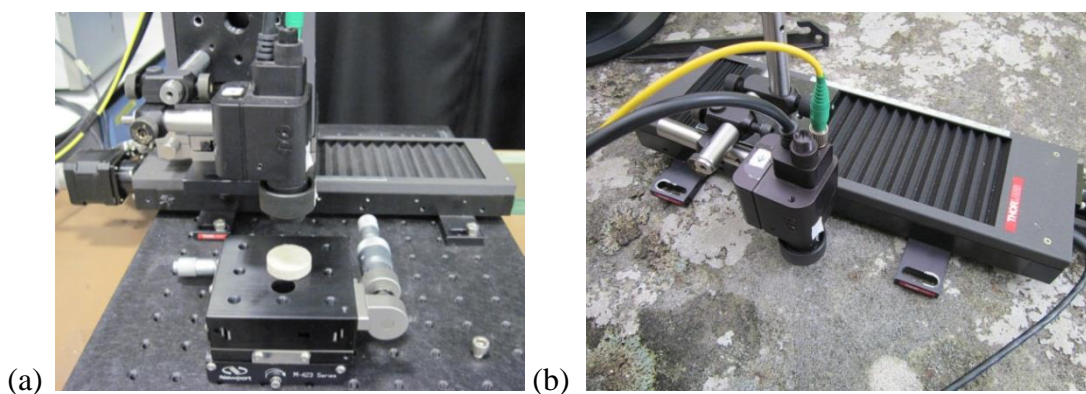


Figure 2.1 OCT probe set up on motorised stage for volume scanning (a) in laboratory (b) in situ at outcrop.

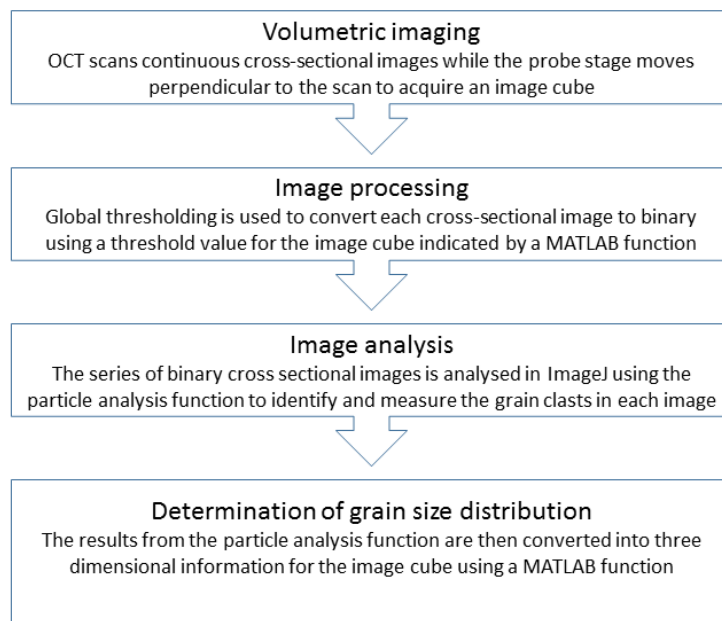


Figure 2.2 Flow chart summarising the OCT method to determine the grain size distribution of sandstone.

Figure 2.2 summarises the method by which OCT can be used to image a volume of sandstone to determine the grain size distribution of the sample. The three dimensional image cube is formed from a series of adjacent cross-sectional images which are themselves formed from a series of depth profiles.

Depth profiles (A-Scan) are obtained through a Fast Fourier Transform to retrieve axial information without the need for axial scanning in the system producing a simultaneous ‘virtual depth profile’ without any time lag between the data collected at each depth. The maximum instrumental depth range is 1.6 mm, however, the image depth for sandstones is limited by multiple scattering within the sample.

Laterally adjacent depth profiles (A-scans) are collected each one forming a pixel width column, to produce a two dimensional data set of adjacent depth profiles representing a cross-sectional plane through the material (B-scan). Three dimensional image volumes are formed from

consecutive cross-sectional scans, imaged as the probe is moved across the surface in transverse direction. A schematic of OCT image cube formation is shown in figure 2.3.

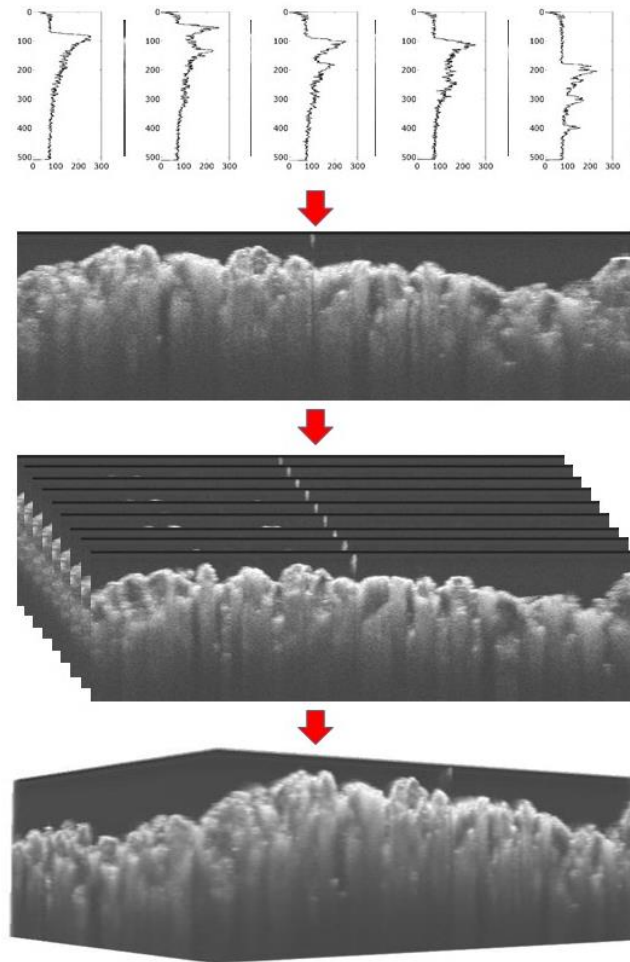


Figure 2.3 each cross-sectional 2D scan (B-Scan) consists of a series of consecutive depth profiles (A-Scan), three dimensional image volumes are formed from consecutive cross-sectional scans.

Figures 2.4 (a) and (b) shown example OCT virtual cross sections of sandstones. Visual examination of the cross-sections can identify the grain clasts within the sandstone, which appear dark in the OCT image, surrounded by the matrix of the stone which appears bright as it scatters the light. The grain clasts in (a), fine grained sandstone, are clearly smaller than those imaged in (b), coarse grained sandstone.

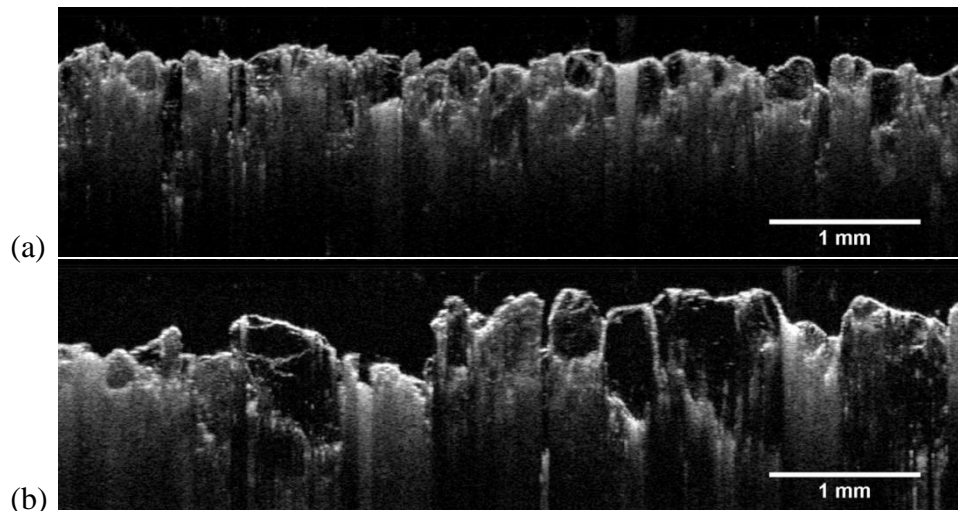


Figure 2.4 OCT virtual “cross sections” of (a) fine and (b) coarse grained sandstones, composite images formed from median pixel values of 100 stationary B-scans with A-scan averaging of 5.

To clarify the interpretation of the OCT images, sandstone samples were mechanically disaggregated in order to image the grain clasts in isolation. Disaggregated sand grains on a glass microscope slide were imaged from above, shown in figure 2.5, the grains appear dark in the OCT image because quartz is transparent. The edges of the grains appear brighter because of scattering due to the cementing particles on the surface of the grains and the strong reflection due to the refractive index discontinuity between quartz and air.

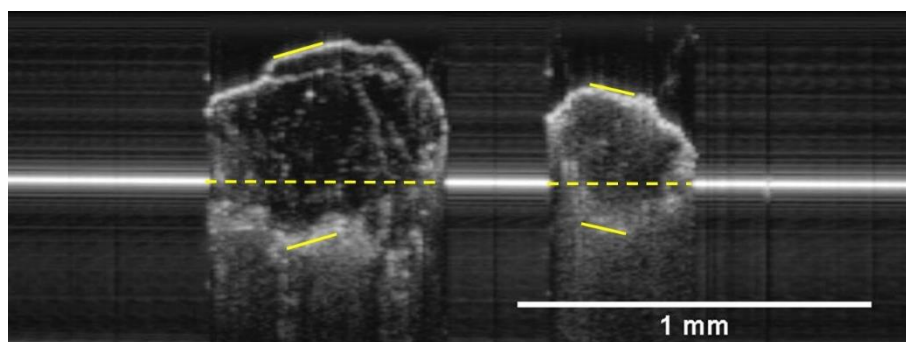


Figure 2.5 OCT virtual cross section through sand grains on a glass microscope slide. The distance between the top interface and the dashed line gives the actual physical thickness, the distance between the top and bottom interface gives the optical thickness of the grains

Since light travels slower in material than in air, OCT registers the optical thickness which is given by the physical thickness multiplied by the refractive index. The refractive index of the

sand grains can be determined from the OCT image from the ratio between the optical thickness and the corresponding physical thickness. The real position of the substrate can be extrapolated under the grain (yellow dashed line). The true surface of the microscope slide, and the apparent position of the grain interface and the height of the grain (yellow lines) indicate a refractive index of 1.54 for both the grains pictured in figure 2.5, consistent with the expected value for quartz. Due to the fact that OCT measures optical distances the axial resolution of the instrument is better in sandstone than in air, because of the refractive index of the material, it therefore translates to  $4.3 \mu\text{m}$  ( $6.5 \div 1.5$ ) in sandstone. In order to characterise system performance as a function of depth, images of reference materials were obtained over a depth range that extends outside the focus. As can be seen in figure 2.6 (a) the pixel intensities in the image decrease with depth. This intensity roll off was investigated using an OCT validation artefact of  $<800 \text{ nm}$  diameter FeO particles embedded in polyurethane. Figure 2.6(b) shows the maximum pixel intensity for an individual particle, monitored at increasing distance from the probe. Pixel intensities increase to the focus position then decrease with depth. Figure 2.6(b) demonstrates the effect of this across the lateral range of the scan, in this case the pixel intensities of the top surface of the artefact imaged at different depths through the range of the instrument.

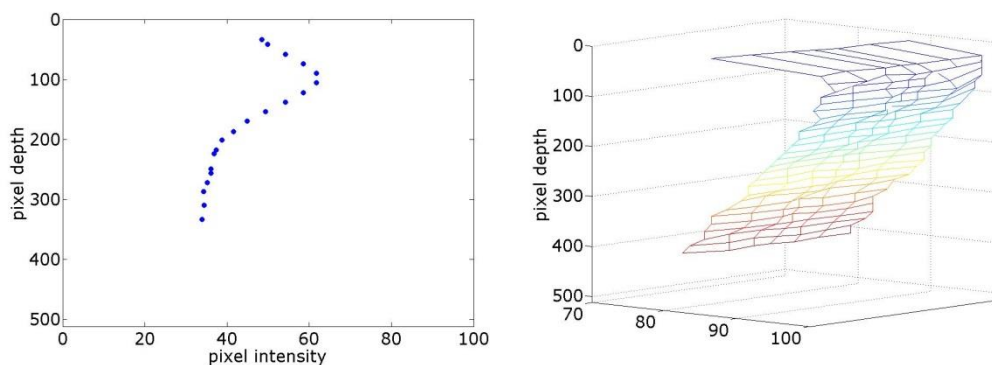


Figure 2.6 (a) Intensity roll off with depth for validation artefact particle. National Physical laboratory OCT PSF Validation Artefact  $<800 \text{ nm}$  diameter FeO in Polyurethane  $n=1.482$  (1300 nm) (b) Surface of NPL Validation Artefact imaged at 0.05 mm step difference.

## Samples

The two selected samples were collected from the sites of rock art panels at Weetwood Moor (WM) and Chatton Park in Northumberland. The samples were loose cairn stones from the area of the rock art panels, selected as proxy samples and considered by visual inspection of colour, grain size and composition to be lithologically representative of the panels. The un-weathered surface was obtained by slicing the samples using a diamond edged water cooled saw to access the interior un-weathered stone.

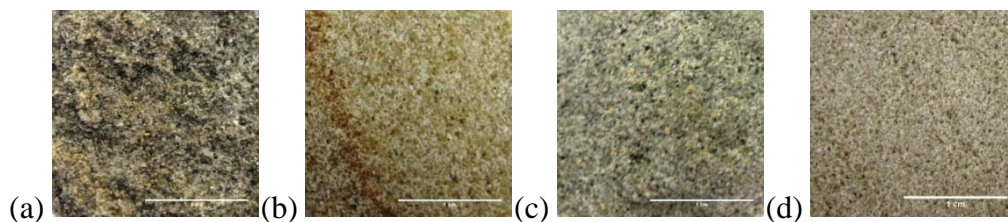


Figure 2.7 surface of sandstone sample from Chatton Park (a) naturally weathered (b) un-weathered; Weetwood Moor (c) naturally weathered (d) un-weathered.

### 2.3 Image acquisition

Unlike in-vivo biomedical applications where rapid acquisition speeds are required to reduce motion artefacts, in this application the sample is stationary and unchanged for the duration of a scan. This enables scanning at speeds which produce multiple depth profiles within the lateral resolution of the instrument to create a composite image with improved signal to noise ratio.

The phenomenon of speckle is manifested when a spatially coherent light source, such as a laser, is reflected from a microscopically rough surface causing a granular pattern [19]. The coherent incident light, that enables the interference of backscattered light with the light reflected from the reference mirror to form the OCT image, is also scattered by the different points on the microscopically roughness surface of the material, causing the interference between these backscattered light [20]. This constructive and destructive interference causes a speckle pattern of bright and dark within the image.

Multiple scattering within the sample as well as speckle, photon noise (shot noise) and instrumental thermal noise creates a graininess within the image that degrades the image quality and impairs boundary detection. The presence of noise features in the image makes detection of boundaries and image segmentation problematic making it difficult to differentiate grain structures. As the sample beam scans across the sample, the sequence of scattering events changes generating random intensity variations across the image, with the assumption that at every pair of coordinates (x, y) the noise is uncorrelated and has zero average value.

### 2.3.1 Image optimisation

Over-sampling of depth profiles within the lateral and transverse resolution range enables spatial averaging without significant degradation in transverse resolution of the resulting image; multiple depth profiles are collected at a slightly different position and then averaged, to increase the effective integration time thereby increasing the signal-to-noise ratio. The occurrence of vibration also act to de-correlate speckle patterns between scans.

An initial investigation was carried out to determine the effect of averaging while imaging a single cross-section. The improvement in image quality as a result of over-sampling was quantified using the contrast ratio of the image to determine the reduction in noise as a result of averaging.

An image contrast is defined as;

$$contrast = \frac{I_{\max} - I_{\min}}{I_{\max} + I_{\min}},$$

where  $I_{\max}$  is the maximum intensity in the image and  $I_{\min}$  is the minimum intensity in the image. In this case the contrast calculated is for the images in logarithmic intensity scales.

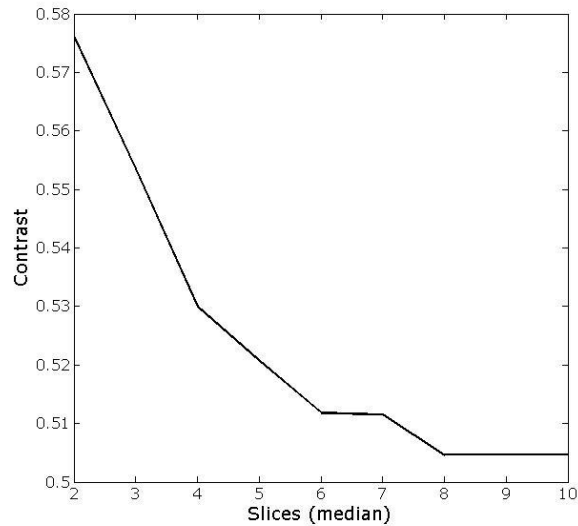


Figure 2.8 Image contrast as a function of the number of slices stacked to produce median intensity values from a stationary scan using an A-scan averaging factor of 5.

As shown in figure 2.8, the image contrast levels off at around 5 median averaged slices for an individual cross-section. Therefore a single image produced from a median of 5 slices in the transverse y-direction (spatially separated by 2 microns) with an A-scan averaging factor of 5 in the x-direction is effective for removing speckle noise which results in a decrease in the image contrast.

Post-acquisition image enhancement to reduce speckle was investigated through the use of spatial averaging of image pixels. The use of mean and median kernel filtering was investigated; each pixel is replaced by a value determined by the pixels in a defined neighbourhood around it. Mean kernel filtering results in a blurring effect while median kernel filtering reduces outlying pixel values. While both methods reduced the appearance of speckle within the images, the loss of clarity of structural edges accompanying the reduction of noise features rendered these methods inappropriate for this application.

### 2.3.2 Imaging protocol

To optimise imaging when the probe was in motion perpendicular to the cross section to acquire a volumetric image, scans were repeated over a section of the rock for each of the depth profile averaging options for the instrument (1 to 5 scans). For each depth profile averaging option, a series of scans were performed at the appropriate speed to allow a set number of cross sections within the lateral resolution of the instrument (1 to 10 frames). The optimum imaging protocol determined is described below.

1800 finely spaced depth profiles are collected across the 6 mm X-range with every 3 consecutive scans averaged to produce each of the 600 A-scans that form a B-scan cross sectional image, this also increases the effective integration time thereby increasing the signal-to-noise ratio in the shot noise (photon noise) dominated regime. The random arrival of photons is governed by Poisson statistics, whereby the photon noise is proportional to the square root of the number of photons. Averaging was performed in the transverse Y direction of the scan by setting the probe speed such that 8 depth scans were performed within the 9  $\mu\text{m}$  lateral resolution range. The pixel intensity values for every 8 consecutive scans were then averaged to produce composite cross sectional scans, the combined averaging protocol is illustrated in figure 2.9.

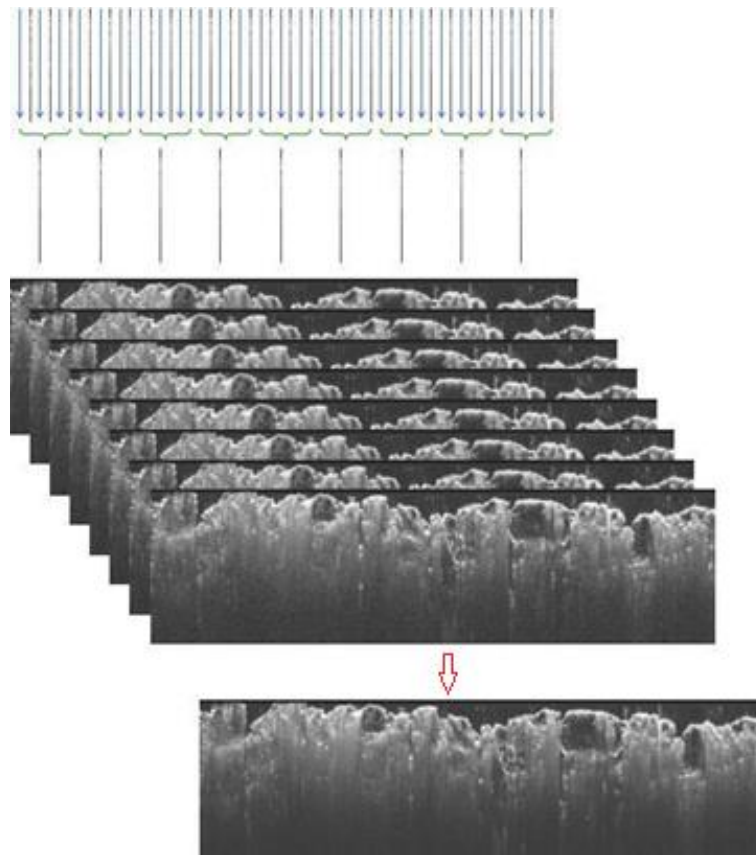


Figure. 2.9. Schematic illustration of spatial averaging protocol to improve image quality

This protocol of spatial averaging of both cross sectional scans and depth scans to create a composite image reduces noise features and improves the quality of the images. The success of image enhancement is determined by how well the image histogram can be partitioned enabling differentiation between grain and matrix regions.

Figure 2.10 (a) the virtual cross section no averaging and (b) histograms for pixels from grain and matrix regions show significant overlap. Figure 2.11 (b) shows an increased separation between pixel intensity values for grain and matrix regions improving the ability to partition the grain clasts by segmentation.

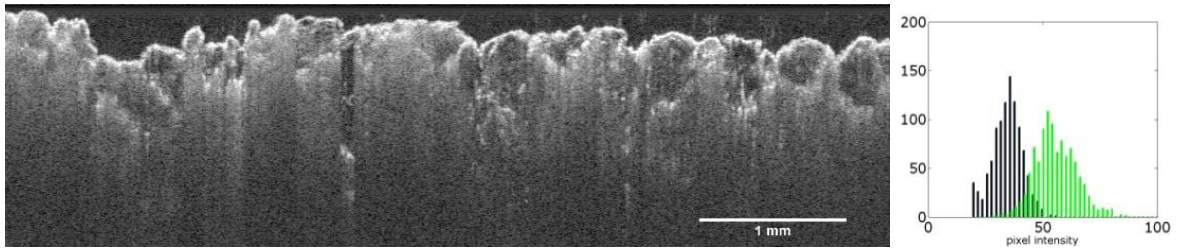


Figure 2.10. (a) OCT cross section image with no averaging (b) histogram of grain (blue) and matrix (green) regions.

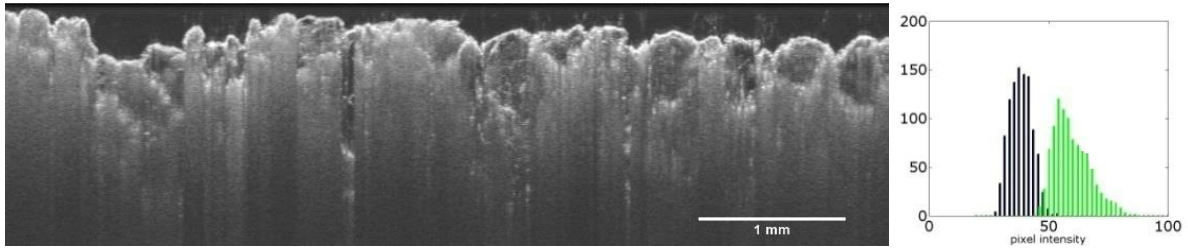


Figure 2.11 (a) OCT cross section image with optimal averaging (b) histogram of grain (blue) and matrix (green) regions.

For each combination of averaging, histograms of grain and matrix region pixel intensities were produced; a comparison between the histograms identified that a depth profile averaging of 3 combined with a cross section averaging of 8 produced the histogram with the greatest differentiation between pixel intensities for grain and matrix regions. Further averaging increased imaging time with no appreciable improvement in image quality.

The effect of spatial motion during scanning was investigated by performing 24 stationary scans and producing a median composite cross section image, which was then compared to composite formed using 8 spatially consecutive cross section images within the  $9\ \mu\text{m}$  resolution unit each formed of 600 columns produced by averaging 3 consecutive depth profiles.

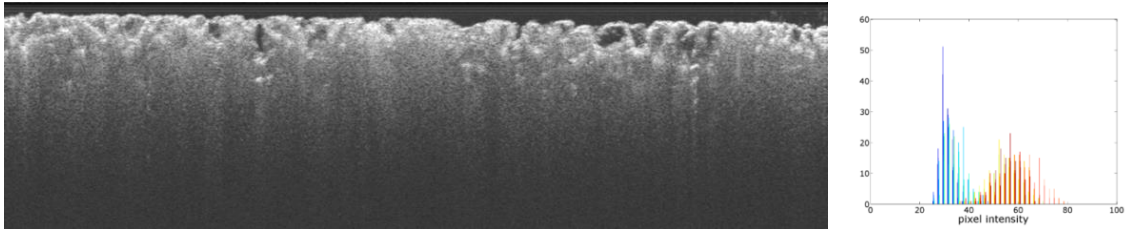


Figure 2.12 (a) Cross-section formed of 24 stationary B-scans (b) histogram of grain and matrix regions.

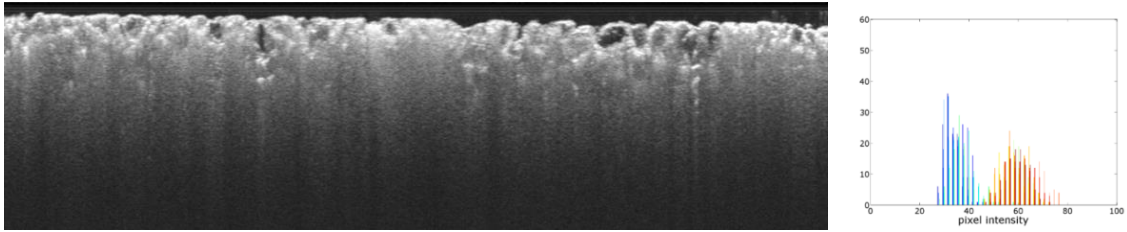


Figure 2.13 (a) Cross-section formed of 8 B-scans imaged within 9µm lateral movement with A-scan averaging of 3 (b) histogram of grain and matrix regions.

The histograms for pixel intensities of grain and matrix regions of the two images are similar but a greater separation between the two regions is seen for the moving scans.

Volumes imaged with the optimal averaging protocol show clear differences in the distributions of pixel intensities for grain and matrix regions shown in figure 2.14, improving the ability to detect and measure the grains.

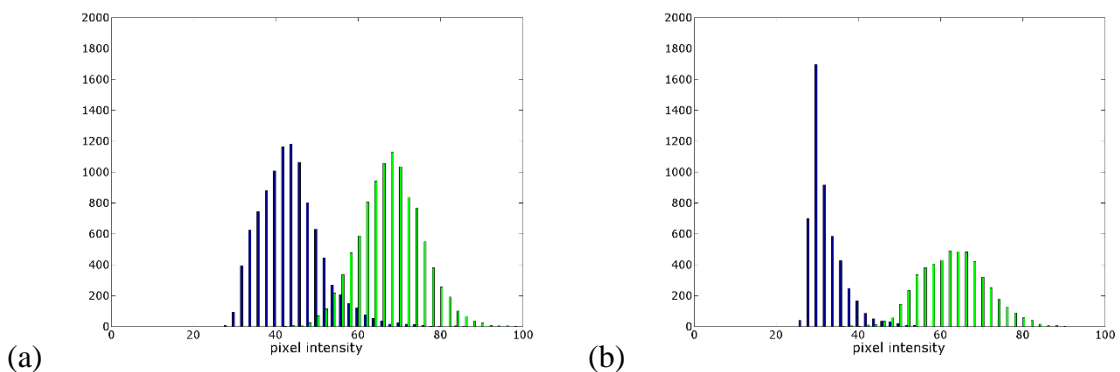


Figure 2.14 Optimal averaging protocol imaged WM (a) and CP (b) histogram of 10000 grain and 10000 matrix pixels

This protocol of spatial averaging of both cross sectional scans and depth profiles to create a composite image reduces noise features and improves the quality of the images.

## 2.4 Image analysis

Segmentation is an important step for feature extraction, subdividing an image into its constituent regions or phases. Since the sample has only two material phases; grain and matrix, segmentation based on a threshold value is appropriate and computationally simple and fast.

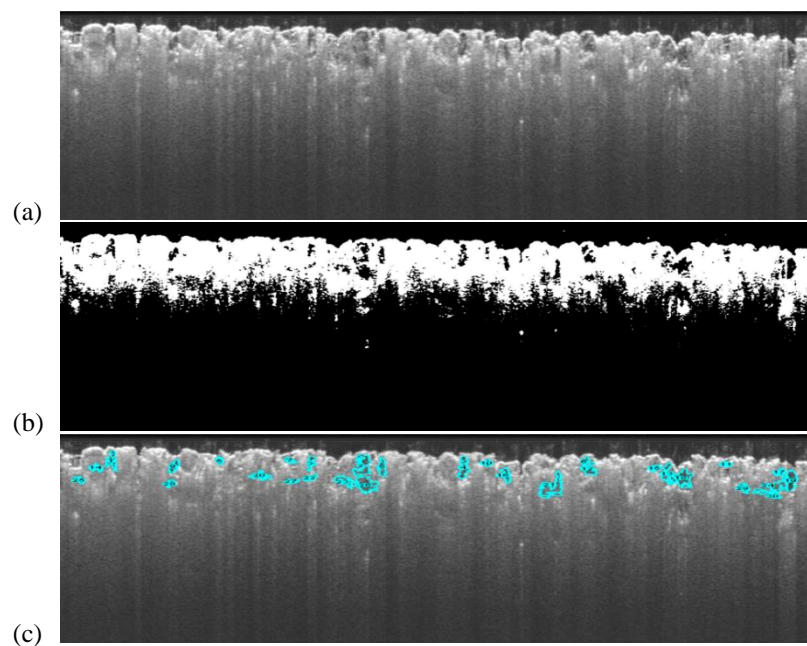


Figure 2.15 Grey scale image (6 mm x 0.9 mm), where grain clasts is dark and sandstone matrix is bright (6 mm x 0.9 mm); b) Binary image computed by thresholding image in (a), (c) Outlines of grain clasts identified from thresholded image (b) superimposed in blue on the grey scale image.

A threshold value is selected and the grey scale image is divided into a binary image of groups of pixels having intensity values less than the threshold and groups of pixels with values greater than or equal to the threshold. One threshold value was selected for the entire image stack based on the image histogram. Black colour in segmented image indicates clast grains and white indicates the solid matrix of the sandstone. Silica grains are transparent and so appear dark, the matrix of the sandstone contains many scattering particles so appears bright in the image. OCT

virtual cross-section for disaggregated grain clasts are shown in figure 2.16 for Chatton Park (CP) and 2.17 for Weetwood Moor (WM).

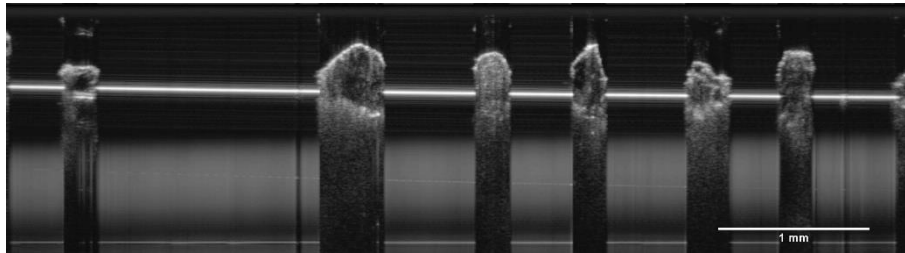


Figure 2.16 Disaggregated gains from CP samples on a glass microscope slide imaged from above.

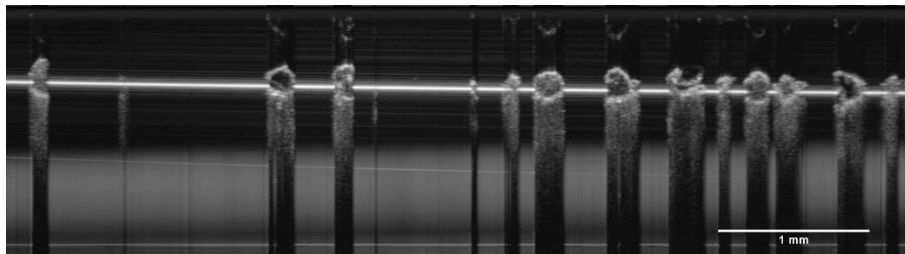


Figure 2.17 Disaggregated gains from WM samples on a glass microscope slide imaged from above.

In both images the material of the clast appears dark because it is transparent, while the edges of the gains appears bright because of scattering due to the presence of cementing material on the outside of the grains and the refractive index discontinuity between the grain and air.

The use of automated thresholding can result in large portions of the image being assigned to the wrong phase (grain or matrix) due to an incorrect threshold value. Figure 2.18 shows the number of grains identified as a function of the threshold level applied to the OCT image, demonstrating the effect of threshold selection on the analysis of OCT images.

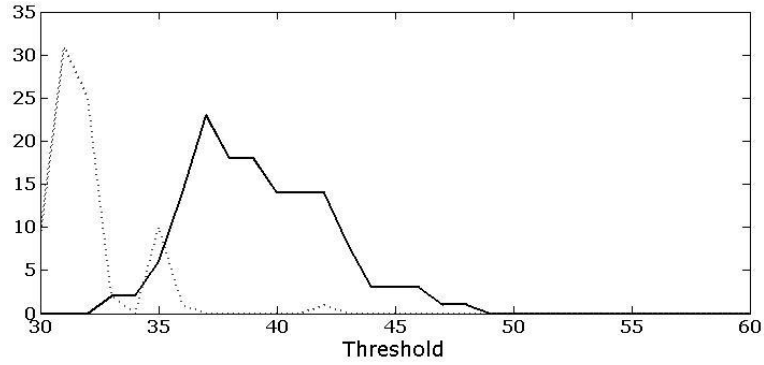


Figure 2.18 Number of grain regions identified as a function of threshold level; solid line represents grain regions correctly identified, dashed line indicates regions incorrectly identified as clast grains.

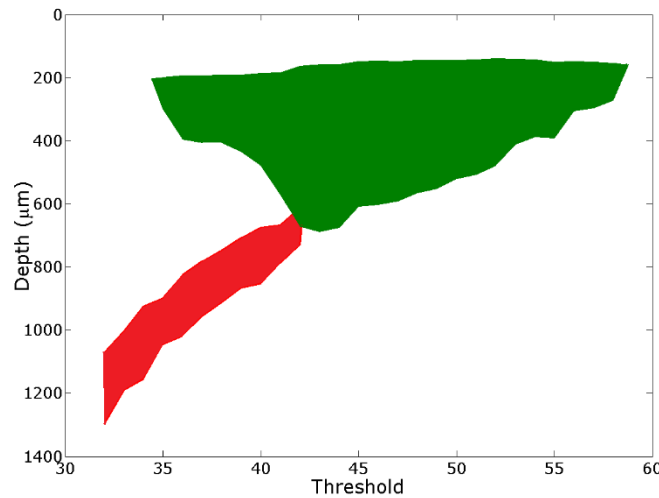


Figure 2.19 Depth range over which grains were correctly identified by automated analysis (green infill) as a function of the threshold value selected prior to grain finding. The region filled in red indicates the depth range where artefacts and noise in the image were incorrectly identified as grains.

Despite the intrinsic intensity roll off of FD-OCT, adaptive thresholding with depth was not helpful in this case. Global thresholding using a single value for the three dimensional image volume was found to be effective as well as computationally fast and efficient. A function was developed in MATLAB in order to sample pixel intensity values for grain and matrix regions and display a histogram of their distributions in order to determine the proper threshold value

with greater accuracy and reliability than visual evaluation. An investigation of 100 cross-section images by this function indicated that the appropriate threshold value can be determined from a single slice of the stack of images; the mean value for 100 cross-sections indicated an effective threshold value of  $44 \pm 1$  with a histogram bin size of 2.

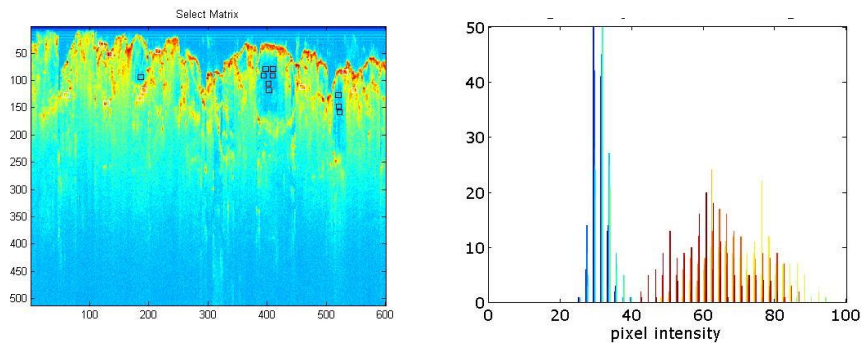


Figure 2.20 MATLAB function to determine appropriate value for thresholding

The refractive index discontinuity between grains and surrounding material detected by the OCT appears as a discontinuity in pixel intensity in the image which enables delineation of grains through edge detection. The particle analysis function in ImageJ was used to count and measure objects in the thresholded binary images using edge detection. Each object is outlined, measured and then filled to be made invisible, it then resumes scanning until it reaches the end of the image and moves on through the image stack. These results were then converted into three dimensional information using a MATLAB code.

The automated grain finding function was validated by visual inspection of 100 slices to identify any grain regions unidentified, or regions incorrectly identified as grains. The grain size distribution for automated (blue) and additional grains found by visual inspection (grey) are shown in figure 2.21, no incorrectly identified grain regions were found and automated grain finding was found to be  $\sim 90\%$  effective across the range of grain sizes found.

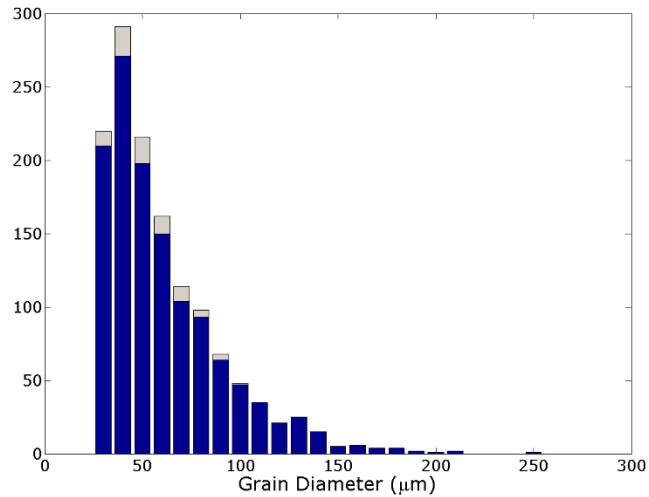


Figure 2.21 Grain size distribution found by automated particle analysis (blue) and visual inspection (grey).

Volume scans were performed with a B-scan cross-sectional width of 6 mm with the probe scanning continuously as it moved 6mm perpendicular to the B-scan axis at  $0.005 \text{ mm s}^{-1}$  to produce the imaged volume of a 6 x 6 mm region to a depth of 0.9 mm.

The grain size distributions found from volume scans WM 1 and 2 are shown in figure 2.22. Volume scan WM 1 was performed on the fresh cut surface of a sample from the interior of the WM cairn stone. Within this volume 1709 grains were identified, representing 15% of the total volume, the size distribution of which is shown by the blue bars. The minimum grain size detected was  $31 \mu\text{m}$ , the maximum  $162 \mu\text{m}$  with a mean of  $57 \mu\text{m}$  and standard deviation of 26.

Volume scan WM 2 was performed on the weathered surface of a sample from the exterior of the WM cairn stone. Within this volume 921 grains were identified, representing 13% of the total volume, the size distribution of which is shown by the green bars. The minimum grain size detected was  $31\mu\text{m}$ , the maximum  $223 \mu\text{m}$  with a mean of  $60 \mu\text{m}$  and standard deviation of 30.

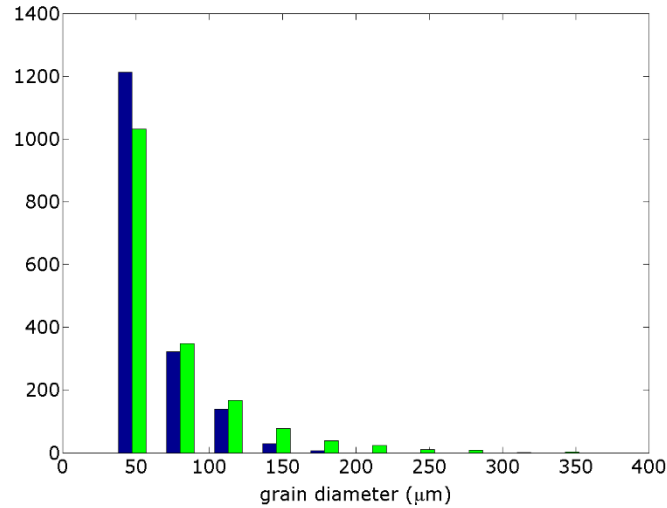


Figure 2.22 Representative grain size distributions for WM sample fresh (blue bars) and weathered surfaces (green bars).

The grain size distributions found from volume scans CP 1 and 2 are shown in figure 2.23. Volume scan CP 1 was performed on the fresh cut surface of a sample from the interior the of CP cairn stone. Within this volume 2511 grains were identified, representing 22% of the total volume, the size distribution of which is shown by the blue bars. The minimum grain size detected was 31 μm, the maximum 271 μm with a mean of 62 μm and standard deviation of 37.

Volume scan CP 2 was performed on the weathered surface of a sample from the exterior of the CP cairn stone. Within this volume 1230 grains were identified, representing 31% of the total volume, the size distribution of which is shown by the green bars. The minimum grain size detected was 31 μm, the maximum 359 μm with a mean of 69 μm and standard deviation of 45.

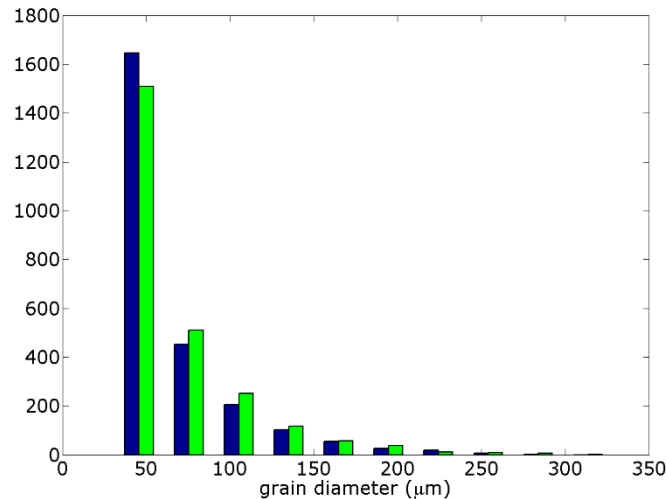


Figure 2.23 Representative grain size distributions for CP sample fresh (blue bars) and weathered surfaces (green bars).

Statistical analyses were performed to determine whether weathering had an effect on the grains size distributions of the samples, through the dissolution or fracturing of grains. The Kolomogorov-Smirnov (KS) test is a non-parametric test of probability distributions, which is used to determine whether samples are drawn from the same distribution. A two sample KS test is used to determine whether two distributions are part of the same parent distribution. The two sample Kolomogorov-Smirnov tests performed for each sample indicate that both weathered and un-weathered grain size distributions for each sample are from the same parent population, indicating that there was no change due to weathering, while the distributions for WM and CP are distinct populations.

The grain size distributions for the samples are consistent with those reported in previous studies of the locations and the Fell sandstone group [7, 8].

The OCT image volumes can also be used for surface profilometry to monitor changes due to weathering at the surface of the stone. Stone decay produces uneven surfaces by differential weathering of constituent materials and topographical features that may be the result of

granular disintegration and material loss, surface profiles for the fresh cut and weathered samples are shown in figure 2.24.

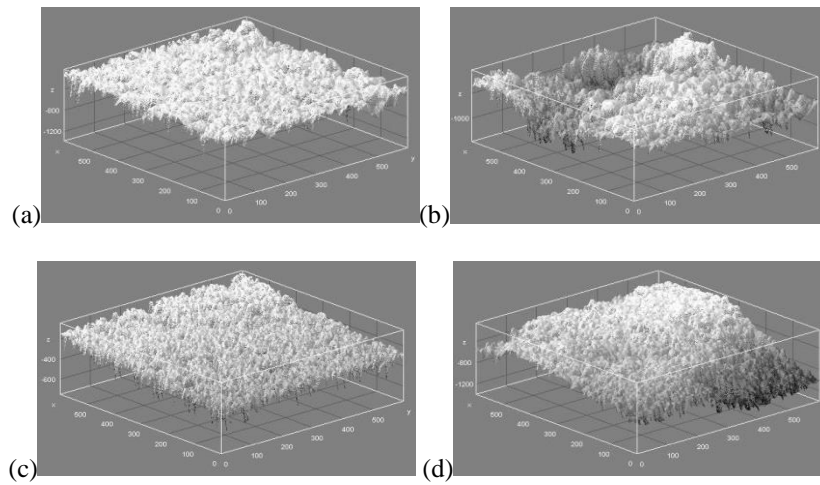


Figure 2.24. Surface profiles for 6 x 6 mm scanned for (a) CP un-weathered; (b) CP weathered; (c) WM un-weathered; (d) WM weathered

To enable a comparison of the technique with another imaging method x-ray micro-computed tomography (micro-CT) volumetric imaging of samples was performed at Nikon Metrology. Data is generated using an x-ray source that rotates around the object; which is then integrated to generate three-dimensional volumetric information. Samples were imaged with a voxel size of  $5.18 \mu\text{m}$  (comparable to the resolution of the OCT images), shown in figure 2.25.

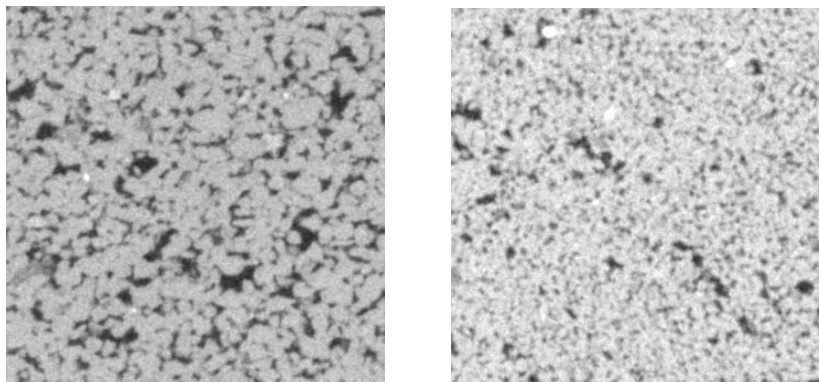


Figure 2.25 Micro-CT imaging of a 6 x 6 mm area of CP (a) and WM (b) samples, the pore spaces within the sample appear dark while the grains and matrix appear bright.

Micro-CT enables three dimensional visualisation of the internal microstructure of the sample according to the composition and density. Each pixel in a tomographic slice corresponds to a voxel in a three dimensional image, the grey scale value of the voxel is determined by the x-ray absorption of the material at that point. The greater the absorption of the x-ray the brighter the voxel appears, the pore spaces within the sample appear dark while the grains and matrix appear bright.

Unlike OCT images where the refractive index discontinuity enables edge detection to identify and measure the grains, in micro-CT the density discontinuity between grains that are of similar composition was insufficient to allow the grains to be delineated. Visual inspection of CT images showed grain sizes to be consistent with those found by OCT imaging.

## **2.5 Summary**

Optical coherence tomography is an effective non-invasive method to determine grain size distributions that will enable measurements over different areas of an outcrop rather than relying on small sample to be representative or the use of a proxy material.

The depth range of imaging covers the subsurface structure of the stone at its interaction with the environment where the majority of weathering effects are likely to occur. The method can detect grain sizes from coarse silt (0.031-0.063 mm) to coarse sand (0.50-1.00 mm) determined by the resolution of the instrument and its depth range in the sample. The percentage of sandstone volume imaged as detectable grains varies with the sample but can be used to produce a representative grain size distribution.

It also enables measurements of the rock art motifs themselves to determine any effect on the subsurface structure due to their formation and to be repeated on the same point of the outcrop to monitor changes over time due to weathering processes.

## References

1. R. Prikryl, Assessment of rock geomechanical quality by quantitative rock fabric coefficients: Limitations and possible sources of misinterpretations. *Engineering Geology*. 87, 149-162. (2006)
2. F.G. Bell, P. Lindsay, The petrographic and geomechanical properties of some sandstones from the Newspaper Member of the Natal Group near Durban, South Africa. *Engineering Geology*, 53, 57-81 (1999)
3. B. Fitzner, K. Heinrichs, D. La Bouchardiere. Weathering Damage on Pharonic sandstone monuments in Luxor Egypt. *Building and Environment*, 38, 1089-1103 (2003)
4. H. Siedel, S. Pfefferkon, E. von Plehwe-Leisen, H. Leisen. Sandstone weathering in a tropical climate: Results of low-destructive investigations at the temple of Angkor Wat, Cambodia. *Engineering Geology*, 115, 182-192 (2010)
5. P. Martinec, M. Vavro, J. Scucka, M. Maslan. Properties and durability assessment of glauconitic sandstone: A case study on Zamel sandstone from the Bohemian Cretaceous Basin (Czech Republic). *Engineering Geology*, 115, 175-181 (2010)
6. C. Sancho, R. Fort, A. Belmonte. Weathering rates of historic sandstone structures in semiarid environments (Ebro basin, NE Spain). *Catena*, 53, 53-64, (2003)
7. F.G. Bell, The physical and mechanical properties of the Fell Sandstones, Northumberland, England. *Engineering Geology*, 12, 1-29, (1978)
8. English Heritage Report: Prehistoric Rock Art in Northumberland. C/300192/A/001, 006007555, 324/9130, (2006)
9. D. Huang, E.A. Swanson, C.P.Lin, J.S. Schuman, W.G. Stinson, W. Chang, M.R. Hee, T. Flotte, K. Gregory, C.A. Puliafito and J.G. Fujimoto. Optical Coherence Tomography. *Science* 254, 1178-1181 (1991)

10. P. Targowski, B. Rouba, M. Wojtkowski, A. Kowalczyk. Application of optical coherence tomography to non-destructive examination of museum objects. *Stud. Conserv.*, 49, 107-114, (2004)
11. H. Liang, R. Cucu, G. M. Dobre, D.A. Jackson, J. Pedro, C. Pannell, D. Sanders, A.G. Podoleanu. Application of OCT to examination of easel paintings. *Proc. SPIE* 5502, 378, (2004)
12. H. Liang, M. Cid, R. Cucu, G. Dobre, A. Podoleanu, J. Pedro, D. Sanders. En-face optical coherence tomography – a novel application of non-invasive imaging to art conservation, *Opt. Express* 13, 6133-6144, (2005)
13. P. Targowski, M. Iwanicka. Optical coherence tomography: its role in the non-destructive structural examination and conservation of cultural heritage objects – a review, *Appl. Phys. A*, 106, 265-277, (2012)
14. H. Liang, B. Peric, M. Hughes, A. Podoleanu, M. Spring, S. Roehrs. Optical coherence tomography in archaeology and conservation science – a new emerging field. *Proc. SPIE*, 7139, 713915, (2008)
15. URL: <http://www.oct4art.eu>.
16. M.L. Yang, C.W. Lu, I.J. Hsu, C.C. Yang. The use of optical coherence tomography for monitoring the subsurface morphologies of archaic jades. *Archaeometry*, 46, 171-182 (2004)
17. S. Chang, Y. Mao, G. Chang, C. Flueraru. Jade detection and analysis based on optical coherence tomography images. *Opt. Eng.*, 49, 063602, (2010)
18. A.F. Fercher, C.K. Hizenberger, G. Kamp, S.Y. El-Zaiat. Measurement of intraocular distances by backscattering spectral interferometry. *Opt. Commun.* 117, 43-48, (1995)
19. Hecht, E. *Optics*, Addison-Wesley Publishing, Reading MA (1987)

20. J. Kim, D.T. Miller, E. Kim, S. Oh, J. Oh, T.E. Milner, Optical coherence speckle reduction by a partially coherent source, *Journal of Biomedical Optics*, 10 (6), (2005)

## **Chapter 3. Optical Coherence Tomography measurement of Hydraulic Conductivity**

### **3.1 Introduction**

Capillary rise of groundwater and associated transport of mineral salt and other pollution into the porous network of stones has been reported as a significant cause of weathering damage at many cultural heritage sites [1, 2].

Most deterioration effects in porous sandstone arise as a direct or indirect consequence of water [3]. Deterioration can be as a result of chemical, physical and biological processes. The movement of water through the stone can result in solutional material loss [4]. The penetration of water in sandstones causes mechanical stresses due to the swelling of clay minerals causing differential pressures. Water transports soluble salts and impurities that can crystallize, putting pressure on the pore walls. The water absorption properties of the stone can be used to predict the vulnerability to these common decay mechanisms [3]. Similar mechanical stresses occur as a result of freeze-thaw cycles acting on stone materials [3]. The availability of water and soluble nutrients also encourages the growth of organisms responsible for bio deterioration [4]. Water absorption properties of rocks have been used for some time as durability estimators of stone and building materials [6]. Liquid invasion into the porous network is controlled by material properties, such as porosity and pore size distribution. Hydraulic conductivity is the velocity of the wetting front and describes the ease with which water can move through the pore spaces of the material.

Several methods have been used for in situ measurement of water ingress into stone for stone conservation applications. Water absorption tube testing such as RILEM test method 11.4, is a simple method used to evaluate the water absorption of a porous material. When a water column is applied on the surface of a porous material, the water volume absorbed after a definite time is a characteristic of the material. The technique provides bulk measurement but

cannot identify variations in depth from the surface, so it cannot detect the early stages of deterioration to the stone surface before it progresses to the interior of the stone.

Electrical resistivity methods [7] have been used to profile moisture ingress and distribution, by measuring the resistance between two points attached or tapped in to the surface of the object. The technique is based on the concept that the electrical resistance of a material will decrease when water is present. The quantitative estimation of water content from resistivity measurement is less reliable because of the potentially disruptive influence of dissolved salts. The use of probes may influence the absorption of water at the surface and limits the technique to centimetre scale resolution.

Nuclear magnetic resonance can be used to investigate the presence and flow behaviour of water within saturated porous materials, but in general it requires orders of magnitude longer measurement times as described in Chapter 5 and has much lower resolution, especially for in situ measurements [8]. It is not suited to monitoring transient events in situ.

The increasing emphasis on non-destructive testing in conservation and the demand for through characterisation of materials in situ can be met through the application of portable diagnostic methods, such as optical coherence tomography (OCT).

The use of OCT for investigation of water within porous materials is based on the fact that as water displaces air in the porous network of the sample it reduces refractive index mismatch. Water has a refractive index (RI) of 1.33 (c.f. air refractive index of 1) closer to quartz (RI of 1.54), the primary constituent of sandstone samples. The effect of this is to reduce scattering within the sample and decrease the pixel intensity values of the image. Optical clearing is a well-known technique in OCT imaging of biological tissues [9, 10]. OCT produces non-invasive and non-destructive depth resolved quantification of hydraulic conductivity in sandstones and other porous materials to determine the vulnerability of the material to

weathering. This is analogous to OCT monitoring the permeability coefficient of aqueous glucose solution in biological tissues [11, 12]. The method for determining the hydraulic conductivity of a material is summarised in figure 3.1.

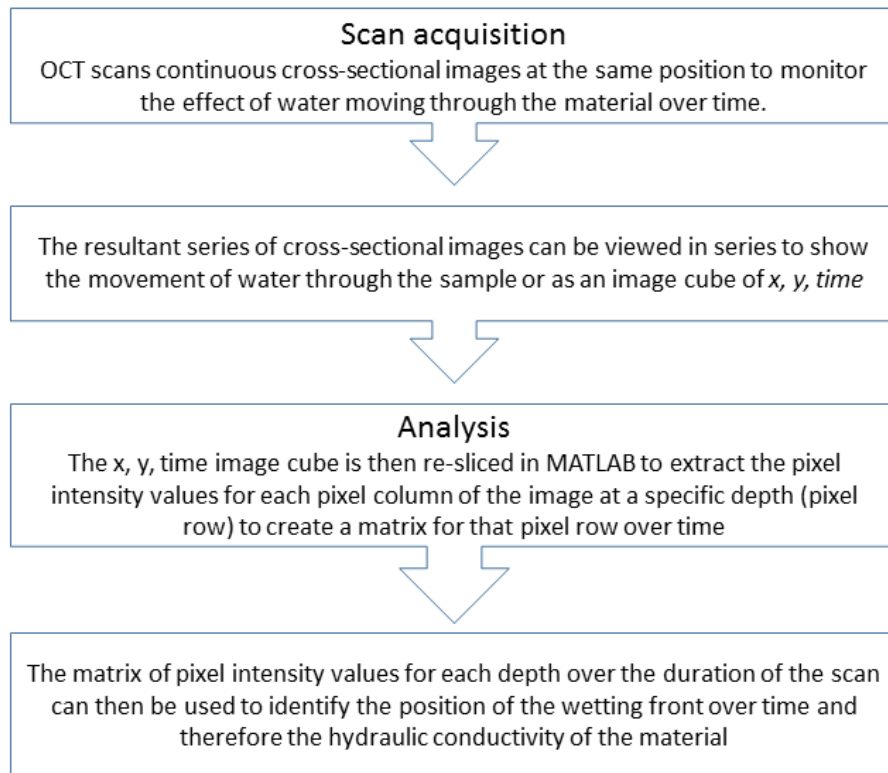


Figure 3.1 Flow chart summarising OCT method to determine hydraulic conductivity of materials.

## 3.2. Materials and methods

### 3.2.1 Samples

#### Sintered discs

Sintered discs are porous filtration discs composed of quartz glass granules that have been fused together. They were selected as porous materials with a similar refractive index as

sandstone, to model the technique with the simplification of a single component material and homogenous structure.

### Sandstone

The two selected materials were collected from the sites of rock art panels at Weetwood Moor (WM) and Chatton Park (CP) in Northumberland. The samples were fine grained with a mean pore size of 2  $\mu\text{m}$  (WM) and medium grained with a mean pore size of 5  $\mu\text{m}$  (CP). These pore sizes were determined from mercury intrusion porosimetry (MIP) [13].

### 3.2.2 Measurement Procedure

Measurements were made at a distance of 10 mm from the imbibition point at the sample surface (figure 3.2). Water is added at a rate to ensure that a surface droplet is on the surface throughout the experiment, thus matching supply to imbibition and preventing water flooding across the surface of the sample.

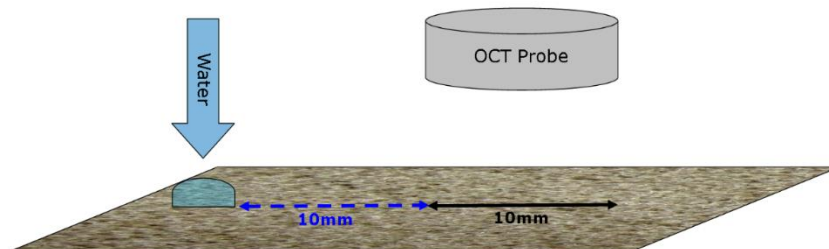


Figure 3.2. Schematic of measurement procedure: water is added 10 mm away from the 10 mm lateral range of the scan to allow water to penetrate through the depth of the sample before spreading laterally by capillary action.

Measurements were also performed with the sample in a vertical position with water added below the observed range to investigate the influence of gravity on wetting.

OCT images were recorded with the probe stationary, monitoring a 10mm transverse range at 1.14 frames per second continuously for the duration of the experiment. Each 'virtual' cross section (B scan) is produced from 1000 depth profiles (A scans), giving an image size of 10 mm by 1.6 mm formed of 1000 x 512 pixels, with measurements taking from under a minute to several minutes in duration. The technique provides depth resolved measurement but with limited penetration depth into the sample due to the level of scattering; the effect of water can only be registered to a depth of ~ 1 mm depending on the material.

The image acquisition speed of the instrument was set appropriate to the requirements of the application, optimising the signal to noise ratio within the time scale of the wetting process investigated. Unlike biomedical imaging applications where fast imaging speeds are required to reduce motion artefacts, in this case the imaging speed required is determined by the time taken for water to travel across the 10 mm range of the sample under observation. This allows for slower imaging to increase the signal to noise ratio to improve the detection of changes in the scattering properties of the sample due to the presence of water. With the set image application time of 0.88 seconds per frame (B scan), if the wetting front moves across a 10 mm range within a single image frame, its velocity is above  $1 \text{ cm s}^{-1}$  and can therefore be considered to be permeable with regards to hydraulic conductivity [13]. In a 2 hour observation time under these settings and taking 0.1 mm (10 columns of A scans) as the minimum distance range of detectable water movement, wetting velocities down to  $10^{-6} \text{ cm s}^{-1}$  can be measured; that is, the stone can be considered impervious to water. The full range of hydraulic conductivities that are likely to occur in natural sandstones ( $10^{-6}$  to  $1 \text{ cm s}^{-1}$ ) can be detected by this imaging speed.

Virtual cross sectional images of samples are shown when dry and wet in figures 3.3 and 3.5 for sintered discs and figures 3.8 and 3.10 for sandstones. The presence of water in the sample will reduce scattering as it reduces the refractive index mismatch; consequently features can be seen to a greater depth within the sample. Water acts as a clearing agent for sandstone and

sintered discs. The stack of cross-sectional images over time can be displayed as an  $(x, y, t)$  image cube as shown in figure 3.3.

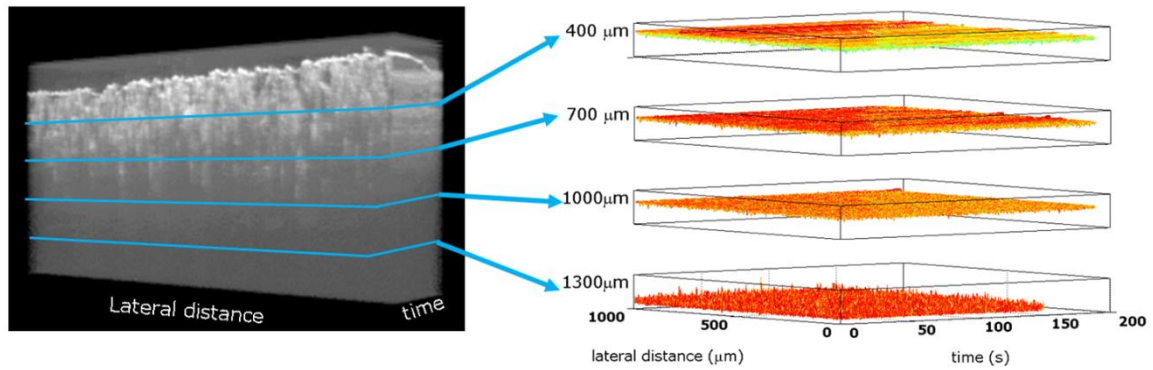


Figure 3.3. Stack of OCT cross sections as a function of time displayed as a  $(x, y, t)$  image cube from which depth “slices”  $(x, time)$  can be extracted.

Pixel intensity values across a single row representing a specific depth were extracted from each cross section in MATLAB over the duration of the measurement to create a matrix of pixel intensity values at a specific depth over time.

### 3.3 Results and discussion

Figures 3.5 and 3.7 show the decrease in the pixel intensity values due to the reduction of scattering in the two sintered discs caused by the presence of water in the pore network. In figures 3.5(a) and 3.7(a), depth scan intensity values were averaged across the 10 mm lateral range of the cross section for both a wet and a dry sample. The initial peak centred at approximately 250-300  $\mu\text{m}$  is due to scattering at the surface of the sample. There is a slight shift in the peak position for wet and dry samples in figure 3.5 (a) because a film of water was formed at the surface due to capillary action. The rougher surface due to the larger glass particles of the 5-15  $\mu\text{m}$  pore range sintered disc results in a broader peak in figure 3.5 (a)

compared to figure 3.7(a) where the smooth surface of the 1-2  $\mu\text{m}$  pore diameter disc gives a sharper peak.

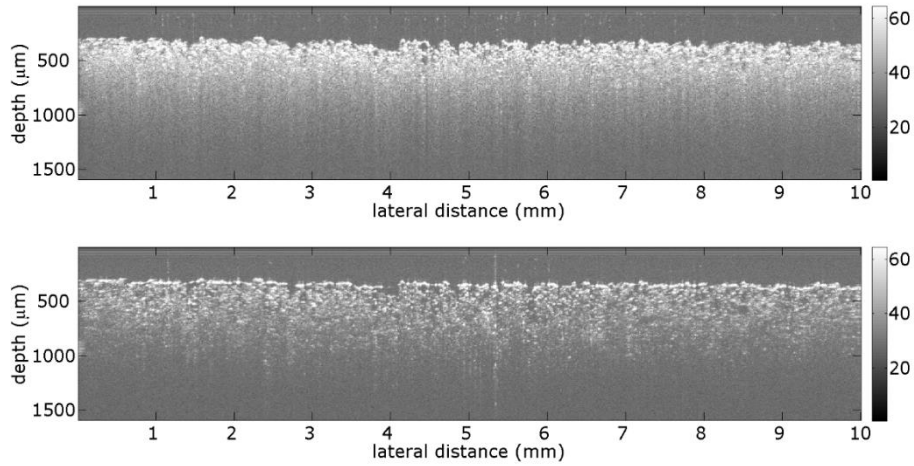


Figure 3.4. OCT virtual cross sections of sintered disc (5-15  $\mu\text{m}$  pore size) when (a) dry and (b) wet.

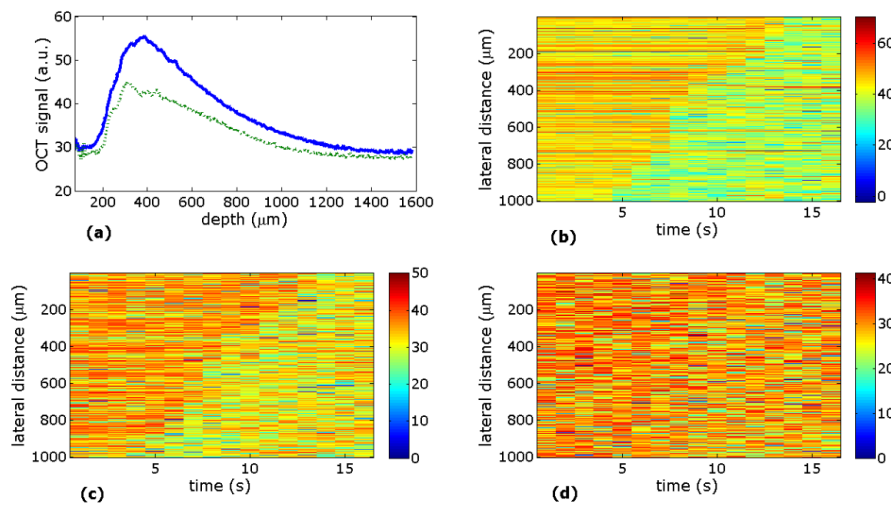


Figure 3.5. Sintered disc (5-15  $\mu\text{m}$  pore size): (a) pixel intensity values averages across the 10 mm cross sections when dry (solid blue line) and wet (dotted green line); signal intensity values at depth of (b)  $\sim 400 \mu\text{m}$ , (c)  $\sim 700 \mu\text{m}$ , and (d)  $\sim 1000 \mu\text{m}$  across the lateral range of the scan over time. The OCT signals are in log scales.

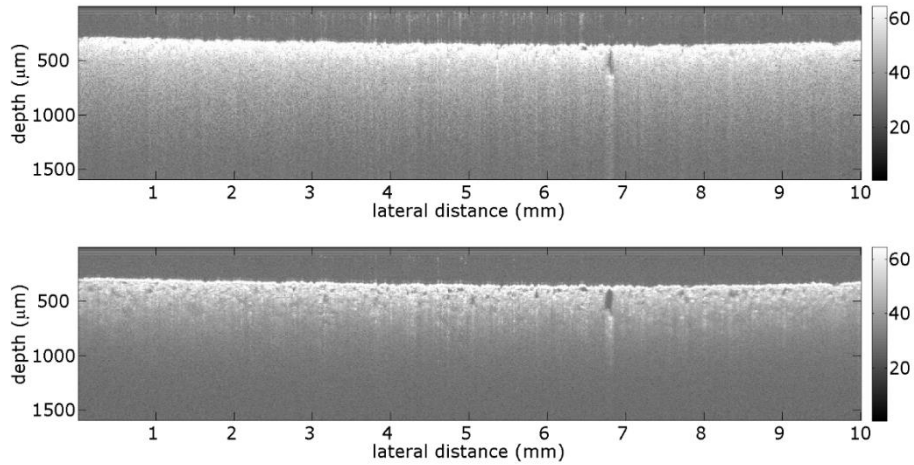


Figure 3.6. OCT virtual cross sections of sintered disc (1-2  $\mu\text{m}$  pore size) when (a) dry and (b) wet.

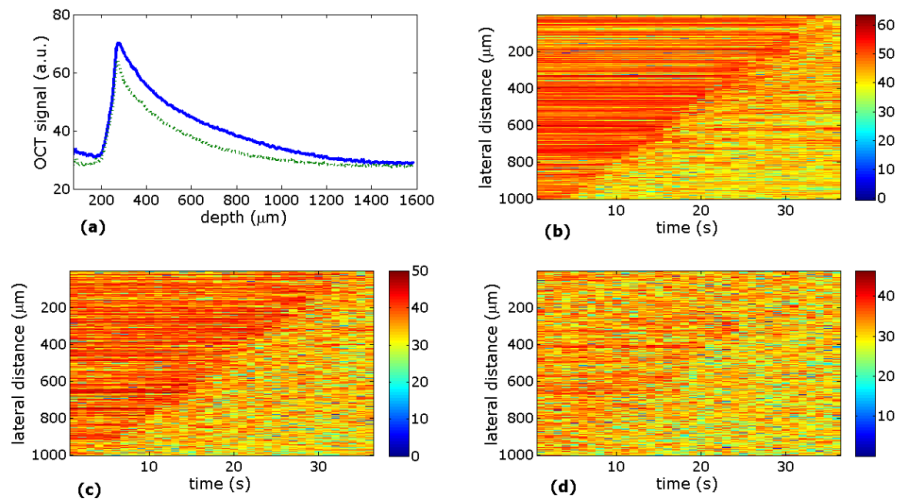


Figure 3.7. Sintered disc (1-2  $\mu\text{m}$  pore size): (a) pixel intensity values averages across the 10 mm cross sections when dry (solid blue line) and wet (dotted green line); signal intensity values at depth of (b)  $\sim 400 \mu\text{m}$ , (c)  $\sim 700 \mu\text{m}$ , and (d)  $\sim 1000 \mu\text{m}$  across the lateral range of the scan over time. The OCT signals are in log scales.

Pixel intensity values decreased more significantly for the 5-15  $\mu\text{m}$  pore diameter sintered disc than the 1-2  $\mu\text{m}$  pore diameter disc across the image irrespective of depth until the effects of water can no longer be detected at approximately 1 mm.

The  $(x, y, t)$  image cube is then resliced in MATLAB to show depth resolved changes over time (figures 3.5(b) –3.5(d) and 3.7(b)-3.7(d)). The wetting front can be seen moving across the

lateral distance of the scan at different depths within the sample to identify any changes within the properties of the sample with depth from the surface. Pixel rows were selected at different depths within the sample and are shown for depths of  $\sim 400 \mu\text{m}$ ,  $700 \mu\text{m}$  and  $1000 \mu\text{m}$  across the lateral range of the scan over time for sintered discs with pore diameter range of  $5\text{-}15 \mu\text{m}$  in figure 3.4 and  $1\text{-}2 \mu\text{m}$  in figure 3.6. In figure 3.5(b)-3.5(d) water enters at 3 s at 10 mm and crosses the lateral range to 0 mm at 14 s, and in figures 3.7(b)-3.7(d) it enters at 3 s and crosses the lateral range by 44 s, showing little difference in water movement speed in the lateral direction between the different depths.

The hydraulic conductivity is given by the velocity of the wetting front. Figure 3.8 shows that the hydraulic conductivity of the sintered disc with  $5\text{-}15 \mu\text{m}$  pores is  $\sim 4$  times as high as the disc with  $1\text{-}2 \mu\text{m}$  pores.

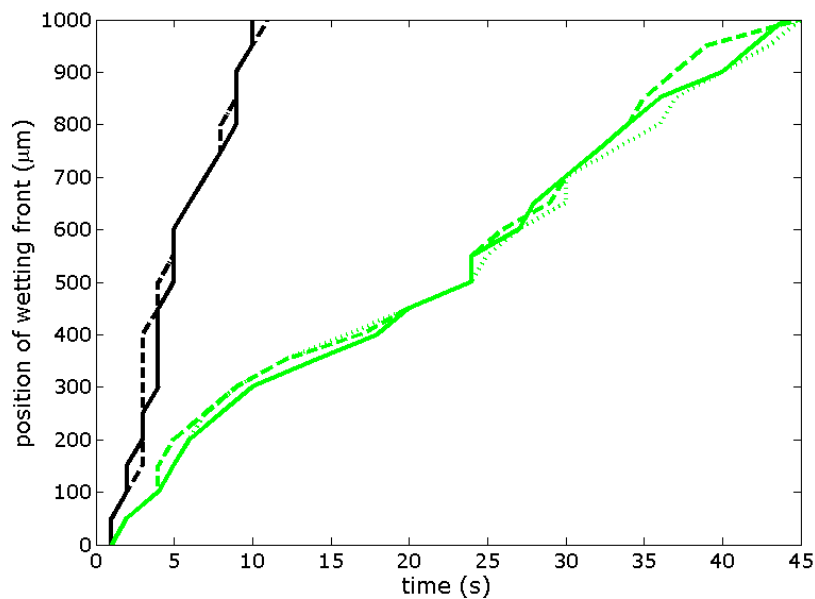


Figure 3.8. Position of the wetting front over time for sintered discs with  $5\text{-}15 \mu\text{m}$  pore size range (black lines) and  $1\text{-}2 \mu\text{m}$  pore size range (green lines) shown at depths of  $\sim 400 \mu\text{m}$  (solid line),  $\sim 700 \mu\text{m}$  (dashed line) and  $1000 \mu\text{m}$  (dotted line) into the sample.

Figures 3.10 and 3.12 show that the pixel intensity values decreased for the WM sandstone and the CP sandstone due to the penetration of water across the image irrespective of depth until

the effects of water can no longer be detected at approximately 1 mm in the sandstone samples. The depth penetration for the technique is similar for both sandstone samples. The initial peak centred at approximately 200-250  $\mu\text{m}$  on figure 3.10(a) and figure 3.12(a) is due to scattering at the surface of the sample. Figures 3.10(b) to 3.10(d) and 3.12(b) to 3.12(d) sample the signal intensity at a specific depth of 400, 700 and 1000  $\mu\text{m}$  over the duration of the experiment, there is no depth dependent difference in the hydraulic conductivity in the WM and CP samples. In figures 3.10(b)-3.10(d) water enters at 25 s at 10 mm and crosses the lateral range to 0 mm at 127 s and in figures 3.12(b)-3.12(d) it enters at 10 s and crosses the lateral range by 51 s, showing little difference in water movement speed in the lateral direction between different depths. The change in signal due to water cannot be detected below 1 mm.

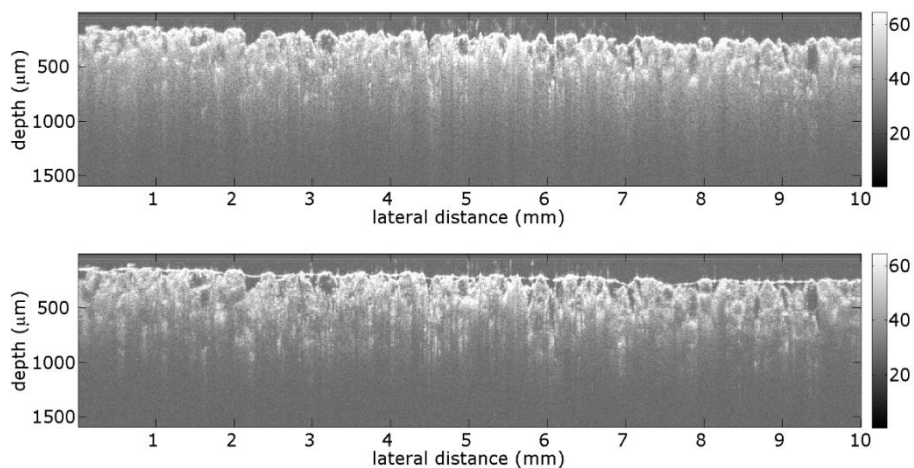


Figure 3.9. OCT virtual cross sections of WM sandstone sample when (a) dry and (b) wet.

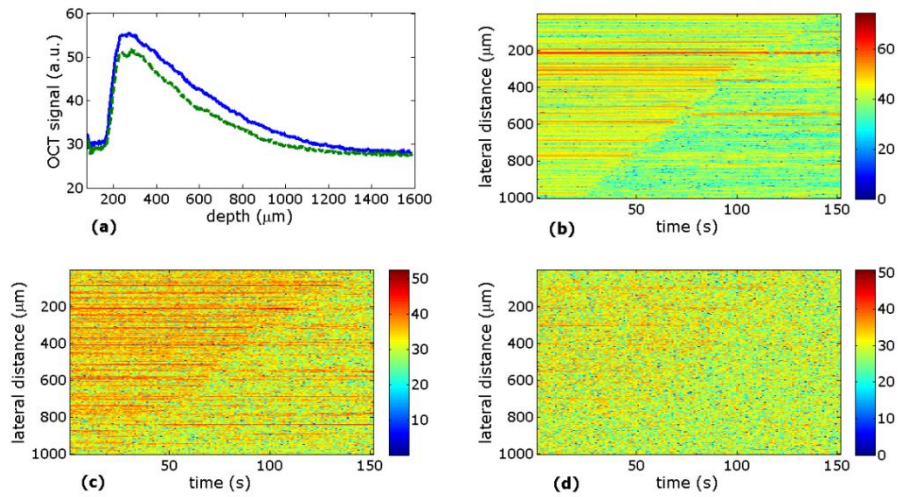


Figure 3.10. WM sandstone sample: (a) pixel intensity values averages across the 10 mm cross sections when dry (solid blue line) and wet (dotted green line); signal intensity values at depth of (b)  $\sim 400 \mu\text{m}$ , (c)  $\sim 700 \mu\text{m}$ , and (d)  $\sim 1000 \mu\text{m}$  across the lateral range of the scan over time. The OCT signals are in log scales.

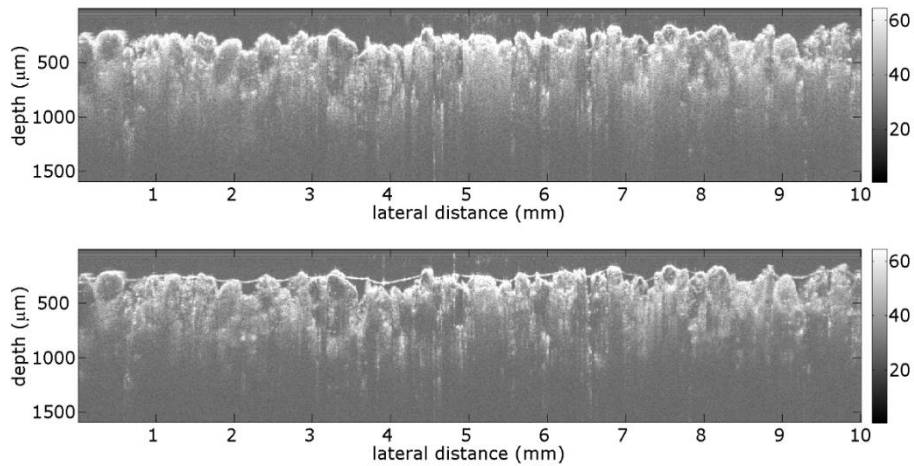


Figure 3.11. OCT virtual cross sections of WM sandstone sample when (a) dry and (b) wet.

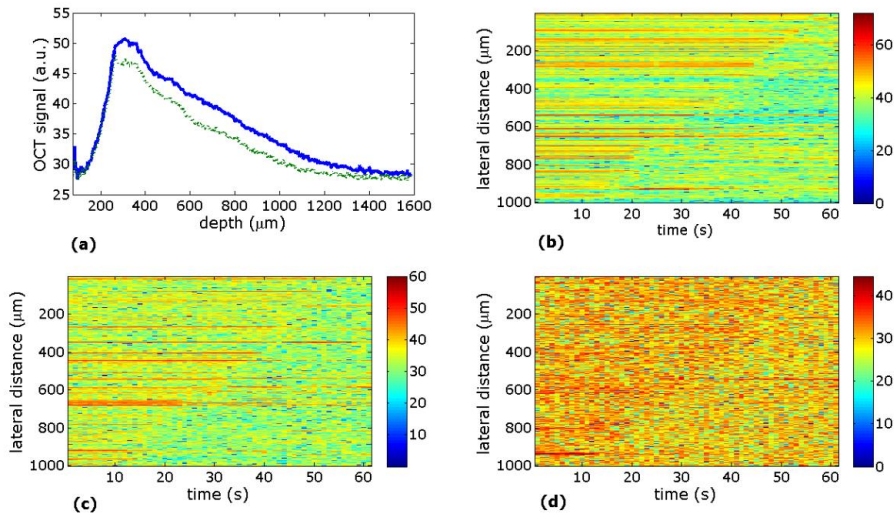


Figure 3.12. CP sandstone sample: (a) pixel intensity values averages across the 10 mm cross sections when dry (solid blue line) and wet (dotted green line); signal intensity values at depth of (b)  $\sim 400 \mu\text{m}$ , (c)  $\sim 700 \mu\text{m}$ , and (d)  $\sim 1000 \mu\text{m}$  across the lateral range of the scan over time. The OCT signals are in log scales.

For the sintered disc samples, the hydraulic conductivity showed no depth dependency as was expected with the structurally and compositionally homogenous materials. The velocity of the wetting front is constant across the observed time range. Sintered discs with pore diameters of 5-15  $\mu\text{m}$  show a wetting front velocity of  $0.091 \pm 0.005 \text{ cm s}^{-1}$  and can be considered pervious. Sintered discs with pore diameters of 1-2  $\mu\text{m}$  show a hydraulic conductivity of  $0.024 \pm 0.001 \text{ cm s}^{-1}$  and are pervious to semi-pervious.

Figure 3.13 shows that the wetting front velocities for sandstone samples were  $0.024 \pm 0.001 \text{ cm s}^{-1}$  for CP (mean pore size 5  $\mu\text{m}$ ) and  $0.0098 \pm 0.0005 \text{ cm s}^{-1}$  for WM (mean pore size 2  $\mu\text{m}$ ). Both are semi-pervious with the CP sample bordering on pervious. The values are in the expected range for sandstones [13].

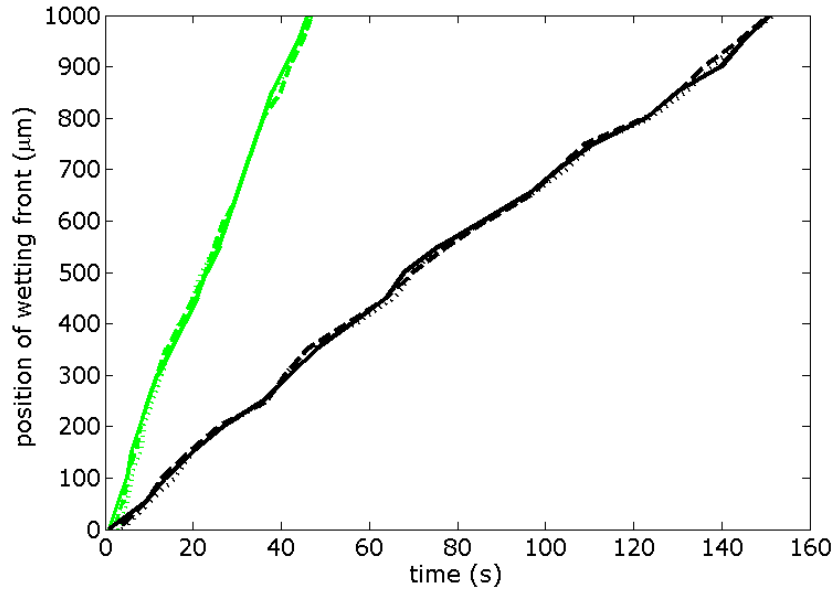


Figure 3.13. Position of the wetting front over time for WM (black lines) and CP (green lines) sandstone samples shown at depths of  $\sim 400 \mu\text{m}$  (solid line),  $\sim 700 \mu\text{m}$  (dashed line) and  $\sim 1000 \mu\text{m}$  (dotted line) into the samples.

Hydraulic conductivities found in this study for WM and CP sandstone samples are qualitatively consistent with permeability values found from MIP investigations of the samples. MIP measures the mercury injection pressure through a rock sample, and the pore size distribution is then derived from the relationship between minimum pore neck size and mercury injection pressure [13]. Permeability derived from MIP measurements relies on the determination of the characteristic pore size and the critical pressure at which mercury spans the sample and is a property of the rock derived from the measured microstructural length scale of the rock [14]. In contrast, hydraulic conductivity measured in this method depends not only on the intrinsic permeability but also on the level of water saturation of the rock. It is therefore difficult to quantitatively compare directly the MIP derived permeability (in units of area) and the OCT measured hydraulic conductivity (in units of speed). In OCT applications to biological tissues, fluid flow rate is often quoted as permeability coefficient [11, 12], which is not the same as the intrinsic permeability described above.

Hydraulic conductivity measurements with OCT taken with samples in a vertical orientation showed that wetting front velocities for sandstone samples were  $0.024 \pm 0.001 \text{ cm s}^{-1}$  for CP samples and  $0.0098 \pm 0.0005 \text{ cm s}^{-1}$  for WM samples, which are the same as their corresponding values for horizontal hydraulic conductivity, indicating that the material properties dominate the movement of water in the samples rather than gravity.

### **3.4. Conclusion**

This study demonstrates the capability of OCT to register the movement of water through the porous network of dry samples to measure the depth resolved hydraulic conductivity of materials. Water acts as a clearing agent for OCT imaging of sandstone. The difference in pixel intensity values between dry and wet samples is shown to be an effective parameter with which to register the position of the wetting front. For this application, the image acquisition speed was set at 1.14 frames per second, enabling the technique to detect wetting front velocities from  $1 \text{ cm s}^{-1}$  to  $10^{-6} \text{ cm s}^{-1}$  covering the full range of hydraulic conductivities likely to be found in natural sandstone, from pervious to impervious within a 2 hour observation time.

### **3.5. Further work**

The technique has the potential to dynamically monitor the application and drying of conservation treatments in order to investigate penetration patterns, as well as to evaluate the effect on the hydraulic conductivity of the material at the time of treatment and for long term monitoring of its effectiveness *in situ*.

Preliminary experiments were performed, applying a solution of dilute titanium oxide pigment using the method described to investigate the potential of tracer particles to monitor the penetration of fluids into stone.

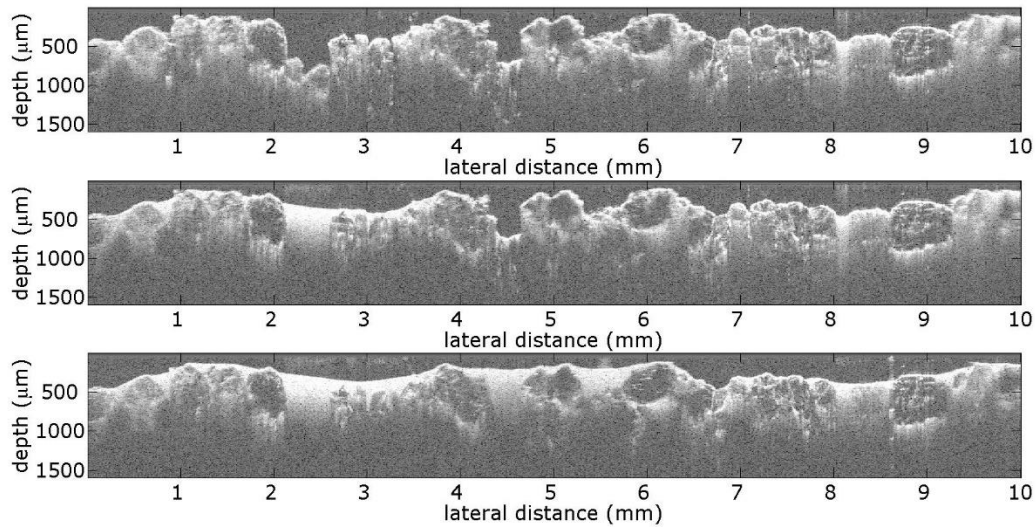


Figure 3.13 OCT ‘virtual’ cross-sections of sandstone (a) before application of pigmented solution (b) when solution has penetrated to 5 mm across from 0 (c) when solution has penetrated across full lateral range.

The wetting of coarse grained sandstone with a solution of titanium oxide pigment in water is shown in figure 3.13; before application, when the solution had penetrated halfway across the lateral range, and when fully wetted. The solution moved through the sandstone with a wetting front velocity of  $0.0071 \pm 0.001 \text{ cm s}^{-1}$ , compared to the hydraulic conductivity of  $0.0093 \pm 0.001 \text{ cm s}^{-1}$  for the same sample, the addition of the pigment solution to the water has presumably increased its viscosity, slowing its movement through the porous network. The presence of titanium oxide particles results in light scattering in the fluid making it appear bright in the OCT images, giving greater contrast to visualise the grain clasts. Areas that appear bright in the subsurface after the fluid has penetrated across may indicate the porous network of the stone.

A further test was carried out to monitor the penetration of the stone treatment IKO PRO Waterseal through sandstone, shown in figure 3.14; before application, when the solution had penetrated halfway across the lateral range, and when fully wetted. Waterseal is primarily composed of a mix of hydrocarbon liquids with a refractive index of around 1.50, closer to

that of quartz (1.54) than water (1.33) enhancing the effect of optical clearing as it causes a greater reduction in the refractive index mismatch when it displaces air in the porous network of the stone.

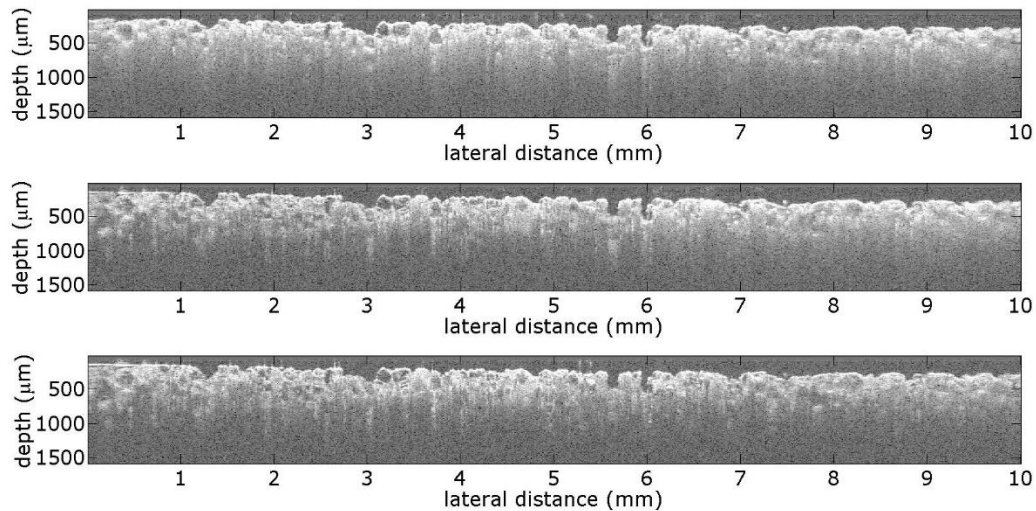


Figure 3.14 OCT ‘virtual’ cross-sections of sandstone (a) before application of stone treatment solution (b) when solution has penetrated to 5 mm across from 0 (c) when solution has penetrated across full lateral range.

The treatment penetrated through the sample quickly, with a wetting front velocity of  $0.054 \pm 0.001 \text{ cm s}^{-1}$ , compared to the hydraulic conductivity of  $0.0098 \pm 0.0005 \text{ cm s}^{-1}$  measured for the same sample. The mix of hydrocarbon fluids that form the solvent of the treatment have a lower density and viscosity than water, enabling it to move more rapidly through the porous network of the stone.

An attempt to measure the hydraulic conductivity of the stone once the treatment had dried found that the treatment had rendered the originally pervious sample impervious to water. Long term monitoring of treated surfaces with this method would enable the determination of longevity of stone conservation treatments *in situ*.

## References

1. H. Siedel, S. Pfefferkorn, E. Plehwe-Leisen, H. Leisen, "Sandstone Weathering in Tropical climate: Results for low-destructive investigations at the temple of Angkor Wat, Cambodia.", *Engineering Geology* 115, 182-192 (2010)
2. B. Fitzner, K. Heinrichs, D. La Bouchardiere, "Weathering damage on Pharonic sandstone monuments in Luxor-Egypt", *Building and Environment* 38, 1089-1103 (2003)
3. A.V. Turkington, T.R. Paradise, "Sandstone weathering: a century of research and innovation" *Geomorphology* 67, 229-253 (2005)
4. R.A.L. Wray, "A global review of solutional weathering forms on quartz sandstones" *Earth Science Reviews*, 42, 137-160 (1997)
5. Th. Warscheid, J. Braams, "Biodeterioration of stone: a review" *International Biodeterioration and Biodegradation* 46, 343-368 (2000)
6. E. Molina, G. Cultrone, E. Sebastian, F.J.Alonso, L. Carrizo, J. Gisbert, O. Buj, "The pore system of sedimentary rocks as a key factor in the durability of building materials," *Engineering Geology* 118, 110-121, (2011)
7. O. Sass, H.A. Viles, "Wetting and drying of masonry walls: 2D-resistivity monitoring of driving rain experiments on historic stonework in Oxford, UK". *Journal of Applied Geophysics* 70, 72-83 (2010)
8. A. T. Watson, C. T. P. Chang, "Characterizing porous media with NMR methods", *Progress in Nuclear Magnetic Resonance Spectroscopy* 31, 343-386 (1997)
9. M. Kinnunen, R. Myllylä, S. Vainio, "Detecting glucose-induced changes in in vitro and in vivo experiments with optical coherence tomography", *Journal of Biomedical Optics*, 13(2), 021111 (2008)

10. M. G. Ghosn, E. F. Carbajal, N. A. Befrui, "Differential permeability rate and percent clearing of glucose in different regions in rabbit sclera", *Journal of Biomedical Optics*, 13(2), 021110 (2008)
11. H. Xiong, Z. Guo, C. Zeng, L. Wang, Y. He, S. Liu, "Application of hyperosmotic agent to determine gastric cancer with optical coherence tomography ex vivo in mice", *Journal of Biomedical Optics* 14(2), 024029 (2009)
12. A. F. Fercher, C. K. Hizenberger, G. Kamp and S. Y. El-Zaiat, "Measurement of intraocular distances by backscattering spectral interferometry", *Optics Communications*, 117, 43-48 (1995)
13. J. Bear, *Dynamics of Fluids in Porous Media*. Dover Publications. ISBN 04866568756, (1972)
14. A. J. Katz, A. H. Thompson, "Quantitative prediction of permeability in porous rock", *Phys. Rev.B*, 34(11), 8179-8181 (1986)

## Chapter 4. Hyperspectral imaging for remote moisture monitoring

### 4.1 Introduction

At sites where rock art is on the walls or ceilings of shelters or caves, the panels can be inaccessible to monitoring techniques. Most deterioration effects in porous sandstone arise as a direct or indirect consequence of water. Deterioration can be as a result of chemical, physical and biological processes. The movement of water through the stone can result in solutional material loss. The penetration of water in sandstones causes mechanical stresses due to the swelling of clay minerals causing differential pressures. Water transports soluble salts and impurities that can crystallize, putting pressure on the pore walls. Dampness in caves can be brought about by the capillary movement of ground water or the infiltration of meteoric water, identifying the ingress point of moisture is key to managing the cave environment.

Most common techniques for monitoring moisture content *in situ* are based on electrical properties and allow only relative measurement. Such methods are not only influenced by the presence of water but on the concentration of ion species and other impurities and require access to and contact with the stone.

The reflectance at water absorption bands in the near infrared (NIR) can be used to remotely and directly monitor the water content in the surface and subsurface of porous media and may provide an indication of the effective porosity in saturated materials.

Spectroscopy is the study of light as a function of wavelength that has been reflected or emitted from a material. Reflected light contains information about the surface and subsurface of the material. The wavelength of absorption features allows us to derive information about the composition of materials with the use of a detector and means of wavelength selection.

Absorption bands are detectable in the spectrum of materials caused by the presence of specific chemical bonds.

Near infra-red spectroscopy detects absorptions due to molecular vibrations at specific wavelengths. Water molecules have three fundamental vibrational modes;  $V_1$ , symmetric OH stretching,  $V_2$ , H-O-H bending and  $V_3$  asymmetric OH stretching, shown in figure 4.1

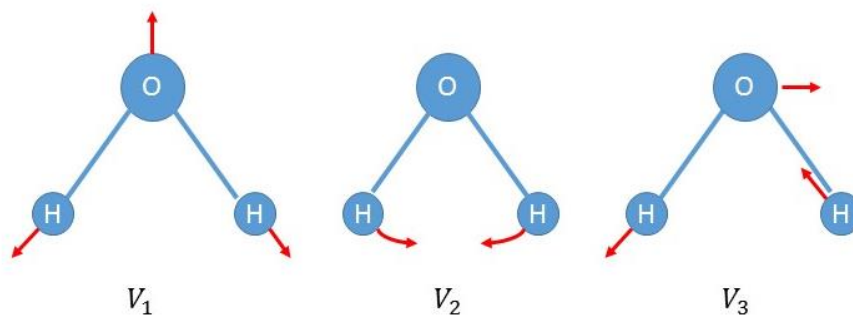


Figure 4.1 Vibrational modes of the water molecule

Water is a strong infrared absorber [1] producing diagnostic spectral features in the NIR range due to combinations of overtones of the fundamental vibrations for  $V_2 + V_3$  at 1947nm and  $V_1 + V_3$  at 1450nm, for water molecules in the liquid phase [2].

Hyperspectral imaging is the integration of imaging and spectroscopy techniques into one system, as a means of obtaining a spectrum at each position in a large array of spatial positions so that any one spectral wavelength can be used to make a recognisable image. Hyperspectral imaging has been adapted from its origins in the field of remote sensing to a wide range of applications. There are three conventional acquisition modes for hyperspectral imaging; point scanning, line scanning and area scanning.

Point scanning records the spectrum iteratively at a single point for each spatial element. Line scanning records spectral measurements from a spatial line across the sample collected with an array detector and is suitable for applications where the samples are moving, such as on a

conveyor belt. In an area scanning mode the field of view is fixed, with the selected wavelengths then scanned sequentially for the whole spatial range.

A grey scale image is produced for each waveband where each pixel intensity is determined by the reflectance for that waveband at that spatial point, to create an image hypercube of  $x$ ,  $y$ ,  $\lambda$  dimensions shown in figure 4.2.

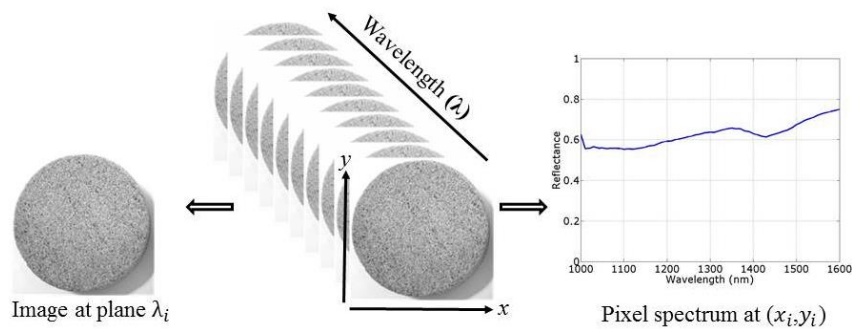


Figure 4.2 Schematic representation of an imaging hypercube produced by area scanning, showing the relationship between spectral and spatial dimensions.

There are 3 key characteristics of hyperspectral imaging systems which determine their capability: spectral range, spectral bandwidth and spatial resolution.

The spectral range must be appropriate to cover spectral absorptions diagnostic to the problem under investigation, for near infra-red applications a range of 1000-1600 nm is commonly used [3, 4] based on sensitivity range of the relatively inexpensive InGaAs detectors.

The spectral resolution of a system is determined by the width of an individual spectral channel in the spectrometer, the narrower the bandwidth the narrower the absorption line feature that can be accurately measured, a 10 nm resolution is sufficient for most applications [5].

The spatial resolution is the image pixel size in the final hypercube, it determines the detail by which the spatial variation of the composition can be determined.

Hyperspectral imaging to determine the water content of materials has found widespread use in a range of industrial applications, particularly in the fields of food science and pharmacology.

Within the food industry, the water content of products is an indicator of microbial stability and key parameter for quality and shelf life. Moisture content is also used to monitor ripening, drying and rehydrating processes of a wide range of food products [3, 5, 6, 7, 8, 9, 10, 11] such as fruits and vegetables, meat, fish, dairy products and grain.

Moisture assays of pharmacological materials were an early application of near-infrared spectroscopy, the presence of water can affect the physical and chemical stability as well as their quality and shelf life [4, 12, 13, 14]. The technique has been applied to a wide range of other materials including polymers [15] and cement mortar [16].

In order to extract useful and quantitative information from raw images following their acquisition, calibration is necessary to prepare the data for analysis.

Calibration is required to transform image data into units of reflectance, dark images are collected with the lens cap in place, and white images are collected with a white spectral reference target (such as a Labsphere Spectralon white standard) filling the field of view at the same position as the sample. The grey scale values for the pixels of the corrected image ( $I$ ) are then in units of reflectance.

$$I = \frac{I_0 - D}{W - D} \times 100$$

$I$  = corrected hyperspectral image

$I_0$  = original hyperspectral image

$D$  = dark image

$W$  = white reference image

The image hypercube contains a large quantity of spatial and spectral data, some of which may be redundant to the application in question. For applications where a large number of samples of similar composition are to be analysed, data reduction methods are used.

Spectral data analysis is carried out using mathematical procedures to filter the information relevant to the application and analyte in question, such as water. Multivariate data analysis (Chemometrics) is often used to determine optimal wavelengths for the classification and characterisation of the chemical attributes of interest in the sample. Principal component analysis (PCA) and Partial least squares regression (PLS) are widely used for the detection of defects and contaminants on products, as well as the determination their composition [3, 5, 7, 11, 17, 18].

The absorption feature at 1450 nm is widely used for the determination of water content because of the availability of relatively low cost systems of an appropriate spectral range for its detection.

As a rapid non-destructive technique enables batch testing and evaluation of conformity rather than selected representative samples, and the automation of assessment of quality and consistency of products are achieved during processing.

## **4.2 Instrument**

PRISMS (Portable Remote Imaging System for Multispectral Scanning) is a system designed for in situ, remote multispectral and hyperspectral imaging [19, 20] up to distance of 30 m, shown in figure 4.3.

To enable sequential spectral filtering, the system is fitted with Gooch & Housego acoustic-optical tunable filter (AOTF) which provides fast switching between the spectral bands and flexibility in terms of the tuning selection of the central wavelength and bandwidth of the filters.

Filter tuning is software controlled from a laptop, the wavelength selected by changing the acoustic radio frequency waves applied to a birefringent crystal [20]. A Near infrared Spectral range of 1000-1600 nm is used to cover diagnostic spectral absorption for water centred at 1450 nm. A 10 nm bandwidth filter set was used across the full spectral range of the instrument to enable characterization of the continuum slope as well as the feature of interest. Integration times are adjusted for each individual spectral channel to optimize signal to noise ratio, 61 filter channels are used sequentially to image the object to produce a final spatial and spectral image cube in  $x$ ,  $y$ ,  $\lambda$  dimensions.



Figure 4.3 PRISMS imaging system

The system uses a Meade EXT-90AT telescope with 90 mm aperture and 1250 mm focal length and Xenics InGaAs detector array to give a resolution of 30  $\mu\text{m}$  per pixel imaging at a distance of 4 m from the target. The focus is automated and the integration times are automatically selected for each wavelength band such that the maximum signal intensity is at around 90% of the detector saturation level. A Tungsten Halogen (82 V 300 W) source is used for illumination providing a smooth and stable spectrum source with a relatively flat light distribution.

Images were calibrated through dark subtraction to eliminate thermal electron contribution and spectral calibration by imaging a CERAM white standard tile with known spectral reflectance at the same position as the target sample. White calibration corrects for the spectral response

of the system to transform the raw data into reflectance units by comparison with the spectra of standard reference material imaged under the same conditions, which also acts as a flat field image (when it fills the field of view) to correct for any spatial inhomogeneity of illumination.

### 4.3 Results and discussion

The sandstone samples were collected from the site of rock art panels at Weetwood Moor (WM) in Northumberland. The sample was loose cairn stones from the area of the rock art panel, selected as proxy samples and considered by visual inspection of colour, grain size and composition to be lithologically representative of the panels. The un-weathered surface was obtained by slicing the samples using a diamond edged water cooled saw to access the interior un-weathered stone, shown in figure 4.4(a).

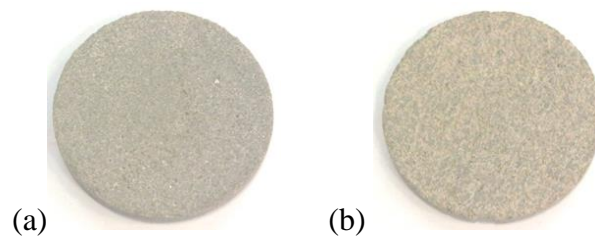


Figure 4.4 Samples (a) WM sandstone (b) Indiana Limestone

The method was also tested using a sample of Indiana Limestone, a medium grained calcarenite grainstone composed of microfossil fragments, shown in figure 4.4 (b), to determine its applicability across rock types. The sandstone and limestone samples are primarily composed of the minerals silica and calcite respectively. The spectra for both minerals are flat having no spectral features in the NIR range of interest as shown in figure 4.5.

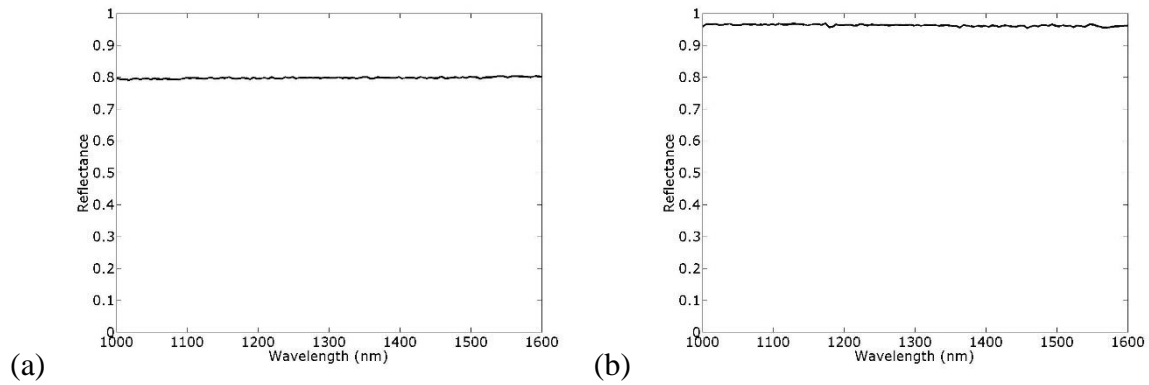


Figure 4.5 Reference spectra for quartz (a) and calcite (b) for the NIR range of interest (USGS Spectral reference library [21]).

Samples were immersed in water prior to imaging and then positioned on a balance in the field of view of the system, at a distance of 4 m, so that the sample filled the field of view. The sample was then imaged repeatedly while the mass is recorded at the start of each image to determine the water content; in order to produce a series of image hypercubes at different moisture contents, the spectra of which can then be analysed and compared to the gravimetrically measured water content. NIR spectra for the WM sandstone sample while drying are shown in figure 4.6; as the sample dries the reflectance across the whole spectrum increases and area of the absorption feature decreases.

Absorptions in a spectrum have two components, the individual spectral line features and the continuum onto which they are superimposed, the depth of an absorption feature is related to the abundance of the absorber.

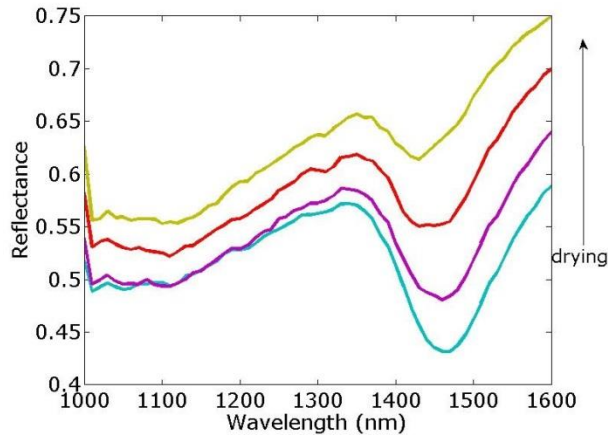


Figure 4.6 NIR spectra for sandstone sample while drying, showing vibrational absorbance band due to water centred at 1450 nm.

The sloping continuum causes an apparent shift in the reflectance minima of the absorption feature. The continuum slope was removed by division to isolate the spectral feature to allow comparison between spectra. In order to quantify the absorption feature, its equivalent width ( $W_\lambda$ ) was calculated.

$$W_\lambda = \int (1 - F_\lambda / F_0) d\lambda$$

$F_0$  = the continuum intensity on either side of the absorption feature

$F_\lambda$  = the intensity across the entire wavelength range of interest

$W_\lambda$  = the width of a hypothetical absorption line which drops to an intensity of zero

and has the same integrated flux deficit from the continuum as the true one

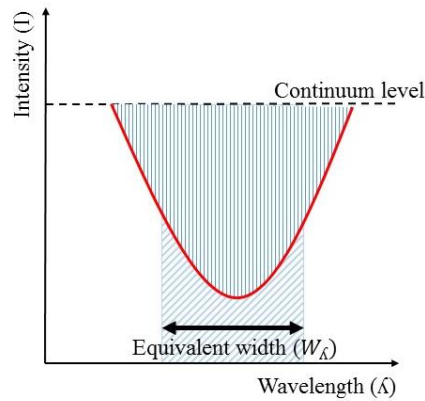


Figure 4.7 Schematic of the determination of the equivalent width of an absorbance feature.

The equivalent width is defined as the width of the continuum flux that contains the same area on the plot as the spectral line, indicating the strength of the absorption line, shown in figure 4.7. The strength of an absorption is relative to the concentration of the absorber in the sample. The water content of the sample was determined gravimetrically for each measured spectra and calculated as;

$$\text{Water content} = \frac{M_w - M_D}{M_D} \times 100$$

$M_D = \text{dry mass}$   $M_W = \text{wet mass}$

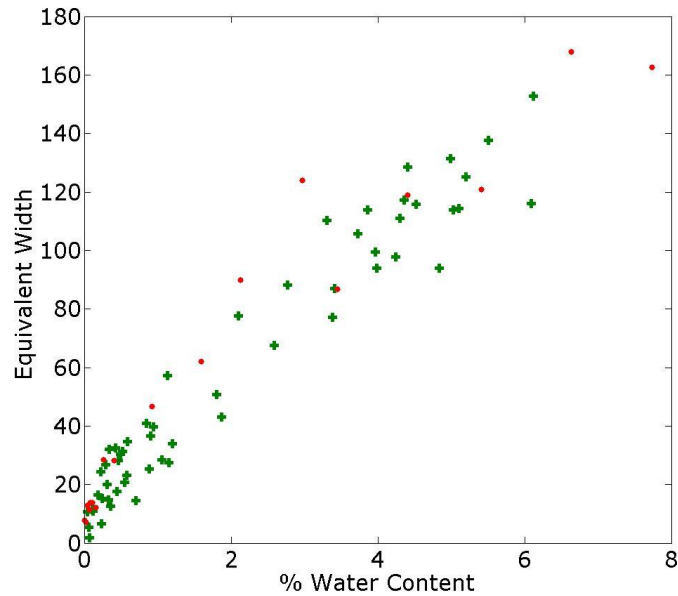


Figure 4.8 Plot of equivalent width against water content of sample for Indiana Limestone (green crosses) and WM Sandstone (red dots)

A plot of the equivalent width of the absorption feature centred at 1450 nm and the gravimetrically determined water content is shown in figure 4.8, for the WM sandstone (red dots) and Indiana Limestone (green crosses). The data plotted includes 7 drying runs for the Indiana limestone sample imaged from saturated until dry, and 3 drying runs for the WM sandstone sample. The technique is capable at detecting water content as low as 0.07% by mass in both the limestone and sandstone, a level which cannot be detected by visual or tactile assessment of the samples. The equivalent width has a strong correlation with the water content by mass present in both sandstone and limestone samples, it is an effective analysis to determine the concentration of water in these geological materials.

#### 4.4 Conclusions

Near infrared hyperspectral imaging of rock art sites can be used for the identification and mapping of the presence of water by spectral feature analysis to quantitatively monitor the spatial variation and movement of water through the panel remotely.

This method enables measurement of water at the surface and subsurface of the sample. If the depth of penetration is shallow and the water is not homogeneously distributed in depth through the sample the determined water may not be representative for the bulk of the sample gravimetric measurement of water content. However, it can still give the relative spatial distribution of water.

The spectral range does not cover combined O-H and H-O-H absorption feature at 1947 nm so cannot determine the extent to which the feature is due to the sole presence of hydroxyl in hydroxyl bearing minerals such as kaolinite [2].

## References

1. J. Curico, C. Petty, The near infrared absorption spectrum of liquid water, *Journal of the Optical Society of America*, 41, 302-304 (1951)
2. R.N. Clark, Chapter 1: Spectroscopy of Rocks and Minerals, and Principals of Spectroscopy, in *Manual of Remote Sensing, Volume3, Remote Sensing for the Earth Sciences*, (A.N. Rencz, ed.) John Wiley and Sons, New York, p3-58, (1999)
3. J. M. Amigo, I. Marti, A. Gowen, Chapter 9: Hyperspectral Imaging and Chemometrics: A Perfect Combination for the Analysis of Food Structure, Composition and Quality, in *Data Handling in Science and Technology*, 28, p343-370 (2013)
4. N.L.T. Padivitage, J.P. Smuts, D.W. Armstrong, Chapter 11: Water Determination, in *Specification of Drug Substances and Products*, p223-241, (2014)
5. B.M. Nicolai, K. Beullens, E. Bobelyn, A. Peirs, W. Saeys, K.I. Theron, J. Lammertyn. Nondestructive measurement of fruit and vegetable quality by means of NIR spectroscopy: A review, *Postharvest Biology and Technology*, 46, p99-118, (2007)

6. N. Sinelli, E. Casiraghi, S. Barzaghi, A. Brambilla, G. Giovanelli, Near infrared (NIR) spectroscopy for monitoring blueberry osmo-air dehydration process, *Food Research International*, 44, p1427-1433, (2011)
7. S. Mahesh, D.S. Jayas, J. Paliwal, N.D.G. White, Hyperspectral imaging to classify and monitor quality of agricultural materials, *Journal of Stored Products Research*, 61, p17-26, (2015)
8. L. Pan, R. Lu, Q. Zhu, J.M. McGrath, K. Tu, Measurement of moisture, soluble solids, sucrose content and mechanical properties in sugar beet using portable visible and near-infrared spectroscopy, *Postharvest Biology and Technology*, 102, p42-50, (2015)
9. C. Collell, P. Gou, J. Arnau, J. Comaposada, Non-destructive estimation of moisture, water activity and NaCl at ham surface during resting and drying using NIR spectroscopy, *Food Chemistry*, 129, p601-607, (2011)
10. D. Liu, D. Sun, J. Qu, X. Zeng, H. Pu, J. Ma, Feasibility of using hyperspectral imaging to predict moisture content of porcine meat during salting process, *Food Chemistry*, 152, p197-204, (2014)
11. A. Iqbal, D. Sun, P. Allen, An overview on principle, techniques and application of hyperspectral imaging with special reference to ham quality evaluation and control, *Food Control*, 46, p242-254, (2014)
12. J. Mantanus, E. Ziemons, P. Lebrun, E. Rozet, R. Klinkenberg, B. Streel, B. Evrard, P. Hubert, Moisture content determination of pharmaceutical pellets by near infrared spectroscopy: Method development and validation, *Analytica Chimica Acta*, 642, p186-192, (2009)
13. A. Pestieau, F. Krier, G. Thoorens, A. Dupont, P. Chavez, E. Ziemons, P. Hubert, B. Evrard, Towards a real time release approach for manufacturing tablets using NIR

- spectroscopy, *Journal of Pharmaceutical and Biomedical Analysis*, 98, p60-67, (2014)
14. M. Brulls, S. Folestad, A. Sparen, A. Rasmuson, J. Salomonsson, Applying spectral peak area analysis in near-infrared spectroscopy moisture assays, *Journal of Pharmaceutical and Biomedical Analysis*, 44, p127-136, (2007)
  15. S. Begus, G. Beges, J. Drnovsek, D. Hudoklin, A novel NIR laser-based sensor for measuring the surface moisture in polymers, *Sensors and Actuators A: Physical*, 221, p53-59, (2015)
  16. M. Ghandehari, C.S. Vimer, I. Ioannou, A. Sidelev, W. Jin, P. Spellane, In-situ measurement of liquid phase moisture in cement mortar, *NDT&E International*, 45, p162-168, (2012)
  17. G. ElMasry, D. Sun. Chapter 1: Principles of Hyperspectral Imaging Technology. *Hyperspectral Imaging for Food Quality Analysis and Control*. Elsevier (2010)
  18. J. Qin. Chapter 2: Hyperspectral and multispectral imaging in the food and beverage industries. *Computer vision technology in the food and beverage industries*. Woodhead Publishing Limited (2012)
  19. H. Liang, A. Lucian, R. Lange, C. S. Cheung, B. Su. Remote spectral imaging with simultaneous extraction of 3D topography for historic wall painting. *ISPRS Journal of Photogrammetry and Remote Sensing*, 95, 13-22, (2014)
  20. Liang, H., Keita, K., Pannell, C., Ward, J., A SWIR hyperspectral imaging system for art history and art conservation, in IX CONGRESO NACIONAL DEL COLOR. ALICANTE (2010), Publicaciones de la Universidad de Alicante, p189-192  
<http://rua.ua.es/dspace/handle/10045/17114?locale=en>

21. N. Gat. Imaging Spectroscopy using Tunable Filters: A Review. Proc. SPIE  
Vol.4056, 50-64, Wavelet Applications VII, H. Szu, M. Vetterli, W. J. Campbell, J.  
R. Buss. Ed. (2000)
22. <http://speclab.cr.usgs.gov/spectral-lib.htm>

## Chapter 5 Nuclear Magnetic Resonance investigation of porosity

### 5.1 Introduction

Sandstones are principally composed of mineral grains, cement or matrix and pore space. Porosity is defined as the ratio of volume of pore space to the total volume of the stone expressed as a percentage.

$$\text{porosity } \phi = \frac{V \text{ void}}{V \text{ bulk}}$$

The volume and size distribution of the pore space affects the behaviour of stones over time. Pore characteristics are one of the main factors that control the intensity of stone deterioration [1] and determine their stability against biological attack. Weathering processes cause progressive changes in rock porosity due to changes in pore size distribution, pore connectivity, pore infilling and new pore formation [2]. Significant correlations between porosity and pore size distribution in rocks and their behaviour including sandstone have been used previously to develop durability estimators [3, 4]. However standard methods to investigate pore characteristics such as mercury intrusion porosimetry and micro-CT require samples to be removed from the site for laboratory analysis.

A technique which can measure the porosity at different depths from the surface *in situ* could determine changes to the porosity at the surface and subsurface due to weathering processes as well as indicating the stones vulnerability to further weathering.

Mobile single sided NMR is based on the principles of unilateral inside out NMR (where the sample is placed outside the magnet) initially developed to travel down bore holes for the purpose of well logging [5]. Oil industry analysis of NMR signals provides information about the fluids in the porous network of the surrounding rock matrix and, in favourable conditions, about the permeability of the stone [6].

In recent years NMR has been applied to the analysis of cultural heritage materials for the purpose of determining the stratigraphy of paintings, the deterioration of paper materials and for evaluating the density of wood in violins [7, 8]. It has also been used to measure the water content over time in stone and decorated walls and to determine the stratigraphy of wetted walls [8]. It can assess changes to pore size distributions following conservation treatments to stone and fresco walls [9, 10]. NMR measurements are not influenced by the presence of most common pollutants but can be affected by the presence of ferromagnetic minerals such as magnetite [11, 12, 13].

The NMR signal is produced by applying a series of radio-frequency electromagnetic pulses to a sample within an externally applied polarizing magnetic field, which are absorbed and re-emitted by hydrogen nuclei. If the polarising field exhibits specific properties in terms of its spatial gradient this enables the spatially resolved detection of a hydrogen containing fluid (e.g. water H<sub>2</sub>O) within the sample. The amplitude of the proton NMR signal is directly proportional to the amount of mobile hydrogen (i.e. in a liquid or soft solid) in the sensitive volume investigated which provides the water content of the material, directly determining porosity in fully saturated samples.

Hydrogen nuclei have the properties of a magnetic dipole and also possess an angular momentum resulting in what is commonly known as the “nuclear spin”. A radio frequency pulse is used to excite hydrogen nuclei and the NMR signal is collected as relaxation occurs. NMR relaxation refers to the dissipation of energy into the environment due to the loss of magnetisation of the spin system (T<sub>1</sub> relaxation), and also the loss of synchronisation of spins (T<sub>2</sub> relaxation). The T<sub>1</sub> longitudinal relaxation or spin-lattice relaxation refers to the transfer of energy into the surroundings until equilibrium is reached. A schematic of NMR excitation and response for the determination of T<sub>1</sub> is shown in figure 5.1. The T<sub>1</sub> value provides a good indicator for the surface to volume ratio of the pores within a saturated sandstone sample [14].

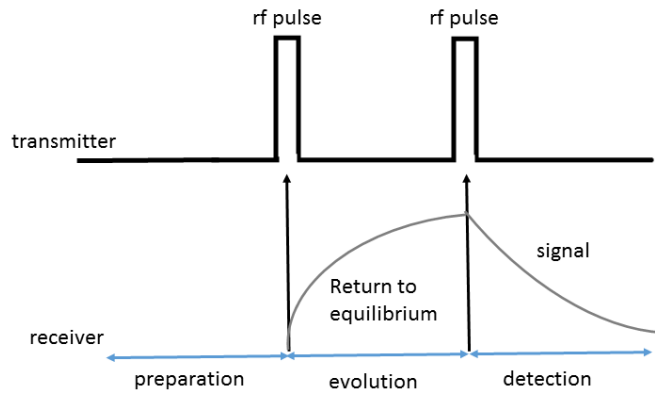


Figure 5.1 Schematic of NMR excitation and response to determine  $T_1$  given by the exponential decay time of the signal during detection.

The  $T_2$  transverse relaxation or spin-spin relaxation refers to the loss of phase coherence between spins. After excitation, spins precess synchronously then decay.

The NMR signal intensity is proportional to the total amount of hydrogen nuclei, while the relaxation time ( $T_1$  and  $T_2$ ) depends on the interaction between the nuclear spins and the surroundings. In a pore containing water, the bulk water exhibits a single exponential decay. However the water close to the pore wall surface exhibits a faster relaxation time. The  $T_2$  relaxation rate is inversely proportional to the surface to volume ratio of the pore [14]. The resulting NMR signal is a composite of all the NMR signals from the different pore sizes in the volume under investigation. The relaxation curve of the signal can be processed by an inverse Laplace transformation to separate it into its component parts, the distribution of which can be interpreted in terms of pore size distribution [6].

To determine the  $T_2$  relaxation a CPMG (Carr, Purcell, Meiboom and Gill) [15, 16] radio frequency pulse sequence is used to generate a train of echoes with an echo decay envelope that describes the  $T_2$  relaxation. A schematic showing the NMR excitation and response to determine  $T_2$  relaxation using a CPMG pulse sequence is shown in figure 5.2.

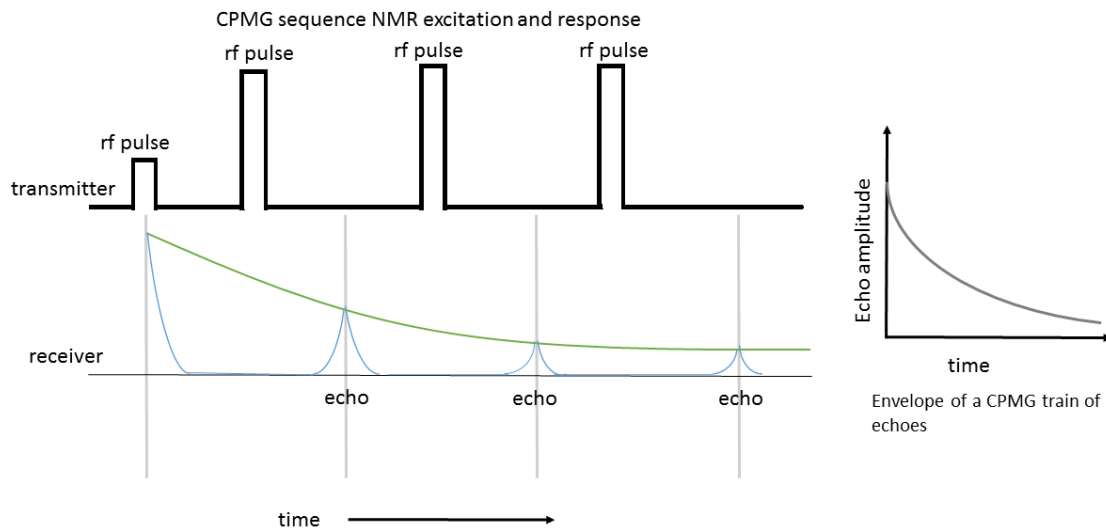


Figure 5.2 Schematic of NMR excitation and response to determine  $T_2$  using a CPMG echo sequence

Key parameters for the CPMG sequence are the repetition time (TR) which defines the time between two such successive excitation pulses given to allow spins to regain thermal equilibrium and the echo time (TE) spacing between the application of two successive refocussing rf pulse and the collection of the NMR signals. The number of accumulated experiments describes the number of measurements averaged to produce each point.

## 5.2 Materials and methods

### 5.2.1 Instrument

The NMR-MOUSE<sup>®</sup> (MOBile Universal Surface Explorer) is a portable one-sided instrument that can be placed at the site of the measurement enabling the characterization of near surface volumes of arbitrarily large objects. The MOUSE<sup>®</sup> is mounted on a computer controlled precision lift to enable depth profiles into materials shown in figure 5.3. The thin sensitive volume is above the sensor surface and as the sensor retreats from the sample surface, the sensitive volume can be placed at the desired depth positions to produce a profile



Figure 5.3 NMR MOUSE® mounted on a computer controlled precision lift

The instrument can be used in either a vertical or horizontal position and can be inverted to investigate materials from their top surface.

### 5.2.2 Sintered discs

Sintered discs are porous filtration discs composed of quartz glass granules that have been fused together. They were selected as porous materials to model the technique with the simplification of a single component material and homogenous structure.

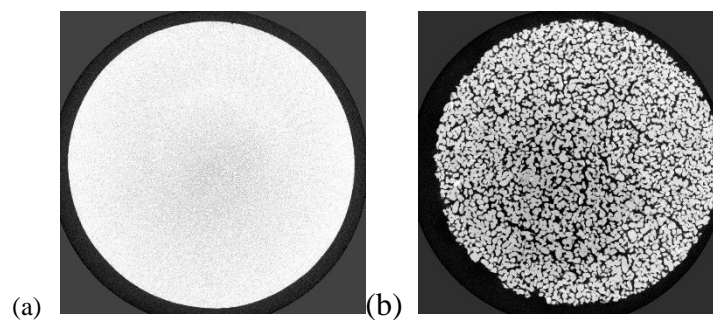


Figure 5.4 Micro-CT tomographic slices of Sintered disc grade 4 (a) and grade 0 (b)

X-ray micro-computed tomography (micro-CT) volumetric imaging of samples was performed to determine their porosity from image analysis of the tomographic slices. The determined

porosity was 13.3% for the grade 4 sintered disc shown in figure 2(a) and 34.2% for the grade 0 sintered disc in figure 3(b).

NMR data for the sintered discs was collected using a CPMG sequence with 256 spin echoes (echo time TE=300  $\mu$ s, repetition time TR=4 s, number of accumulated experiments = 256) over an experimental time of 36 hours per profile. The sintered discs were immersed in water for 24 hours prior to the measurement.

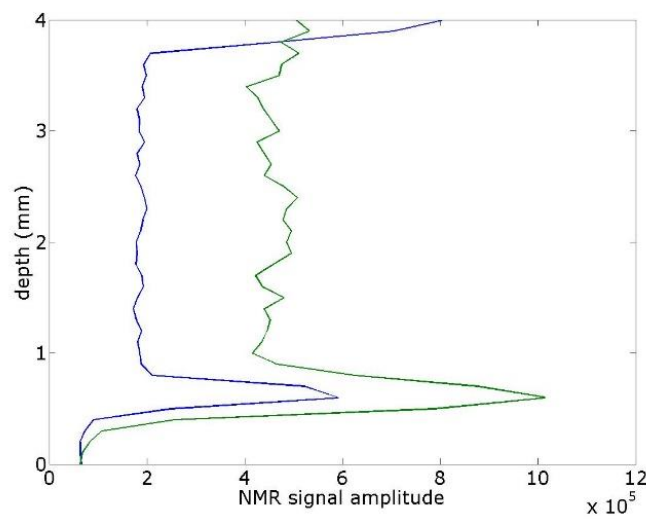


Figure 5.5 NMR profiles of sintered disc grade 4 (blue) and grade 0 (green)

NMR depth profiles through the sintered discs are shown in figure 5.5. The profile is measured with the sample in a sample holder placed on top of the instrument at a 0 depth. The initial low signal is due to the plastic sample holder, both profiles show a peak due to a water pooling effect where the surface of the sample is in contact with the sample holder. Sintered disc grade 4 shows a similar peak at the top of the profile due to a film of water on the top surface of the sample. The variation of the profile within the sample is due to the different sizes of glass beads that have been fused to create the disc grade 0, 500  $\mu$ m and grade 4, 10  $\mu$ m. An NMR profile of bulk water was used to determine the percentage water content at each point in the sample profiles providing direct measurement of the fluid filled porosity of the sintered discs of 13%

for grade 4 and 33% for grade 0. The porosity values are consistent with those found for the discs from image analysis of micro-CT tomographic slices.

### 5.2.3 Sandstone

The two selected samples were collected from the sites of rock art panels at Weetwood Moor (WM) and Chatton Park (CP) in Northumberland. The samples were loose cairn stones from the area of the rock art panels, selected as proxy samples and considered by visual inspection of colour, grain size and composition to be lithologically representative of the panels. The unweathered surface was obtained by coring and slicing the samples using a diamond edged water cooled saw, sample discs shown in figure 5.6.

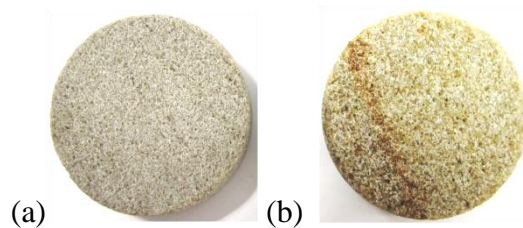


Figure 5.6 Sandstone samples from Weetwood Moor (a) and Chatton Park (b) (25 mm diameter discs)

Sandstone samples were immersed in water for 24 hours under atmospheric pressure to allow water to infiltrate the porous network as fully as possible under conditions achievable in-situ at the sites of rock art panels. A Perspex sample holder was designed to maintain water saturation for the duration of the experiment.

NMR data was collected using a CPMG sequence with 512 spin echoes (echo time  $TE=150\ \mu\text{s}$ , repetition time  $TR=2\ \text{s}$ , number of accumulated experiments = 648) at 50 points with a step spacing of  $100\ \mu\text{m}$  to cover a depth of 5 mm that included both the samples, with a disc of CP sandstone stacked on top of a 3 mm thick disc of WM sandstone.

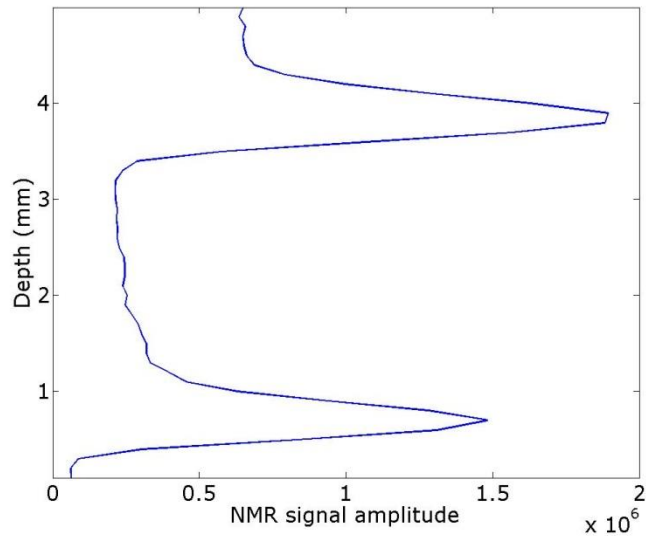


Figure 5.7 NMR profile of CP sample on top of WM sample

The profile of NMR signal amplitude with depth through the two samples is shown in figure 5.7. The initial low signal at zero depth is due to the measurement point being in the plastic sample holder, the initial peak is due to a water pooling effect where the surface of the WM sample is in contact with the sample holder. A similar peak at the interface between the two samples at depth position of 4 mm in figure 5.7 is presumably due to a film of water between the surfaces. A NMR profile of bulk water was used to determine the percentage water content at each point in the sample profiles providing direct measurement of the fluid filled porosity of the sandstone samples of 10% for WM and 15% for CP. Due to the sensitivity of the instrument the signal to noise level required to reliably perform an inverse Laplace transform to infer the pore size distribution for the profile was not achievable within the time constraints of the experiment due to access to the instrument.

Further experiments were performed to determine the effectiveness of the technique for *in situ* work, constrained by a duration achievable in the field using a portable generator, with an approximately 4 hour running capacity at full power before the requirement to switch off and

refuel. The 4 hour limit to the experiment time determined the number of measurement points, and measurements accumulated for averaging.

$T_1$  and  $T_2$  values were measured before each profile with the sensitive volume placed at the centre of the samples, at 2 mm depth, in order to establish an appropriate value for the repetition time for the CPMG sequence. For a water saturated WM sample, repeated measurements of  $T_1$  gave an average values of 206 ms (standard deviation of 30), and  $T_2$  of 6 ms (SD 0.5). Measurements for the water saturated CP sample gave an average  $T_1$  value of 294 ms (SD 19), and  $T_2$  of 5 ms (SD 0.7); compared to the bulk water measurement with values for  $T_1$  of 3251 ms and  $T_2$  of 12 ms. NMR data was collected using a CPMG sequence with 128 spin echoes (echo time  $TE=150 \mu s$ , repetition time  $TR=700$  ms, number of accumulated experiments = 256) at 20 points with a step spacing of  $200 \mu m$  to cover a depth of 3.5 mm within the samples.

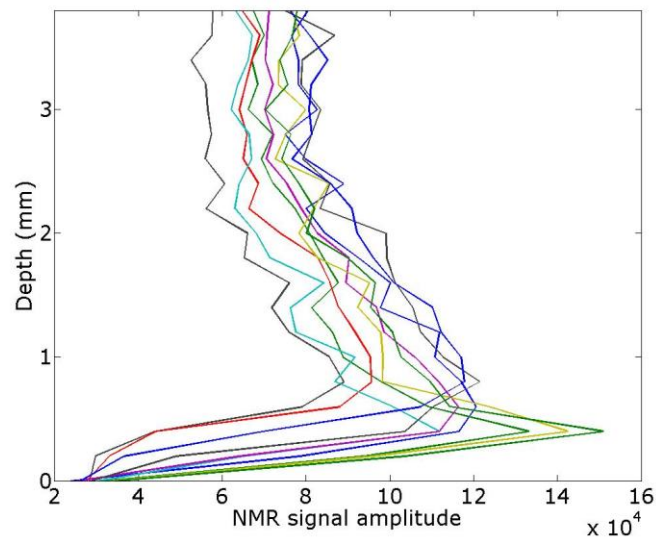


Figure 5.8 Repeat profiles of CP sample

Repeated NMR depth profiles through the sample of CP sandstone are shown in figure 5.8. As seen in the previous data set, the initial low signal at zero depth is due to the plastic sample

holder, all the profiles show a peak due to a water pooling effect where the surface of the sample is in contact with the sample holder.

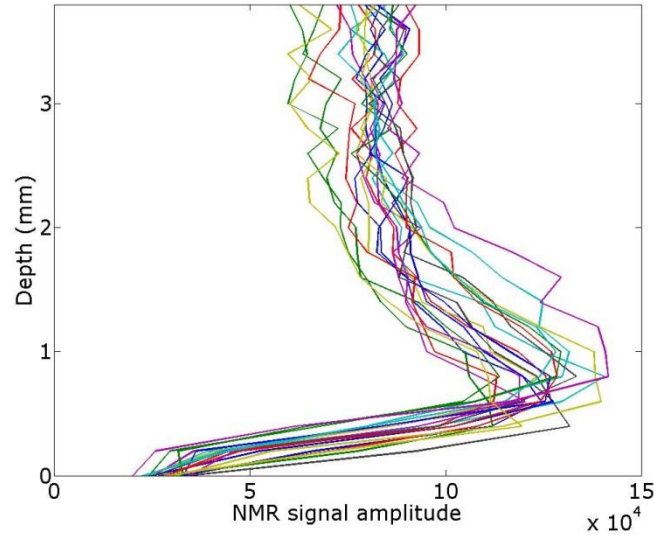


Figure 5.9 Repeat profiles of WM sample

Repeated NMR depth profiles through the sample of WM sandstone are shown in figure 5.9. The initial low signal at zero depth is due to the plastic sample holder, all the profiles show a peak due to a water pooling effect where the surface of the sample is in contact with the sample holder. The repeated measurement profiles shown in figure 5.8 and 5.9 for single samples of CP and WM sandstones show a range in values for each depth beyond the 10% variance due to thermal noise that would be expected for the measurement conditions.

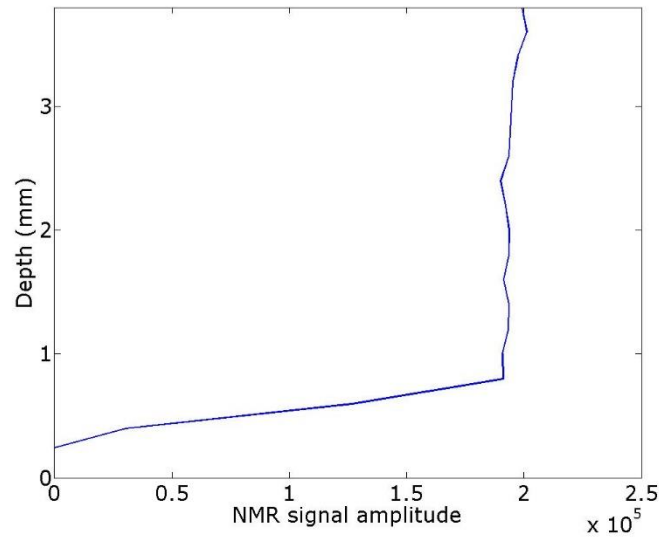


Figure 5.10 NMR profile of bulk water in the sample holder

As done for the previous experiments an NMR profile of bulk water, shown in figure 5.10, was used to determine the percentage water content at each point in the sample profiles, providing direct measurement of the fluid filled porosity of the sandstone samples giving an average porosity of 8.4% for CP samples and 7.8% for WM sandstone.

### 5.3 Considerations for in-situ measurements

Large objects create an antenna effect for radio frequencies particularly in an open air location, which substantially increases the noise in the NMR ultra-sensitive system.



Figure 5.11 NMR in situ with portable Faraday cage

A portable faraday cage, with dimensions sufficient to enclose the object under investigation along with the sensor in its lift, was custom built in an attempt to shield against this effect, shown in figure 5.11. The cage needs to shield the instrument from the surroundings as well as the control PC which also produces interfering rf signals. The cage was built from a framework of hexagonal steel wire mesh covered in six layers of “space blanket” composed of metallized polyethylene terephthalate (MPET), and resulted in a reduction in noise of 30%. Due to the high sensitivity of the instrument to noise, the leakage of radio frequency noise still overwhelmed the useful signal and as a result in situ NMR investigation of large objects such as rock panels is limited by radio signal interference which is particular severe in a densely populated area.

## **5.4 Comparison with other techniques**

### **5.4.1 X-ray micro-computed tomography**

Micro-CT enables three dimensional visualisation of the internal microstructure of the sample according to the composition and density, to produce high resolution 3D images to characterise the internal structure and provide information about the porous network.

X-ray micro-computed tomography (micro-CT) volumetric imaging of samples was performed at Nikon Metrology. Data is generated using an x-ray source that rotates around the object; which is then integrated to generate three-dimensional volumetric information. Figure 5.10 (a) shows the volumetric image of the sintered discs and sandstone samples stacked together with tomographic slices for the CP and WM sandstones samples shown in figure 5.10 (b, c). Each pixel in a tomographic slice corresponds to a voxel in a three dimensional image, the grey scale value of the voxel is determined by the x-ray absorption of the material at that point. The greater

the absorption of the x-ray the brighter the voxel appears, the pore spaces within the sample appear dark and can be identified by applying a threshold to the pixel grey scale values to isolate voxels in the pore volume. Samples were imaged with a voxel size of 17.58  $\mu\text{m}$  in each of the 3 dimensions as shown in figure 5.10 (a); with a further scan focused on the sandstone samples with a voxel size of 5.18  $\mu\text{m}$  shown in figure 5.10 (b) and (c).

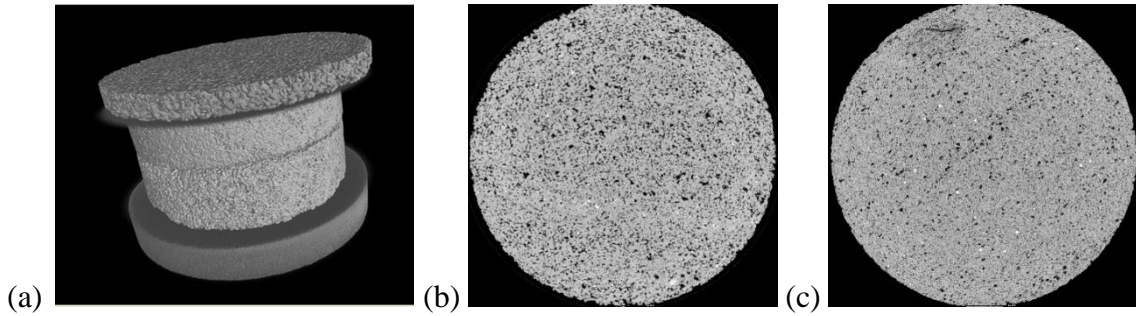


Figure 5.10 micro-CT images of (a) stacked samples (from bottom; sintered disc grade 4, CP sandstone, WM sandstone, sintered disc grade 0), tomographic slices of (b) CP sandstone (c) WM sandstone.

Analysis of the Micro-CT tomographic images determined a porosity of 22% for CP and 15% for WM sandstones, with a mean pore size of 94  $\mu\text{m}$  and 55  $\mu\text{m}$  respectively. The image analysis enables direct measurement of the size of the pore elements.

The pore size distributions found from micro-CT imaging of CP and WM sandstone samples are shown in figures 5.11 and 5.12. The volume of the sample used for the analysis was the same for both distributions. As can be seen from both figure 5.11 and figure 5.12, a large proportion of the pore elements are below the resolution of 18  $\mu\text{m}$  represented by the red bars.

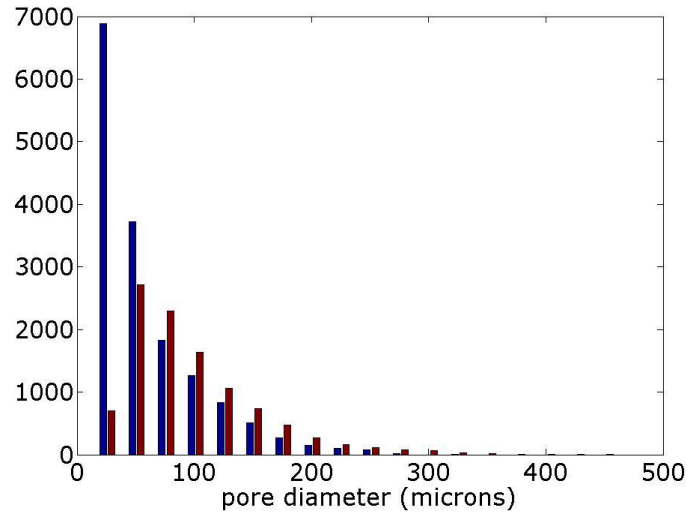


Figure 11. Pore size distribution determined from tomographic slice of CP sandstone (blue bar distribution found from 5.18  $\mu\text{m}$  resolution images, red bar distribution found from 17.58  $\mu\text{m}$  resolution images).

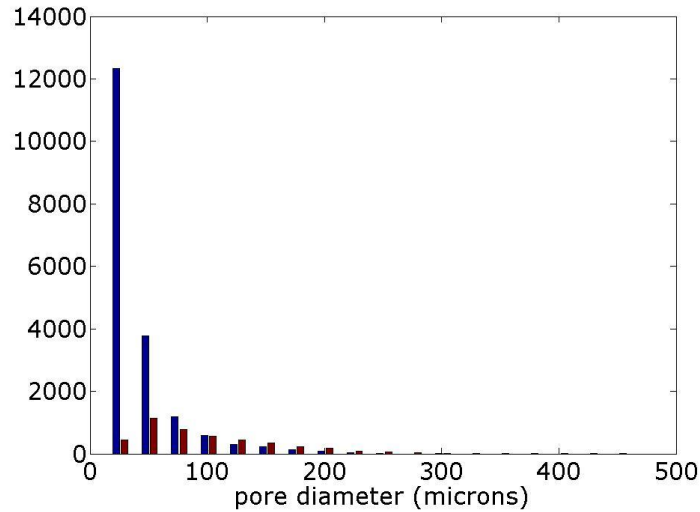


Figure 12. Pore size distribution determined from tomographic slice of WM sandstone (blue bar distribution found from 5.18  $\mu\text{m}$  resolution images, red bar distribution found from 17.58  $\mu\text{m}$  resolution images).

Elements of the porous network smaller than the 18 or 6  $\mu\text{m}$  resolution of the instrument cannot be detected by this technique.

### 5.4.2 Mercury Intrusion Porosimetry

Mercury intrusion Porosimetry (MIP) characterizes the porosity of a sample by applying various amounts of pressure to a sample immersed in mercury [17]. The pressure required to intrude the mercury into the sample pores is inversely proportional to the size of the pore openings. Intrusion porosimetry provides bulk pore information on samples and is the most common technique used to characterize the porosity for geological and building materials. Mercury is a non-wetting fluid and will not spontaneously penetrate pores by capillary action; it must be forced into pores by the application of external pressure. Intrusion pressure values are directly converted into the corresponding pore size using the Washburn equation:

$$D = \left(\frac{1}{P}\right) 4 \gamma \cos \varphi$$

where D is pore diameter, P is the applied pressure,  $\gamma$  the surface tension of the mercury, and  $\varphi$  the contact angle between the mercury and the sample. By measuring the volume of mercury that intrudes into the sample with each pressure change, the volume of pores in the corresponding size class is known. The volume of mercury that enters pores is measured by a mercury penetrometer that is constructed of glass and filled with mercury. The stem of the penetrometer is a capillary that acts as a reservoir for the analytical volume of mercury. MIP analysis of samples was performed at the University of Nottingham with a Micromeritics AutoPore IV 9500 V 1.05 using a penetrometer with 5 ml bulb and 1.131 stem volume, the results are shown in Table 5.1. The technique has a detection range of 3.5 nm – 1 mm, with the assumption that pores are cylindrical and the measured value corresponds to the largest connection from the sample surface to that pore.

The technique cannot be used for repeat measurements of a sample because mercury remains trapped in the sample after depressurisation, necessitating appropriate destruction of the sample following the measurement.

## 5.5 Summary

The results from the different techniques are summarised in table 5.1, also included are the gravimetrically determined porosities for the samples (measured after immersion in water for 120 hours under normal conditions).

	<b>WM porosity (%)</b>	<b>WM mean pore size (µm)</b>	<b>CP porosity (%)</b>	<b>CP mean pore size (µm)</b>
<b>NMR (4 hour)</b>	7.8	n/a	8.4	n/a
<b>NMR (20 hour)</b>	10	n/a	15	n/a
<b>MIP</b>	14	13	19	26
<b>Micro CT</b>	15	55	22	94
<b>Gravimetric</b>	14	n/a	16	n/a

Table 5.1 summary of porosity measurements

Techniques that rely on the intrusion of fluid into the sample, (NMR, MIP, gravimetric) produce results that are ultimately related to the access to the external surface and the connectivity of the pore system. Pores that are inaccessible to an intruded fluid can only be observed with direct imaging techniques.

NMR provides direct information about the surface to volume ratio of fluid filled pore bodies but does not provide information about the shape of the pore elements. If the required experimental conditions can be met (i.e. no rf signal interference), the technique enables measurement of

porosity *in situ* without sampling. The difference in the results for the different experimental durations highlights issue of acquisition time for the technique [7, 10].

Micro-CT image analysis can give direct visualisation of the shape of pore elements and the connections between them, within the resolution limit of the technique. Elements of the porous network smaller than the 5  $\mu\text{m}$  resolution of the instrument cannot be detected. The technique is laboratory based and requires the removal of a sample from the site but the sample is not effected by the measurement.

MIP shows smaller pore sizes because it measures the largest entrance of the pore from its connection to the sample surface rather than the size of the pore body itself. Due to this effect the technique will always show smaller pore sizes than methods of direct measurement. The technique requires a small sample size, but each sample must be destroyed following the measurement to limit the environmental impact of mercury use.

The results of the techniques are not directly comparable, as they rely on different physical principles and the measurements are limited by the resolution range for the technique. Thorough characterisation of the porosity of a material can be achieved by a combination of techniques.

## **References**

1. S. Yu, C. T. Oguchi. Role of pore size distribution in salt uptake, damage, and predicting salt susceptibility of eight types of Japanese building stone. *Engineering Geology*. 115, 226-236. (2010)
2. A. Tugrul. The effect of weathering on pore geometry and compressive strength of selected rock types from Turkey. *Engineering Geology*. 15, 215-227, (2004)

3. E.Molina, G. Cultrone, E. Sebastian, F.J. Alonso, L. Carrizo, J. Gisbert, O. Buj. The pore system of sedimentary rocks as a key factor in durability of building materials. *Engineering Geology*. 118, 110-121, (2011)
4. D. Benavente, M.A. Garcia del Cura, R. Fort, S. Ordonez. Durability estimation of porous building stones from pore structure and strength. *Engineering Geology*. 74, 113-127, (2004)
5. R.L. Kleinberg. Well Logging. *Encyclopaedia of Nuclear Magnetic Resonance*. John Wiley & Sons. 4960-4968, (2002)
6. B. Blümich, J. Perlo, F. Casanova. Mobile single-sided NMR. *Progress in Nuclear Magnetic Resonance Spectroscopy*, 52, 197-269, (2008)
7. B. Blümich, F. Casanova, J. Perlo, F. Presciutti, C. Anselmi, B. Doherty. Noninvasive Testing of Art and Cultural Heritage by Mobile NMR. *Accounts of Chemical Research*. 43, 6, 761-770. (2010)
8. D. Capitani, V. Di Tullio, N. Proietti, Nuclear Magnetic Resonance to characterise and monitor Cultural Heritage. *Progress in Nuclear Resonance Spectroscopy*. 64, 29-69. (2012)
9. S. Sharma, F. Casanova, W. Wache, A. Segre, B. Blümich. Analysis of historical porous building materials by the NMR-MOUSE®. *Magnetic Resonance Imaging*. 21, 249-255. (2003)
10. T. Poli, L. Toniolo, M. Valentini, G. Bizzaro, R. Melzi, F. Tedoldi, G. Cannazza. A portable NMR device for the evaluation of water presence in building materials. *Journal of Cultural Heritage*. 8, 134-140. (2007)
11. M. Brai, C. Casieri, F. De Luca, P. Fantazzini, M. Gombia, C. Terenzi. Validity of NMR pore-size analysis of cultural heritage ancient building materials containing magnetic impurities. *Solid State Nuclear Magnetic Resonance*. 32, 129-135. (2007)

12. K. Keating, R. Knight, A laboratory study to determine the effect of iron oxides on proton NMR measurements. *Geophysics*. 72, 1, 27-32. (2007)
13. K. Keating, R. Knight, A laboratory study of the effect of Magnetite on NMR relaxation rates. *Journal of Applied Geophysics*, 66, 188-196. (2008)
14. M. H. Cohen, K. S. Mendelson. Nuclear magnetic relaxation and the internal geometry of sedimentary rocks. *J. Appl. Phys*, 53, 2, 1127-1135. (1982)
15. H.Y. Carr, E.M. Purcell, Effects of diffusion on free precession in nuclear magnetic resonance experiments. *Phys. Rev.* 94, 688-638, (1954)
16. S. Meiboom, D. Gill, Modified spin-echo method for measuring nuclear relaxation times, *Rev. Sci. Instrum.* 29, 688-691, (1958)
17. H. Giesche. Mercury Porosimetry: a General (Practical) Overview. *Part. Part. Syst. Charact.* 23, 1-11. (2006)

## Chapter 6 Studies of Historic stone *in situ*

In this chapter the methods described in Chapters 2 and 3; Optical Coherence Tomography measurement of grain size distribution and hydraulic conductivity, will be applied to the study of historic stone *in situ*.

An initial test study was carried out on sandstone headstones at Nottingham General Cemetery, then a further study was done at the archeologically sensitive sites of presumed Neolithic standing stones in Derbyshire. The methods were then applied to the study of prehistoric rock art sites in Northumberland.

A summary of the methods applied in-situ are included below.

- Optical coherence tomography imaging of subsurface structures to determine grain size distribution

The OCT probe is attached to a motorized micrometre linear stage, to obtain an image cube as the stage scans in the transverse y-direction perpendicular to the x-range of the scan, shown in use in-situ in figure 6.1.

Volume scans were performed with a B-scan cross-sectional width of 6 mm with the probe scanning continuously as it moved 6 mm perpendicular to the B-scan axis at  $0.005 \text{ mm s}^{-1}$  to produce the imaged 6 x 6 mm volume to a depth of 0.9 mm.



Figure 6.1 OCT volumetric imaging in-situ

The method can detect grain sizes from coarse silt (0.031-0.063 mm) to coarse sand (0.50-1.00 mm) determined by the resolution of the instrument and its depth range in the sample. The percentage of sandstone volume imaged as detectable grains varies with the sample but can be used to produce a representative grain size distribution.

- Optical Coherence Tomography measurement of Hydraulic conductivity

Measurements were made at a distance of 10 mm from the imbibition point at the sample surface (see Chapter 3 figure 3.1). Water is added at a rate to ensure that a surface droplet is on the surface throughout the experiment, thus matching supply to imbibition and preventing water flooding across the surface of the sample.

Where measurements were performed with the surface in a vertical orientation water is added below the observed range. Hydraulic conductivity measurements, demonstrated in Chapter 3, with OCT taken with samples in a vertical orientation showed that wetting front velocities for sandstone samples are the same as their corresponding values for horizontal hydraulic conductivity, indicating that the material properties dominate the movement of water in the samples rather than gravity.

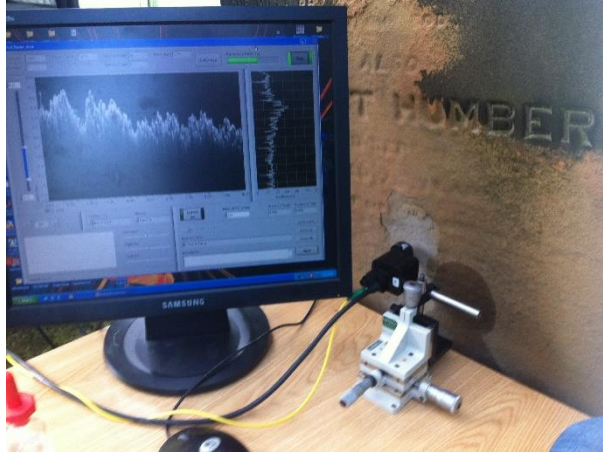


Figure 6.3. OCT measurement of hydraulic conductivity *in situ*.

With the set image application time of 0.88 seconds per frame (B scan), if the wetting front moves across a 10 mm range within a single image frame, its velocity is above  $1 \text{ cm s}^{-1}$  and can therefore be considered to be permeable with regards to hydraulic conductivity. In a 2 hour observation time under these settings and taking 0.1 mm (10 columns of A scans) as the minimum distance range of detectable water movement, wetting velocities down to  $10^{-6} \text{ cm s}^{-1}$  can be measured; that is, the stone can be considered impervious to water. The full range of hydraulic conductivities that are likely to occur in natural sandstones, from pervious to impervious ( $1$  to  $10^{-6} \text{ cm s}^{-1}$ ), can be detected by this imaging speed within a 2 hour observation time.

These methods were applied to the study of historic stone in-situ at the locations described in the following sections;

### 6.1 Sandstone headstones at Nottingham General Cemetery

An initial test study was carried out on historic sandstone headstones at Nottingham General Cemetery. The site provided a natural laboratory of stone weathering with a variety of sandstone placed in the same semi-controlled environment over a range of exposure times from 128 – 165

years, with an average exposure of 140 years. The hydraulic conductivity measurements were performed at the different levels of surface recession for each stone to investigate effect of the intensity of weathering features. Volumetric imaging was performed on headstones where the interior of the stone was exposed in order to determine the representative grain size distribution of the stone without the impact of stone polish from masonry finishing.

<b>Headstone</b>	<b><i>In situ</i> measurements performed</b>
BG1873	Hydraulic conductivity measured at 7 positions
GC1876	Hydraulic conductivity measured at 4 positions Volumetric imaging for grain size distribution Cross-sectional imaging of inscription and surface detachment
JG1873	Hydraulic conductivity measured at 4 positions
WW1881	Hydraulic conductivity measured at 5 positions Volumetric imaging for grain size distribution
AF1875	Hydraulic conductivity measured at 4 positions Volumetric imaging for grain size distribution
WS1887	Hydraulic conductivity measured at 3 positions Volumetric imaging for grain size distribution
HB1877	Hydraulic conductivity measured at 4 positions Volumetric imaging for grain size distribution

AT1850	Hydraulic conductivity measured at 2 positions
WK1884	Hydraulic conductivity measured at 3 positions Volumetric imaging for grain size distribution

6.2 Derbyshire standing stones at Barbrook I and Gardom’s Edge

A further test study was performed in an area of early human activity in the Peak District, the standing stones of Barbrook I and Gardom’s edge were identified as suitable locations to determine any modifications to procedures required by archeologically sensitive sites. The standing stones are in proximity to a rock art panel which has been reinterred and replaced with a fibre glass replica at the surface.

<b>Location</b>	<b><i>In situ</i> measurements performed</b>
Barbrook I	Diagnostic mapping of weathering features Hydraulic conductivity measurement of primary stone
Gardom’s Edge Monolith	Diagnostic mapping of weathering features Access assessment of site

6.3 Northumberland rock art at Chatton Park and Roughting Linn

The sites selected for this study are rock art panels at Chatton Park and Roughting Linn, they represent some of the best examples of prehistoric rock art.

Chatton Park is a hill top location with panels of rock art motifs on areas of the bedding plane exposed at the surface.

<b>Study area</b>	<b><i>In situ</i> measurements performed</b>
Host rock	Hydraulic conductivity measurement at 1 position Volumetric imaging for grain size distribution
Rock art motifs	Hydraulic conductivity measurement at 7 positions Volumetric imaging for grain size distribution
Historical graffiti	Hydraulic conductivity measurement at 3 positions

Roughting Linn is the site of an elongated dome shaped outcrop with extensive rock art motifs, the outcrop is in a clearing surrounded by trees within a lowland basin.

<b>Study area</b>	<b><i>In situ</i> measurements performed</b>
Host rock	Hydraulic conductivity measurement at 1 position Volumetric imaging for grain size distribution
Rock art motifs	Hydraulic conductivity measurement at 9 positions Volumetric imaging for grain size distribution

## **Chapter 6.1 Sandstone headstones at Nottingham General Cemetery**

The use of gravestones for the assessment of weathering rates is well established [1-5]. Cemeteries provide a natural laboratory of stone weathering in an open air environment, as they provide a variety of stones placed in the same environmental conditions. The differing rates and forms of weathering occurring will depend upon factors intrinsic to the stone. The use of stone grave monuments is historically wide spread and they are typically marked with their date of emplacement, though there may be some uncertainty over the time lapse between the date indicated on the stone and its emplacement in situ.

Nottingham General Cemetery is a closed historic cemetery now owned by the local council and classified under Parks and Open Spaces (OS Grid Reference SK56557 40348). The site has a total area of 18 acres that forms part of a long shallow valley in the urban environment of Nottingham city centre. It is included in the English Heritage register of Parks and Gardens of Special Historic Interest (Grade II Reference GD4619). The cemetery was opened by a private company in 1837 and was used for over 29,000 burials before its closure in 1954.

The headstones studied were selected based on criteria to reduce the variation in their microenvironments. All headstones studied were at a similar orientation to avoid variation in weathering due to differing insolation, within 10 degrees of their original vertical position and away from trees which could influence weathering through differing microclimates and biological deposits. The stones selected all have legible inscriptions for the reference date including an area where the inscription appears crisp as a measure of the original surface. The headstones range in exposure time from 128 to 165 years with an average exposure of 140 years.

### 6.1a BG1873

Headstone BG1873 is a complex shouldered rounded-top sandstone tablet of dimensions: height 145 cm, width 76 cm, depth 10 cm. The stone has decorative and incised carving on its north face shown in figure 6.1a.1.



Figure 6.1a.1. Complex sandstone tablet incised on north face dated 1873: images of north, east, south and west faces.

A schematic of weathering features to north and south faces is shown in figure 6.1a.2. The north face has a central area of discoloration lighter than the rest of the tablet with alteration to the surface textures causing granular roughness and slight rounding to incised lettering. There is region of lichen encrustation and moss growth above grass height in the lower third of the stone. On the north face there is a central area with a rough surface texture, patches of discoloration and surface cracking due to early stages of contour scaling. Centimeter scale contour scaling with ~ 5 mm surface recession. The lower section shown with a dashed margin in figure 6.1a.2 shows surface pitting and granulation causing a rough uneven surface resessed by ~0.5 cm due to contour scaling,

patches of orange colouration. Lichen are growing in patches at base above grass height, yellow and white encrustations are approximately 1 cm in diameter.

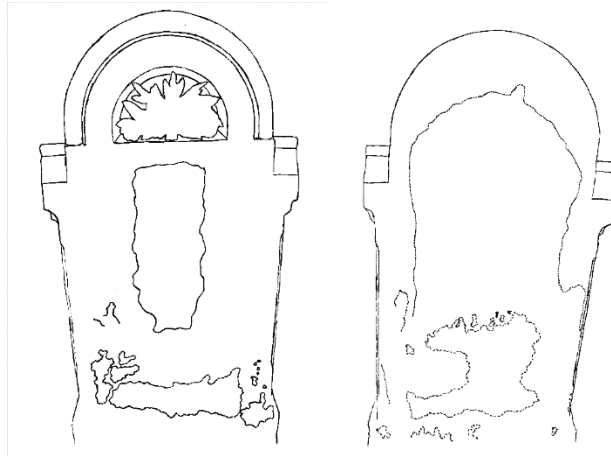


Figure. 6.1a.2 Schematic of weathering features on north and south face of gravestone BG1873

BG1873 wetting scan 1 (BGWS1) was performed with the OCT probe positioned between the lines of the inscription on the north face shown in figure 6.1a.3. The surface of the stone is discoloured and has a granular texture at this position.



Figure 6.1a.3 Position of wetting scan BGWS1

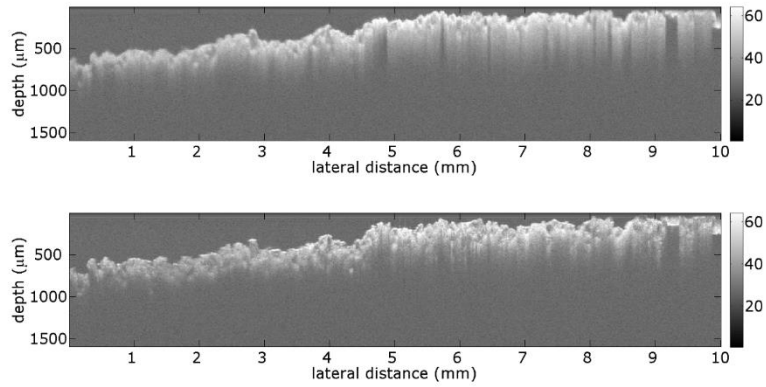


Figure 6.1a.4. OCT virtual cross sections of BGWS1 scan position when (a) dry and (b) wet.

Virtual cross sectional images of the scan position for BGWS1 are shown in figure 6.1a.4 when dry and wet. The presence of water in the sample reduces scattering as it reduces the refractive index mismatch, features can be seen to a greater depth within the stone.

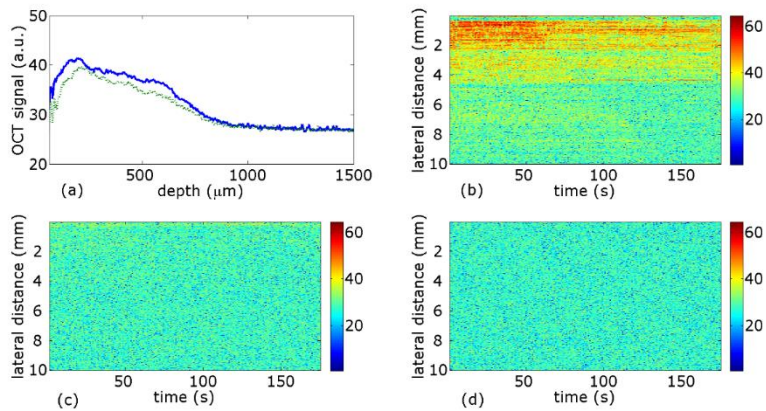


Figure 6.1a.5. BGWS1: (a) pixel intensity values averaged across the 10 mm cross section when dry (solid blue line) and wet (dotted green line); signal intensity values at depths of (b)  $\sim 400 \mu\text{m}$ , (c)  $\sim 700 \mu\text{m}$ , and (d)  $\sim 1000 \mu\text{m}$  across the lateral range of the scan over time. The OCT signals are in log scales.

Figure 6.1a.5 (a) shows the peak centered at approximately 150-200  $\mu\text{m}$  is due to scattering at the surface of the stone. The breadth of the peak is due to the rough sloped surface of the stone. Figure 6.1a.5 (b) – (d) sample the signal intensity at a specific depth of 400, 700 and 1000  $\mu\text{m}$  over the duration of the measurement. Water enters at 58 s crossing the lateral range of the scan by 158 s, showing little difference in water movement speed in the lateral direction between the different depths. The change in signal due to water cannot be detected below 1 mm. The 100 s time to cross the lateral range of the 10mm gives a wetting scan velocity of  $0.010 \pm 0.001 \text{ cm s}^{-1}$ . The hydraulic conductivity at this point is in the high range of semi-pervious which is consistent within expected values for sandstone

BG1873 wetting scan 2 (BGWS2) was performed with the OCT probe positioned between incised letters, approx 5 cm above BGWS1, the tablet surface is discoloured and has a granular texture, shown in figure 6.1a.6.



Figure 6.1a.6. Position of wetting scan BGWS2

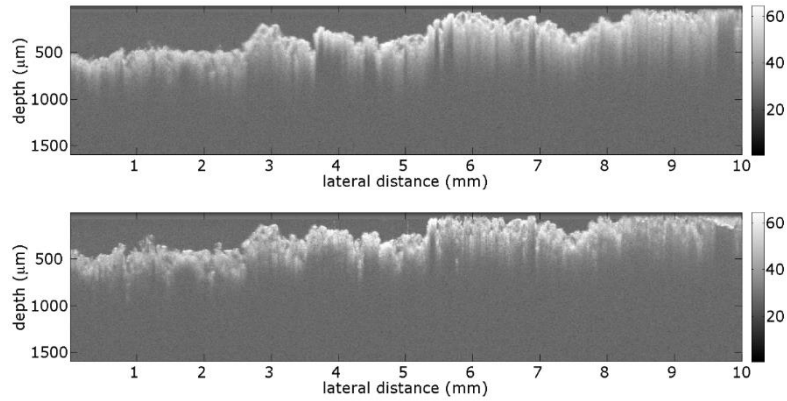


Figure 6.1a.7. OCT virtual cross sections of BGWS2 scan position when (a) dry and (b) wet.

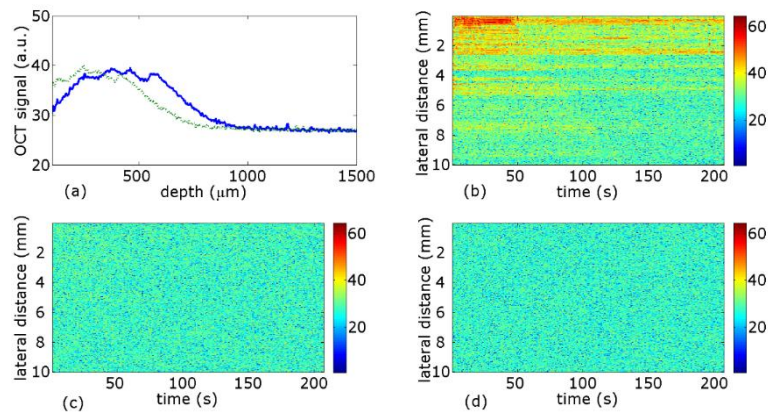


Figure 6.1a.8. BGWS2: (a) pixel intensity values averaged across the 10 mm cross section when dry (solid blue line) and wet (dotted green line); signal intensity values at depths of (b)  $\sim 400 \mu\text{m}$ , (c)  $\sim 700 \mu\text{m}$ , and (d)  $\sim 1000 \mu\text{m}$  across the lateral range of the scan over time. The OCT signals are in log scales.

The peak in figure 6.1a.8 (a) is centered at approximately  $200\text{--}250 \mu\text{m}$ , the shift in peak is due to small shift in the probe towards the surface during the scan, shown in figure 6.1a.7. The breadth of the peak is due to the rough sloped surface of the stone. Figures 6.1a.8. (b) – (d) sample the signal intensity at a specific depth of  $400$ ,  $700$  and  $1000 \mu\text{m}$  over the duration of the measurement. Water enters at  $46 \text{ s}$  crossing the lateral range of the scan by  $137 \text{ s}$ , the  $91 \text{ s}$  time to cross the lateral range of the  $10 \text{ mm}$  gives a wetting scan velocity of  $0.011 \pm 0.001 \text{ cm s}^{-1}$ . The hydraulic conductivity at this point is in the high range of semi-pervious.

BG1873 wetting scan 3 (BGWS3) was performed with the OCT probe positioned approximately 10 cm above BGWS2, the surface has slight discoloration to surface and surface roughness as shown in figure 6.1a.9.



Figure 6.1a.9. Position of wetting scan BGWS3

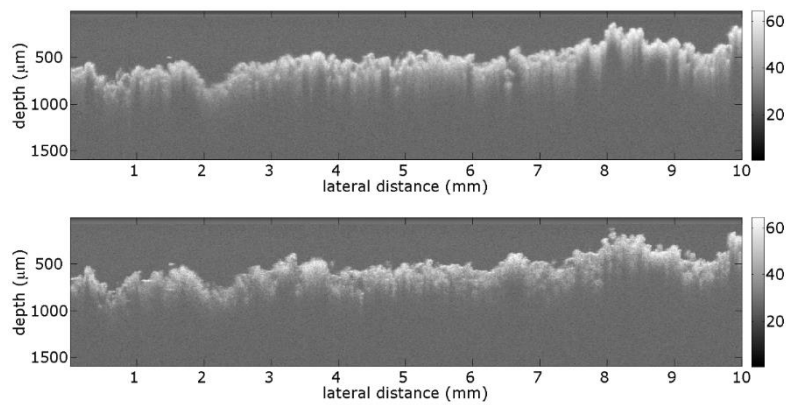


Figure 6.1a.10 OCT virtual cross sections of BGWS3 scan position when (a) dry and (b) wet.

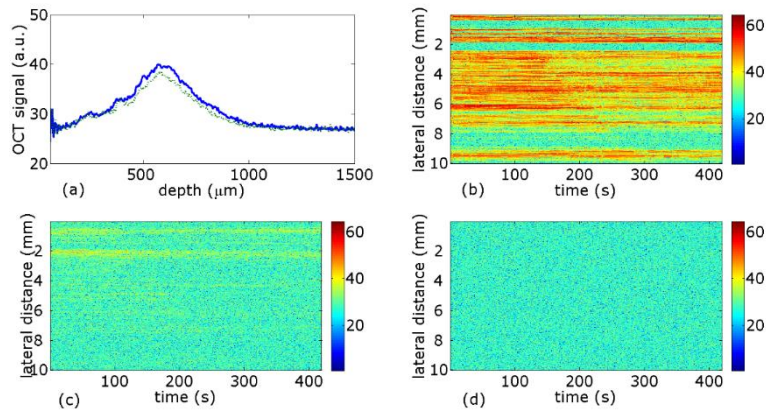


Figure 6.1a.11. BGWS3: (a) pixel intensity values averaged across the 10 mm cross section when dry (solid blue line) and wet (dotted green line); signal intensity values at depths of (b) ~400  $\mu\text{m}$ , (c) ~700  $\mu\text{m}$ , and (d) ~ 1000  $\mu\text{m}$  across the lateral range of the scan over time. The OCT signals are in log scales.

The peak in figure 6.1a.11 (a) centered at approximately 550-600  $\mu\text{m}$ , the breadth of the peak is due to the rough surface of the stone, shown in figure 6.1a.10. Figures 6.1a.11 (b) – (d) sample the signal intensity at a specific depth of 400, 700 and 1000  $\mu\text{m}$  over the duration of the measurement. Water enters at 89 s crossing the lateral range of the scan by 299 s, the 210 s time to cross the lateral range of the 10 mm gives a wetting scan velocity of  $0.0048 \pm 0.0005 \text{ cm s}^{-1}$ . The hydraulic conductivity at this point is in the middle range of semi-pervious.

BG1873 wetting scan 4 (BGWS4) was performed with the OCT probe positioned on the east shoulder of the tablet shown in figure 6.1a.12. There is a surface crust and evidence of granular loss as well as indications of mechanical damage by chipping.



Figure 6.1a.12. Position of wetting scan BGWS4

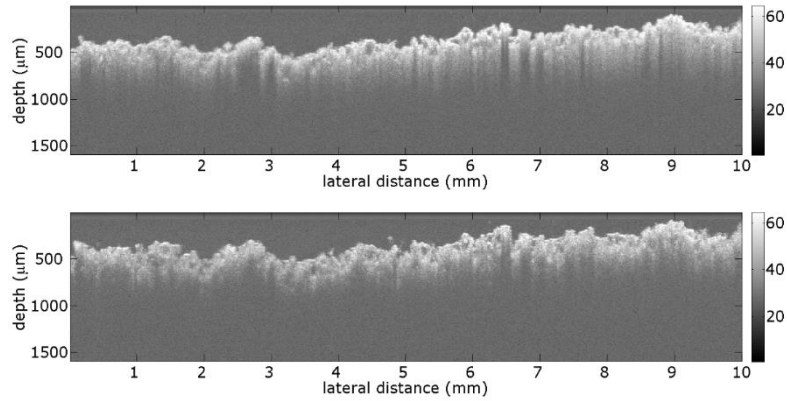


Figure 6.1a.13. OCT virtual cross sections of BGWS4 scan position when (a) dry and (b) wet.

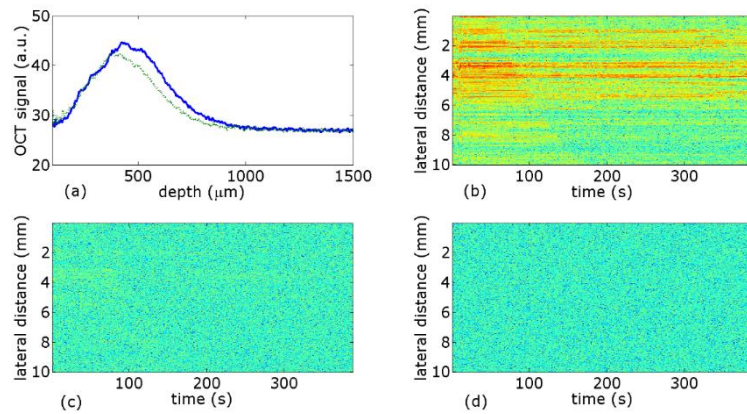


Figure 6.1a.14. BGWS4: (a) pixel intensity values averaged across the 10 mm cross section when dry (solid blue line) and wet (dotted green line); signal intensity values at depths of (b)  $\sim 400 \mu\text{m}$ , (c)  $\sim 700 \mu\text{m}$ , and (d)  $\sim 1000 \mu\text{m}$  across the lateral range of the scan over time. The OCT signals are in log scales.

The peak in figure 6.1a.14 (a) is centered at approximately  $450\text{--}500 \mu\text{m}$ , the breadth of the peak is due to the rough surface of the stone, shown in figure 6.1a.13. Figures 6.1.14 (b) – (d) sample the signal intensity at a specific depth of 400, 700 and 1000  $\mu\text{m}$  over the duration of the measurement. Water enters at 53 s crossing the lateral range of the scan by 176 s, the 123 s time to cross the lateral range of the 10 mm gives a wetting scan velocity of  $0.0081 \pm 0.0005 \text{ cm s}^{-1}$ . The hydraulic conductivity at this point is in the middle range of semi-pervious.

BG1873 wetting scan 5 (BGWS5) was performed with the OCT probe positioned on the undecorated south face on an area with a thin black deposit discolouring the surface.

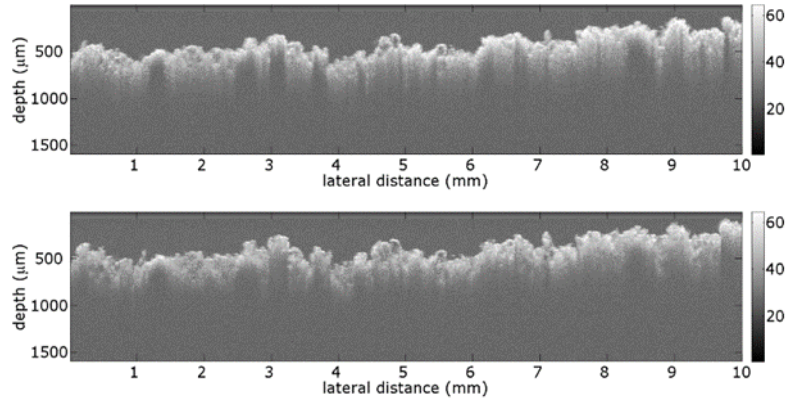


Figure 6.1a.15. OCT virtual cross sections of BGWS5 scan position when (a) dry and (b) wet.

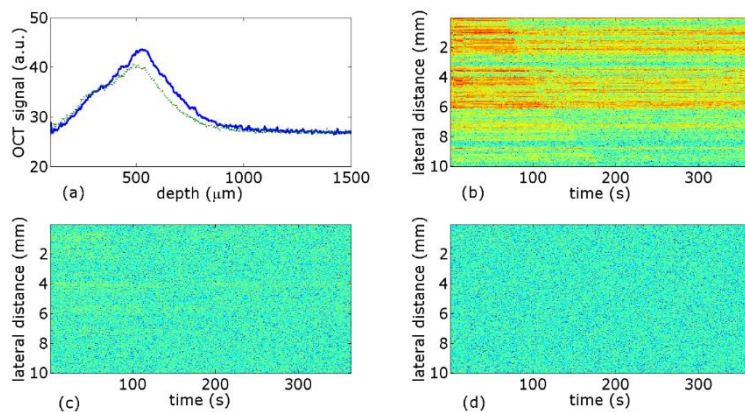


Figure 6.1a.16. BGWS5: (a) pixel intensity values averaged across the 10 mm cross section when dry (solid blue line) and wet (dotted green line); signal intensity values at depths of (b)  $\sim 400 \mu\text{m}$ , (c)  $\sim 700 \mu\text{m}$ , and (d)  $\sim 1000 \mu\text{m}$  across the lateral range of the scan over time. The OCT signals are in log scales.

The peak in figure 6.1a.16. (a) is centered at approximately 500-550  $\mu\text{m}$ , the breadth of the peak is due to the rough surface of the stone, shown in figure 6.1a.15. Figures 6.1a.16. (b) – (d) sample the signal intensity at a specific depth of 400, 700 and 1000  $\mu\text{m}$  over the duration of the measurement. Water enters at 64 s crossing the lateral range of the scan by 184 s, the 120 s time to cross the lateral range of the 10 mm gives a wetting scan velocity of  $0.0084 \pm 0.0005 \text{ cm s}^{-1}$ . The hydraulic conductivity at this point is in the middle range of semi-pervious.

BG1873 wetting scan 6 (BGWS6) was performed with the OCT probe positioned on the undecorated south face, on an area with surface yellowing and slightly rough texture.

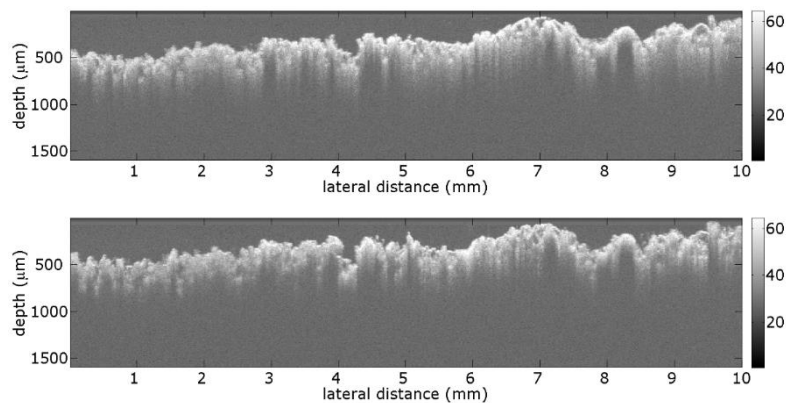


Figure 6.1a.17. OCT virtual cross sections of BGWS6 scan position when (a) dry and (b) wet.

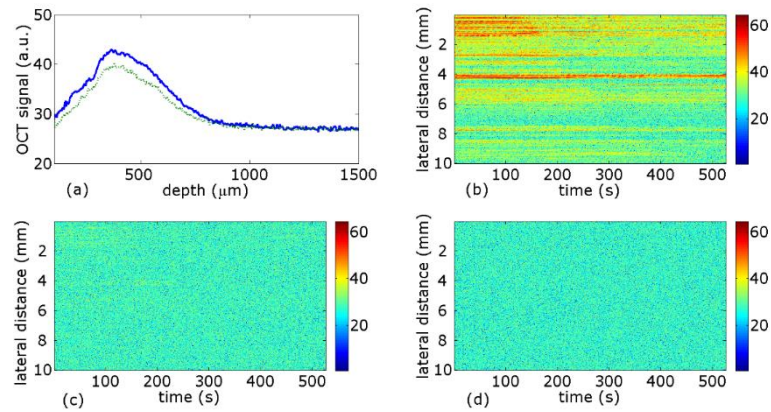


Figure 6.1a.18. BGWS6: (a) pixel intensity values averaged across the 10 mm cross section when dry (solid blue line) and wet (dotted green line); signal intensity values at depths of (b) ~400  $\mu\text{m}$ , (c) ~700  $\mu\text{m}$ , and (d) ~ 1000  $\mu\text{m}$  across the lateral range of the scan over time. The OCT signals are in log scales.

The peak in figure 6.1a.18 (a) is centered at approximately 400-450  $\mu\text{m}$ , the breadth of the peak is due to the rough surface of the stone, shown in figure 6.1.17. Figure 6.1.18. (b) – (d) sample the signal intensity at a specific depth of 400, 700 and 1000  $\mu\text{m}$  over the duration of the measurement. Water enters at 128 s crossing the lateral range of the scan by 436 s, the 308 s time to cross the lateral range of the 10 mm gives a wetting scan velocity of  $0.0032 \pm 0.0005 \text{ cm s}^{-1}$ . The hydraulic conductivity at this point is in the low middle range of semi-pervious.

BG1873 wetting scan 7 (BGWS7) was performed with the OCT probe positioned on the undecorated south face on an area of intact surface with no discoloration or surface roughening.

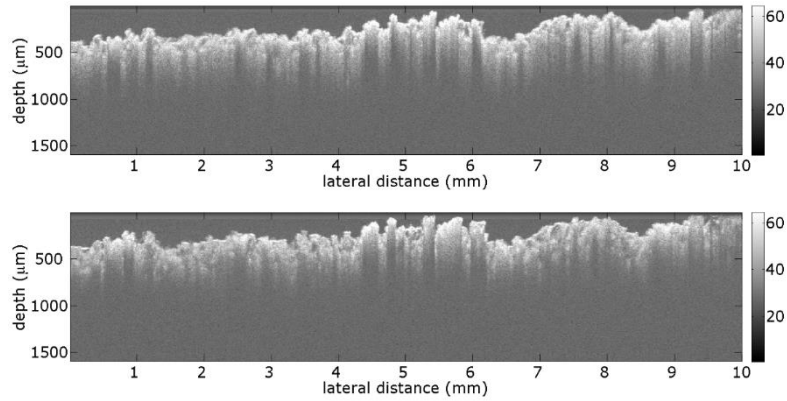


Figure 6.1a.19. OCT virtual cross sections of BGWS7 scan position when (a) dry and (b) wet.

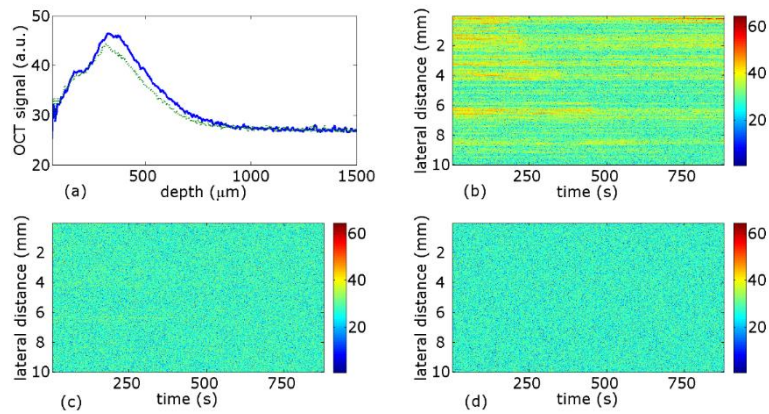


Figure 6.1a.20. BGWS7: (a) pixel intensity values averaged across the 10 mm cross section when dry (solid blue line) and wet (dotted green line); signal intensity values at depths of (b)  $\sim 400 \mu\text{m}$ , (c)  $\sim 700 \mu\text{m}$ , and (d)  $\sim 1000 \mu\text{m}$  across the lateral range of the scan over time. The OCT signals are in log scales.

The peak in figure 6.1a.20. (a) is centered at approximately  $400\text{--}450 \mu\text{m}$  the breadth of the peak is due to the rough surface of the stone, shown in figure 6.1a.19. Figures 6.1a.20. (b) – (d) sample the signal intensity at a specific depth of 400, 700 and 1000  $\mu\text{m}$  over the duration of the measurement. Water enters at 184 s crossing the lateral range of the scan by 753 s, the 569 s time to cross the lateral range of the 10 mm gives a wetting scan velocity of  $0.0018 \pm 0.0005 \text{ cm s}^{-1}$ . The hydraulic conductivity at this point is in the low middle range of semi-pervious.

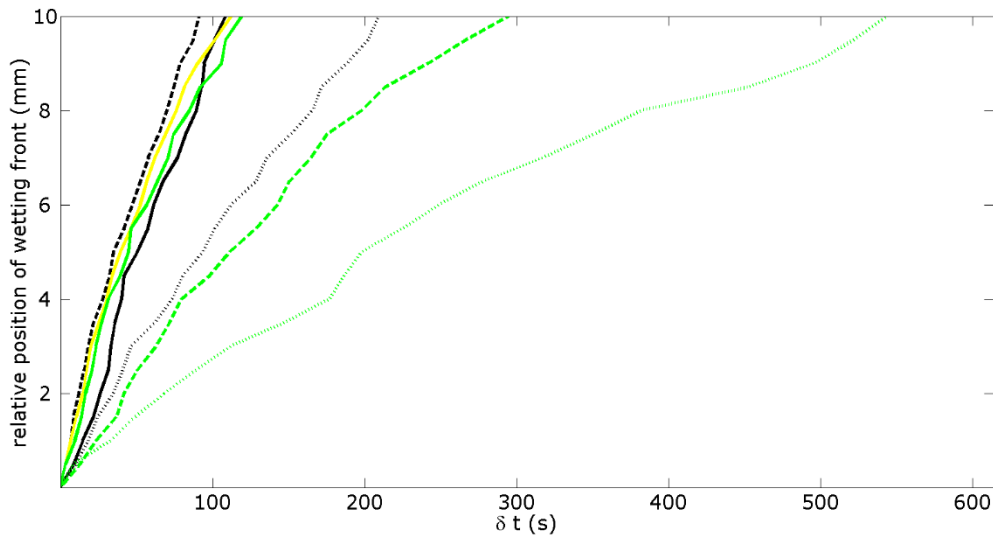


Figure 6.1a.21. Position of the wetting front over time for BGWS1 (black solid line), BGWS2 (black dashed line), BGWS3 (black dotted line), BGWS4 (yellow solid line), BGWS5 (green solid line), BGWS6 (green dashed line), BGWS7 (green dotted line).

Wetting front velocities for all scans are shown in figure 6.1a.21. Scan BGWS7 is on a surface area with no roughness or discoloration providing the freshest surface with hydraulic conductivity of  $0.0018 \pm 0.0005 \text{ cm s}^{-1}$  as a reference measurement. Scans BGWS3 and BGWS6 are both on surfaces with slight discoloration and slight increase in roughness. BGWS3 shows very slight light discoloration to surface and surface roughness with hydraulic conductivity of  $0.0048 \pm 0.0005 \text{ cm s}^{-1}$ , BGWS6 scan position is on the undecorated south face, slight discoloration, surface yellowing and slightly rough surface texture with hydraulic conductivity of  $0.0032 \pm 0.0005 \text{ cm s}^{-1}$ . Slight changes to the surface due to weathering have increased the hydraulic conductivity compared to the fresh surface. Scans BGWS4 and BGWS5 are in positions where a surface crust is present. BGWS4 has orange surface crust and granular loss, with hydraulic conductivity of  $0.0081 \pm 0.0005 \text{ cm s}^{-1}$ . BGWS5 scan position is on undecorated south face surface discoloration, thin black surface deposit with hydraulic conductivity of  $0.0084 \pm 0.0005 \text{ cm s}^{-1}$ . A further increase in hydraulic conductivity is found when a crust is present on the weathered surface. Scans BGWS1 and BGWS2 are both on a

surface with light discoloration and a granular rough surface texture where BGWS1 has  $0.010 \pm 0.001 \text{ cm s}^{-1}$  and BGWS2 has  $0.011 \pm 0.001 \text{ cm s}^{-1}$ . Where the surface exhibits a surface discoloration and mm scale granular surface with rounding to incised carving, the greatest increase in hydraulic conductivity is seen. Hydraulic conductivity measurements show a general increase corresponding with increased intensity of surface weathering features on this stone.

### 6.1b GC1876

Headstone GC1876 is a complex style ornamented rounded-top sandstone tablet of dimensions: height 152 cm, width 76 cm, depth 8 cm. The stone has decorative and incised carving on its north face shown in figure 6.1b.1.



Figure 6.1b.1. Complex sandstone tablet incised on north face dated 1876: images of north, east, south and west faces.

The north face has a central area of surface recession due to contour scaling with a central area recessed by 2 mm surrounded by an area of 1 mm recession with a margin of detached surface flakes. Below the area of recession, surface detachment is occurring around the letters of the inscription. There is a region of light discoloration and granular surface texture below the inscription. The tablet has an ornamented top margin with black surface deposit and an

ornamental dove panel with remnants of a white paint surface in the margins, there is an area of white residue below the dove motif. The south face shows more intense surface detachment by contour scaling with recession between 1 and 4 mm, a schematic of weathering features to north and south faces is shown in figure 6.1b.2.



Figure 6.1b.2. Schematic of weathering features on north and south face of gravestone GC1876

The representative grain size distribution was determined from an OCT volume scan over an area of 6 x 6 mm using the imaging protocol described in Chapter 2. Within this volume 86 grains were identified, the size distribution of which is shown in figure 6.1b.3.

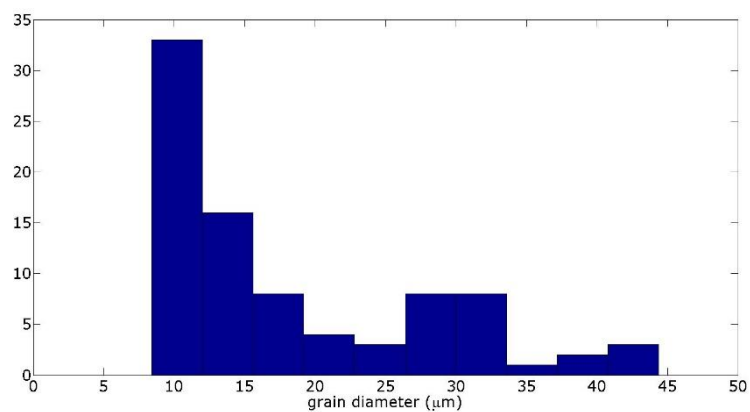


Figure 6.1b.3 Representative grain size distribution for GC1876

The minimum grain size detected, 10  $\mu\text{m}$ , is determined by the spatial resolution of the instrument, the maximum is found to be 44  $\mu\text{m}$  with a mean of 18  $\mu\text{m}$  and standard deviation of 10. The detected grain sizes are in the range of medium to coarse silt.

OCT imaging can be used to monitor the rounding and roughening of the incised inscriptions on the sandstone surface to monitor the effect of weathering.

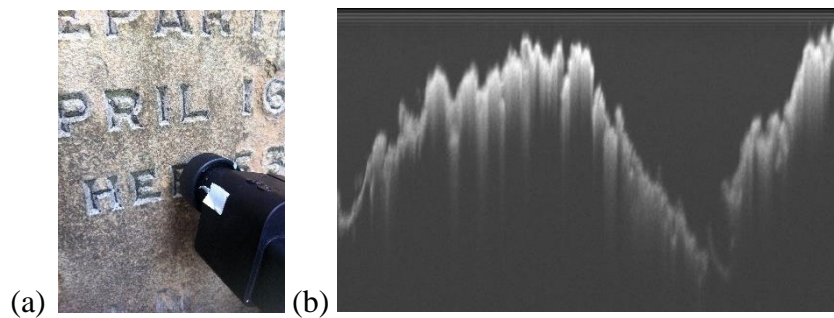


Figure 6.1b.4 (a) Position of image scan GC 'R' (b) OCT virtual cross sections of incised letter R (8.5 x 1.5 mm)

Stone surface has a granular texture, the alteration is present within the incised carving shown in the roughed V cross section in figure 6.1b.4 for the letter R.

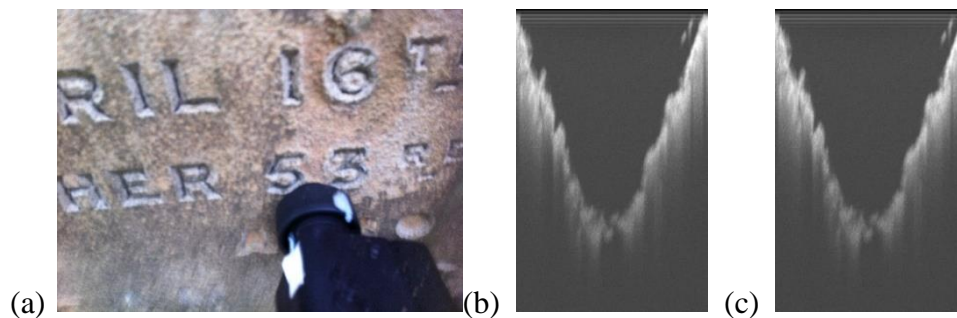


Figure 6.1b.5. (a) Position of image scan GC '5' and '3' (b) OCT virtual cross sections of incised number 5 (image width 3, height 1.5 mm), (c) OCT virtual cross sections of incised number 3 (image width 3, height 1.5 mm).

Surface loss to a depth of 2 mm has occurred around the incised inscription but the original surface is present within the incisions of numbers 5 and 3 which has a crisp V shaped cross

section shown in figure 6.1b.5. OCT imaging can also be used to monitor surface detachment due to contour scaling and flaking; as shown in figure 6.1b.6 to the left of the image the fainter recessed surface after the surface has detached and the brighter area of surface flaking to the right.

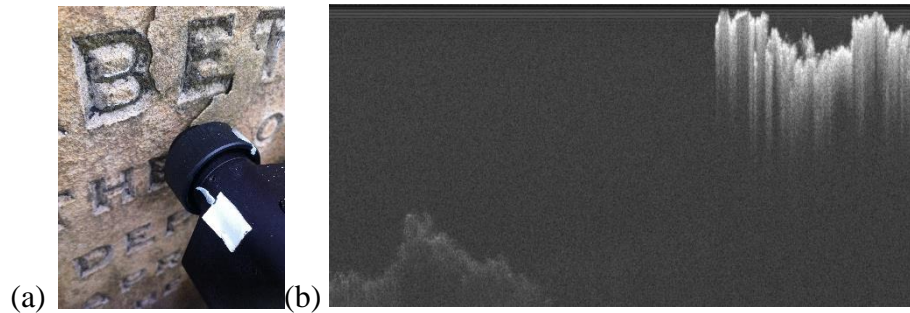


Figure 6.1b.6.(a) Position of image scan of contour scale detachment,(b) OCT virtual cross section of surface detachment.

This imaging technique can be used to monitor the development and detachment of surface flakes during weathering processes. Repeated imaging of the same position over time can be performed to track the progression and distance of surface detachment.

GC1876 wetting scan 1 (GCWS1) was performed with the OCT probe positioned on the north side on an area recessed by 2 mm due to contour scaling. The recessed surface is discoloured and undergoing granular loss shown in figure 6.1b.7.



Figure 6.1b.7. Position of wetting scan GCWS1

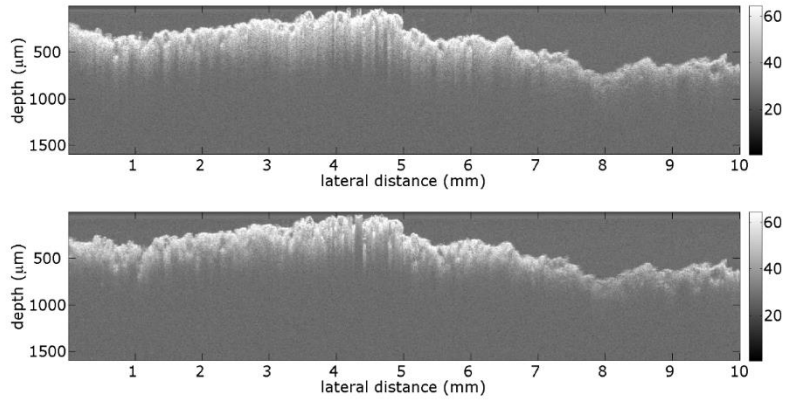


Figure 6.1b.8. OCT virtual cross sections of GCWS1 scan position when (a) dry and (b) wet.

Virtual cross sectional images of the scan position for GCWS1 are shown in figure 6.1b.8. when dry and wet. The presence of water in the sample reduces scattering as it reduces the refractive index mismatch, features can be seen to a greater depth within the stone.

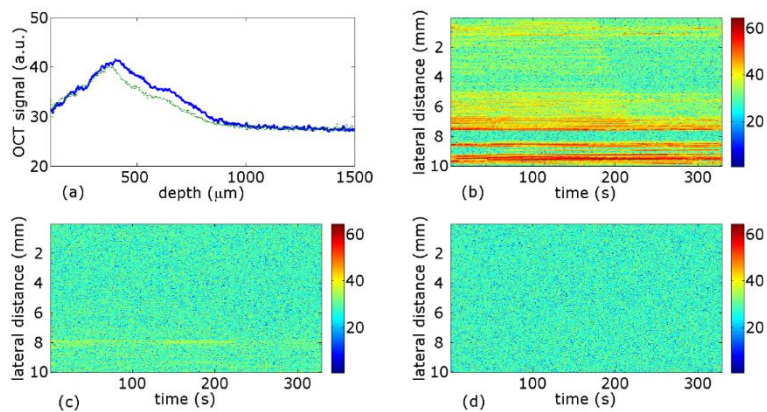


Figure 6.1b.9. GCWS1: (a) pixel intensity values averaged across the 10 mm cross section when dry (solid blue line) and wet (dotted green line); signal intensity values at depths of (b)  $\sim 400 \mu\text{m}$ , (c)  $\sim 700 \mu\text{m}$ , and (d)  $\sim 1000 \mu\text{m}$  across the lateral range of the scan over time. The OCT signals are in log scales.

Figure 6.1b.9. (a) shows the decrease in pixel intensity values due to the reduction of scattering in the sandstone caused by the presence of water in the pore network. Depth scan intensity values were averaged across the 10 mm lateral range of the cross sections when both wet and

dry. The peak centered at approximately 400-450  $\mu\text{m}$  is due to scattering at the surface of the stone. The breadth of the peak is due to the rough sloped surface of the stone. Figures 6.1b.9.(b) – (d) sample the signal intensity at a specific depth of 400, 700 and 1000  $\mu\text{m}$  over the duration of the measurement. Water enters at 177 s crossing the lateral range of the scan by 303 s, showing little difference in water movement speed in the lateral direction between the different depths. The change in signal due to water cannot be detected below 700  $\mu\text{m}$ . The 126 s time to cross the lateral range of the 10 mm gives a wetting scan velocity of  $0.0079 \pm 0.0005 \text{ cm s}^{-1}$ . The hydraulic conductivity at this point is in the middle range of semi-pervious which is consistent within expected values for sandstone.

GC1876 wetting scan 2 (GCWS2) was performed with the OCT probe positioned on north face between incised letters, in an area where the original surface is discoloured with patches of white encrustation.



Figure 6.1b.10. Position of wetting scan GCWS2

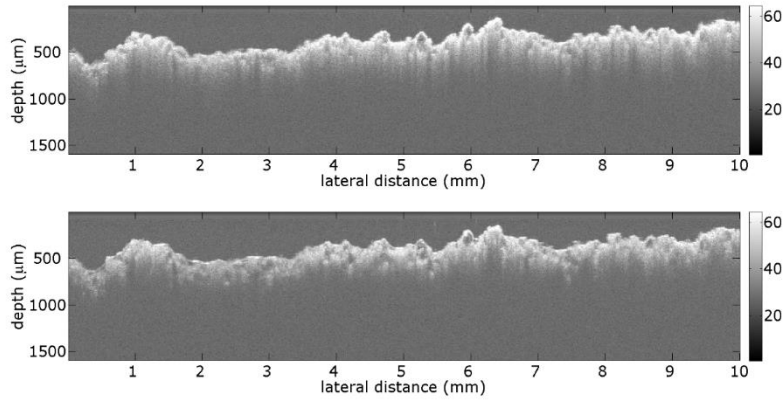


Figure 6.1b.11. OCT virtual cross sections of GCWS2 scan position when (a) dry and (b) wet.

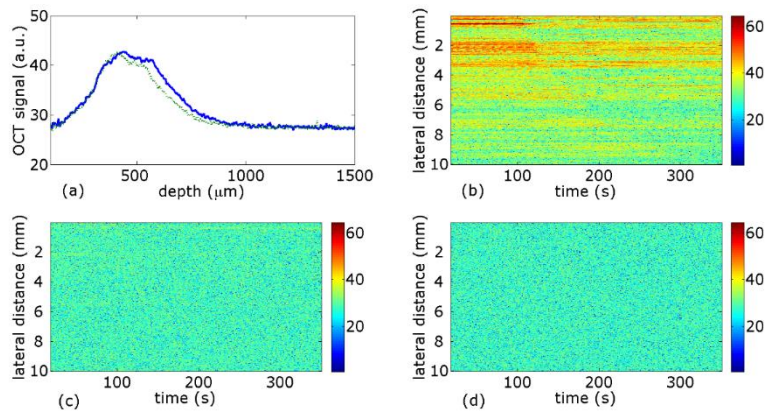


Figure 6.1b.12. GCWS2: (a) pixel intensity values averaged across the 10 mm cross section when dry (solid blue line) and wet (dotted green line); signal intensity values at depths of (b)  $\sim 400 \mu\text{m}$ , (c)  $\sim 700 \mu\text{m}$ , and (d)  $\sim 1000 \mu\text{m}$  across the lateral range of the scan over time. The OCT signals are in log scales.

The peak in figure 6.1b.12 (a) centered at approximately  $450\text{-}500 \mu\text{m}$  is due to scattering at the surface of the stone. The breadth of the peak is due to the rough sloped surface of the stone shown in figure 6.1b.11. Figures 6.3.12. (b) – (d) sample the signal intensity at a specific depth of  $400$ ,  $700$  and  $1000 \mu\text{m}$  over the duration of the measurement. Water enters at  $99 \text{ s}$  crossing the lateral range of the scan by  $320 \text{ s}$ . The  $221 \text{ s}$  time to cross the lateral range of the  $10 \text{ mm}$  gives a wetting scan velocity of  $0.0045 \pm 0.0005 \text{ cm s}^{-1}$ . The hydraulic conductivity at this point is in the middle range of semi-pervious.

GC1876 wetting scan 3 (GCWS3) was performed with the OCT probe positioned on the north face of the stone on an area with light discoloration and slight roughness to surface texture.

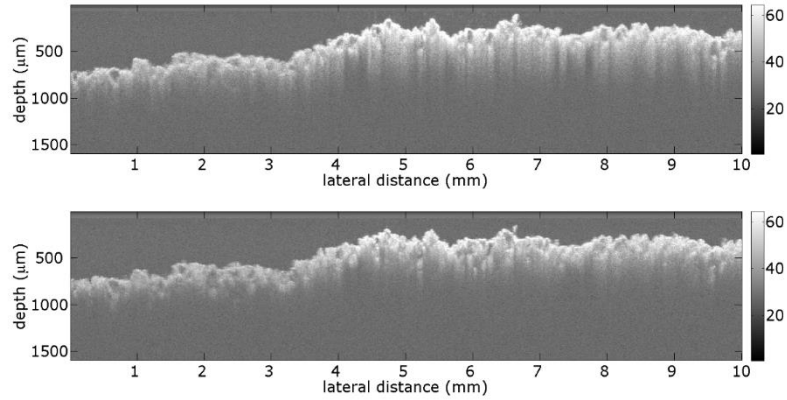


Figure 6.1b.13. OCT virtual cross sections of GCWS3 scan position when (a) dry and (b) wet.

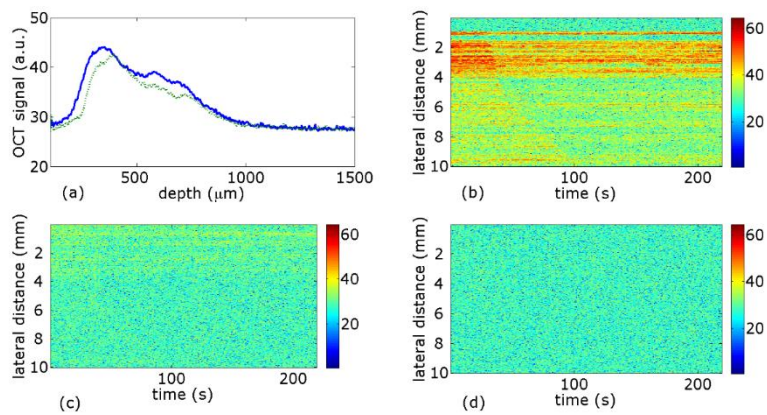


Figure 6.1b.14. GCWS3: (a) pixel intensity values averaged across the 10 mm cross section when dry (solid blue line) and wet (dotted green line); signal intensity values at depths of (b)  $\sim 400 \mu\text{m}$ , (c)  $\sim 700 \mu\text{m}$ , and (d)  $\sim 1000 \mu\text{m}$  across the lateral range of the scan over time. The OCT signals are in log scales.

The peak in figure 6.1b.14. (a) is centered at approximately  $400\text{-}450 \mu\text{m}$  is due to scattering at the surface of the stone. The breadth of the peak is due to the rough sloped surface of the stone shown in figure 6.1b.13. Figure 6.1b.14 (b) – (d) sample the signal intensity at a specific depth of  $400$ ,  $700$  and  $1000 \mu\text{m}$  over the duration of the measurement. Water enters at  $26 \text{ s}$

crossing the lateral range of the scan by 118 s. The 92 s time to cross the lateral range of the 10 mm gives a wetting scan velocity of  $0.011 \pm 0.001 \text{ cm s}^{-1}$ . The hydraulic conductivity at this point is in the mid to high range of semi-pervious.

GC1876 wetting scan 4 (GCWS4) was performed with the OCT probe positioned on the north face of the stone, on the neck of the carved dove motif, shown in figure 6.1b.15. The original white paint finish has been lost leaving the unfinished surface exposed.



Figure 6.1b.15. Position of wetting scan GCWS4

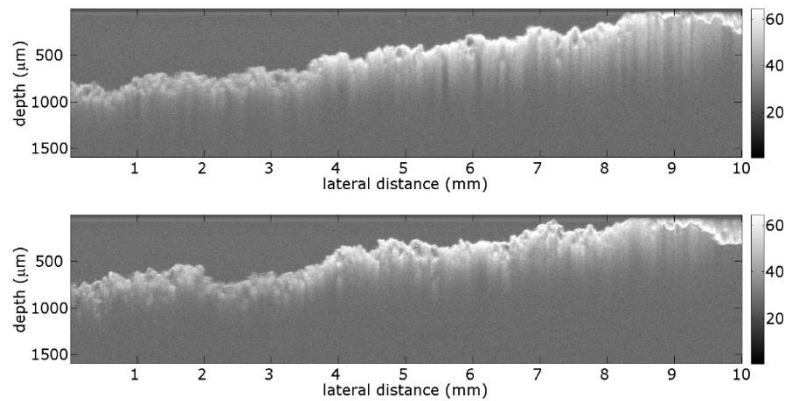


Figure 6.1b.16. OCT virtual cross sections of GCWS4 scan position when (a) dry and (b) wet.

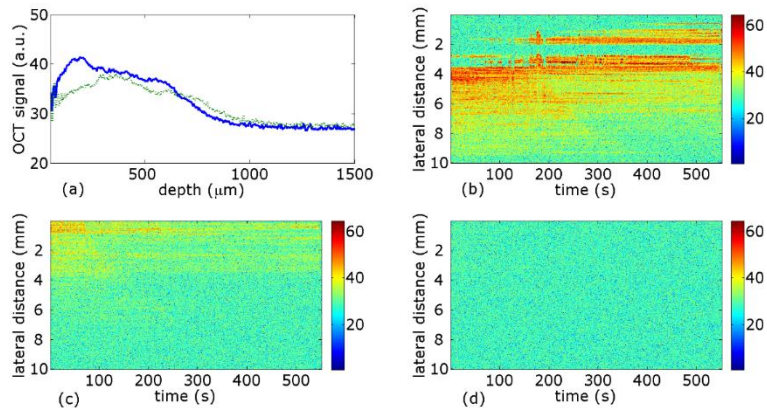


Figure 6.1b.17. GCWS4: (a) pixel intensity values averaged across the 10 mm cross section when dry (solid blue line) and wet (dotted green line); signal intensity values at depths of (b)  $\sim 400 \mu\text{m}$ , (c)  $\sim 700 \mu\text{m}$ , and (d)  $\sim 1000 \mu\text{m}$  across the lateral range of the scan over time. The OCT signals are in log scales.

The peak in figure 6.3.17. (a) is centered at approximately 100-150  $\mu\text{m}$  is due to scattering at the surface of the stone, the shift in peak is due to a small shift in the probe towards the surface during the scan. The breadth of the peak is due to the rough sloped surface of the stone shown in figure 6.1b.16. Figure 6.3.17. (b) – (d) sample the signal intensity at a specific depth of 400, 700 and 1000  $\mu\text{m}$  over the duration of the measurement. Water enters at 65 s crossing the lateral range of the scan by 427 s. The 362 s time to cross the lateral range of the 10 mm gives a wetting scan velocity of  $0.0028 \pm 0.0005 \text{ cm s}^{-1}$ . The hydraulic conductivity at this point is in the middle range of semi-pervious.

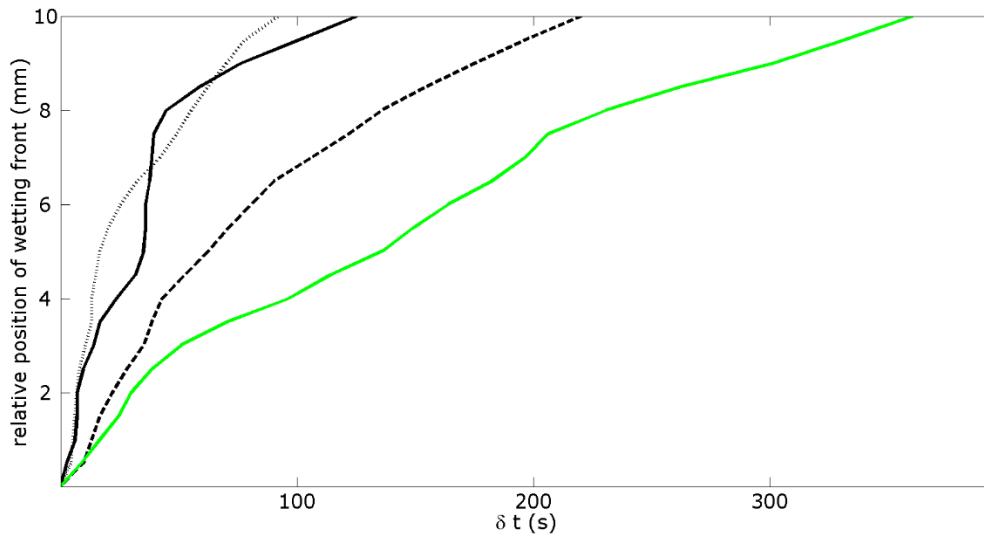


Figure 6.1b.18. Position of the wetting front over time for GCWS1 (black solid line), GCWS2 (black dashed line), GCWS3 (black dotted line), GCWS4 (green solid line).

Wetting front velocities for all scans are shown in figure 6.1b.18. Scan GCSW4 is on the neck of the ornamental dove, the margins of the dove retain flakes of the white painted finish which has been lost. The sandstone surface has been exposed for less time than the rest of the stone and has a hydraulic conductivity of  $0.0028 \pm 0.0005 \text{ cm s}^{-1}$ . Scan GCWS2 is between incised inscription on a surface with light discolouration and surface roughening and has a hydraulic conductivity of  $0.0045 \pm 0.0005 \text{ cm s}^{-1}$ . Scan GCWS1 is on recessed sandstone surface due to contour scaling and has a hydraulic conductivity of  $0.0079 \pm 0.0005 \text{ cm s}^{-1}$ . Scan GCSW3 is on a light discoloured surface with a granular texture below the dove ornament, the surface appears to have a residue of white paint. It has hydraulic conductivity of  $0.011 \pm 0.001 \text{ cm s}^{-1}$ . The hydraulic conductivity of the sandstone increases with increased intensity of weathering forms with the exception of GCWS3 which may be influenced by the presence of paint residue.

### 6.1c JG1873

Headstone JG1873 is a complex shouldered gothic-point sandstone tablet of dimensions: height 146.5 cm, width 75.8 cm, depth 8 cm. The stone has incised carving on the north face shown in figure 6.1c.1.



Figure 6.1c.1. Complex sandstone tablet incised on north face dated 1873: images of north, east, south and west faces.

The north face has a region of total surface loss to a depth of 2 mm due to contour scaling leaving a pitted surface texture with a central area of honeycomb weathering recessed to 4 mm. The region extends upwards with a central area of contour scaling recessed to 1 mm with a pitted surface texture. The incised inscription has been recessed to the same degree as the surrounding surface, the inscription is rounded but legible over most of the stone. The south face has a corresponding pattern of surface loss due to contour scaling causing a pitted surface texture recessed between 1 and 4 mm with a central area of honeycombing. A schematic of weathering features to north and south faces is shown in figure 6.1c.2

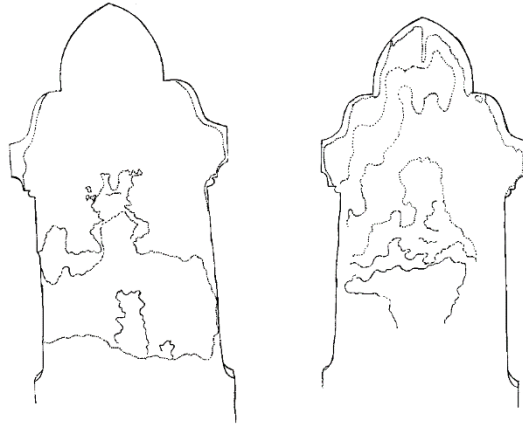


Figure 6.1c.2. Schematic of weathering features on north and south face of gravestone JG1873.

JG1873 wetting scan 1 (JGWS1) was performed with the OCT probe positioned within an area of 4 mm surface recession which shows loss of colouration, granular loss at surface and the development of honeycomb weathering shown in figure 6.1c.3.



Figure 6.1c.3. Position of wetting scan JGWS1

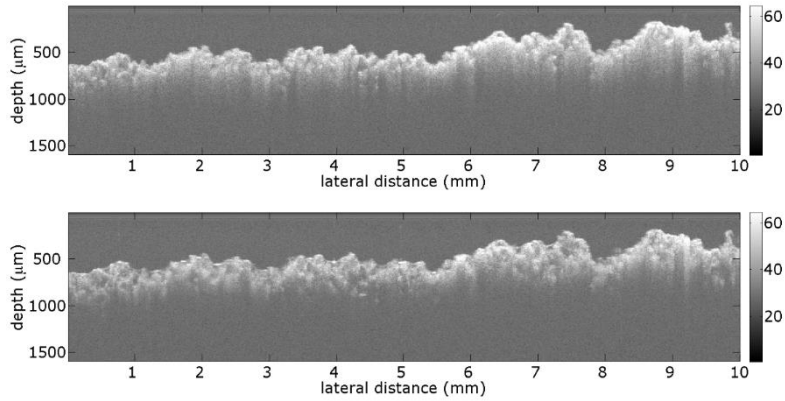


Figure 6.1c.4. OCT virtual cross sections of JGWS1 scan position when (a) dry and (b) wet.

Virtual cross sectional images of the scan position for JGWS1 are shown in figure 6.1c.4. when dry and wet. The presence of water in the sample reduces scattering as it reduces the refractive index mismatch, features can be seen to a greater depth within the stone. A film of water formed over the stone surface due to capillary action as it saturated.

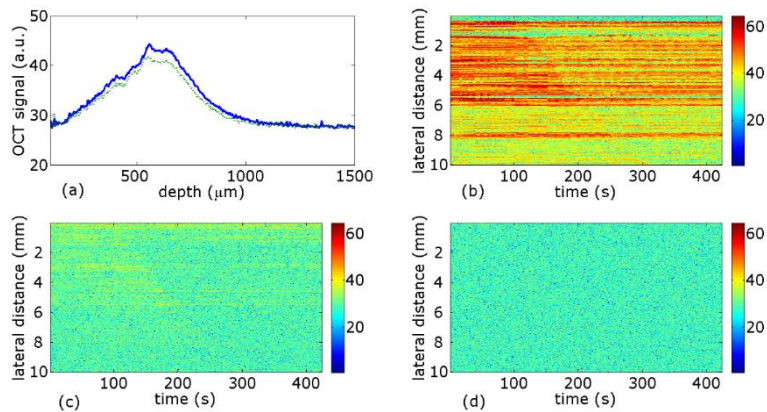


Figure 6.1c.5 . JGWS1: (a) pixel intensity values averaged across the 10 mm cross section when dry (solid blue line) and wet (dotted green line); signal intensity values at depths of (b) ~400  $\mu\text{m}$ , (c) ~700  $\mu\text{m}$ , and (d) ~ 1000  $\mu\text{m}$  across the lateral range of the scan over time. The OCT signals are in log scales.

Figure 6.1c.5 (a) shows the decrease in pixel intensity values due to the reduction of scattering in the sandstone caused by the presence of water in the pore network. Depth scan intensity

values were averaged across the 10 mm lateral range of the cross sections when both wet and dry. The peak centered at approximately 550-600  $\mu\text{m}$  is due to scattering at the surface of the stone, the shift in peak is due to a small shift in the probe towards the surface during the scan. The breadth of the peak is due to the rough sloped surface of the stone. Figure 6.1c.5. (b) – (d) sample the signal intensity at a specific depth of 400, 700 and 1000  $\mu\text{m}$  over the duration of the measurement. Water enters at 103 s crossing the lateral range of the scan by 311 s, showing little difference in water movement speed in the lateral direction between the different depths. The change in signal due to water cannot be detected below 700  $\mu\text{m}$ . The 208 s time to cross the lateral range of 10 mm gives a wetting front velocity of  $0.0048 \pm 0.0005 \text{ cm s}^{-1}$ . The hydraulic conductivity at this position is in the middle range of semi-pervious.

JG1873 wetting scan 2 (JGWS2) was performed with the OCT probe positioned within an area of 2 mm surface recession with a pitted surface texture and orange discolouration shown in figure 6.1c.6.



Figure 6.1c.6. Position of wetting scan JGWS2

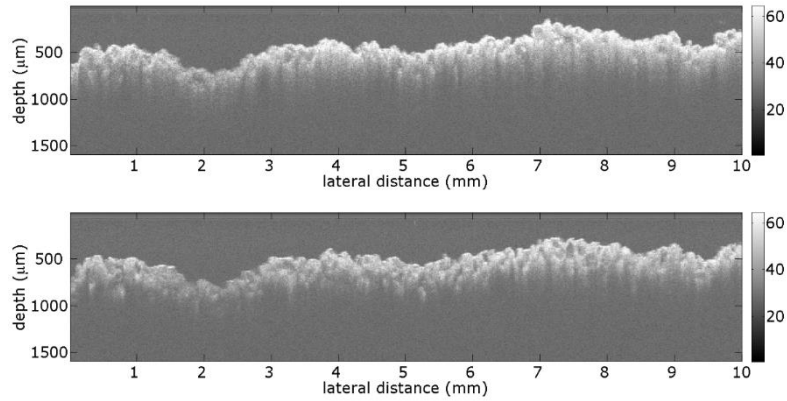


Figure 6.1c.7. OCT virtual cross sections of JGWS2 scan position when (a) dry and (b) wet.

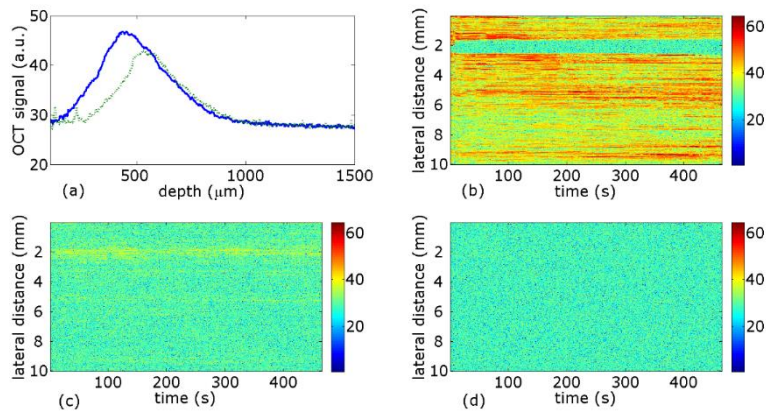


Figure 6.1c.8. JGWS2: (a) pixel intensity values averaged across the 10 mm cross section when dry (solid blue line) and wet (dotted green line); signal intensity values at depths of (b)  $\sim 400 \mu\text{m}$ , (c)  $\sim 700 \mu\text{m}$ , and (d)  $\sim 1000 \mu\text{m}$  across the lateral range of the scan over time. The OCT signals are in log scales.

The peak in figure 6.1c.8. (a) is centered at approximately  $450\text{--}550 \mu\text{m}$ , the shift in peak is due to a small shift in the probe towards the surface during the scan. The breadth of the peak is due to the rough surface of the stone shown in figure 6.1c.7. Figure 6.1c.8. (b) – (d) sample the signal intensity at a specific depth of  $400$ ,  $700$  and  $1000 \mu\text{m}$  over the duration of the measurement. Water enters at  $107 \text{ s}$  crossing the lateral range of the scan by  $423 \text{ s}$ . The  $316 \text{ s}$  time to cross the lateral range of  $10 \text{ mm}$  gives a wetting front velocity of  $0.0032 \pm 0.0005 \text{ cm s}^{-1}$ . The hydraulic conductivity at this position is in the middle range of semi-pervious.

JG1873 wetting scan 3 (JGWS3) was performed with the OCT probe positioned within an area of 1 mm surface recession with a pitted surface texture, surface loss is due to contour scaling of surface flake shown in figure 6.1c.9.



Figure 6.1c.9. Position of wetting scan JGWS3

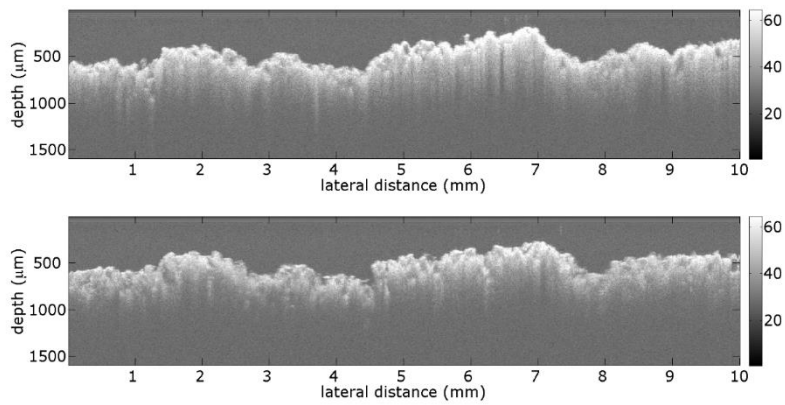


Figure 6.1c.10. OCT virtual cross sections of JGWS3 scan position when (a) dry and (b) wet.

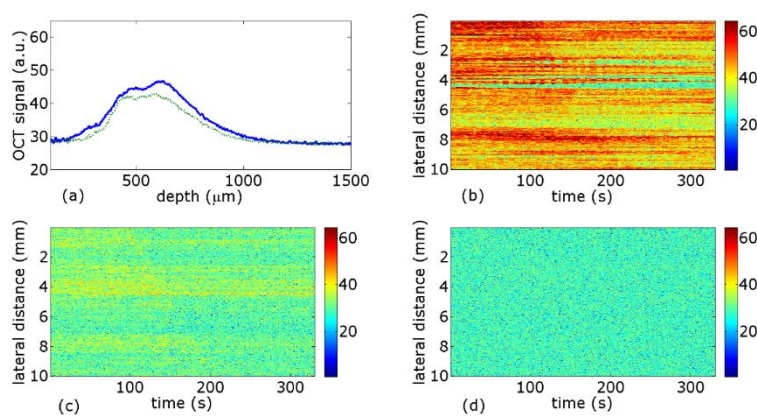


Figure 6.1c.11. JGWS3: (a) pixel intensity values averaged across the 10 mm cross section when dry (solid blue line) and wet (dotted green line); signal intensity values at depths of (b) ~400  $\mu\text{m}$ , (c) ~700  $\mu\text{m}$ , and (d) ~1000  $\mu\text{m}$  across the lateral range of the scan over time. The OCT signals are in log scales.

The peak in figure 6.1c.11. (a) is centered at approximately 500-600  $\mu\text{m}$  is due to scattering at the surface of the stone. The breadth of the peak is due to the roughness and slight slope of the surface shown in figure 6.1c.10. Figure 6.1c.11 (b) – (d) sample the signal intensity at a specific depth of 400, 700 and 1000  $\mu\text{m}$  over the duration of the measurement. Water enters at 128 s crossing the lateral range of the scan by 261 s. The 133 s time to cross the lateral range of 10 mm gives a wetting front velocity of  $0.0071 \pm 0.0005 \text{ cm s}^{-1}$ . The hydraulic conductivity at this position is in the high range of semi-pervious.

JG1873 wetting scan 3 (JGWS3) was performed with the OCT probe positioned on the original surface of the stone between incised letters, in an area with black discoloration shown in figure 6.1c.12.



Figure 6. 1c.12. Position of wetting scan JGWS3

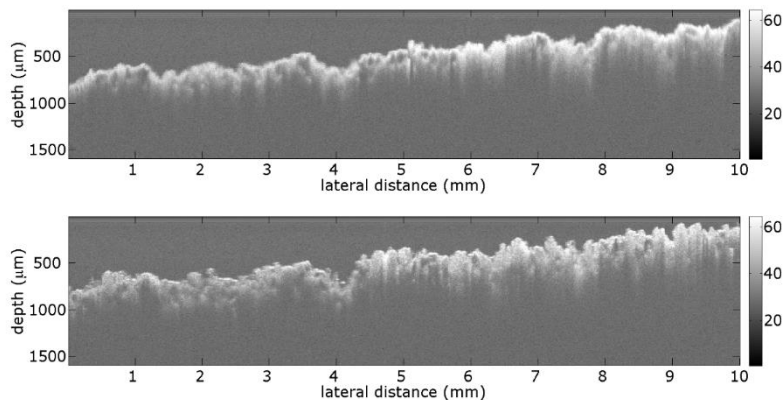


Figure 6.1c.13. OCT virtual cross sections of JGWS4 scan position when (a) dry and (b) wet.

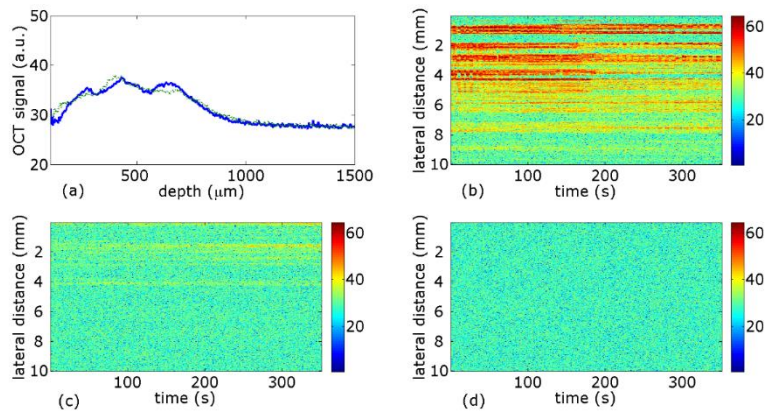


Figure 6.1c.14. JGWS4: (a) pixel intensity values averaged across the 10 mm cross section when dry (solid blue line) and wet (dotted green line); signal intensity values at depths of (b)  $\sim 400 \mu\text{m}$ , (c)  $\sim 700 \mu\text{m}$ , and (d)  $\sim 1000 \mu\text{m}$  across the lateral range of the scan over time. The OCT signals are in log scales.

The peak in figure 6.1c.14. (a) is centered at approximately  $200\text{-}250 \mu\text{m}$  is due to scattering at the surface of the stone, the shift in peak is due to a small shift in the probe towards the surface during the scan. The breadth of the peak is due to the rough sloped surface of the stone shown in figure 6.1c.13. Figure 6.4.14. (b) – (d) sample the signal intensity at a specific depth of 400, 700 and  $1000 \mu\text{m}$  over the duration of the measurement. Water enters at  $128 \text{ s}$  crossing the lateral range of the scan by  $261 \text{ s}$ . The  $133 \text{ s}$  time to cross the lateral range of  $10 \text{ mm}$  gives a wetting front velocity of  $0.0075 \pm 0.0005 \text{ cm s}^{-1}$ . The hydraulic conductivity at this position is in the middle range of semi-pervious.

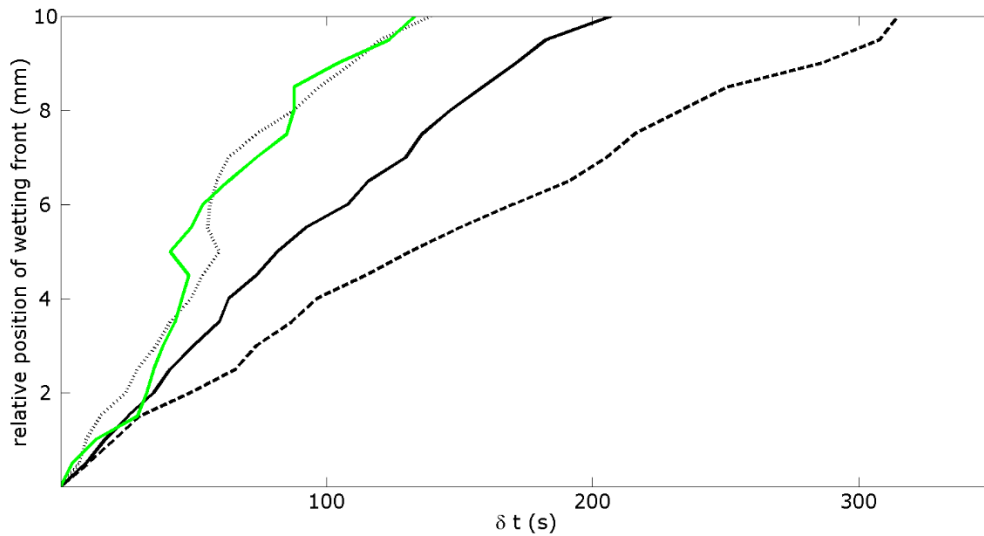


Figure 6.1c.15. Position of the wetting front over time for JGWS1 (black solid line), JGWS2 (black dashed line), JGWS3 (black dotted line), JGWS4 (green solid line).

Scans in regions of surface recession show lower hydraulic conductivities over the range of the scan. The presence of orange discolouration on the weathered surface may indicate the deposition iron minerals weathering out from the stone. Wetting front velocities for all scans are shown in figure 6.1c.15. The position of scan JGWS1 of weathered surface recessed by 4 mm from the original surface, has a granular texture with detaching grains, with a hydraulic conductivity of  $0.0048 \pm 0.0005 \text{ cm s}^{-1}$ . Scan JGWS2 on a weathered surface recessed by 2 mm from the original surface has a similar texture with orange discolouration with a hydraulic conductivity of  $0.0032 \pm 0.0005 \text{ cm s}^{-1}$ . Scan JGWS3 is within an area of 1 mm surface recession due to contour scaling of surface flake. The weathered surface has a granular texture with hydraulic conductivity of  $0.0071 \pm 0.0005 \text{ cm s}^{-1}$ . Scan JGWS4 is on the original surface with crust of black deposit with a hydraulic conductivity of  $0.0075 \pm 0.0005 \text{ cm s}^{-1}$ . The scans on areas of surface recession of 2 – 4 mm with soft granular surface texture show a significant decrease in hydraulic conductivity, in comparison with the original surface and area of 1 mm recession due to the loss of surface by flaking.

### 6.1d WW1881

Headstone WW1881 is a gothic-point sandstone tablet of dimensions: height 140 cm, width 70 cm, depth 7.5 cm. There is decorative and incised carving to north face of stone and surface loss to south face of stone, shown in figure 6.1d.1.



Figure 6.1d.1. Complex sandstone tablet incised on north face dated 1881: images of north, east, south and west faces.

A schematic of weathering features to north and south faces is shown in figure 6.5.2. The north face has areas of surface detachment near the base, a ~ 1 mm thick surface scale separating from the tablet around the incised inscription. There is an area of black deposit encrusting the surface around the top half of the inscription. The south face has significant surface loss due to the detachment of multiple flakes developing into honeycomb weathering in the lower third.

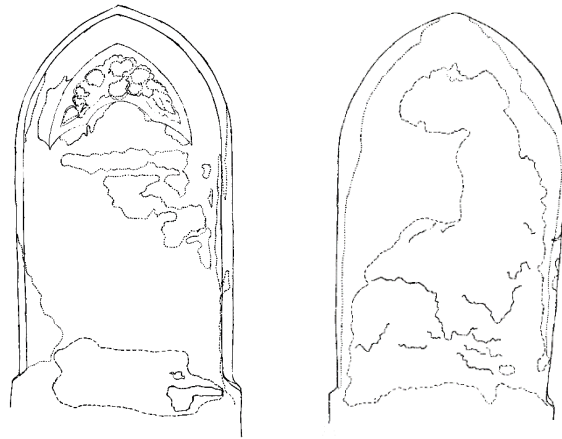


Figure 6.1d.2. Schematic of weathering features on north and south face of gravestone WW1881.

The representative grain size distribution for the stone was determined from an OCT volume scan over an area of 6 x 6 mm using the imaging protocol described in chapter 2. Within this volume, 120 grains were identified, the size distribution of which is shown in figure 6.1d.3.

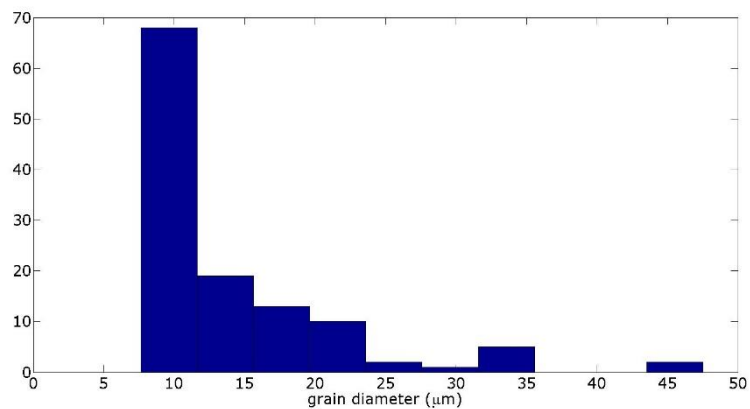


Figure 6.1d.3 representative grain size distribution for WW1881

The minimum grain size detected, 10 µm, is determined by resolution of instrument, the maximum size is 48 µm with a mean of 14 µm and standard deviation of 8. The detected grain sizes are in the range of medium to coarse silt.

WW1881 wetting scan 1 (WWWS1) was performed with the OCT probe positioned on the original surface of the south face, shown in figure 6.1d.4. the surface shows discolouration and slight algal growth.



Figure 6.1d.4. Position of wetting scan WWWS1

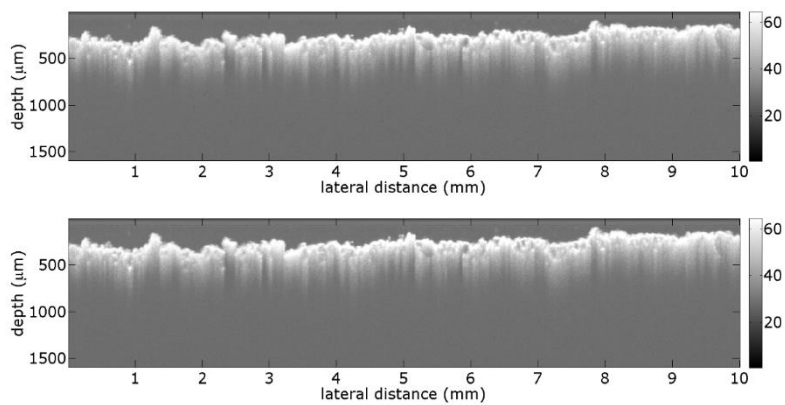


Figure 6.1d.5. OCT virtual cross sections of WWWS1 scan position at (a) start and (b) end of scan.

Virtual cross sectional images of the scan position for WWWS1 are shown in figure 6.1d.5. at the start and end of scan. No water was absorbed into the stone so there is no change in the images for the duration of the scan.

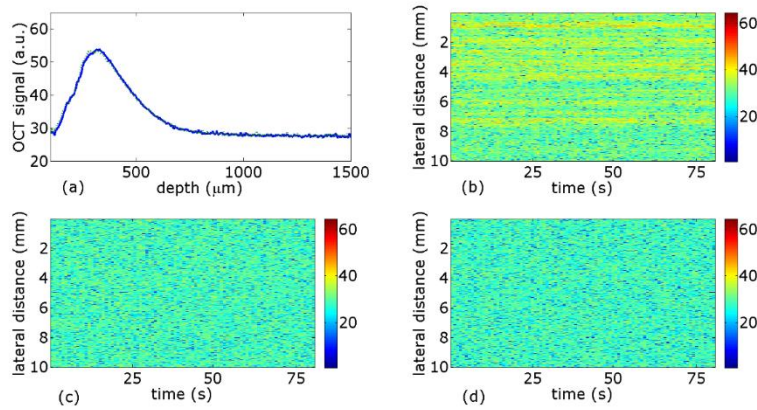


Figure 6.1d.6. WWWS1: (a) pixel intensity values averaged across the 10 mm cross section at the start (solid blue line) and end (dotted green line) of the scan; signal intensity values at depths of (b)  $\sim 400 \mu\text{m}$ , (c)  $\sim 700 \mu\text{m}$ , and (d)  $\sim 1000 \mu\text{m}$  across the lateral range of the scan over time. The OCT signals are in log scales.

The peak in figure 6.1d.6. (a) is centered at approximately 350-400  $\mu\text{m}$  is due to scattering at the surface of the stone, no change occurred in the duration of the scan. Figure 6.1d.6. (b) – (d) sample the signal intensity at a specific depth of 400, 700 and 1000  $\mu\text{m}$  over the duration of the measurement. Water is not absorbed into the stone over the duration of the scan so there is no change to pixel intensity values. With regard to hydraulic conductivity, the stone surface may be considered slightly pervious to impervious.

WW1881 wetting scan 2 (WWWS2) was performed with the OCT probe positioned on the south face in an area of surface recession due to the loss to 1 mm by flaking, shown in figure 6.1d.7. The recessed area is discoloured and has a rough pitted surface.



Figure 6.1d.7. Position of wetting scan WWWS2

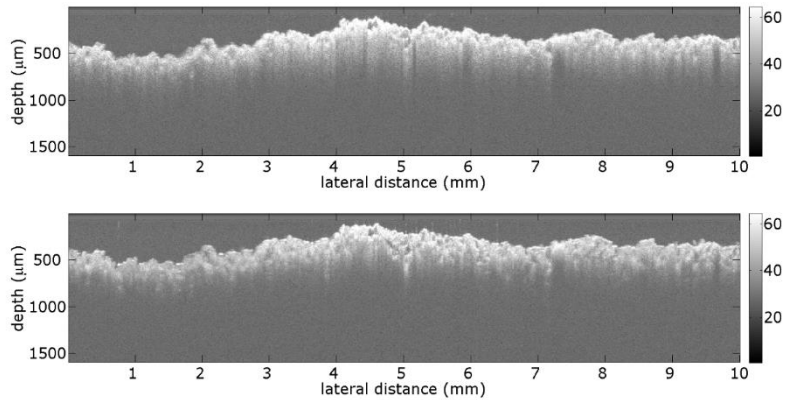


Figure 6.1d.8. OCT virtual cross sections of WWWS2 scan position when (a) dry and (b) wet.

Virtual cross sectional images of the scan position for WWWS2 are shown in figure 6.1d.8. when dry and wet. The presence of water in the sample reduces scattering as it reduces the refractive index mismatch, features can be seen to a greater depth within the stone.

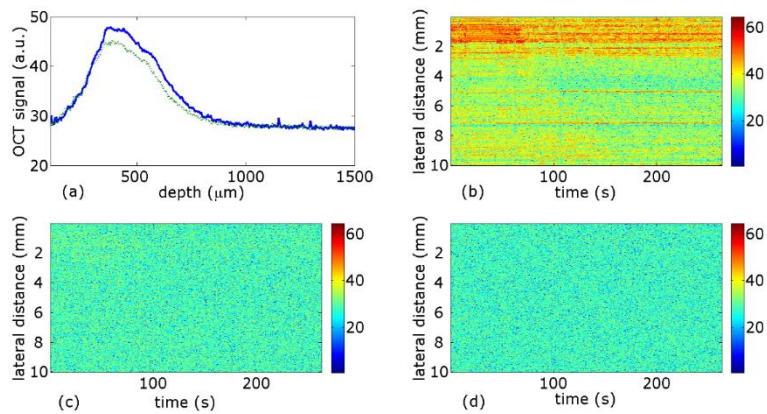


Figure 6.1d.9. WWWS2: (a) pixel intensity values averaged across the 10 mm cross section when dry (solid blue line) and wet (dotted green line); signal intensity values at depths of (b)  $\sim 400 \mu\text{m}$ , (c)  $\sim 700 \mu\text{m}$ , and (d)  $\sim 1000 \mu\text{m}$  across the lateral range of the scan over time. The OCT signals are in log scales.

Figure 6.1d.9. (a) shows the decrease in pixel intensity values due to the reduction of scattering in the sandstone caused by the presence of water in the pore network. Depth scan intensity values were averaged across the 10 mm lateral range of the cross sections when both wet and dry. The peak centered at approximately 400-450  $\mu\text{m}$  is due to scattering at the surface of the stone. The breadth of the peak is due to the rough surface of the stone shown in figure 6.1d.8. Figure 6.1d.9. (b) – (d) sample the signal intensity at a specific depth of 400, 700 and 1000  $\mu\text{m}$  over the duration of the measurement. Water enters at 60 s crossing the lateral range of the scan by 163 s, showing little difference in water movement speed in the lateral direction between the different depths. The change in signal due to water cannot be detected below 1 mm. The 103 s time to cross the lateral range of 10 mm gives a wetting front velocity of  $0.0097 \pm 0.0005 \text{ cm s}^{-1}$ . The hydraulic conductivity is in the mid to high range of semi-pervious which is consistent within expected values for sandstone.

WW1881 wetting scan 3 (WWWS3) was performed with the OCT probe positioned on the recessed surface of the south face with a pitted texture and orange colouration, shown in figure 6.1d.10.



Figure 6.1d.10. Position of wetting scan WWWS3

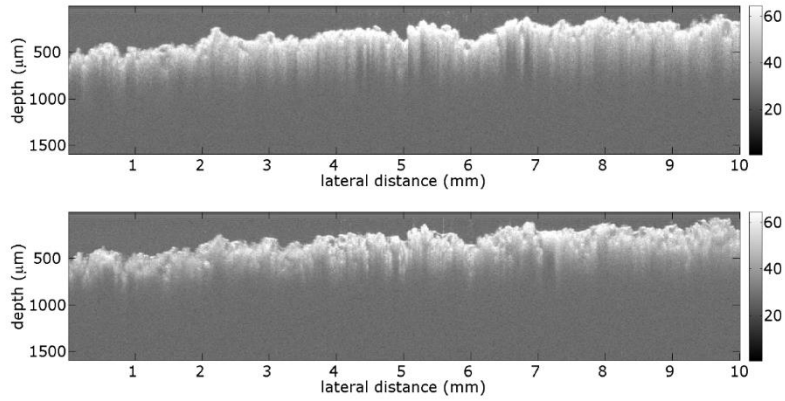


Figure 6.1d.11. OCT virtual cross sections of WWWS3 scan position when (a) dry and (b) wet.

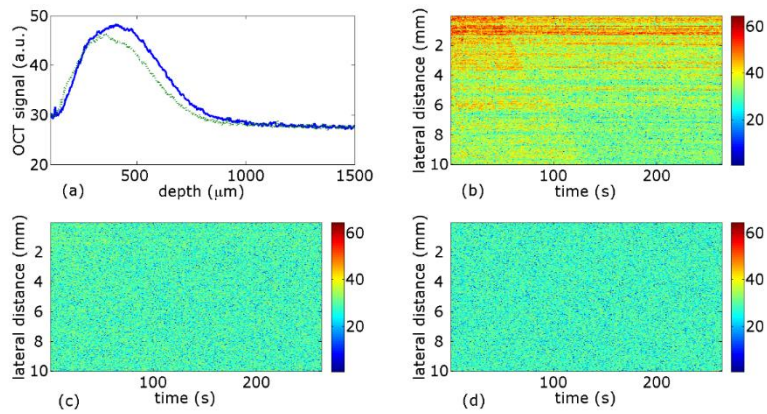


Figure 6.1d.12. WWWS3: (a) pixel intensity values averaged across the 10 mm cross section when dry (solid blue line) and wet (dotted green line); signal intensity values at depths of (b)  $\sim 400 \mu\text{m}$ , (c)  $\sim 700 \mu\text{m}$ , and (d)  $\sim 1000 \mu\text{m}$  across the lateral range of the scan over time. The OCT signals are in log scales.

The peak in figure 6.1d.12. (a) centered at approximately  $450\text{--}500 \mu\text{m}$  is due to scattering at the surface of the stone. The breadth of the peak is due to the rough sloped surface of the stone, shown in figure 6.1d.11. Figure 6.1d.12. (b) – (d) sample the signal intensity at a specific depth of 400, 700 and 1000  $\mu\text{m}$  over the duration of the measurement. Water enters at 49 s crossing the lateral range of the scan by 134 s. The 85 s time to cross the lateral range of the 10 mm gives a wetting front velocity of  $0.012 \pm 0.001 \text{ cm s}^{-1}$ . The hydraulic conductivity is in the high range of semi-pervious.

WW1881 wetting scan 4 (WWWS4) was performed with the OCT probe positioned on the original surface of the south face adjacent to flake detachment shown in figure 6.1d.13.



Figure 6.1d.13. Position of wetting scan WWWS4

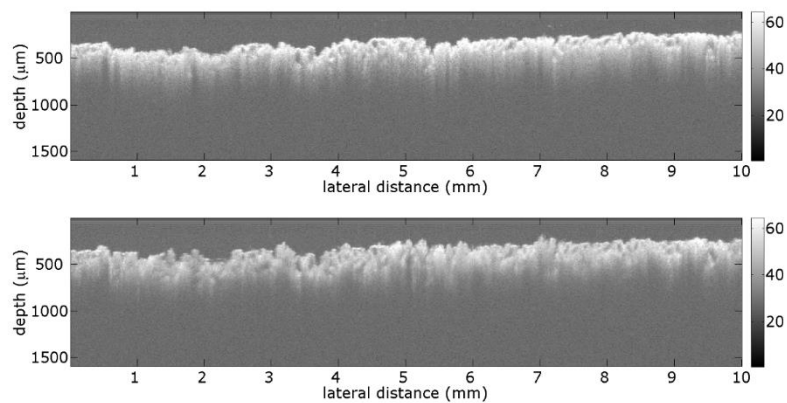


Figure 6.1d.14. OCT virtual cross sections of WWWS4 scan position when (a) dry and (b) wet.

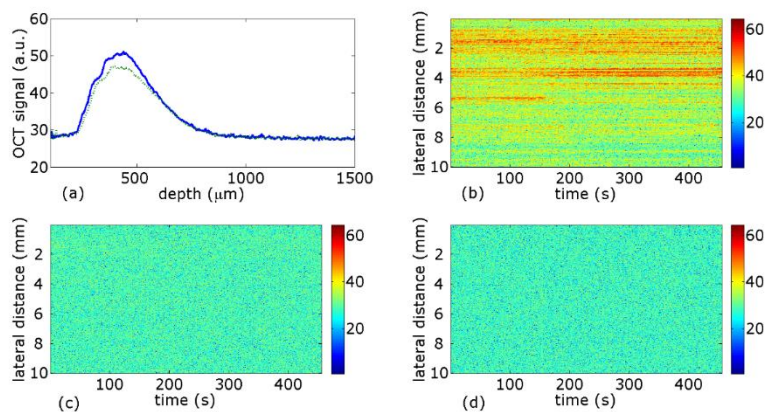


Figure 6.1d.15. WWWS4: (a) pixel intensity values averaged across the 10 mm cross section when dry (solid blue line) and wet (dotted green line); signal intensity values at depths of (b) ~400 μm, (c) ~700 μm, and (d) ~ 1000 μm across the lateral range of the scan over time. The OCT signals are in log scales.

The peak in figure 6.1d.15. (a) is centered at approximately 450-500  $\mu\text{m}$  is due to scattering at the surface of the stone. The breadth of the peak is due to the rough surface of the stone, shown in figure 6.1d.14. Fig. 6.1d15. (b) – (d) sample the signal intensity at a specific depth of 400, 700 and 1000  $\mu\text{m}$  over the duration of the measurement. Water enters at 99 s crossing the lateral range of the scan by 230 s. The 131 s time to cross the lateral range of the 10 mm gives a wetting front velocity of  $0.0076 \pm 0.0005 \text{ cm s}^{-1}$ . The hydraulic conductivity is in the middle range of semi-pervious.

WW1881 wetting scan 5 (WWWS5) was performed with the OCT probe positioned between lines of inscription on the original surface of the north face of the stone, shown in figure 6.1d.16.



Figure 6.1d.16. Position of wetting scan WWWS5

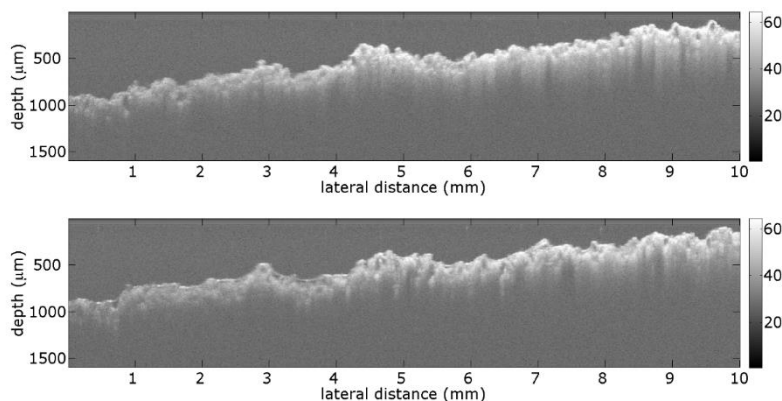


Figure 6.1d.17. OCT virtual cross sections of WWWS5 scan position when (a) dry and (b) wet.

The blurring to images seen in figures 6.1d.17 and 18 is due to vibrations affecting the probe during the scan.

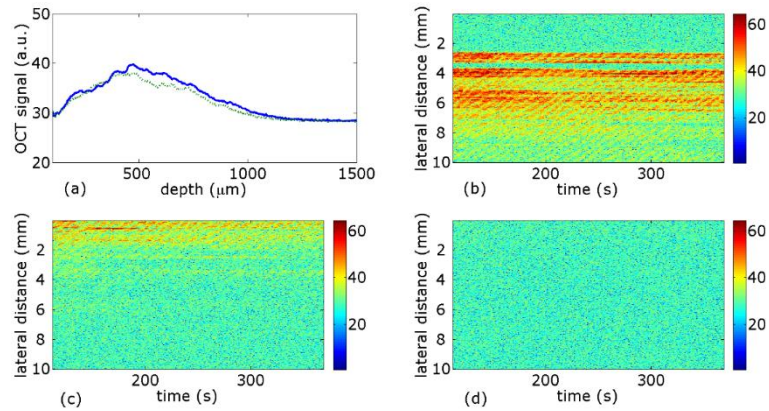


Figure 6.1d.18. WWWS5: (a) pixel intensity values averaged across the 10 mm cross section when dry (solid blue line) and wet (dotted green line); signal intensity values at depths of (b) ~400  $\mu\text{m}$ , (c) ~700  $\mu\text{m}$ , and (d) ~ 1000  $\mu\text{m}$  across the lateral range of the scan over time. The OCT signals are in log scales.

The peak in figure 6.1d.18. (a) is centered at approximately 450-500  $\mu\text{m}$  is due to scattering at the surface of the stone. The breadth of the peak is due to the rough sloped surface of the stone, shown in figure 6.1d.17. Figure 6.1d.18. (b) – (d) sample the signal intensity at a specific depth of 400, 700 and 1000  $\mu\text{m}$  over the duration of the measurement. Water enters at 133 s crossing the lateral range of the scan by 344 s. The 211 s time to cross the lateral range of the 10 mm gives a wetting front velocity of  $0.0047 \pm 0.0005 \text{ cm s}^{-1}$ . The hydraulic conductivity is in the middle range of semi-pervious.

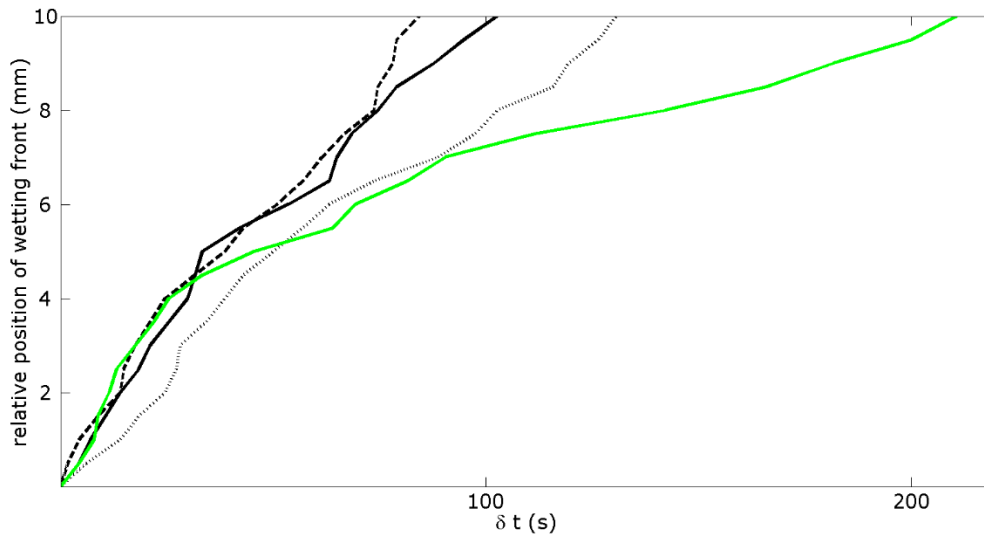


Figure 6.1d.19. Position of the wetting front over time for WWWS2 (black solid line), WWWS3 (black dashed line), WWWS4 (black dotted line), WWWS5 (green solid line).

Wetting front velocities for all scans are shown in figure 6.1d.19. Scan WWWS1 on the remaining original surface showed no water imbibition at the surface and therefore is slightly pervious to impervious. Where the original surface is lost on the south face, the recessed surface shows hydraulic conductivities of  $0.0097 \pm 0.0005 \text{ cm s}^{-1}$  and  $0.012 \pm 0.001 \text{ cm s}^{-1}$ . The material below the impervious surface layer is semi-pervious in comparison. Scan WWWS4 is located on the original surface showing alteration in colour and texture close to the margin of detachment with semi-pervious hydraulic conductivity  $0.0076 \pm 0.0005 \text{ cm s}^{-1}$ . The scan on the north, less weathered face is positioned on the original surface with a hydraulic conductivity of  $0.0047 \pm 0.0005 \text{ cm s}^{-1}$  indicating that the original surface is semi pervious. These results suggest a process by which the loss of the surface of the south face occurred; capillary rise of ground water through the stone becomes trapped at the stone surface, the resulting pressure may be the cause of the detachment and loss of the impervious surface.

### 6.1e AF1875

Headstone AF1875 is a complex shouldered gothic-point sandstone tablet of dimensions: height 135 cm, width 74.8 cm, depth 7.8 cm. There is decorative and incised carving to north face of stone and significant surface loss to south face of stone, shown in figure 6.1e.1.



Figure 6.1e.1. Complex sandstone tablet incised on north face dated 1875: images of north, east, south and west faces.

The original surface on all faces is discoloured with a thin black surface crust with algal greening to the top third of the stone. The lower third on the north face has surface loss due to the detachment of scales approximately 1.5 mm thick. The stone surface appears to show swelling and blistering with detachment focused around the incised carving. On the south face three phases of surface recession are present due to contour scaling to depths of approximately 2, 4 and 7 mm. The greatest surface recession is occurring on the lower third with granular disintegration and surface detachment. A schematic of weathering features to north and south faces is shown in figure 6.1e.2.



Figure 6.1e.2. Schematic of weathering features on north and south face of gravestone AF1875

The representative grain size distribution for the stone was determined from an OCT volume scan over an area of 6 x 6 mm using the imaging protocol described in chapter 2. Within this volume 85 grains were identified, the size distribution of which is shown in figure 6.1e.3.

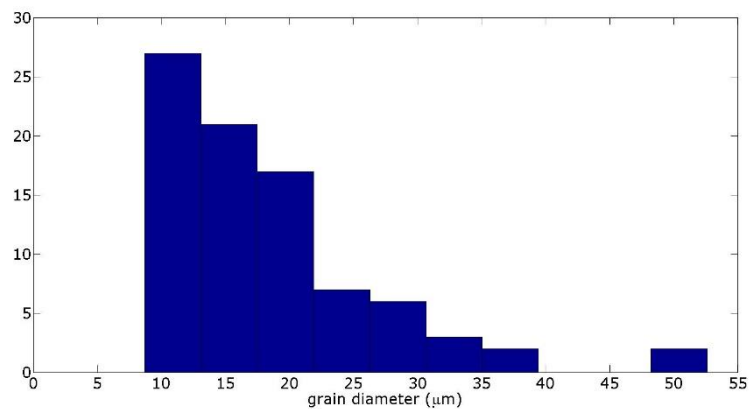


Figure6.1e.3. representative grain size distribution for AF1875

The minimum grain size detected, 10 µm, is determined by the resolution of the instrument, the maximum grain size is 52 µm. The detected grain sizes are in the range of medium to coarse silt.

AF1875 wetting scan 1 (AFWS1) was performed with the OCT probe positioned on the original surface of the north face between line of inscription on an area with a rough surface texture and black discoloration shown in figure 6.1e.4.



Figure 6.1e.4. Position of wetting scan AFWS1

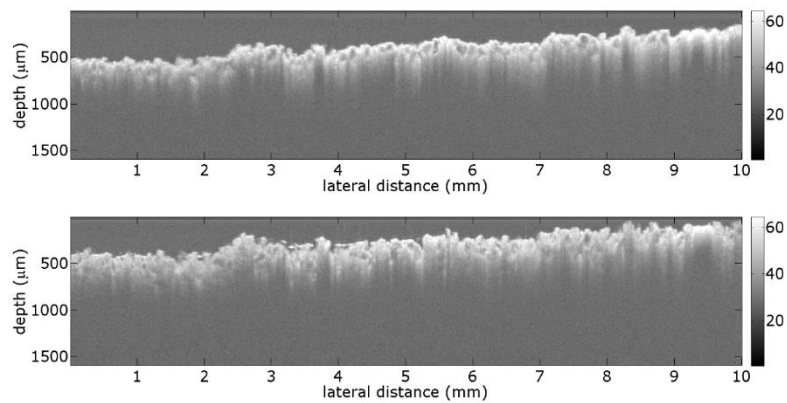


Figure 6.1e.5. OCT virtual cross sections of AFWS1 scan position when (a) dry and (b) wet.

Virtual cross sectional images of the scan position for AFWS1 are shown in figure 6.1e.5. when dry and wet. The presence of water in the sample reduces scattering as it reduces the refractive index mismatch, features can be seen to a greater depth within the stone.

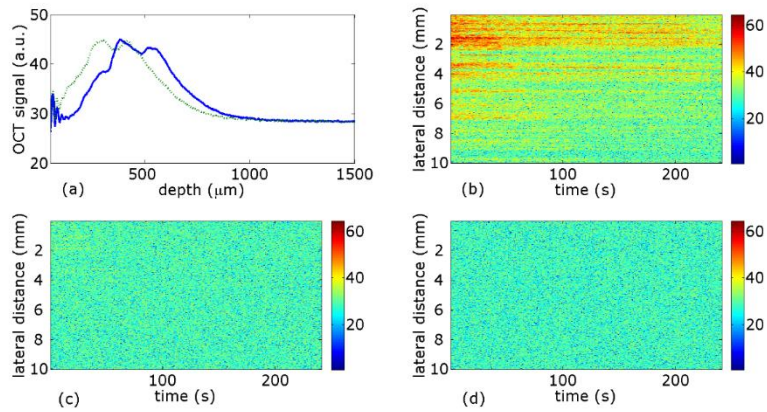


Figure 6.1e.6. AFWS1: (a) pixel intensity values averaged across the 10 mm cross section when dry (solid blue line) and wet (dotted green line); signal intensity values at depths of (b) ~400  $\mu\text{m}$ , (c) ~700  $\mu\text{m}$ , and (d) ~ 1000  $\mu\text{m}$  across the lateral range of the scan over time. The OCT signals are in log scales.

Figure 6.1e.6 (a) shows the decrease in pixel intensity values due to the reduction of scattering in the sandstone caused by the presence of water in the pore network. Depth scan intensity values were averaged across the 10 mm lateral range of the cross sections when both wet and dry. The peak centered at approximately 400-450  $\mu\text{m}$  is due to scattering at the surface of the stone, the shift in peak is due to a small shift in the probe towards the surface during the scan. The breadth of the peak is due to the rough sloped surface of the stone shown in figure 6.1e.5. Figure 6.1e.6 (b) – (d) sample the signal intensity at a specific depth of 400, 700 and 1000  $\mu\text{m}$  over the duration of the measurement. Water enters at 26 s crossing the lateral range of the scan by 123 s, showing little difference in water movement speed in the lateral direction between the different depths. The change in signal due to water cannot be detected below 0.5 mm. The 97 s time to cross the lateral range of 10 mm gives a wetting front velocity of  $0.010 \pm 0.001 \text{ cm s}^{-1}$ . The hydraulic conductivity is in the high middle range of semi-pervious.

AF1875 wetting scan 2 (AFWS2) was performed with the OCT probe positioned on the original surface of the north face above the incised lettering on an area with a rough surface texture and green discoloration shown in figure 6.1e.7.



Figure 6.1e.7. Position of wetting scan AFWS2

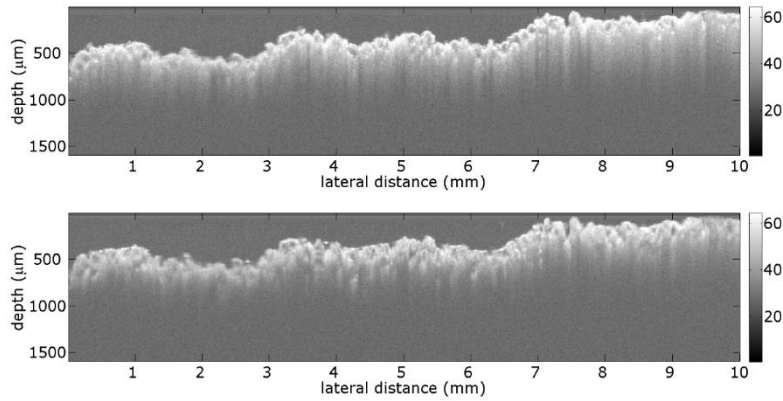


Figure 6.1e.8. OCT virtual cross sections of AFWS2 scan position when (a) dry and (b) wet.

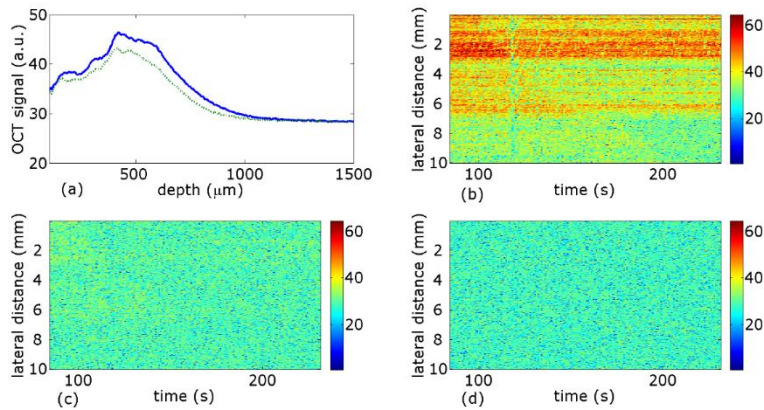


Figure 6.1e.9. AFWS2: (a) pixel intensity values averaged across the 10 mm cross section when dry (solid blue line) and wet (dotted green line); signal intensity values at depths of (b)  $\sim 400 \mu\text{m}$ , (c)  $\sim 700 \mu\text{m}$ , and (d)  $\sim 1000 \mu\text{m}$  across the lateral range of the scan over time. The OCT signals are in log scales.

The peak in figure 6.1e.9. (a) is centered at approximately  $400\text{-}450 \mu\text{m}$  is due to scattering at the surface of the stone. The breadth of the peak is due to the rough sloped surface of the stone shown in figure 6.1e.8. Figure 6.6.9 (b) – (d) sample the signal intensity at a specific depth of

400, 700 and 1000  $\mu\text{m}$  over the duration of the measurement. Water enters at 99 s crossing the lateral range of the scan by 211 s. The 112 s time to cross the lateral range of the 10 mm gives a wetting front velocity of  $0.0089 \pm 0.0005 \text{ cm s}^{-1}$ . The hydraulic conductivity is in the high middle range of semi-pervious.

AF1875 wetting scan 3 (AFWS3) was performed with the OCT probe positioned on the south face within a recessed area of honeycomb weathering, on a pitted surface recessed by 4 mm from the intact surface, shown in figure 6.1e.10.



Figure 6.1e.10. Position of wetting scan AFWS3

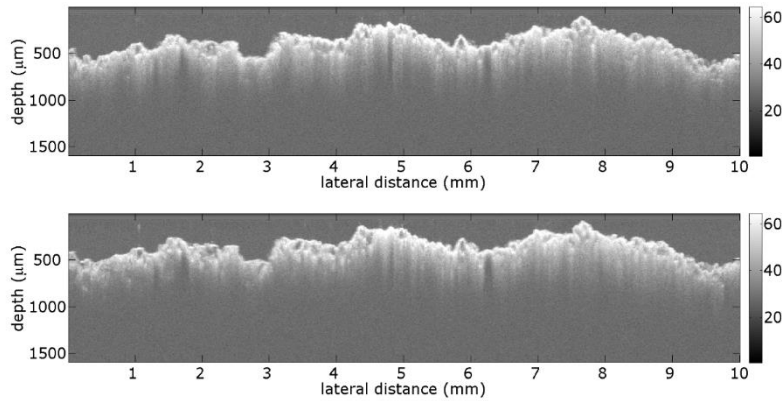


Figure 6.1e.11. OCT virtual cross sections of AFWS3 scan position when (a) dry and (b) wet.

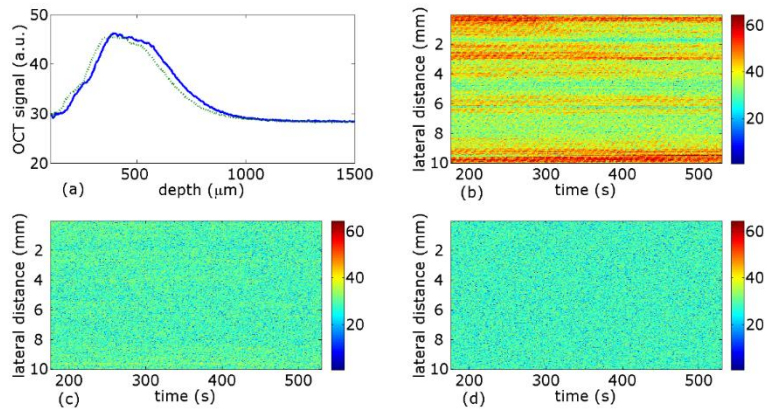


Figure 6.1e.12. AFWS3: (a) pixel intensity values averaged across the 10 mm cross section when dry (solid blue line) and wet (dotted green line); signal intensity values at depths of (b) ~400  $\mu\text{m}$ , (c) ~700  $\mu\text{m}$ , and (d) ~ 1000  $\mu\text{m}$  across the lateral range of the scan over time. The OCT signals are in log scales.

The peak in figure 6.1e.12 (a) is centered at approximately 450-500  $\mu\text{m}$  is due to scattering at the surface of the stone. The breadth of the peak is due to the rough surface of the stone shown in figure 6.1e.11. Figure 6.1e.12 (b) – (d) sample the signal intensity at a specific depth of 400, 700 and 1000  $\mu\text{m}$  over the duration of the measurement. Water enters at 318 s and crosses to 5 mm halfway across the lateral range of the scan by 499 s. The 438 s time to cross the lateral range of the 10 mm gives a wetting scan velocity of  $0.0023 \pm 0.0005 \text{ cm s}^{-1}$ . The hydraulic conductivity is in the middle range of semi-pervious.

AF1875 wetting scan 4 (AFWS4) was performed with the OCT probe positioned on the south face within a recessed area of honeycomb weathering, on a pitted surface recessed by 2 mm from the intact surface.

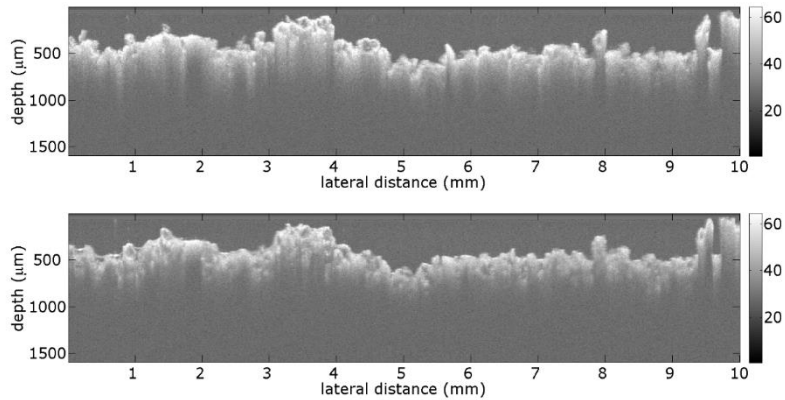


Figure 6.1e.13. OCT virtual cross sections of AFWS4 scan position when (a) dry and (b) wet.

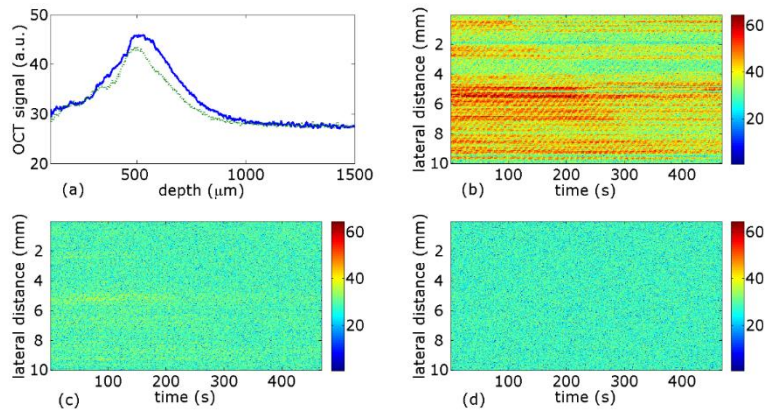


Figure 6.1e.14. AFWS4: (a) pixel intensity values averaged across the 10 mm cross section when dry (solid blue line) and wet (dotted green line); signal intensity values at depths of (b)  $\sim 400 \mu\text{m}$ , (c)  $\sim 700 \mu\text{m}$ , and (d)  $\sim 1000 \mu\text{m}$  across the lateral range of the scan over time. The OCT signals are in log scales.

The peak in figure 6.1e.14 (a) centered at approximately  $500\text{-}550 \mu\text{m}$  is due to scattering at the surface of the stone. The breadth of the peak is due to the rough surface of the stone and the narrowing of the peak when wet is due to the capillary rise of water smoothing the surface, shown in figure 6.1e.13. Figure 6.1e.14 (b) – (d) sample the signal intensity at a specific depth of  $400$ ,  $700$  and  $1000 \mu\text{m}$  over the duration of the measurement. Water enters at  $92 \text{ s}$  crossing the lateral range of the scan by  $388 \text{ s}$ . The  $296 \text{ s}$  time to cross the lateral range of  $10 \text{ mm}$  gives

a wetting scan velocity of  $0.0034 \pm 0.0005 \text{ cm s}^{-1}$ . The hydraulic conductivity is in the middle range of semi-pervious.

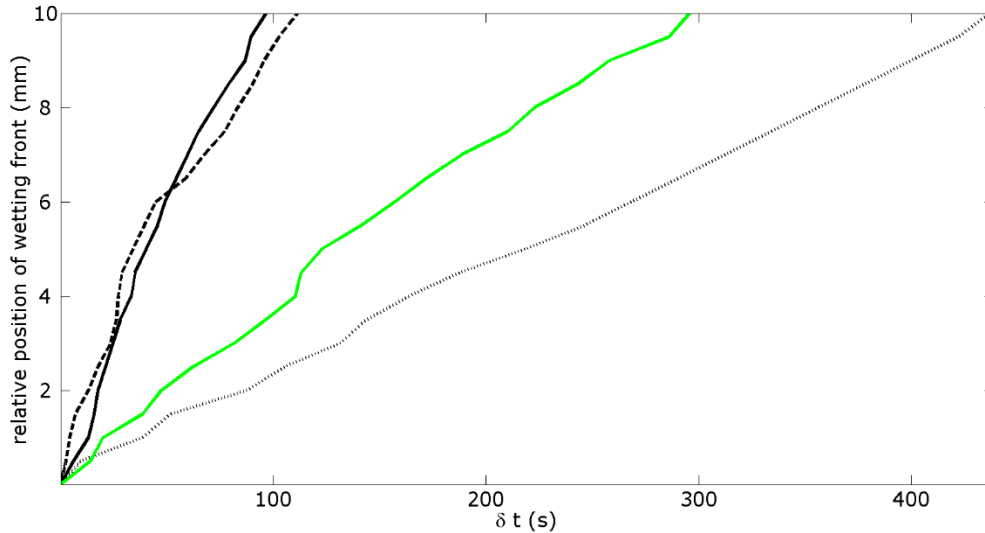


Figure 6.1e.15. Position of the wetting front over time for AFWS1 (black solid line), AFWS2 (black dashed line), AFWS3 (black dotted line), AFWS4 (green solid line).

Scans in regions of surface recession show significantly lower hydraulic conductivities over the range of the scans. The presence of orange discolouration on the weathered surface may indicate the deposition of iron minerals weathering out from the stone. Wetting front velocities for all scans are shown in figure 6.1e.15. Scan AFWS1 positioned on the original surface with rough texture and black discoloration has a hydraulic conductivity of  $0.010 \pm 0.001 \text{ cm s}^{-1}$ . Scan AFWS2 positioned on the original surface with rough texture and green discoloration has hydraulic conductivity of  $0.0089 \pm 0.0005 \text{ cm s}^{-1}$ . Scan AFWS4 is positioned within an area honeycomb weathering, on a pitted surface recessed by 2 mm from original surface with hydraulic conductivity of  $0.0034 \pm 0.0005 \text{ cm s}^{-1}$ . Scan AFWS3 is positioned within an area of honeycomb weathering, on pitted surface recessed by 4 mm from original surface with hydraulic conductivity of  $0.0023 \pm 0.0005 \text{ cm s}^{-1}$ . The scans on the original surface show

hydraulic conductivities within the higher range of semi-pervious, with increasing depth of surface recession, the hydraulic conductivity decreases to the middle range of semi-pervious.

### 6.1f WS1887

Headstone WS1887 is a complex style ornamented gothic-point sandstone tablet of dimensions: height 164 cm, width 76.5 cm, depth 7.5 cm. There is incised carving to the north face of the stone and surface loss to the south face of the stone shown in figure 6.1f.1.



Figure 6.1f.1 Complex sandstone tablet incised on north face dated 1887: images of north, east, south and west faces.

The lower half of the north face has textured surface with recession to 2 mm and an area of surface loss to a 3 mm depth. The decorative carving and ornate top margin show areas of a black deposit encrusting the surface. The south face has more intense weathering features over the lower half with recession to 5 mm and an area of orange discoloration where granular disaggregation is occurring. The upper half has significant areas of black and green encrustation. A schematic of weathering features to north and south faces is shown in figure 6.1f.2.

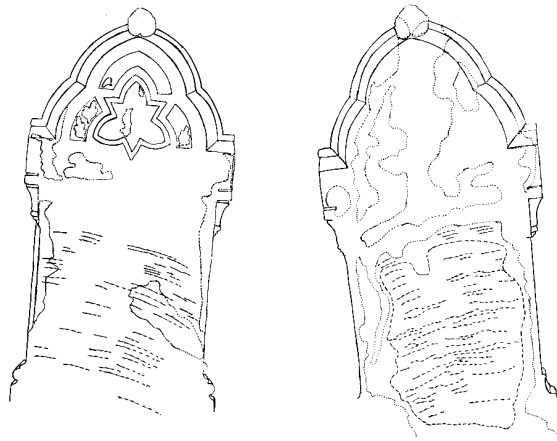


Figure 6.1f.2 Schematic of weathering features on north and south face of gravestone WS1887

The representative grain size distribution for the stone was determined from an OCT volume scan over an area of 6 x 6 mm using the imaging protocol described in chapter 2. Within this volume 202 grains were identified, the size distribution of which is shown in figure 6.1f.3.

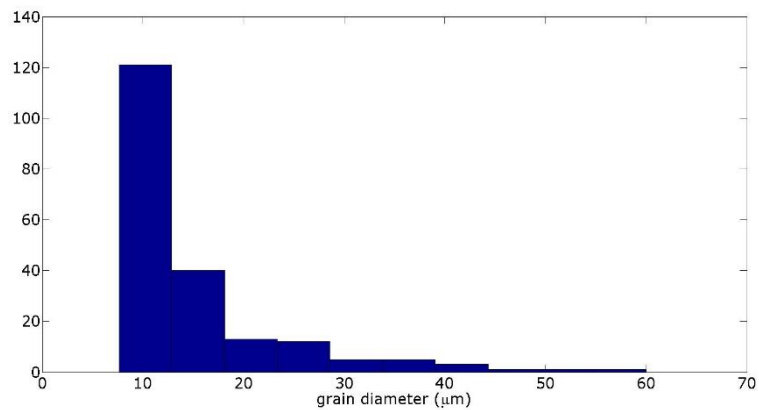


Figure 6.1f.3 Representative grain size distribution for WS1887

The minimum grain size detected, 10 µm, is determined by the resolution of the instrument, the maximum grain size is 60 µm. The detected grain sizes are in the range of medium silt to very fine sand.

WS1887 wetting scan 1 (WSWS1) was performed with the OCT probe positioned on the weathered surface of the north face, shown in figure 6.1f.4. The surface shows textural weathering out of sedimentary features to a depth of 2 mm.



Figure 6.1f.4. Position of wetting scan WSWS1

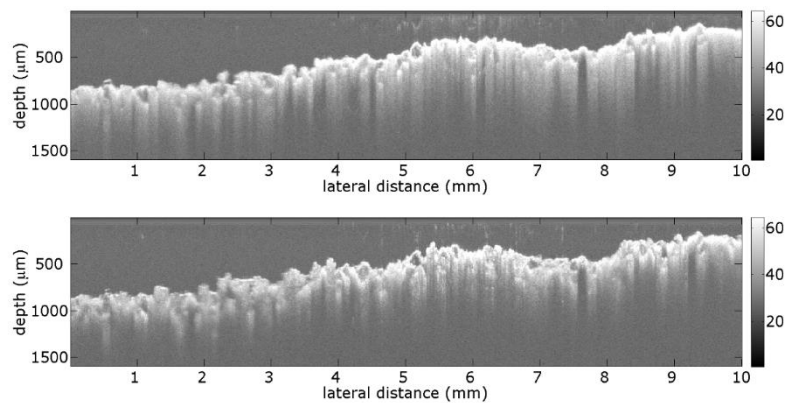


Figure 6.1f.4. OCT virtual cross sections of WSWS1 scan position when (a) dry and (b) wet.

Virtual cross sectional images of the scan position for WSWS1 are shown in figure 6.1f.4 when dry and wet. The presence of water in the sample reduces scattering as it reduces the refractive index mismatch, features can be seen to a greater depth within the stone.

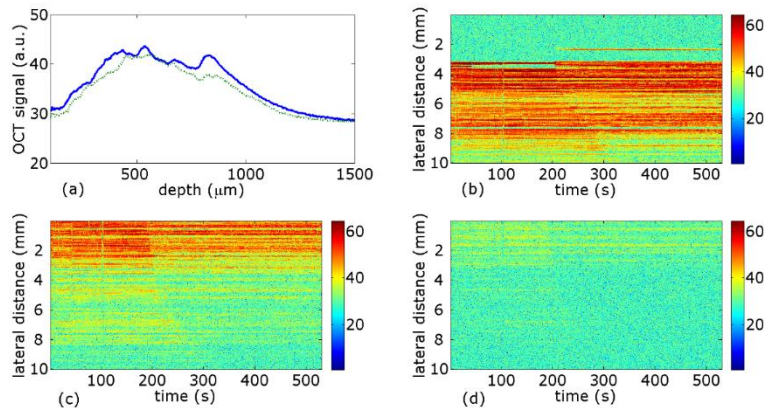


Figure 6.1f.5. WSWS1: (a) pixel intensity values averaged across the 10 mm cross section when dry (solid blue line) and wet (dotted green line); signal intensity values at depths of (b)  $\sim 400 \mu\text{m}$ , (c)  $\sim 700 \mu\text{m}$ , and (d)  $\sim 1000 \mu\text{m}$  across the lateral range of the scan over time. The OCT signals are in log scales.

Figure 6.1f.5 (a) shows the decrease in pixel intensity values due to the reduction of scattering in the sandstone caused by the presence of water in the pore network. Depth scan intensity values were averaged across the 10 mm lateral range of the cross sections when both wet and dry. The peak centered at approximately  $400\text{--}450 \mu\text{m}$  is due to scattering at the surface of the stone. The breadth of the peak is due to the rough sloped surface of the stone, shown in figure 6.1f.4. Figure 6.1f.5 (b) – (d) sample the signal intensity at a specific depth of 400, 700 and  $1000 \mu\text{m}$  over the duration of the measurement. Water enters at 190 s crossing the lateral range of the scan by 340 s, showing little difference in water movement speed in the lateral direction between the different depths. The change in signal due to water cannot be detected below 1 mm. The 150 s time to cross the lateral range of the 10 mm gives a wetting front velocity of  $0.0067 \pm 0.0005 \text{ cm s}^{-1}$ . The hydraulic conductivity at this position is in the middle range of semi-pervious.

WS1887 wetting scan 2 (WSWS2) was performed with the OCT probe positioned above the weathered surface of the north face, shown in figure 6.1f.6. The surface shows slight roughening but no surface loss.



Figure 6.1f.6. Position of wetting scan WSWS2

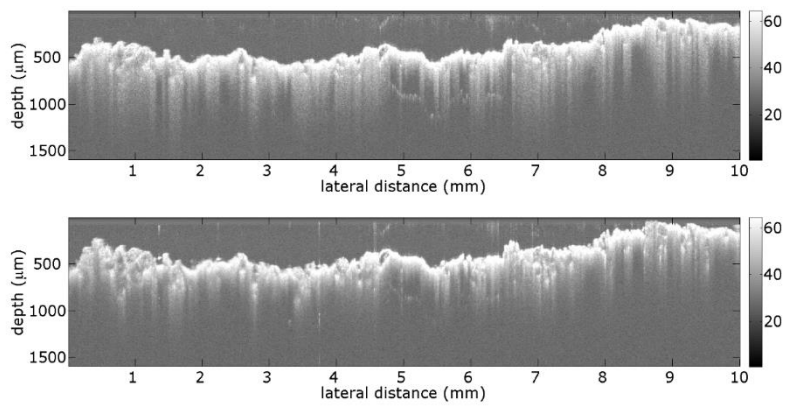


Figure 6.1f.7. OCT virtual cross sections of WSWS2 scan position when (a) dry and (b) wet.

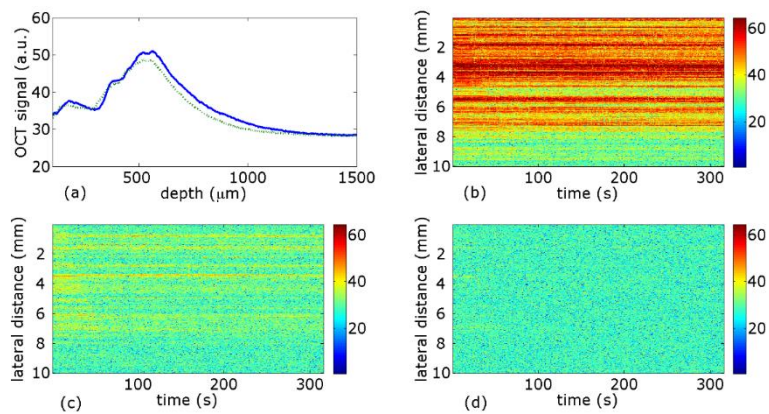


Figure 6.1f.7. WSWS2: (a) pixel intensity values averaged across the 10 mm cross section when dry (solid blue line) and wet (dotted green line); signal intensity values at depths of (b)  $\sim 400 \mu\text{m}$ , (c)  $\sim 700 \mu\text{m}$ , and (d)  $\sim 1000 \mu\text{m}$  across the lateral range of the scan over time. The OCT signals are in log scales.

The peak in figure 6.1f.7 (a) centered at approximately 500-550  $\mu\text{m}$  is due to scattering at the surface of the stone. The breadth of the peak is due to the rough surface of the stone shown in figure 6.1f.6. Figure 6.1f.7 (b) – (d) sample the signal intensity at a specific depth of 400, 700 and 1000  $\mu\text{m}$  over the duration of the measurement. Water enters at 14 s crossing the lateral range of the scan by 111 s. The 97 s time to cross the lateral range of the 10 mm gives a wetting front velocity of  $0.010 \pm 0.001 \text{ cm s}^{-1}$ . The hydraulic conductivity at this point is in the high range of semi-pervious.

WS1887 wetting scan 3 (WSWS3) was performed with the OCT probe positioned on the lower third of the south face on an area of surface recession weathering out sedimentary structures to a depth of approximately 5 mm, shown in figure 6.1f.8.



Figure 6.1f.8. Position of wetting scan WSWS3

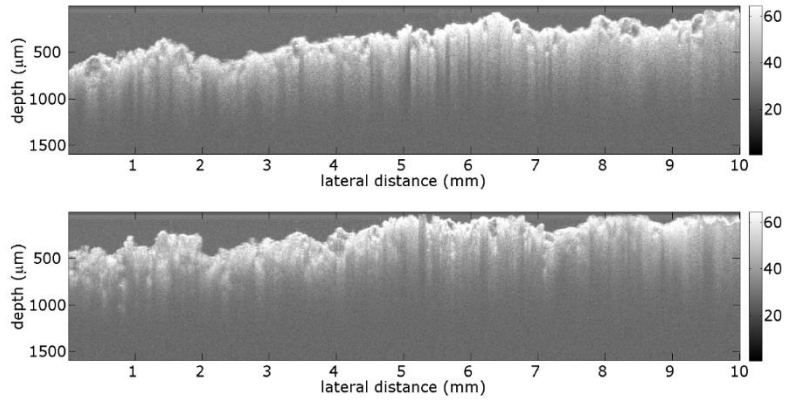


Figure 6.1f.9. OCT virtual cross sections of WSWS3 scan position when (a) dry and (b) wet.

The OCT probe shifted slightly towards the stone surface during scan, (shown in figure 6.1f.9.) without lateral movement.

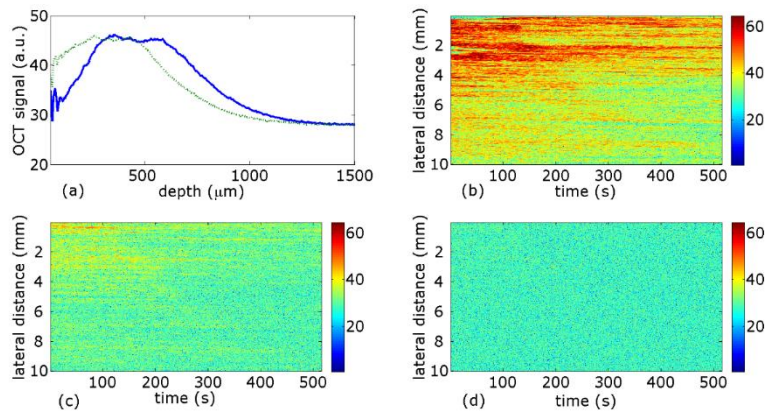


Figure 6.1f.10. WSWS3: (a) pixel intensity values averaged across the 10 mm cross section when dry (solid blue line) and wet (dotted green line); signal intensity values at depths of (b)  $\sim 400 \mu\text{m}$ , (c)  $\sim 700 \mu\text{m}$ , and (d)  $\sim 1000 \mu\text{m}$  across the lateral range of the scan over time. The OCT signals are in log scales.

Figure 6.1f.10 (a) shows the peak centered at approximately 300-350  $\mu\text{m}$  is due to scattering at the surface of the stone, the shift in peak is due to a small shift in the probe towards the surface during the scan. The breadth of the peak is due to the rough sloped surface of the stone.

Figure 6.1f.10(b) – (d) sample the signal intensity at a specific depth of 400, 700 and 1000  $\mu\text{m}$

over the duration of the measurement. Water enters at 122 s crossing the lateral range of the scan by 516 s. The 394 s time to cross the lateral range of 10 mm gives a wetting front velocity of  $0.0025 \pm 0.0005 \text{ cm s}^{-1}$ . The hydraulic conductivity is in the middle range of semi-pervious.

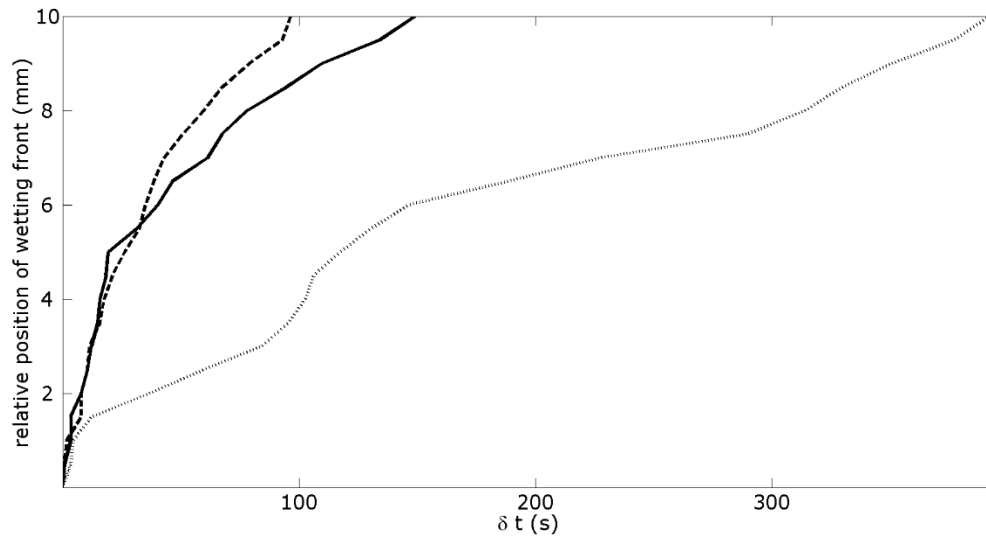


Figure 6.1f.11. Position of the wetting front over time for WSWS1 (black solid line), WSWS2 (black dashed line), WSWS3 (black dotted line).

Wetting front velocities for all scans are shown in figure 6.1f.11. Scan WSWS2 was positioned on the north face on an area of the original surface with a rough surface texture. At this position the hydraulic conductivity was  $0.010 \pm 0.001 \text{ cm s}^{-1}$  in the high range of semi pervious. Scans WSWS1 and WSWS3 were performed on the weathered areas of the north and south face respectively. Scan WSWS1 was positioned on an area with textural weathering out of sedimentary features to a depth of 2 mm and a hydraulic conductivity of  $0.0067 \pm 0.0005 \text{ cm s}^{-1}$ . Scan WSWS3 was performed on an area with similar weathering features at a greater intensity with recession of 5 mm and has a hydraulic conductivity of  $0.0025 \pm 0.0005 \text{ cm s}^{-1}$ . The scans on areas with weathering features and surface recession of 2-5 mm show hydraulic conductivities in the middle range of semi-pervious, a significant decrease from the unweathered area.

### 6.1g HB1877

Headstone HB1877 is a complex style gothic-point sandstone tablet of dimensions: height 165 cm, width 76 cm, depth 8.6 cm. There is incised carving to the north face of the stone. Adjacent to the stone and within the same kerbstone boundary is a second headstone of the same design which has lost its north surface to a depth of approximately 1 cm, shown in figure 6.1g.1.



Figure 6.1g.1. HB1877 with adjacent companion stone; Complex sandstone tablet incised on north face dated 1877: images of north, east, south and west faces.

The north face of the stone is largely undamaged, within the area of black encrustation there are areas of small scale surface blistering and pitting. The south face shows significant surface detachment at a depth of 1 cm, the missing surface of the upper half is lying broken directly behind the stone suggesting a single incident of detachment. The lower half of the stone shows evidence of detachment with cracks at the same depth. The surface detachment appears not to be influenced by the aspect of the stone as the companion stone appears to have undergone the same processes on the opposite face. A schematic of weathering features to north and south faces is shown in figure 6.1g.2.

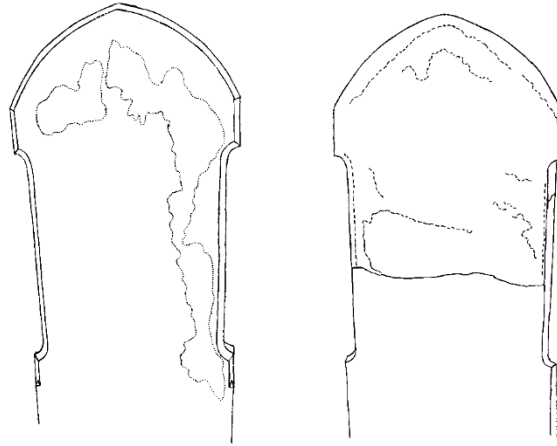


Figure 6.1g.2. Schematic of weathering features on north and south face of gravestone HB1877

The representative grain size distribution for the stone was determined from an OCT volume scan over an area of 6 x 6 mm using the imaging protocol described in chapter 2. Within this volume 86 grains were identified, the size distribution of which is shown in figure 6.1g.3.

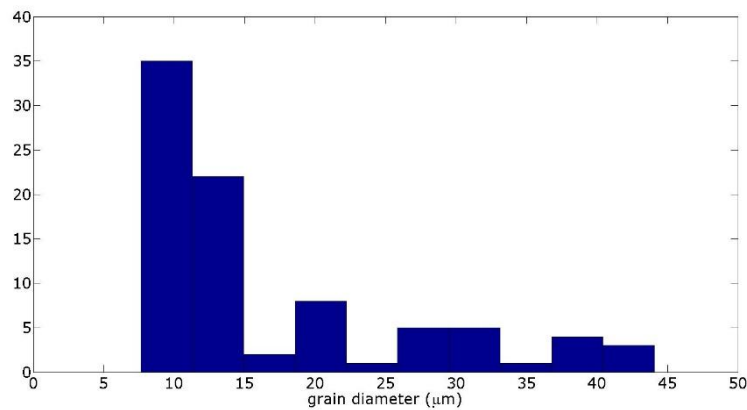


Figure 6.1g.3 Representative grain size distribution for HB1877

The minimum grain size detected, 10 µm, is determined by the resolution of the instrument, the maximum size is 44 µm. The detected grain sizes are in the range of medium to coarse silt.

HB1877 wetting scan 1 (HBWS1) was performed with the OCT probe positioned on the original surface of the north face between the lines of the inscription shown in figure 6.1g.4.



Figure 6.1g.4. Position of wetting scan HBWS1

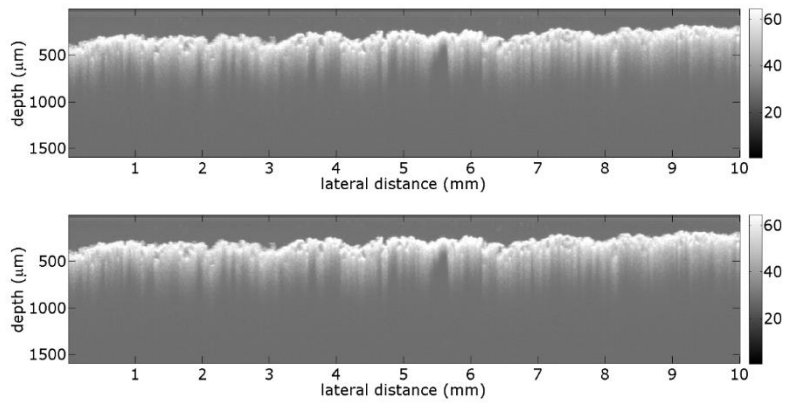


Figure 6.1g.5. OCT virtual cross sections of HBWS1 scan position when (a) start and (b) end of scan.

Virtual cross sectional images of the scan position for HBWS1 are shown in figure 6.1g.5. at the start and end of scan. No water was absorbed into the stone so there is no change in the images for the duration of the scan.

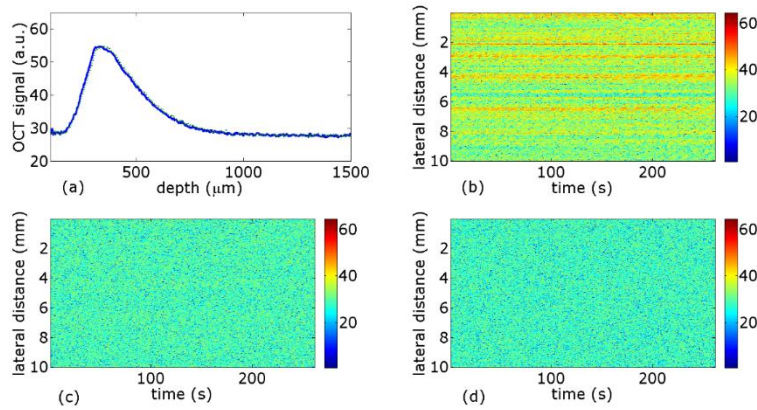


Figure 6.1g.6. HBWS1: (a) pixel intensity values averaged across the 10 mm cross section at the start (solid blue line) and end (dotted green line) of the scan; signal intensity values at depths of (b)  $\sim 400 \mu\text{m}$ , (c)  $\sim 700 \mu\text{m}$ , and (d)  $\sim 1000 \mu\text{m}$  across the lateral range of the scan over time. The OCT signals are in log scales.

Figure 6.1f.6 (a) shows the pixel intensity values in the sandstone at the start and end of the scan, as no water was absorbed into the stone there is no change. The peak centered at approximately  $350\text{--}400 \mu\text{m}$  is due to scattering at the surface of the stone. There is no change to pixel intensity values at any depth. With regard to hydraulic conductivity, the stone surface may be considered slightly pervious to impervious.

HB1877 wetting scan 2 (HBWS2) was performed with the OCT probe positioned on the original surface of the north face between the lines of the inscription shown in figure 6.1g.7 approximately 15 cm above the position of HBWS1.



Figure 6.1g.7. Position of wetting scan HBWS2

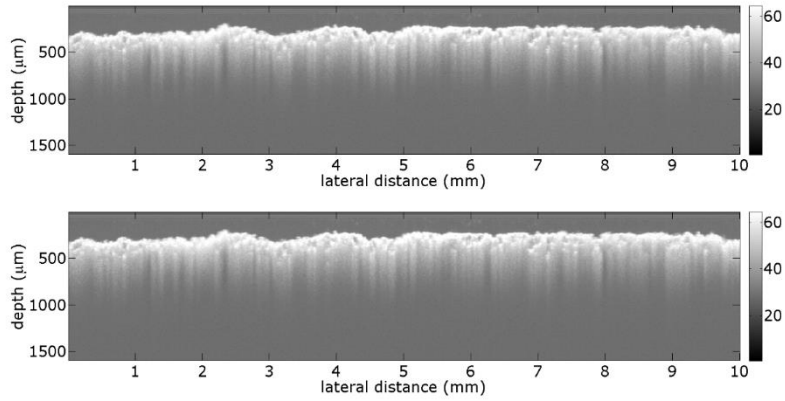


Figure 6.1g.8. OCT virtual cross sections of HBWS2 scan position when (a) start and (b) end of scan.

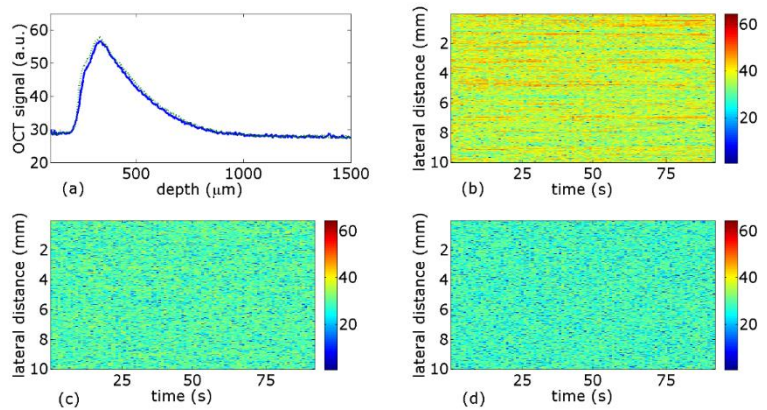


Figure 6.1g.9. HBWS1: (a) pixel intensity values averaged across the 10 mm cross section at the start (solid blue line) and end (dotted green line) of the scan; signal intensity values at depths of (b)  $\sim 400 \mu\text{m}$ , (c)  $\sim 700 \mu\text{m}$ , and (d)  $\sim 1000 \mu\text{m}$  across the lateral range of the scan over time. The OCT signals are in log scales.

Figure 6.1f.9 (a) shows the pixel intensity values in the sandstone at the start and end of the scan. The peak centered at approximately  $350\text{--}400 \mu\text{m}$  is due to scattering at the surface of the stone, shown in figure 6.1g.8. with regard to hydraulic conductivity the stone surface may be considered slightly pervious to impervious.

HB1877 wetting scan 3 (HBWS3) was performed with the OCT probe positioned on the recessed surface of the south face.

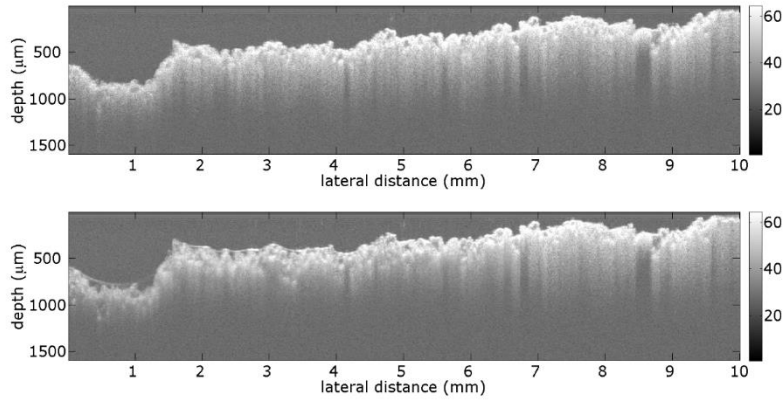


Figure 6.1g.10. OCT virtual cross sections of HBWS3 scan position when (a) dry and (b) wet.

Virtual cross sectional images of the scan position for HBWS3 are shown in figure 6.1g.10 when dry and wet. The presence of water in the sample reduces scattering as it reduces the refractive index mismatch, features can be seen to a greater depth within the stone.

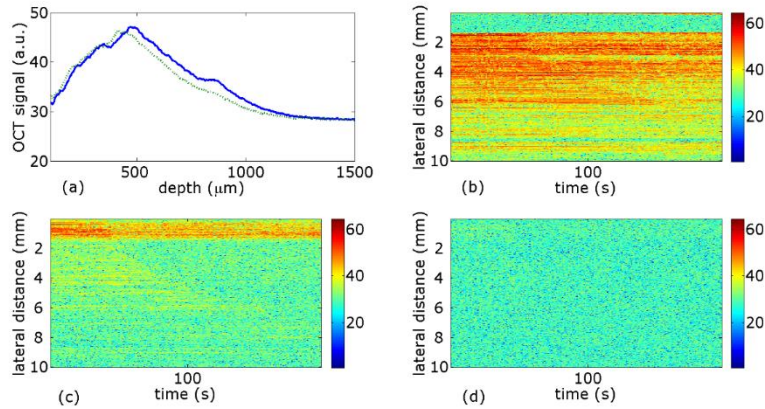


Figure 6.1g.11. HBWS3: (a) pixel intensity values averaged across the 10 mm cross section when dry (solid blue line) and wet (dotted green line); signal intensity values at depths of (b)  $\sim 400 \mu\text{m}$ , (c)  $\sim 700 \mu\text{m}$ , and (d)  $\sim 1000 \mu\text{m}$  across the lateral range of the scan over time. The OCT signals are in log scales.

Figure 6.1g.11 (a) shows the decrease in pixel intensity values due to the reduction of scattering in the sandstone caused by the presence of water in the pore network. Depth scan intensity values were averaged across the 10 mm lateral range of the cross sections when both wet and

dry. The peak centered at approximately 500-550  $\mu\text{m}$  is due to scattering at the surface of the stone. The breadth of the peak is due to the rough sloped surface of the stone. There is a slight shift in the peak position for the dry and wet values because a film of water formed at the stone surface due to capillary action. Figure 6.1g.11 (b) – (d) sample the signal intensity at a specific depth of 400, 700 and 1000  $\mu\text{m}$  over the duration of the measurement. Water enters at 40 s and crosses to 5 mm halfway across the lateral range of the scan by 106 s, showing little difference in water movement speed in the lateral direction between the different depths. The change in signal due to water cannot be detected below 1 mm. The 132 s time to cross the full lateral range of 10 mm gives a wetting scan velocity of  $0.0076 \pm 0.0005 \text{ cm s}^{-1}$ . The hydraulic conductivity at this point is in the middle range of semi-pervious.

HB1877 wetting scan 4 (HBWS4) was performed with the OCT probe positioned on the recessed surface of the south face approximately 20 cm above HBWS3.

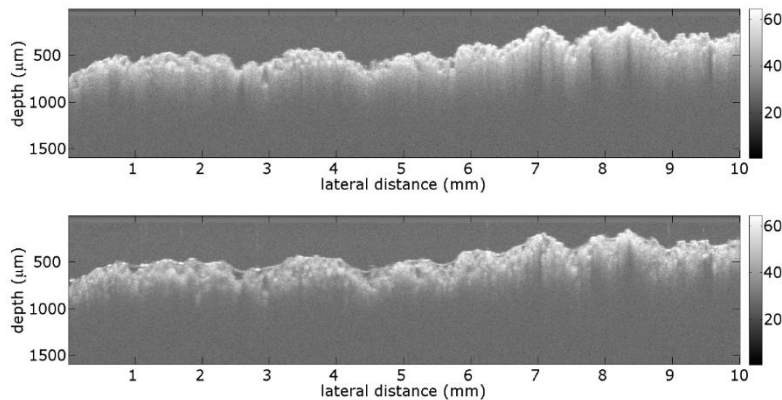


Figure 6.1g.12. OCT virtual cross sections of HBWS4 scan position when (a) dry and (b) wet.

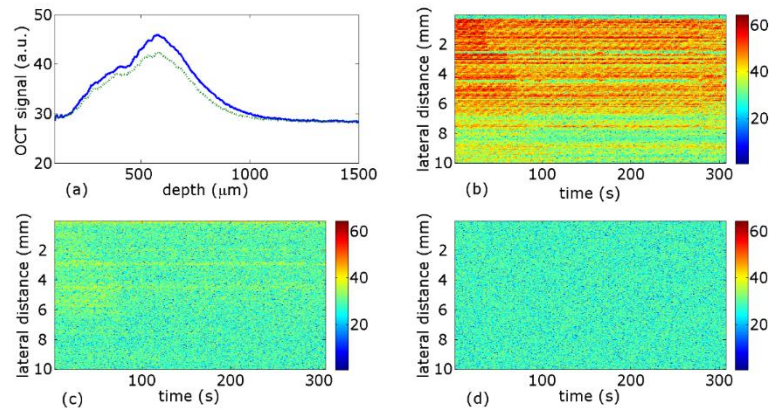


Figure 6.1g13. HBWS4: (a) pixel intensity values averaged across the 10 mm cross section when dry (solid blue line) and wet (dotted green line); signal intensity values at depths of (b) ~400  $\mu\text{m}$ , (c) ~700  $\mu\text{m}$ , and (d) ~ 1000  $\mu\text{m}$  across the lateral range of the scan over time. The OCT signals are in log scales.

The peak in figure 6.1g.13 (a) centered at approximately 550-600  $\mu\text{m}$  is due to scattering at the surface of the stone. The breadth of the peak is due to the rough sloped surface of the stone shown in figure 6.1g.12. Figure 6.1.g.13 (b) – (d) sample the signal intensity at a specific depth of 400, 700 and 1000  $\mu\text{m}$  over the duration of the measurement. Water enters at 23 s crossing the lateral range of the scan by 111 s. The 88 s time to cross the lateral range of 10 mm gives a wetting scan velocity of  $0.011 \pm 0.001 \text{ cm s}^{-1}$ . Hydraulic conductivity in the high range of semi-pervious.

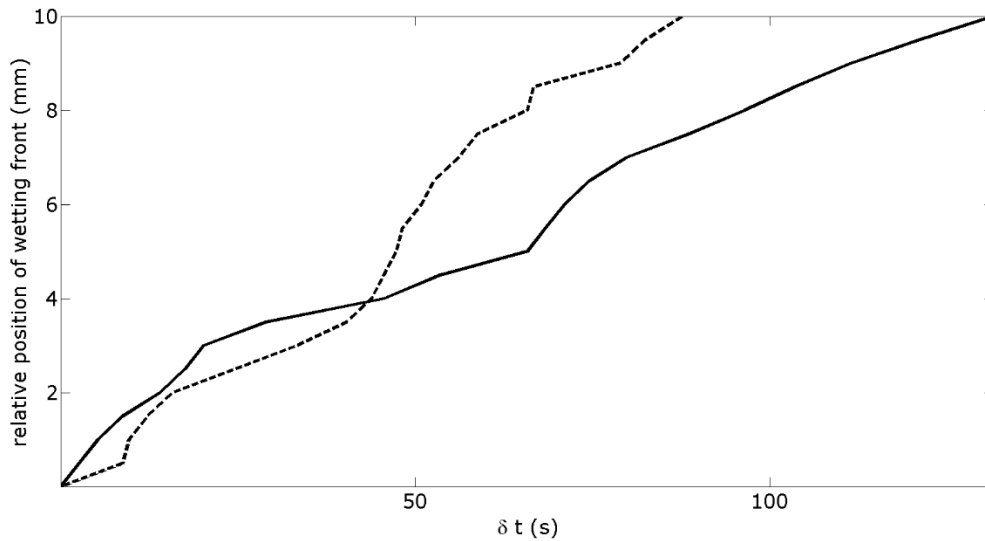


Figure 6.1g.14. Position of the wetting front over time for HBWS3 (black solid line) and HBWS4 (black dashed line).

During scans HBWS1 and HBWS2 on the original surface of the north face no water was absorbed into the stone in the duration of the experiment indicating that the surface is slightly pervious to impervious. Scans HBWS3 and HBWS4 were performed on the recessed surface of the south face where a 1 cm thick slab of the stone surface has detached to reveal the interior of the stone; with hydraulic conductivities of  $0.0076 \pm 0.0005 \text{ cm s}^{-1}$  and  $0.011 \pm 0.001 \text{ cm s}^{-1}$  respectively. Wetting front velocities for both scans are shown in figure 6.1g.14. This indicates that while the stone surface is impervious the interior of the stone is semi pervious and a potential pathway for the rise of ground water by capillary action.

### 6.1h AT1850

Headstone AT1850 is a complex style gothic-point sandstone tablet of dimensions: height 144 cm, width 76 cm, depth 8 cm, there is incised carving to both north and south face of stone, shown in figure 6.1h.1.



Figure 6.1h.1. Complex sandstone tablet incised on north face dated 1850: images of north, south and west faces.

A schematic of weathering features to north and south faces is shown in figure 6.1h.2. There is extensive growth of green algae across stone surface on both north and south face and large areas of black deposits encrusting the stone. The south face has an area of surface detachment in the centre, a ~2 mm thick surface scale separating from the tablet around the incised inscription. Surface detachment is focused around the inscription with the surface of incised letters scaling away.

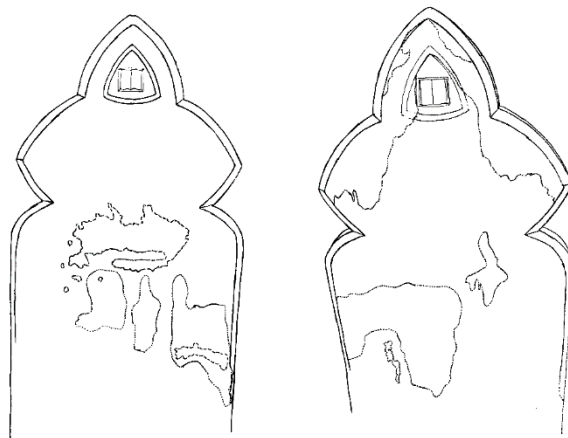


Figure 6.1h2. Schematic of weathering features on north and south face of gravestone AT1850

AT1850 wetting scan 1 (ATWS1) was performed with the OCT probe positioned on the original surface of the south face, shown in figure 6.1h.3. The surface shows black discolouration and green algal growth.



Figure 6.1h.3. Position of wetting scan ATWS1.

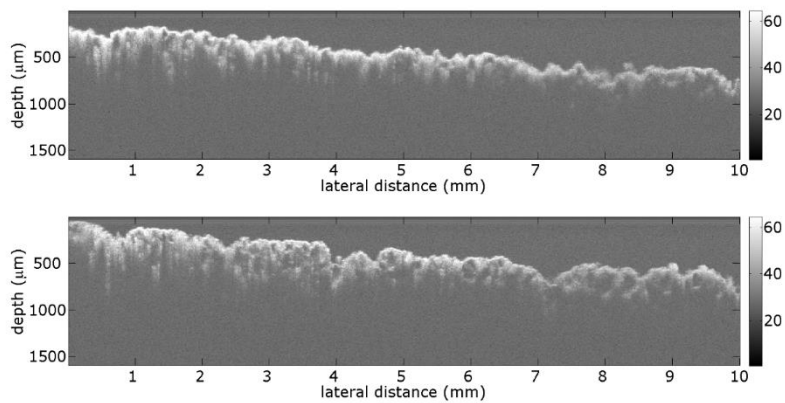


Figure 6.1h.4. OCT virtual cross sections of AFWS1 scan position when (a) dry and (b) wet.

Virtual cross sectional images of the scan position for ATWS2 are shown in figure 6.1h.4 when dry and wet. The presence of water in the sample reduces scattering as it reduces the refractive index mismatch, features can be seen to a greater depth within the stone. The presence of surface crust and algal biofilm at this position appears to reduce the difference in scattering as a result of water within the surface.

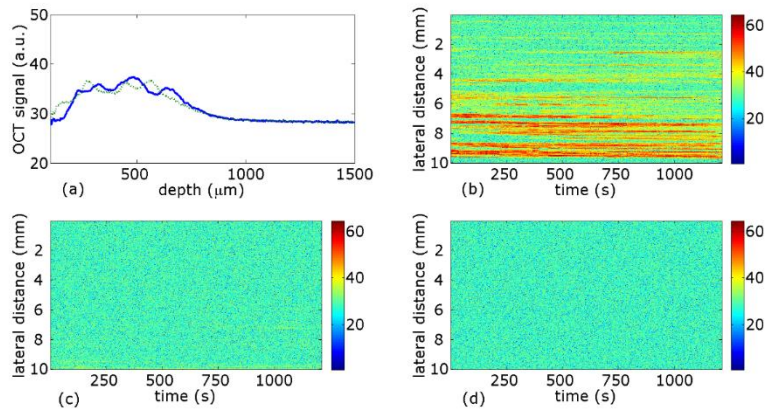


Figure 6.1h.5. ATWS1: (a) pixel intensity values averaged across the 10 mm cross section at the start (solid blue line) and end (dotted green line) of the scan; signal intensity values at depths of (b)  $\sim 400 \mu\text{m}$ , (c)  $\sim 700 \mu\text{m}$ , and (d)  $\sim 1000 \mu\text{m}$  across the lateral range of the scan over time. The OCT signals are in log scales.

The exact position of the wetting front position is difficult to discern throughout the scan. The point of ingress and full wetting can be determined from OCT scan images viewed in sequence. Water crosses the lateral range of in scan in approximately 800 s, giving a wetting front in the order of  $0.001 \text{ cm s}^{-1}$ .

AT1850 wetting scan 2 (ATWS2) was performed with the OCT probe positioned on the recessed surface of the south face, shown in figure 6.1h.6. The surface shows black discolouration and green algal growth.



Figure 6.1h.6. Position of wetting scan ATWS3

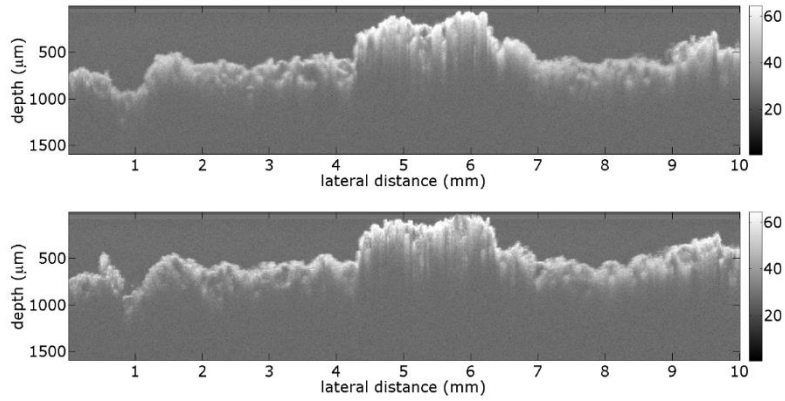


Figure 6.1h7. OCT virtual cross sections of AFWS2 scan position when (a) dry and (b) wet.

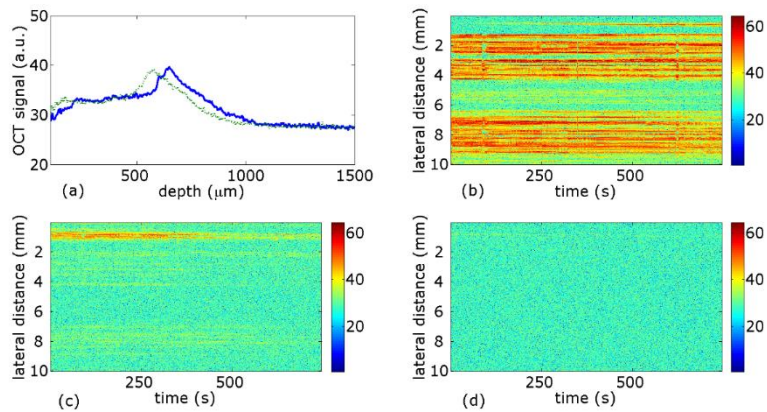


Figure 6.1h8. ATWS2: (a) pixel intensity values averaged across the 10 mm cross section at the start (solid blue line) and end (dotted green line) of the scan; signal intensity values at depths of (b)  $\sim 400 \mu\text{m}$ , (c)  $\sim 700 \mu\text{m}$ , and (d)  $\sim 1000 \mu\text{m}$  across the lateral range of the scan over time. The OCT signals are in log scales.

The exact position of the wetting front position is difficult to discern throughout the scan. The point of ingress and full wetting can be determined from OCT scan images viewed in sequence. Water crosses the lateral range of in scan in approximately 600 s, giving a wetting front in the order of  $0.002 \text{ cm s}^{-1}$ . The OCT wetting scans indicate that the stone is semi pervious with respect to hydraulic conductivity, while also demonstrating a potential limitation of the technique on surfaces encrusted with algal biofilms.

## 6.1i WK1884

Headstone WK1884 is a gothic-point sandstone tablet of dimensions: height 139 cm, width 68.5 cm, depth 8 cm, with damaged incised carving to the north face of the stone, shown in figure 6.1i.1.



Figure 6.1i.1. Complex sandstone tablet incised on north face dated 1884: images of north, east, south and west faces.

The north face has extensive surface loss due to contour scaling leading to granular disintegration and honeycomb weathering with an area of cavernous weathering recessed by 4 cm from the original surface. The original surface is covered with a black crust while the recessed surface shows orange discolouration at 2 mm becoming white with the depth and intensity of weathering features. The south face of the stone is intact with some black and green crust present on the surface. A schematic of weathering features to north and south faces is shown in figure 6.1i.2.

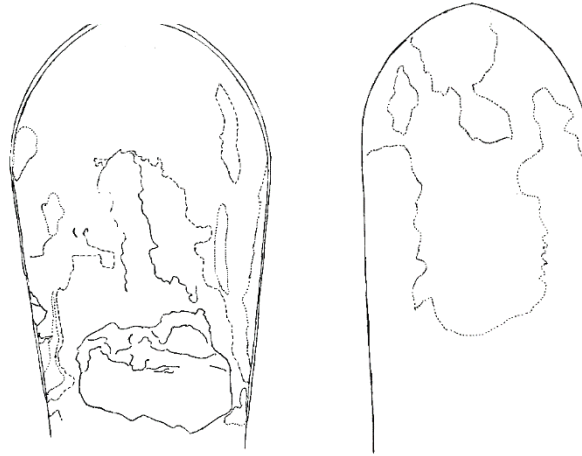


Figure 6.1i.2 Schematic of weathering features on north and south face of gravestone WK1884

The representative grain size distribution for the stone was determined from an OCT volume scan over an area of 6 x 6 mm using the imaging protocol described in chapter 2. Within this volume 265 grains were identified, the size distribution of which is shown in figure 6.1i.3.

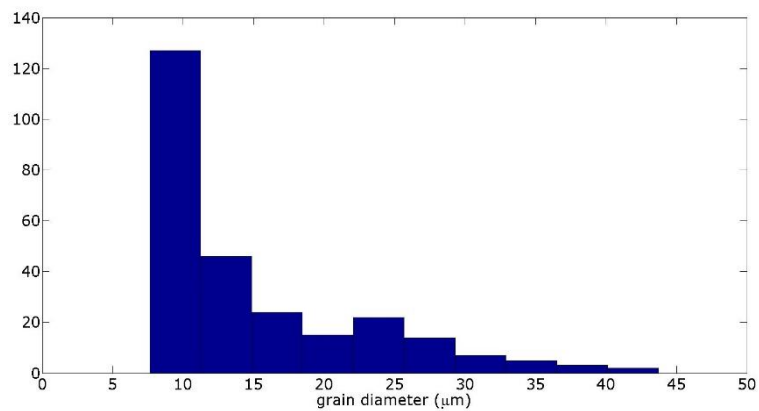


Figure 6.1i.3 Representative grain size distribution for WK1884

The minimum grain size detected, 10 μm is determined by the resolution of the instrument, the maximum size is 44 μm. The detected grain sizes are in the range of medium to coarse silt.

WK1873 wetting scan 1 (WKWS1) was performed with the OCT probe positioned within an area of 4 cm surface recession which shows loss of colouration, granular loss at surface and honeycomb weathering, shown in figure 6.1i.4.



Figure 6.1i.4. Position of wetting scan WKWS1

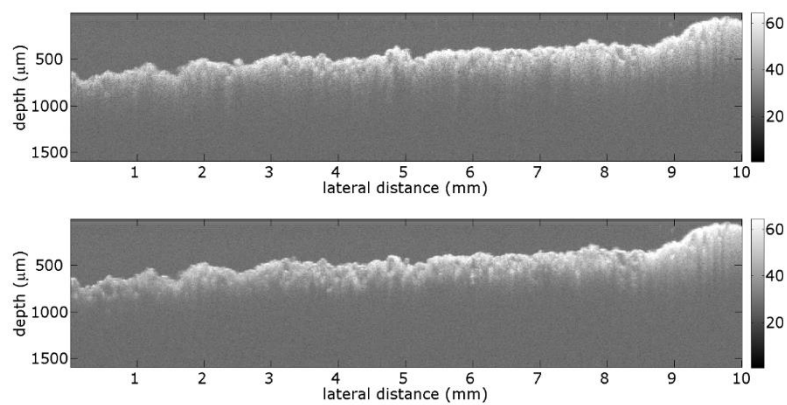


Figure 6.1i.5. OCT virtual cross sections of WKWS1 scan position when (a) dry and (b) wet.

Virtual cross sectional images of the scan position for WKWS1 are shown in figure 6.1i.5. when dry and wet. The presence of water in the sample reduces scattering as it reduces the refractive index mismatch, features can be seen to a greater depth within the stone.

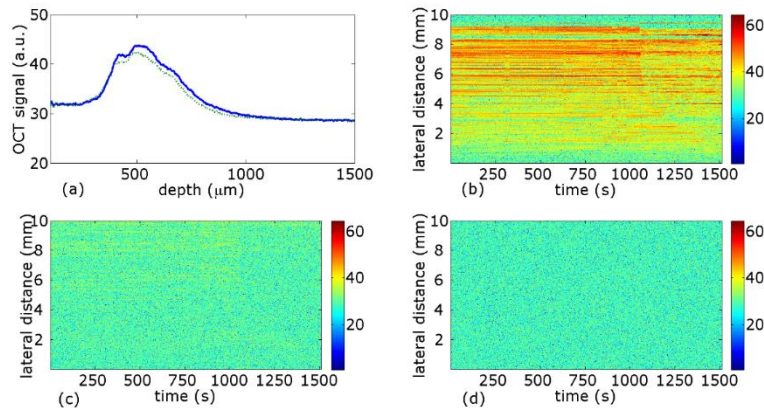


Figure 6.1i.6. WKWS1: (a) pixel intensity values averaged across the 10 mm cross section when dry (solid blue line) and wet (dotted green line); signal intensity values at depths of (b) ~400  $\mu\text{m}$ , (c) ~700  $\mu\text{m}$ , and (d) ~ 1000  $\mu\text{m}$  across the lateral range of the scan over time. The OCT signals are in log scales.

Figure 6.1i.6 (a) shows the decrease in pixel intensity values due to the reduction of scattering in the sandstone caused by the presence of water in the pore network. Depth scan intensity values were averaged across the 10 mm lateral range of the cross sections when both wet and dry. The peak centered at approximately 150-200  $\mu\text{m}$  is due to scattering at the surface of the stone. The breadth of the peak is due to the rough sloped surface of the stone. Figure 6.1i.6 (b) – (d) sample the signal intensity at a specific depth of 400, 700 and 1000  $\mu\text{m}$  over the duration of the measurement. Water enters at 1056 s crossing the lateral range of the scan by 1690 s, showing little difference in water movement speed in the lateral direction between the different depths. The change in signal due to water cannot be detected below 1 mm. The 634 s time to cross the lateral range of 10 mm gives a wetting scan velocity of  $0.0016 \pm 0.0005 \text{ cm s}^{-1}$ . Hydraulic conductivity in the low middle range of semi-pervious.

WK1873 wetting scan 2 (WKWS2) was performed with the OCT probe positioned within an area of 2 mm surface recession with a pitted surface texture and orange discolouration, shown in figure 6.1i.7.



Figure 6.1i.7. Position of wetting scan WKWS2

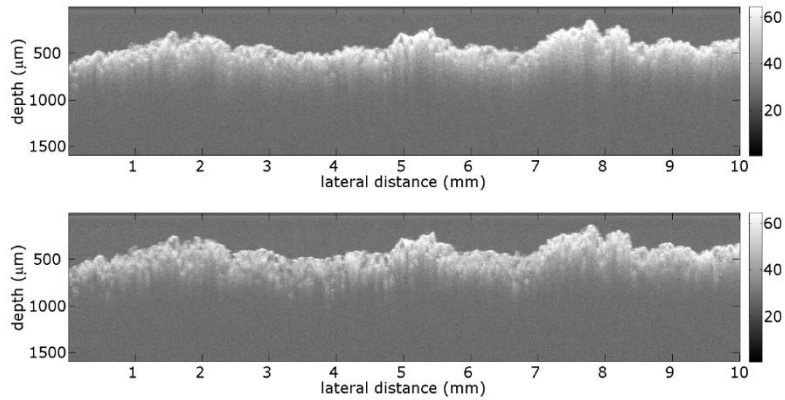


Figure 6.1i.8. OCT virtual cross sections of WKWS2 scan position when (a) dry and (b) wet.

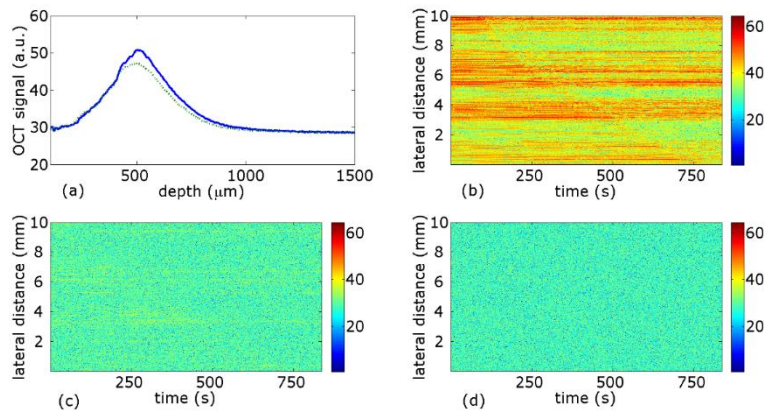


Figure 6.1i.9. WKWS2: (a) pixel intensity values averaged across the 10 mm cross section when dry (solid blue line) and wet (dotted green line); signal intensity values at depths of (b)  $\sim 400 \mu\text{m}$ , (c)  $\sim 700 \mu\text{m}$ , and (d)  $\sim 1000 \mu\text{m}$  across the lateral range of the scan over time. The OCT signals are in log scales.

The peak in figure 6.1i.9. (a) centered at approximately 500-550  $\mu\text{m}$  is due to scattering at the surface of the stone. The breadth of the peak is due to the rough sloped surface of the stone, shown in figure 6.1i.8. Figure 6.1i.9. (b) – (d) sample the signal intensity at a specific depth of 400, 700 and 1000  $\mu\text{m}$  over the duration of the measurement. Water enters at 95 s crossing the lateral range of the scan by 769 s, showing little difference in water movement speed in the lateral direction between the different depths. The 674 s time to cross the lateral range of the 10 mm gives a wetting scan velocity of  $0.0015 \pm 0.0005 \text{ cm s}^{-1}$ . Hydraulic conductivity in the low middle range of semi-pervious.

WK1873 wetting scan 3 (WKWS3) was performed with the OCT probe positioned on the original surface of the stone adjacent to the area of surface loss, in an area with black discolouration, shown in figure 6.1i.10.



Figure 6.1i.10. Position of wetting scan WKWS3

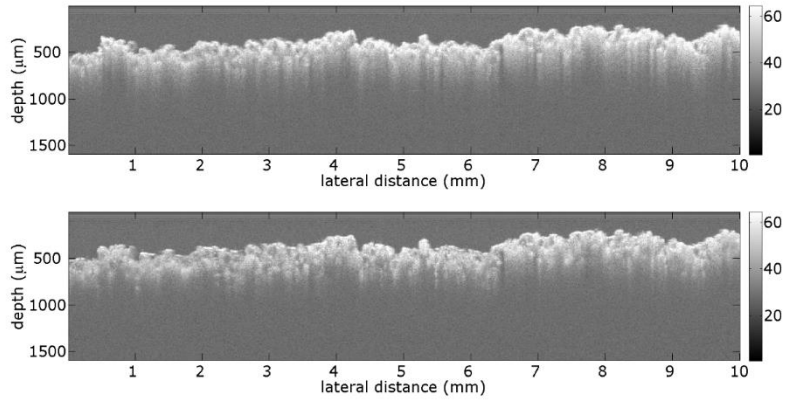


Figure 6.1i.11. OCT virtual cross sections of WKWS3 scan position when (a) dry and (b) wet.

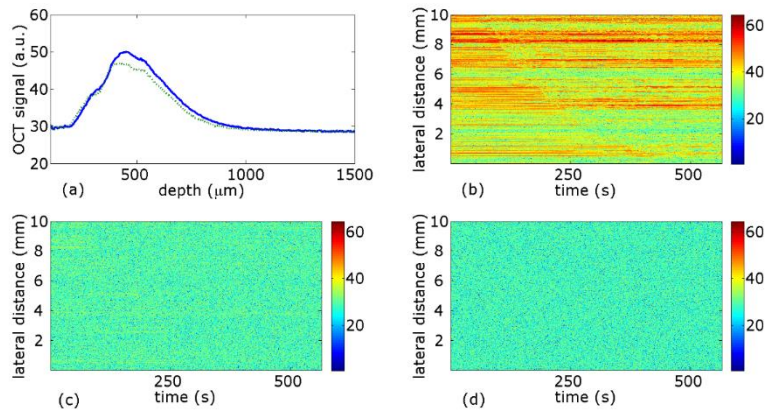


Figure 6.1i.12. WKWS3: (a) pixel intensity values averaged across the 10 mm cross section when dry (solid blue line) and wet (dotted green line); signal intensity values at depths of (b)  $\sim 400 \mu\text{m}$ , (c)  $\sim 700 \mu\text{m}$ , and (d)  $\sim 1000 \mu\text{m}$  across the lateral range of the scan over time. The OCT signals are in log scales.

The peak in figure 6.1i.12 (a) centered at approximately  $450\text{-}500 \mu\text{m}$  is due to scattering at the surface of the stone. The breadth of the peak is due to the rough sloped surface of the stone, shown in figure 6.1i.11. Figure 6.1i.12 (b) – (d) sample the signal intensity at a specific depth of  $400$ ,  $700$  and  $1000 \mu\text{m}$  over the duration of the measurement. Water enters at  $75 \text{ s}$  crossing the lateral range of the scan by  $427 \text{ s}$ . The  $352 \text{ s}$  time to cross the lateral range of  $10 \text{ mm}$  gives

a wetting scan velocity of  $0.0028 \pm 0.0005 \text{ cm s}^{-1}$ . Hydraulic conductivity is in the middle range of semi-pervious.

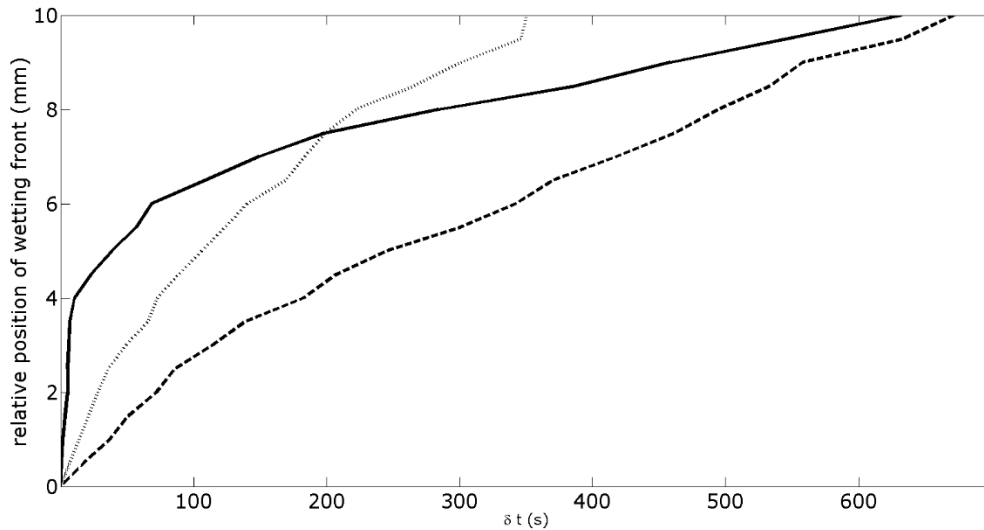


Figure 6.1i.12. Position of the wetting front over time for WKWS1 (black solid line), WKWS2 (black dashed line), WKWS3 (black dotted line).

Wetting front velocities for all scans are shown in figure 6.1i.12. Scan WKWS1 was performed on the surface with the greatest intensity of weathering features within an area of 4 cm surface recession which shows loss of colouration, granular loss at surface and honeycomb weathering with a hydraulic conductivity of  $0.0016 \pm 0.0005 \text{ cm s}^{-1}$ . An area with surface recession of 2 mm was scanned in WKWS2 with a hydraulic conductivity of  $0.0015 \pm 0.0005 \text{ cm s}^{-1}$ , both scans of weathered areas show lower values than for the original surface with a hydraulic conductivity of  $0.0028 \pm 0.0005 \text{ cm s}^{-1}$  given from WKWS3. The hydraulic conductivity of the stone varies from the middle to the low middle of the range of semi pervious with the increasing intensity of weathering features.

## 6.1 Summary of Results and Discussion

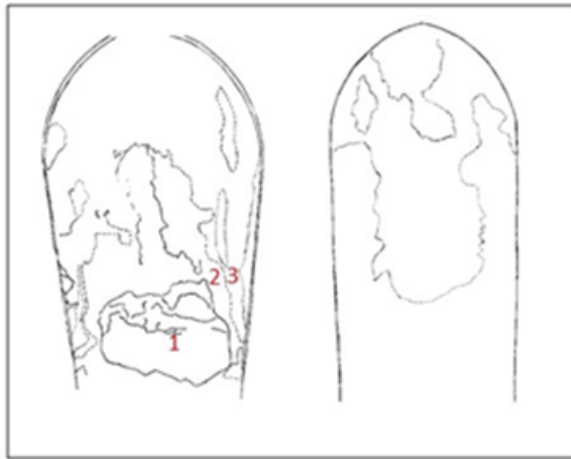
The sandstone headstones at Nottingham General Cemetery provide a study of sandstone weathering under similar environmental conditions and exposure times. The differing types and intensities of weathering forms found are primarily influenced by the intrinsic characteristics of the stones. Weathering features across all the sandstone are dominated by surface breakdown by contour scaling, flaking and granular disintegration. Stones which have areas of decorative and ornamental sculpting are prone to the build-up of encrustation from environmental and atmospheric inputs. The relative intensity weathering features does not correlate with the exposure time of the stones.

Representative grain sizes distributions for all stones are dominated by grains in the range of medium to coarse silt and appear well sorted. The grain size distributions are similar for all the stones studied and there appears to be no correlation with the type or intensity of weathering features.

Measurements of hydraulic conductivities across the sandstones range from slightly pervious to the high end of semi-pervious and vary with position and intensity of weathering features for each stone. The change in hydraulic conductivity of the stones with the intensity of weathering features fell in three groups: three of the headstone showed an increase with increasing surface recession, two a decrease and two showed slightly pervious to impervious original surfaces with semi-pervious interiors. Where surfaces were found to be impervious there was no indication of moisture in the range of the scan during a 2 hour observation time so the hydraulic conductivity of the surface was therefore less than  $10^{-6} \text{ cm s}^{-1}$ .

Headstones WK1887, JG1873, AF1875 and WS1887 all showed lower hydraulic conductivities on areas of surface recession compared to the original surface. For headstone WK1887, the hydraulic conductivity of the stone varies from the middle to the low middle of

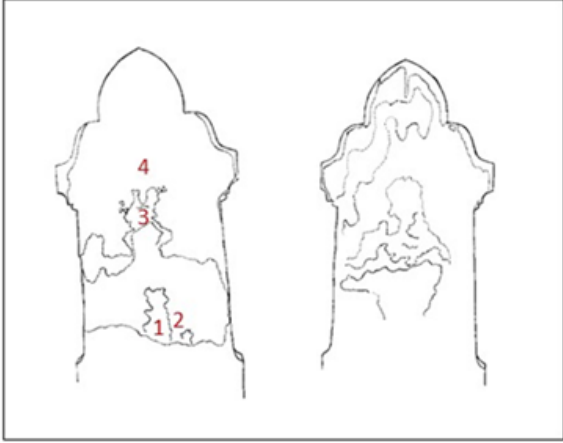
the range of semi pervious with the increasing intensity of weathering features, shown in table 6.1. The stone shows the most severe weathering damage of those studied with extensive surface loss due to contour scaling leading to granular disintegration and honeycomb weathering with an area of cavernous weathering recessed by 4 cm from the original surface.



SCAN	SURFACE WEATHERING	HYDRAULIC CONDUCTIVITY
WK1	4 cm surface recession, 'bleaching', honeycomb	0.0016 cm s <sup>-1</sup>
WK2	2 mm surface recession, orange discolouration, pitting	0.0015 cm s <sup>-1</sup>
WK3	Adjacent to surface detachment, black discolouration	0.0028 cm s <sup>-1</sup>

Table 6.1 Summary of hydraulic conductivity measurements for WK1887

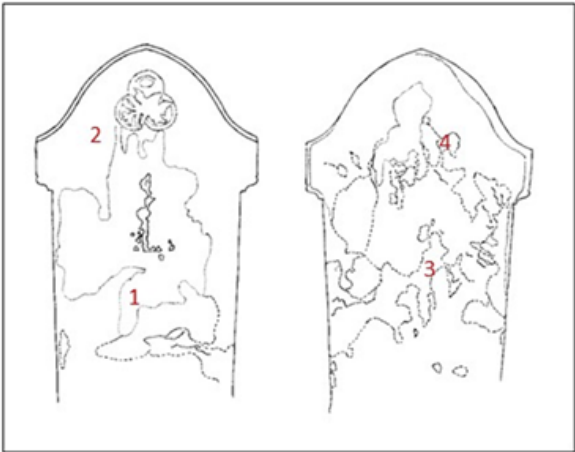
For headstone JG1873 the measurements on areas of surface recession of 2 – 4 mm with soft granular surface texture show a significant decrease in hydraulic conductivity, shown in table 6.2, from the high to middle range of semi pervious in comparison with the original surface and area of 1 mm recession due to the loss of surface by flaking.



SCAN	SURFACE WEATHERING	HYDRAULIC CONDUCTIVITY
JG1	4 mm recession, "bleaching" granular loss, honeycomb	0.0048 cm s <sup>-1</sup>
JG2	2 mm recession, orange discolouration, surface pitting	0.0032 cm s <sup>-1</sup>
JG3	1 mm recession, surface pitting	0.0071 cm s <sup>-1</sup>
JG4	Black discolouration	0.0075 cm s <sup>-1</sup>

Table 6.2 Summary of hydraulic conductivity measurements for JG1873

For AF1875, the scans on the original surface show hydraulic conductivities within the higher range of semi pervious, with increasing depth of surface recession the hydraulic conductivity decreases to the middle range of semi pervious, shown in table 6.3.



SCAN	SURFACE WEATHERING	HYDRAULIC CONDUCTIVITY
AF1	Rough texture, black discolouration	0.010 cm s <sup>-1</sup>
AF2	Rough texture, green discolouration	0.0089 cm s <sup>-1</sup>
AF3	4 mm recession, honeycomb	0.0023 cm s <sup>-1</sup>
AF4	2 mm recession, pitted surface	0.0034 cm s <sup>-1</sup>

Table 6.3 Summary of hydraulic conductivity measurements for AF1875

On all three stones some of the original surface is covered with a black crust while the recessed surface shows orange discolouration at approximately 2 mm becoming white with the depth

and intensity of weathering features. The presence of orange discolouration on the weathered surface may indicate the deposition iron minerals weathering out from the stone, while the ‘bleaching’ of the stone may be due to the loss of ferruginous cement rendering the stone more friable.

Headstone WS1887 showed weathering features unique within this study, as surface recession revealed internal structures within the stone. Scan positions and results are shown in table 6.4.

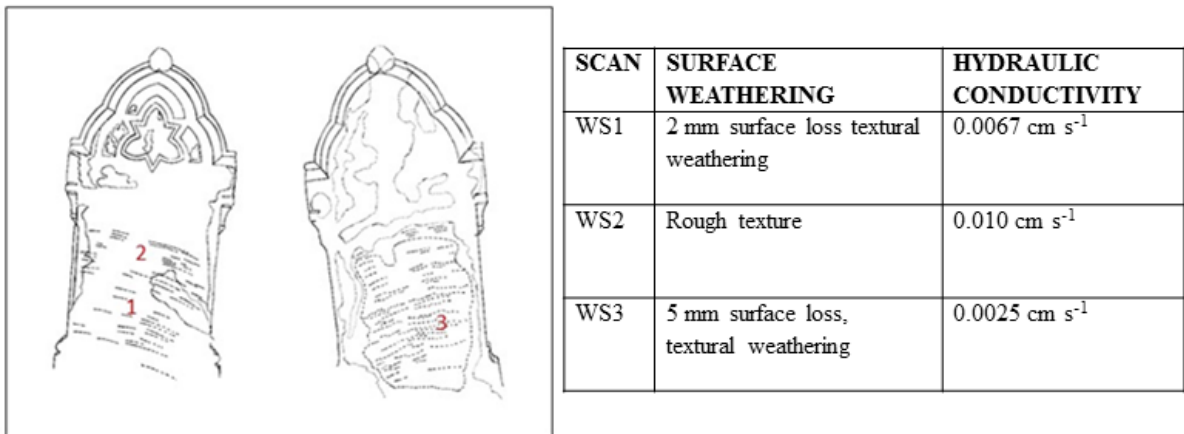
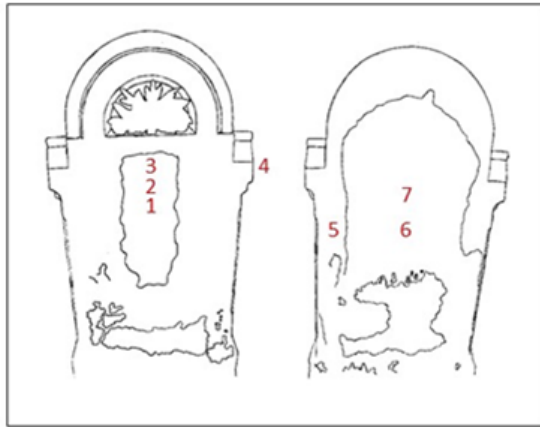


Table 6.4 Summary of hydraulic conductivity measurements for WS1887

The stone appears to have an inhomogeneous composition causing a variable vulnerability to weathering within the stone, which has created a texture of more resistant ridges with signs of granular loss of the stone in between. Hydraulic conductivities range from the high range at the surface down to the middle range of semi-pervious at 5 mm recessed between ridges.

Headstones BG1873 and GC1876 both showed higher hydraulic conductivities on areas of surface recession compared to the original surface. On BG1873 where the surface exhibits a light surface discolouration and mm scale granular surface with rounding to incised carving

the greatest increase in hydraulic conductivity is seen from the middle to high range of semi pervious as shown in table 6.5.



SCAN	SURFACE WEATHERING	HYDRAULIC CONDUCTIVITY
BG1	Light discolouration, granular texture	0.010 cm s <sup>-1</sup>
BG2	Light discolouration, granular texture	0.011 cm s <sup>-1</sup>
BG3	Minor light discolouration, rough texture	0.0048 cm s <sup>-1</sup>
BG4	Surface crust, granular loss	0.0081 cm s <sup>-1</sup>
BG5	Thin black deposit	0.0084 cm s <sup>-1</sup>
BG6	Yellow discolouration, slightly rough texture	0.0032 cm s <sup>-1</sup>
BG7	No apparent weathering	0.0018 cm s <sup>-1</sup>

Table 6.5 Summary of hydraulic conductivity measurements for BG1873

On GC1876 there is an increase in hydraulic conductivity where the surface has light discolouration and surface roughness with a further increase where the surface is recessed from the middle to high range of semi pervious, shown in table 6.6.



SCAN	SURFACE WEATHERING	HYDRAULIC CONDUCTIVITY
GC1	2 mm recessed with discolouration, granular loss	0.0079 cm s <sup>-1</sup>
GC2	Discolouration, white encrustation	0.0045 cm s <sup>-1</sup>
GC3	Light discolouration, slightly rough texture	0.011 cm s <sup>-1</sup>
GC4	Dove motif. Original white finish lost exposed surface	0.0028 cm s <sup>-1</sup>

Table 6.6 Summary of hydraulic conductivity measurements for GC1876

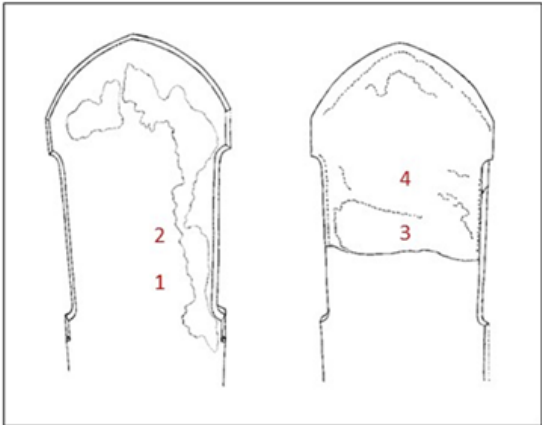
Both stones show increased hydraulic conductivity where the surface has developed a rough texture and discolouration lighter than the original surface.

Two headstone studied showed slightly pervious to impervious original surfaces: WW1881 in table 6.7, and HB1877 in table 6.8. Measurements for both stones showed that the material below the imperious surface layer is semi-pervious in comparison.



SCAN	SURFACE WEATHERING	HYDRAULIC CONDUCTIVITY
WW1	Discolouration, slight algal growth	Impervious <0.000001 cm s <sup>-1</sup>
WW2	1 mm surface recession, discolouration, surface pitting	0.0097 cm s <sup>-1</sup>
WW3	2 mm surface recession orange discolouration, pitting	0.012 cm s <sup>-1</sup>
WW4	Adjacent to surface detachment	0.0076 cm s <sup>-1</sup>

Table 6.7 Summary of hydraulic conductivity measurements for WW1881

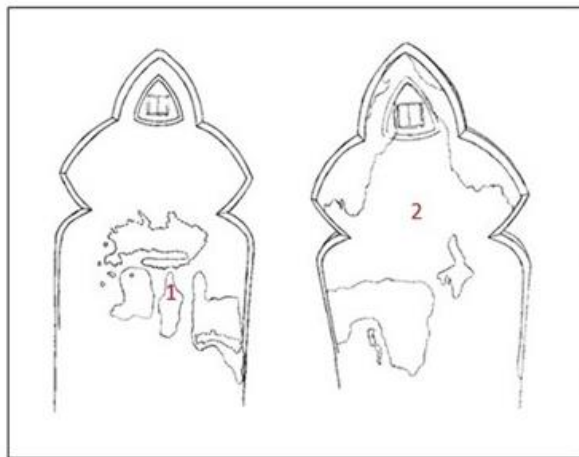


SCAN	SURFACE WEATHERING	HYDRAULIC CONDUCTIVITY
HB1	No apparent weathering	Impervious <0.000001 cm s <sup>-1</sup>
HB2	No apparent weathering	Impervious <0.000001 cm s <sup>-1</sup>
HB3	1 cm surface loss	0.0076 cm s <sup>-1</sup>
HB4	1 cm surface loss	0.011 cm s <sup>-1</sup>

Table 6.8 Summary of hydraulic conductivity measurements for HB1877

These results suggest a process by which the loss of the surface occurred; capillary rise of ground water through the stone becomes trapped at the stone surface, the resulting pressure may be the cause of the detachment and loss of the impervious surface. The surface detachment of HB1877 is a demonstration of the episodic nature of weathering, with rapid loss of material at a threshold point.

Measurements of headstone AT1850 indicate a potential limitation of this technique when applied to stone surfaces encrusted with biological material with such as algal biofilms, scan positions and results shown in table 6.9.



SCAN	SURFACE WEATHERING	HYDRAULIC CONDUCTIVITY
AT1	Algal biofilm, black discolouration	Semi-pervious
AT2	Algal biofilm, black discolouration	Semi pervious

Table 6.9 Summary of hydraulic conductivity measurements for AT1850

The use of OCT for investigating water within porous materials is based on the fact that as water displaces air in the porous network of the stone it reduces the refractive index mismatch. Water has a refractive index of 1.33, closer to that of quartz 1.54 than air. Where biological material is encrusted on the surface it may increase the humidity within the subsurface of the stone decreasing this effect, as well as absorbing some of the incident light. For AT1850 the exact position of the wetting front position is difficult to discern throughout the scan. The point

of ingress and full wetting can be determined from OCT scan images viewed in time sequence and indicate that the stone is semi-pervious with respect to hydraulic conductivity.

## 6.2 Derbyshire standing stones at Barbrook I and Gardom's edge

### 6.2a Barbrook I Stone Circle

Barbrook I is one of the best preserved stone circles in the peak district [6]. It consists of twelve stones in a rough circle with a diameter of 12.5 to 14.5 m surrounded by a rubble bank between 17 and 19 m in diameter. The circle is dominated by one large standing stone at the south-west, shown in figure 6.2.1, that is 1.04m high with eleven smaller stones between 5 and 25 cm in height. The position of the stone circle with road access within a few hundred meters enabled the transport of equipment to the site for *in situ* investigation.



Figure 6.2.1. Photograph of Barbrook I stone circle. (Grid Reference SK28432 7728, Scheduled monument list entry number 1007048)

The circle is constructed of sandstone with a lithology known locally as millstone grit, medium to coarse grained with moderately well sorted sub-angular grains.

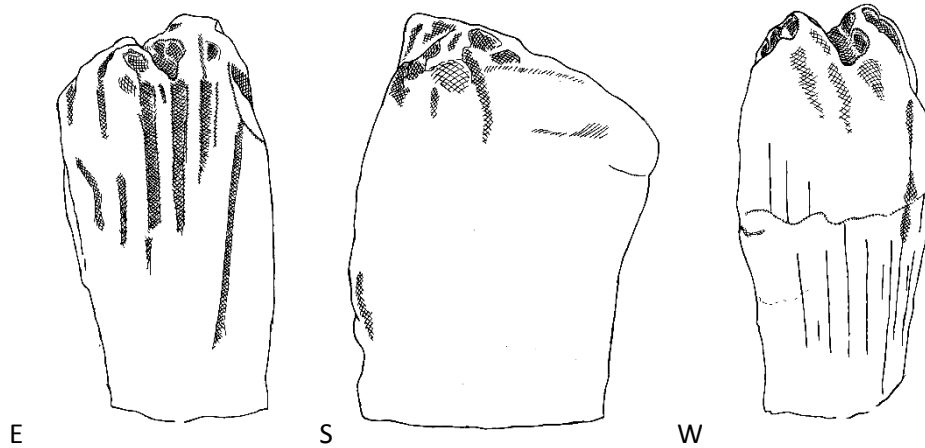


Figure 6.2.2. Schematic diagram of weathering features on Barbrook I primary stone, east, south and west faces.

Decantation flutings dissect the horizontal surface forming vertical channels on the east face of the stone. Solution runnels dissect the inclined surface of the east face and partially the west face of the stone. The runnels run in parallel down the slope and have a U-shaped channel-like cross-section following the orientation of bedding planes, a schematic diagram of the weathering feature is shown in figure 6.2.2. These planes are perpendicular to sedimentary structures in natural outcrops in the area. A wetting scan was performed with the OCT to determine the hydraulic conductivity of the stone, the scan was positioned at the centre of the south face of the primary stone.

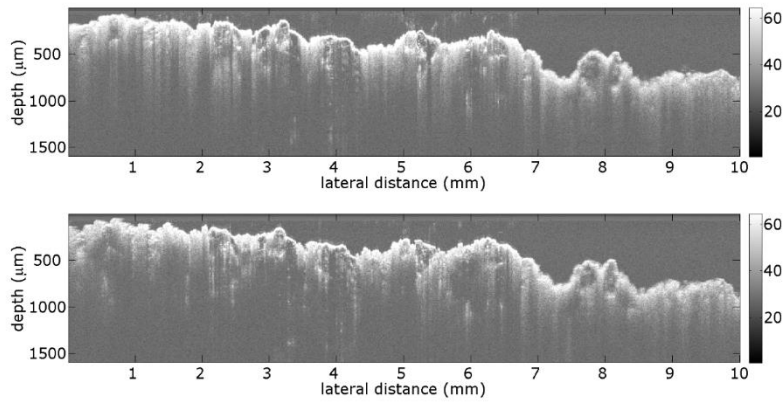


Figure 6.2.3. OCT virtual cross sections of Barbrook I scan position when (a) dry and (b) wet.

Virtual cross sectional images of the south face of the primary stone are shown in figure 6.2.3. when dry and wet. The presence of water in the sample reduces scattering as it reduces the refractive index mismatch, features can be seen to a greater depth within the stone.

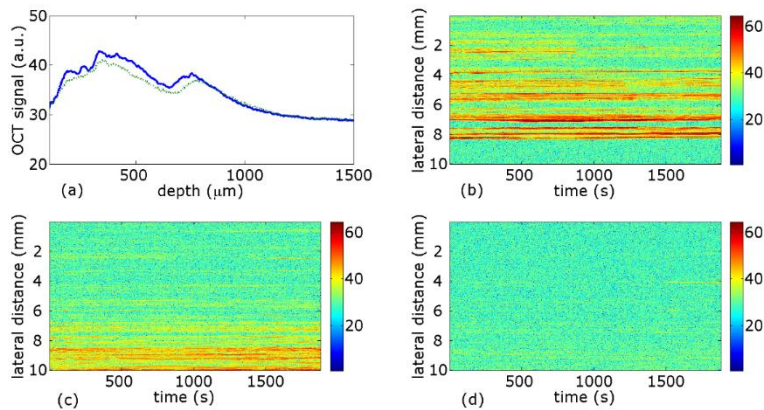


Figure 6.2.4. Barbrook I primary stone: (a) pixel intensity values averaged across the 10 mm cross section when dry (solid blue line) and wet (dotted green line); signal intensity values at depths of (b)  $\sim 400 \mu\text{m}$ , (c)  $\sim 700 \mu\text{m}$ , and (d)  $\sim 1000 \mu\text{m}$  across the lateral range of the scan over time. The OCT signals are in log scales.

Figure 6.2.4. (a) shows the decrease in pixel intensity values due to the reduction of scattering in the sandstone caused by the presence of water in the pore network. Depth scan intensity values

were averaged across the 10 mm lateral range of the cross sections when both wet and dry. The peak centred at approximately 250-300  $\mu\text{m}$  is due to scattering at the surface of the stone. The breadth of the peak is due to the rough sloped surface of the stone. Figure 6.2.4. (b) - (d) sample the signal intensity at a specific depth of 400, 700 and 1000  $\mu\text{m}$  over the duration of the measurement. Water enters at 832 s and crosses to 8.5 mm by 1876 s, showing little difference in water movement speed in the lateral direction between the different depths. The change in signal due to water cannot be detected below 1 mm. The 1044 s time to cross the lateral range of 10 mm gives a wetting scan velocity of  $0.0008 \pm 0.0001 \text{ cm s}^{-1}$ . Hydraulic conductivity in the low range of semi-pervious which is consistent with the expected value for the millstone grit lithology. Measurements were limited due to the difficulty of providing a stable and level mount base for the OCT probe while avoiding any disruption to the surface or subsurface of the ground at the site, which is uneven with loose stones and fern overgrowth. The site is in active use for ritual purposes, the karst solution basins on top surface of the primary stone are used as an offering bowl with coins, flowers and other objects being left. This technique could be used to monitor changes in hydraulic conductivity as a result of offering residues.

The millstone grit lithology has been used in other local monuments which also display similar weathering features. Barbrook I stone circle lies 2275 m to the north-north-east of the Gardom's edge monolith.

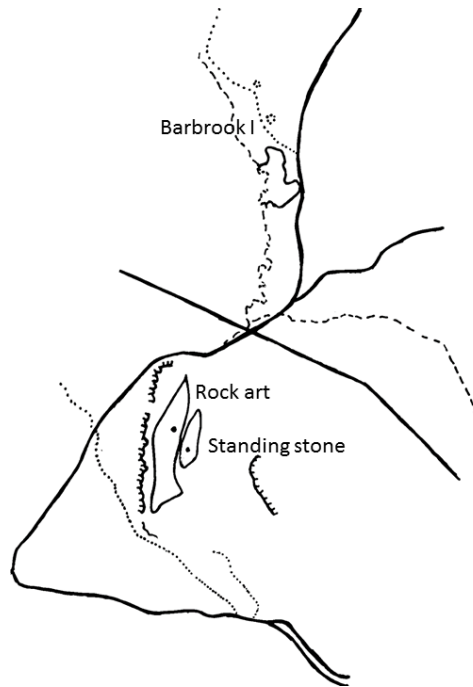


Figure 6.2.5. Map indicating locations of Barbrook I stone circle and Gardom's edge standing stone and rock art panel (1:50000 scale).

The site of the standing stone at Gardom's edge in Derbyshire is also known for an exceptional rock art panel on an earth fast boulder which has now been reinterred and replaced with a fiberglass replica to protect it from sub-aerial weathering processes.

### **6.2b Gardom's Edge monolith**

The monolith at Gardom's Edge on the Eastern Moors Estate is sited in an area of much early human activity ranging from a low density of Mesolithic microliths, rock art, Neolithic enclosures, and Bronze Age field systems. It is likely that the stone is contemporary with the rock art or erected during the establishment of early Bronze Age ritual monuments that have been found across the Eastern Moors Estate associated with periods of cultivation [7].

The 2.2 m high Gardom's stone consists of sandstone with a lithology known locally as millstone grit, medium to coarse grained with moderately well sorted sub-angular grains.



Figure 6.2.6. Photograph of Gardom's edge standing stone (Grid Reference SK28432 77268, Scheduled monument list entry number 1007048)

In its current position sedimentary planes within the stone are near vertical, the east and west face of the monolith being bedding planes. These planes are perpendicular to sedimentary structures in natural outcrops in the area, as is the case with the primary standing stone of Barbrook I. The stone is most likely in its original orientation, indicated by the position and severity of weathering features, and may be intentionally astronomically aligned [8].

Visual inspection and a weathering survey have revealed effects of possible subsidence and erosion. A gradient survey of the north facing side of the standing stone was performed, nine locations were surveyed with regards to their gradient and strike perpendicular to the gradient, giving an average gradient  $(58.3 \pm 2.9)^\circ$  of and a strike of  $(92.0 \pm 2.1)^\circ$ . The stone seems to lean towards West which has been estimated to about  $(4 \pm 4)^\circ$ . If the stone was set up with a tilt, or if even the north facing side of the stone had a slightly steeper tilt cannot be determined at this time. The alignment of the

stone indicates its possible use as a seasonal sundial, casting a shadow to mark the seasons of the year [8].

Erosion has clearly shaped this stone with karstic surface features present such as solution pits, solution runnels and decantation flutings, produced by rainwater pooling on flat surfaces and flowing down rock faces. The type and intensity of these features is influenced by the orientation of the rock face while these erosional processes are in action.

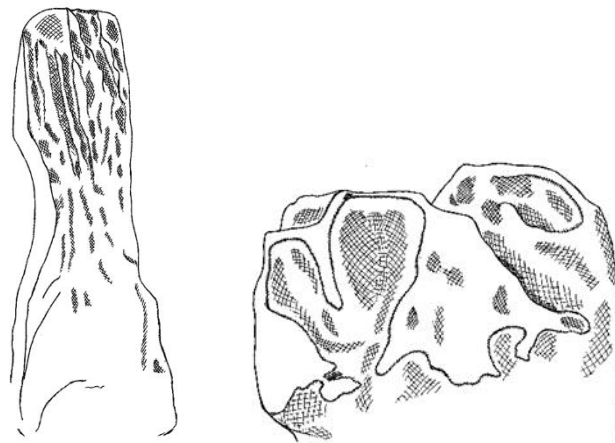


Figure 6.2.7. Schematic diagram of weathering features on Gardom's edge standing stone north face and top surface.

The systematic mapping of the type, scale, and intensity of weathering forms provides an indication of the time scale over which dissolution processes have acted in their current orientation. Solution pits have developed across the flat surface at the top of the sandstone, rounded and sub rounded in shape with sub vertical to convex sidewalls and irregular floors. Pits are laterally linked with sandstone interfluvial ridges forming saddle shaped ridges. Decantation flutings dissect the sub-vertical surfaces forming vertical channels on the south face of the stone. Solution runnels dissect the inclined surface of the north face of the stone. The runnels run in parallel down the slope and have a U-shaped channel like cross-section. The systematic mapping of weathering features

indicates that the stone has been at its current orientation for a significant period. All dissolution features are consistent with erosional processes at this orientation, perpendicular to natural outcrops in the area. The shape and orientation of the stone are unique and point towards an intentional erection. The weathering evidence and packing stones suggest that the stone has not been moved since its likely emplacement in the late Neolithic period. The present subsidence will only marginally have altered the gradient of the north facing side of the stone.

The location in a wooded area and limited access over rough ground prevented the transport of equipment required for in situ OCT investigation, while the instrument itself is easily transportable, the support equipment (such as the generator) required could not be carried over the terrain to the site.

### **6.3 Rock art panels in Northumberland**

Rock art monuments provide a link to our ancient cultural pasts; they possess seeming permanence but are sensitive to their environment. Rapid changes due to anthropogenic land use and climatic variation will cause damage and decay over time. Knowledge of the characteristics of the host rock is vital to inform decisions to ameliorate the impact of decay processes. Almost all British rock art is abstract, created by Neolithic and Bronze age people between 4000 - 6000 years ago, approximately 2500 carved surfaces or 'panels' have been recorded in England on exposed outcrops or earth-fast boulders.

There is no mention of rock art in historical record until the 17th century with references to marks made on stones at sites in Ireland, with cup and ring rock art first 'discovered' in the 1820's in Northumberland. Since 1979 many rock art sites have been protected as Scheduled Monuments under the Ancient Monuments and Archaeological Areas Act [9]. In action since 1998, the Heritage at Risk Register now includes scheduled monuments and conservation areas known to be at risk as a result of neglect, decay or inappropriate development.

Rock art in Northumberland has been comprehensively described on Web Access to Rock Art: the Beckensall Archive of Northumberland Rock Art [10], the website ERA England's rock art [11] and the independent society 'the megalithic portal' [12] and in books such as British Prehistoric Rock Art by Stan Beckensall [13].

The majority of rock art panels appear on outcrops of the 'Fell Sandstone Group', a lithostratigraphical division within the Mississippian Subsystem of the Carboniferous. The Group is variable in thickness and has been estimated to be more than 330 m thick in south Northumberland. It is composed of lenticular or sheet-like bodies of cross stratified quartz arenites

which alternate with shales and ripple laminated siltstones. The sands and silts which now make up the different rock types appear to have been laid down in a complex deltaic environment [14].

The sites selected for this study are rock art panels at Chatton Park and Roughting Linn, they represent some of the best examples of prehistoric rock art. Despite a preliminary visit to the rock art panel at Weetwood Moor it was not possible to gain permission to further access the site.

Both the sites studied were included in the 2014 Heritage at Risk Register [15]. The condition of Chatton Park (List entry: 1002907) is described as generally satisfactory but with significant localised problems. The principle vulnerability at this site is considered to be stock erosion, having a moderate effect, the panels are within a field used for animal grazing. The trend in the condition of the site is listed as unknown. The condition of Roughting Linn (List entry: 1006601) is described as generally unsatisfactory with major localised problems. The principle vulnerability of the site is described as scrub and tree growth having a moderate effect, with a declining trend.

### **6.3a Chatton Park**

#### **6.3a.1 Rock Art Motifs**

The site is located at the top of a hill of altitude 179 m, the primary panel at the site is exposed in an irregular shape approximately  $11.7 \times 6 \text{ m}^2$  in area. The bedding plane has a dip of  $10^\circ$  to the north east.

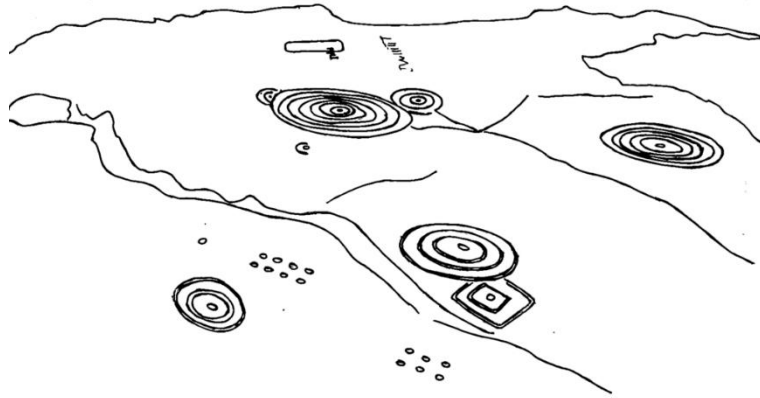


Figure 6.3a.1 Diagram of rock art motifs at Chatton Park primary panel



Figure 6.3a.2 orange discoloration to the surface of rock art motifs at Chatton Park primary panel

The motifs and the panel surface have areas of discolouration, concentrated where water collects in channels and pools on the surface. The orange colour indicates the deposition of iron minerals at the surface which may affect the perviousness of the surface.

The representative grain size distribution for the stone was determined from two OCT volume scans over different areas of  $6 \times 6$  mm using the imaging protocol described in chapter 2.



Figure 6.3a.2 Concentric ring and square motif adjacent to channel

Volume scan 1 was performed on the host rock adjacent to the concentric ring and square motif shown in figure 6.3a.2. Within this volume 965 grains were identified, the size distribution of which is shown in figure 6.3a.3.

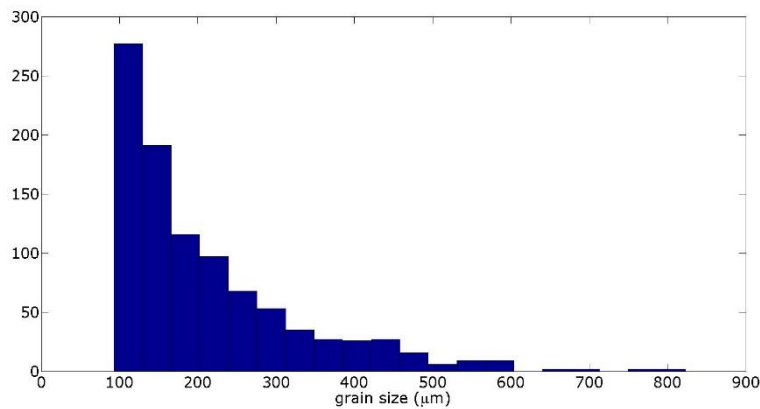


Figure 6.3a.3 Representative grain size distribution for Chatton Park volume scan 1

The minimum grain size detected was  $93 \mu\text{m}$ , the maximum  $823 \mu\text{m}$  with a mean of  $211 \mu\text{m}$  and standard deviation of  $120$ .

Volume scan 2 was performed on the secondary set of concentric rings of the primary motif, on the peak between the second and third ring troughs. Within this volume 981 grains were identified, the size distribution of which is shown in figure 6.3a.4.

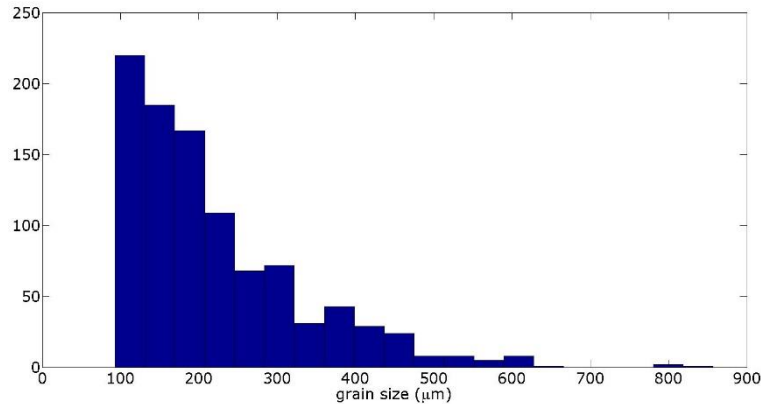


Figure 6.3a.4 Representative grain size distribution for Chatton Park volume scan 2

The minimum grain size detected was  $9.2\ \mu\text{m}$ , the maximum  $856\ \mu\text{m}$  with a mean of  $221\ \mu\text{m}$  and standard deviation of 114. The detected grain sizes from both scans are in the range of very fine to coarse sand, dominated by grains in the range of fine sand. The grain size distributions of the two scans are similar, there is no indication of the fracturing of grains due to the formation of the motifs.

In order to determine whether the hydraulic conductivity was affected by the modification of the stone by the formation of the motifs, a control scan was performed on the unmodified outcrop adjacent to the concentric ring and square motif; Chatton Park wetting scan 1 (CPWS1). The surface appears intact with no surface detachment or discolouration present.

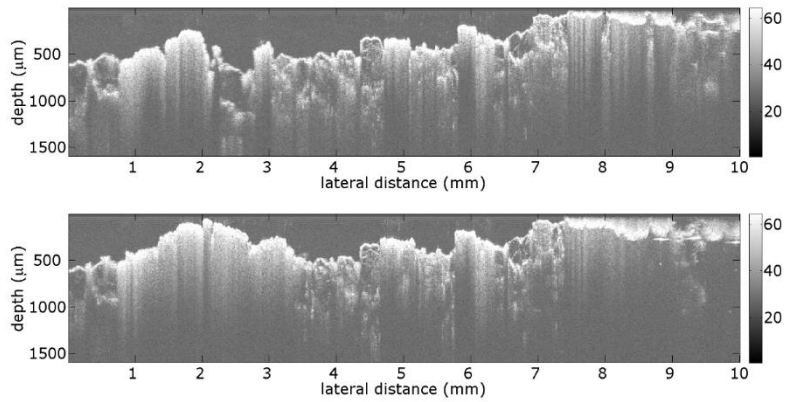


Figure 6.3a.5. OCT virtual cross sections of CPWS1 scan position when (a) dry and (b) wet. Towards the right of the images, the probe was too close to the surface and the surface of the rock is seen to fold back into the image.

Virtual cross sectional images of the scan position for CPWS1 are shown in figure 6.3a.5. when dry and wet. The presence of water in the sample reduces scattering as it reduces the refractive index mismatch, features can be seen to a greater depth within the stone.

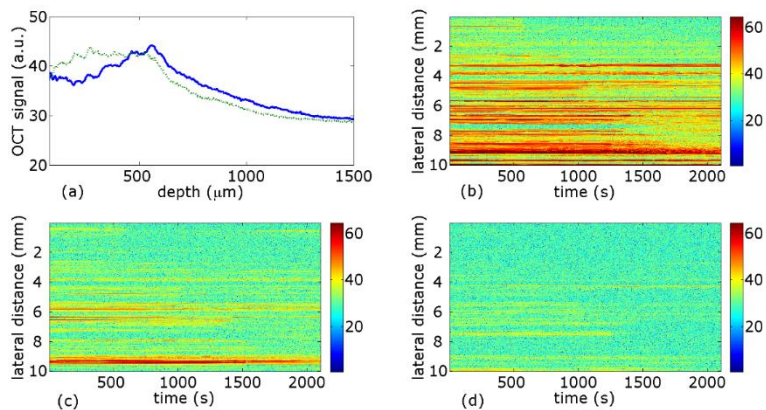


Figure 6.3a.6. CPWS1 : (a) pixel intensity values averaged across the 10 mm cross section when dry (solid blue line) and wet (dotted green line); signal intensity values at depths of (b)  $\sim 400 \mu\text{m}$ , (c)  $\sim 700 \mu\text{m}$ , and (d)  $\sim 1000 \mu\text{m}$  across the lateral range of the scan over time. The OCT signals are in log scales.

Figure 6.3a.6 (a) shows the decrease in pixel intensity values due to the reduction of scattering in the sandstone caused by the presence of water in the pore network. Depth scan intensity values were averaged across the 10 mm lateral range of the cross sections when both wet and dry. The peak centred at approximately 500-550  $\mu\text{m}$  is due to scattering at the surface of the stone. The breadth of the peak is due to the rough sloped surface of the stone, the shift is due to a slight movement of the probe towards the surface during the scan, no lateral movement occurred. Fig 6.3a.6 (b) – (d) sample the signal intensity at a specific depth of 400, 700 and 1000  $\mu\text{m}$  over the duration of the measurement. Water enters at 461 s crossing the lateral range of the scan by 1239 s, showing little difference in water movement speed in the lateral direction between the different depths. The change in signal due to water cannot be detected below 1 mm. The 778 s time to cross the lateral range of the 10 mm gives a wetting front velocity of  $0.0013 \pm 0.0001 \text{ cm s}^{-1}$ . The hydraulic conductivity in the low middle range of semi-pervious.

The dominant motif of the panel is an unusually complex motif of seven concentric rings around the central cup; the outer three rings extending above in a semi-circle around a second cup, with additional third lower cup with three concentric rings.



Figure 6.3a.7 Complex cup and ring motif

Chatton Park wetting scan 2 (CPWS2) was performed with the OCT probe positioned in the trough of fourth ring from centre cup of motif. The trough is rounded and there is a rough channel running perpendicular to it with significant orange discolouration to the surface.

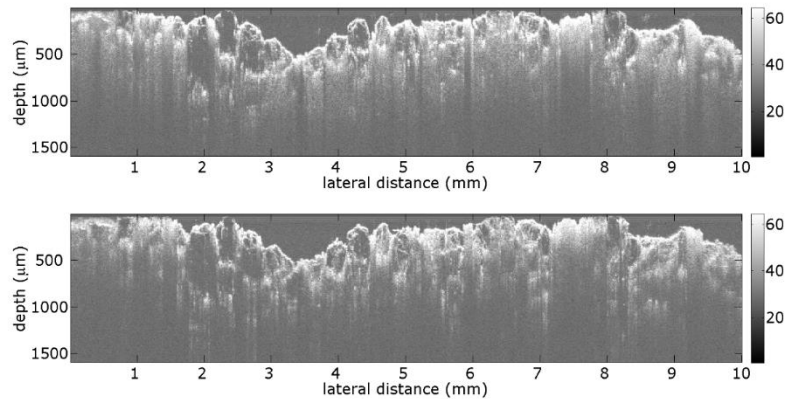


Figure 6.3a.8. OCT virtual cross sections of CPWS2 scan position when (a) dry and (b) wet.

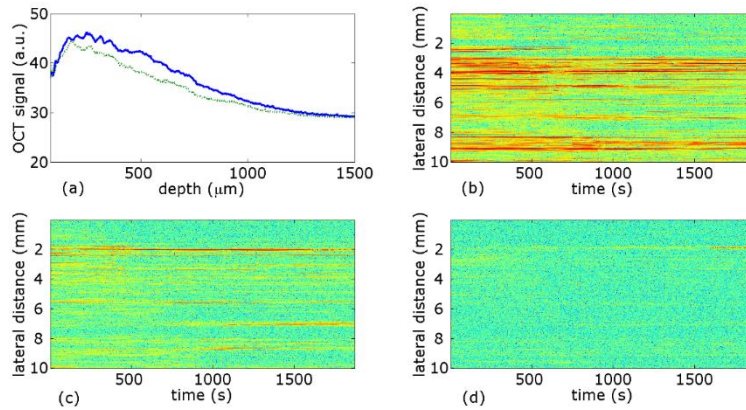


Figure 6.3a.9. CPWS2: (a) pixel intensity values averaged across the 10 mm cross section when dry (solid blue line) and wet (dotted green line); signal intensity values at depths of (b)  $\sim 400 \mu\text{m}$ , (c)  $\sim 700 \mu\text{m}$ , and (d)  $\sim 1000 \mu\text{m}$  across the lateral range of the scan over time. The OCT signals are in log scales.

The peak in figure 6.3a.9 (a) is centered at approximately  $200\text{--}250 \mu\text{m}$  is due to scattering at the surface of the stone. The breadth of the peak is due to the rough sloped surface of the stone shown in figure 6.3b.8. Figure 6.3a.9. (b) – (d) sample the signal intensity at a specific depth of  $400$ ,  $700$  and  $1000 \mu\text{m}$  over the duration of the measurement. Water enters at  $317 \text{ s}$  crossing the lateral range of the scan by  $945 \text{ s}$ . The  $628 \text{ s}$  time to cross the lateral range of  $10 \text{ mm}$  gives a wetting front velocity of  $0.0016 \pm 0.0001 \text{ cm s}^{-1}$ . The hydraulic conductivity at this point is in the low middle range of semi-pervious.

Chatton Park wetting scan 3 (CPWS3) was performed with the OCT probe positioned on the peak between third and fourth ring from central cup of motif. The surface shows no discolouration at this point.

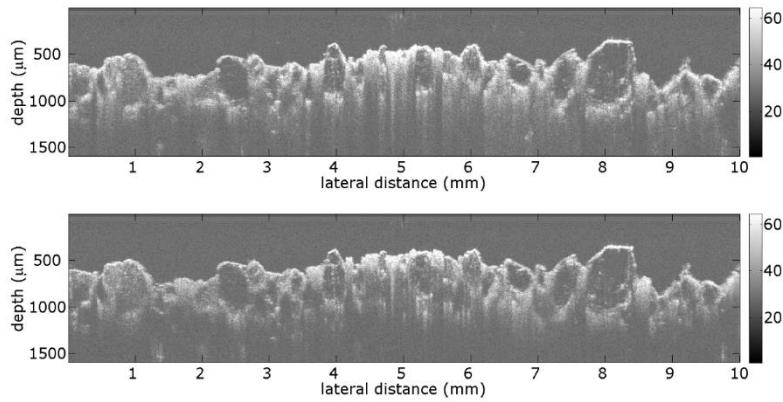


Figure 6.3a.10. OCT virtual cross sections of CPWS3 scan position when (a) dry and (b) wet.

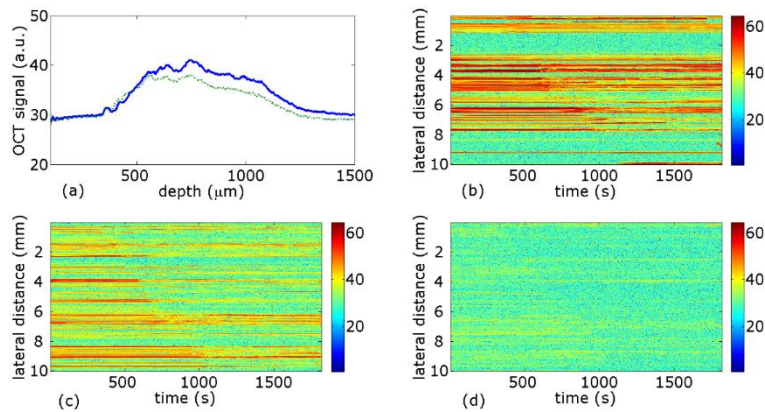


Figure 6.3a.11. CPWS3: (a) pixel intensity values averaged across the 10 mm cross section when dry (solid blue line) and wet (dotted green line); signal intensity values at depths of (b)  $\sim 400 \mu\text{m}$ , (c)  $\sim 700 \mu\text{m}$ , and (d)  $\sim 1000 \mu\text{m}$  across the lateral range of the scan over time. The OCT signals are in log scales.

The peak in figure 6.3a.11 (a) centered at approximately  $600\text{-}650 \mu\text{m}$  is due to scattering at the surface of the stone. The breadth of the peak is due to the rough sloped surface of the stone shown in figure 6.3b.10. Figure 6.3a.11. (b) – (d) sample the signal intensity at a specific depth of 400, 700 and 1000  $\mu\text{m}$  over the duration of the measurement. Water enters at 280 s crossing the lateral range of the scan by 1068 s. The 788 s time to cross the lateral range of 10 mm gives a wetting

front velocity of  $0.0013 \pm 0.0001 \text{ cm s}^{-1}$ . The hydraulic conductivity at this point is in the low middle range of semi-pervious.

Chatton Park wetting scan 4 (CPWS4) was performed with the OCT probe positioned on the recessed rounded area of peak between third and fourth ring from central cup of motif, approximately 10 cm above previous scan. The surface has significant orange discolouration and surface recession of  $\sim 4 \text{ mm}$ .

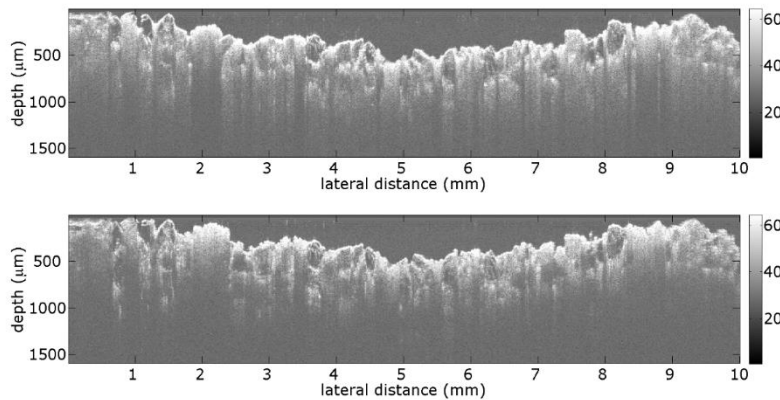


Figure 6.3a.12. OCT virtual cross sections of CPWS4 scan position when (a) dry and (b) wet.

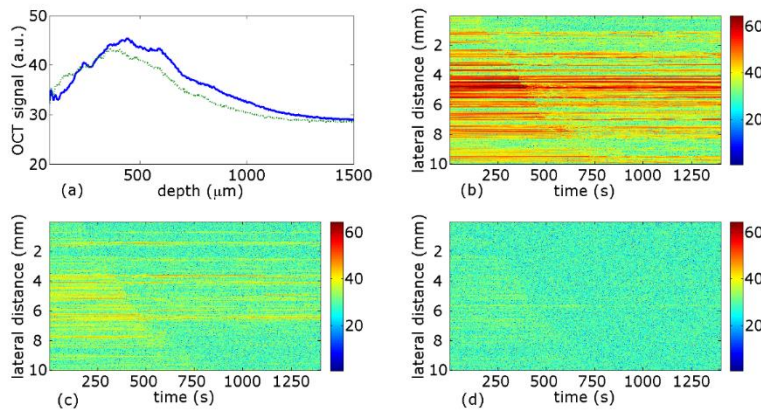


Figure 6.3a.13. CPWS4: (a) pixel intensity values averaged across the 10 mm cross section when dry (solid blue line) and wet (dotted green line); signal intensity values at depths of (b)  $\sim 400 \mu\text{m}$ , (c)  $\sim 700 \mu\text{m}$ , and (d)  $\sim 1000 \mu\text{m}$  across the lateral range of the scan over time. The OCT signals are in log scales.

The peak in figure 6.3a.13 (a) is centered at approximately 450-500  $\mu\text{m}$  is due to scattering at the surface of the stone. The breadth of the peak is due to the rough sloped surface of the stone shown in figure 6.3a.12. Figure 6.3a.13. (b) – (d) sample the signal intensity at a specific depth of 400, 700 and 1000  $\mu\text{m}$  over the duration of the measurement. Water enters at 156 s crossing the lateral range of the scan by 755 s. The 599 s time to cross the lateral range of 10 mm gives a wetting front velocity of  $0.0017 \pm 0.0001 \text{ cm s}^{-1}$ . The hydraulic conductivity at this point is in the low middle range of semi-pervious.



Figure 6.3a.14 Secondary cup and ring set of complex motif

Chatton Park wetting scan 5 (CPWS5) was performed on the lower secondary cup and ring set of the motif, with the OCT probe positioned on the peak between the cup and first ring from the centre. The surface shows no discolouration at this point.

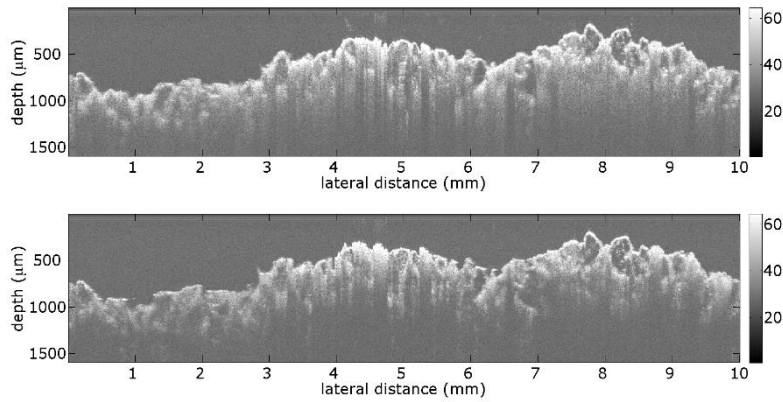


Figure 6.3a.15. OCT virtual cross sections of CPWS5 scan position when (a) dry and (b) wet.

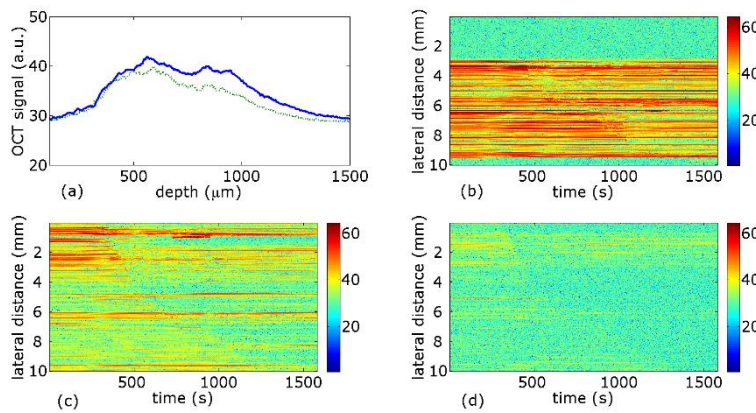


Figure 6.3a.16. CPWS5: (a) pixel intensity values averaged across the 10 mm cross section when dry (solid blue line) and wet (dotted green line); signal intensity values at depths of (b)  $\sim 400 \mu\text{m}$ , (c)  $\sim 700 \mu\text{m}$ , and (d)  $\sim 1000 \mu\text{m}$  across the lateral range of the scan over time. The OCT signals are in log scales.

The peak in figure 6.3a.16 (a) centered at approximately  $550\text{-}600 \mu\text{m}$  is due to scattering at the surface of the stone. The breadth of the peak is due to the rough sloped surface of the stone shown in figure 6.3a.15. Figure 6.3a.16. (b) – (d) sample the signal intensity at a specific depth of  $400$ ,  $700$  and  $1000 \mu\text{m}$  over the duration of the measurement. Water enters at  $275 \text{ s}$  crossing the lateral range of the scan by  $1166 \text{ s}$ . The  $891 \text{ s}$  time to cross the lateral range of  $10 \text{ mm}$  gives a wetting

front velocity of  $0.0017 \pm 0.0001 \text{ cm s}^{-1}$ . The hydraulic conductivity at this point is in the low middle range of semi-pervious.

Chatton Park wetting scan 6 (CPWS6) was performed on the lower secondary cup and ring set of the motif, with the OCT probe positioned in the trough of second ring from centre of third cup. The surface shows a slight orange discolouration at this point.

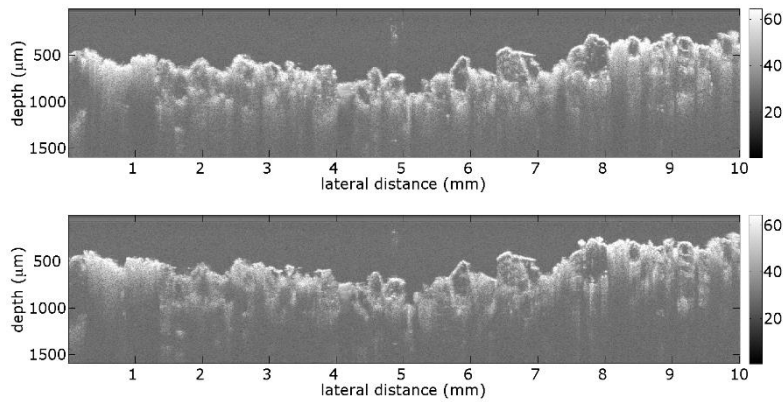


Figure 6.3a.17. OCT virtual cross sections of CPWS6 scan position when (a) dry and (b) wet.

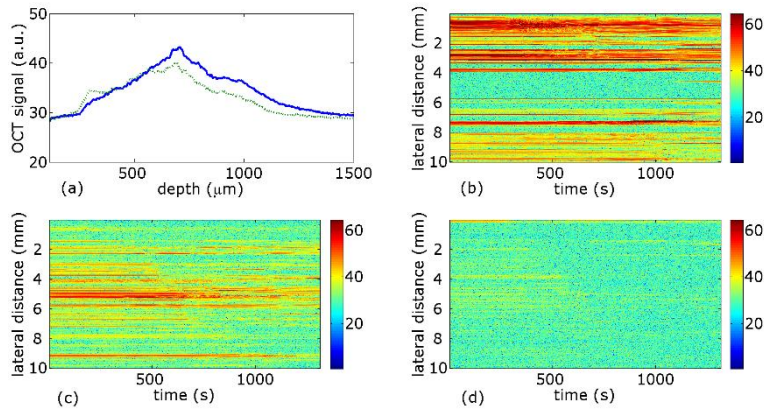


Figure 6.3a.18. CPWS6: (a) pixel intensity values averaged across the 10 mm cross section when dry (solid blue line) and wet (dotted green line); signal intensity values at depths of (b)  $\sim 400 \mu\text{m}$ , (c)  $\sim 700 \mu\text{m}$ , and (d)  $\sim 1000 \mu\text{m}$  across the lateral range of the scan over time. The OCT signals are in log scales.

The peak in figure 6.3a.18 (a) centered at approximately 700-750  $\mu\text{m}$  is due to scattering at the surface of the stone. The breadth of the peak is due to the rough sloped surface of the stone shown in figure 6.3b.17. Figure 6.3a.18. (b) – (d) sample the signal intensity at a specific depth of 400, 700 and 1000  $\mu\text{m}$  over the duration of the measurement. Water enters at 270 s crossing the lateral range of the scan by 996 s. The 726 s time to cross the lateral range of 10 mm gives a wetting front velocity of  $0.0014 \pm 0.0001 \text{ cm s}^{-1}$ . The hydraulic conductivity at this point is in the low middle range of semi-pervious.

Chatton Park wetting scan 7 (CPWS7) was performed with the OCT positioned on the peak between second and third ring troughs from centre of third cup. The scan position is adjacent to two areas of lichen encrustation and shows slight orange discolouration.

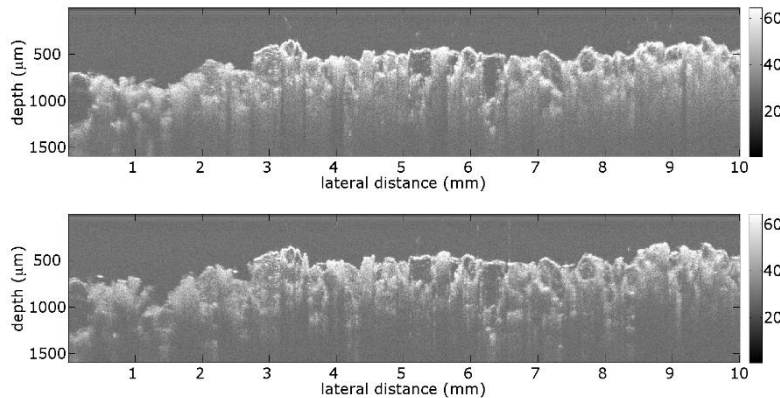


Figure 6.3a.19. OCT virtual cross sections of CPWS7 scan position when (a) dry and (b) wet.

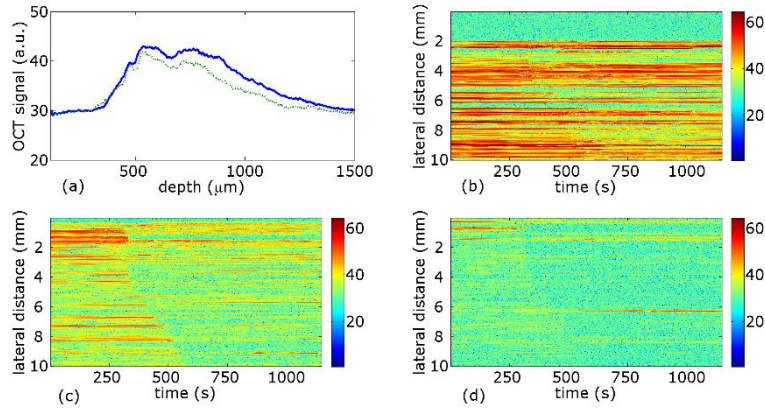


Figure 6.3a.20. CPWS7: (a) pixel intensity values averaged across the 10 mm cross section when dry (solid blue line) and wet (dotted green line); signal intensity values at depths of (b)  $\sim 400 \mu\text{m}$ , (c)  $\sim 700 \mu\text{m}$ , and (d)  $\sim 1000 \mu\text{m}$  across the lateral range of the scan over time. The OCT signals are in log scales.

The peak in figure 6.3a.20 (a) centered at approximately  $550\text{-}600 \mu\text{m}$  is due to scattering at the surface of the stone. The breadth of the peak is due to the rough sloped surface of the stone shown in figure 6.3a.19. Figure 6.3a.20. (b) – (d) sample the signal intensity at a specific depth of 400, 700 and  $1000 \mu\text{m}$  over the duration of the measurement. Water enters at 272 s, crossing the lateral range of the scan by 556 s. The 284 s time to cross the lateral range of 10 mm gives a wetting front velocity of  $0.0035 \pm 0.0001 \text{ cm s}^{-1}$ . The hydraulic conductivity at this point is in the middle range of semi-pervious.



Figure 6.3a.21 Domino motif of cup marks

Chatton Park wetting scan 8 (CPWS8) was performed with the OCT probe positioned within the cup at the bottom right of the “domino” motif. The cups of this motif appear shallow and rounded with surface detachment of scales ~1 mm thick occurring within the depressions. There is an area of lichen encrustation to the side of the motif.

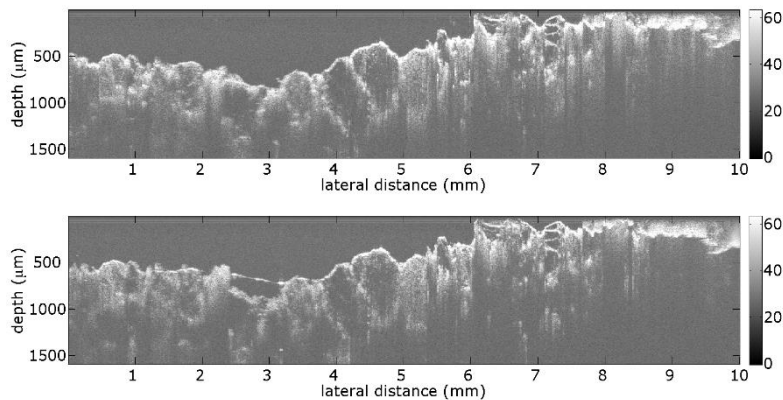


Figure 6.3a.22. OCT virtual cross sections of CPWS8 scan position when (a) dry and (b) wet.

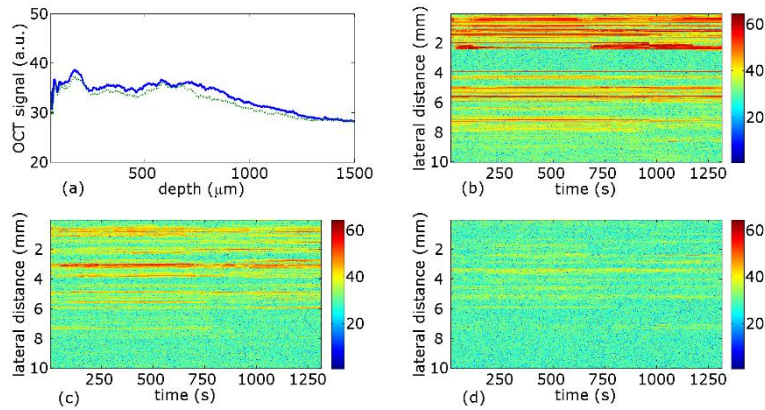


Figure 6.3a.23. CPWS8: (a) pixel intensity values averaged across the 10 mm cross section when dry (solid blue line) and wet (dotted green line); signal intensity values at depths of (b)  $\sim 400 \mu\text{m}$ , (c)  $\sim 700 \mu\text{m}$ , and (d)  $\sim 1000 \mu\text{m}$  across the lateral range of the scan over time. The OCT signals are in log scales.

The peak in figure 6.3a.23 (a) is centered at approximately 100-150  $\mu\text{m}$  is due to scattering at the surface of the stone. The breadth of the peak is due to the rough sloped surface of the stone shown in figure 6.3a.22. Fig 6.3a.23. (b) – (d) sample the signal intensity at a specific depth of 400, 700 and 1000  $\mu\text{m}$  over the duration of the measurement. Water enters at 635 s, crossing the lateral range of the scan by 1215 s. The 581 s time to cross the lateral range of 10 mm gives a wetting front velocity of  $0.0017 \pm 0.0001 \text{ cm s}^{-1}$ . The hydraulic conductivity at this point is in the low middle range of semi-pervious.

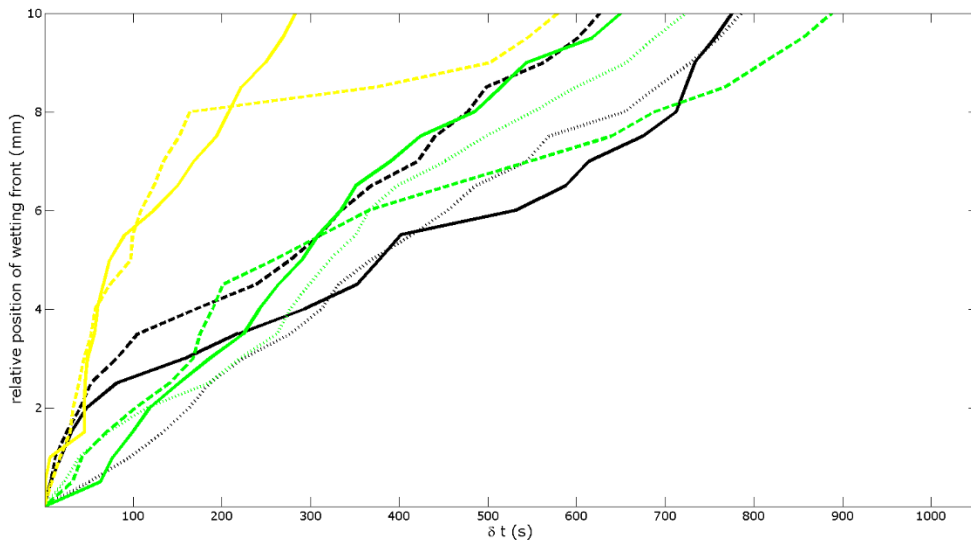


Figure 6.3a.24 Position of the wetting front over time for CPWS1 (black solid line), CPWS2 (black dashed line), CPWS3 (black dotted line), CPWS4 (green solid line), CPWS5 (green dashed line), CPWS6 (green dotted line), CPWS7 (yellow solid line), CPWS8 (yellow dashed line).

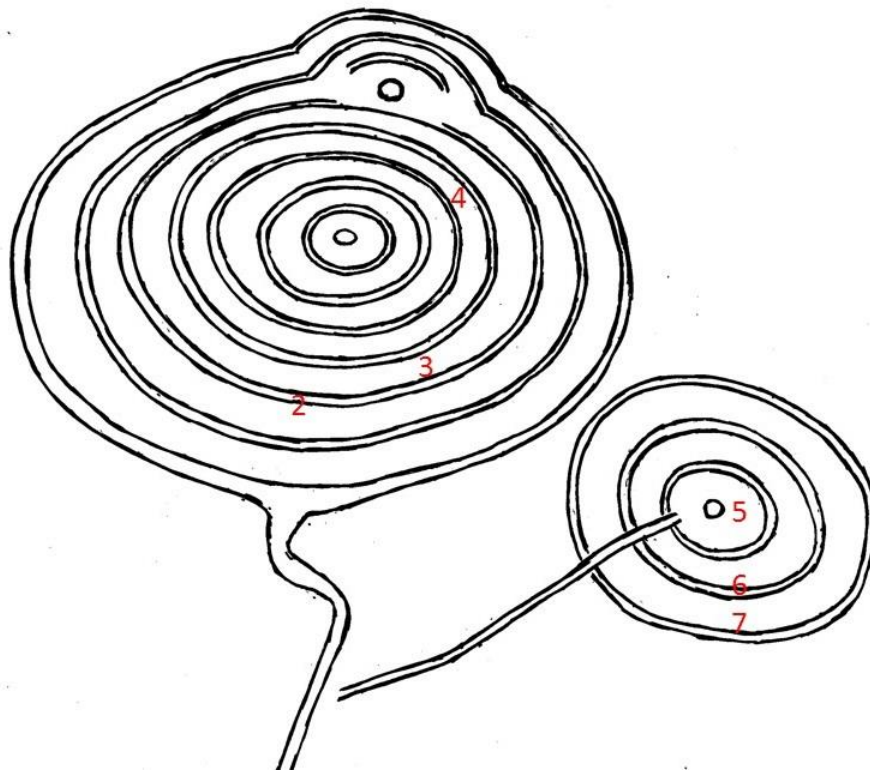


Figure 6.3a.25 Diagram of wetting scan positions on the primary motif

<b>SCAN</b>	<b>POSITION</b>	<b>SURFACE WEATHERING</b>	<b>HYDRAULIC CONDUCTIVITY</b>
CP1	Unmodified outcrop		0.0013 cm s <sup>-1</sup>
CP2	Trough of motif	Rounding, significant orange discolouration	0.0016 cm s <sup>-1</sup>
CP3	Peak of motif		0.0013 cm s <sup>-1</sup>
CP4	Peak of motif	Rounding, significant orange discolouration, surface recession (4 mm)	0.0017 cm s <sup>-1</sup>
CP5	Peak of motif		0.0017 cm s <sup>-1</sup>
CP6	Trough of motif	Slight orange discolouration	0.0014 cm s <sup>-1</sup>
CP7	Peak of motif	Adjacent to lichen encrustation, slight orange discolouration	0.0035 cm s <sup>-1</sup>
CP8	Domino cup	Rounding, detachment of surface flakes (1 mm)	0.0017 cm s <sup>-1</sup>

Table 6.3a.1 Summary of wetting scan results

The positions of measurements of the primary motif are shown in figure 6.3a.25, and the results of all wetting scans are summarised in table 6.3a.1. The panel surface is a bedding plane of the outcropping sandstone, the intensity of weathering features is consistent across the panel, with rounding and surface detachment of ~1 mm scales. There is little variation in the hydraulic conductivity across the rock art panel or between the peaks and troughs of the motifs with a mean hydraulic conductivity of 0.0018 cm s<sup>-1</sup> and a standard deviation of 0.0007, with a measurement

uncertainty of  $0.001 \text{ cm s}^{-1}$ . The presence of orange discolouration due to the deposition of iron minerals on the stone does not affect the hydraulic conductivity of the surface.

The measurement performed in proximity to lichen encrustation shows a higher value hydraulic conductivity, which may indicate an increased bioreceptivity of the panel at this point.

### 6.3a.2 Historical graffiti to the panel

An area of the panel has been defaced by an 1860 graffiti, the incised carving of J. W. Willet appears to have been created with stone masonry tools. The original presumably crisp carving has been significantly rounded in some areas.



Figure 6.3a.24 Historical Graffiti

The position of the J.W.W. inscription overlays a square motif of the original rock art at the second less precisely carved W. The hydraulic conductivity was measured in each of the incised letters which show a varying degree of rounding and apparent surface recession.



Figure 6.3a.25 OCT scan positions on historical graffiti.

Chatton Park wetting scan 9 (CPWS9) was performed with the OCT probe positioned in the incised J in the centre of the straight, the carving is clear but there is rounding to extremities of letter.

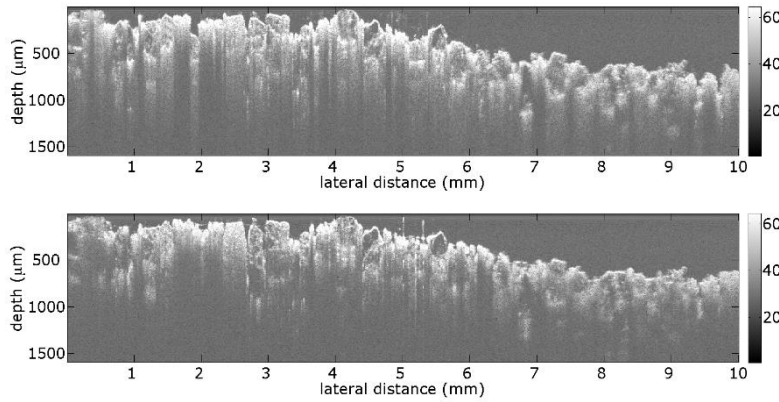


Figure 6.3a.26. OCT virtual cross sections of CPWS9 scan position when (a) dry and (b) wet.

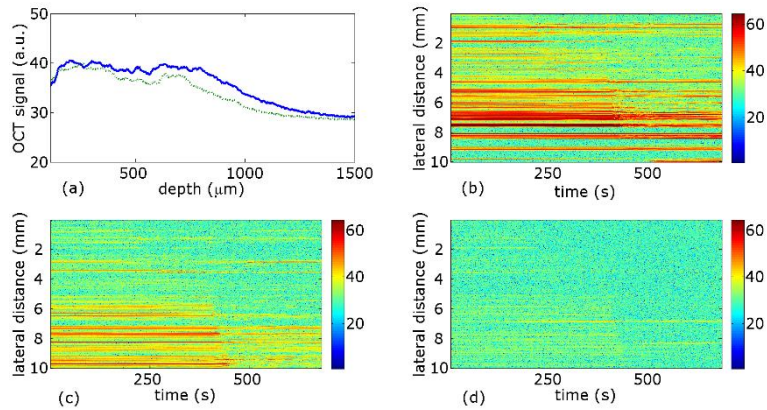


Figure 6.3a.27. CPWS9: (a) pixel intensity values averaged across the 10 mm cross section when dry (solid blue line) and wet (dotted green line); signal intensity values at depths of (b)  $\sim 400 \mu\text{m}$ , (c)  $\sim 700 \mu\text{m}$ , and (d)  $\sim 1000 \mu\text{m}$  across the lateral range of the scan over time. The OCT signals are in log scales.

The peak in figure 6.3a.27 (a) centered at approximately  $100\text{-}150 \mu\text{m}$  is due to scattering at the surface of the stone. The breadth of the peak is due to the rough sloped surface of the stone shown in figure 6.3b.26. Figure 6.3a.27. (b) – (d) sample the signal intensity at a specific depth of 400, 700 and  $1000 \mu\text{m}$  over the duration of the measurement. Water enters at 310 s, crossing the lateral range of the scan by 449 s. The 139 s time to cross the lateral range of 10 mm gives a wetting front velocity of  $0.0071 \pm 0.0005 \text{ cm s}^{-1}$ . The hydraulic conductivity at this point is in the high range of semi-pervious.

Chatton Park wetting scan 10 (CPWS10) was performed with the OCT probe positioned in the incised “W” in the centre of the right straight, the carving is clear but there is rounding and surface loss to the lower extremities of letter.

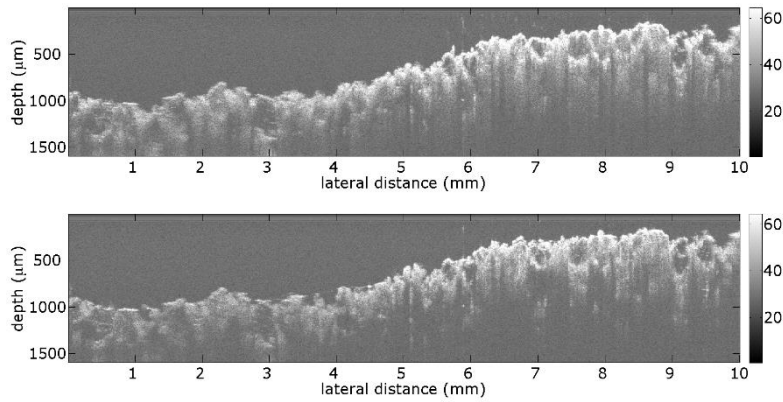


Figure 6.3a.28. OCT virtual cross sections of CPWS10 scan position when (a) dry and (b) wet.

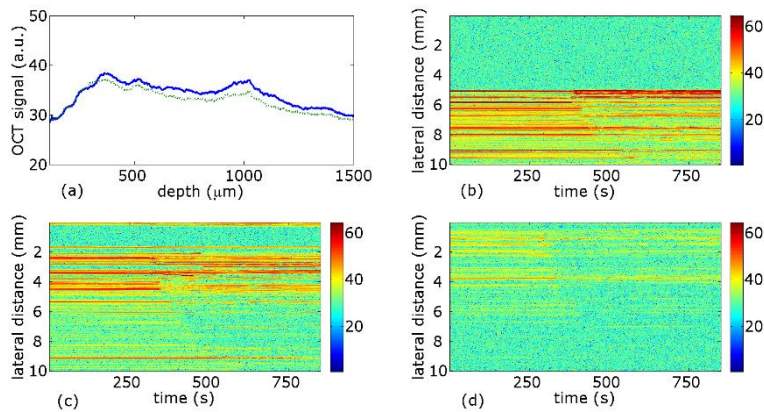


Figure 6.3a.29. CPWS10: (a) pixel intensity values averaged across the 10 mm cross section when dry (solid blue line) and wet (dotted green line); signal intensity values at depths of (b)  $\sim 400 \mu\text{m}$ , (c)  $\sim 700 \mu\text{m}$ , and (d)  $\sim 1000 \mu\text{m}$  across the lateral range of the scan over time. The OCT signals are in log scales.

The peak in figure 6.3a.29 (a) centered at approximately  $300\text{-}350 \mu\text{m}$  is due to scattering at the surface of the stone. The breadth of the peak is due to the rough sloped surface of the stone shown in figure 6.3a.28. Figure 6.3a.29. (b) – (d) sample the signal intensity at a specific depth of 400, 700 and  $1000 \mu\text{m}$  over the duration of the measurement. Water enters at 282 s, crossing the lateral range of the scan by 572 s. The 290 s time to cross the lateral range of 10 mm gives a wetting

front velocity of  $0.0034 \pm 0.0001 \text{ cm s}^{-1}$ . The hydraulic conductivity at this point is in the middle range of semi-pervious.

Chatton Park wetting scan 11 (CPWS11) was performed with the OCT probe positioned in the centre of the second “W”. The inscribed letter is less precisely carved than the others and is imposed on a line of the pre-existing rock art but does not appear to go through it.

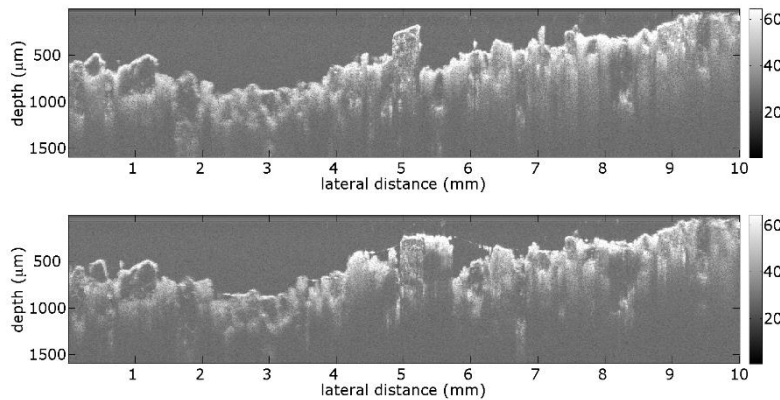


Figure 6.3a.30. OCT virtual cross sections of CPWS11 scan position when (a) dry and (b) wet.

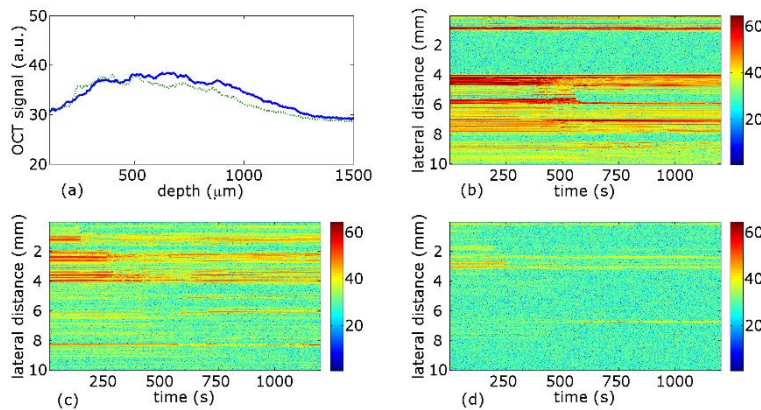


Figure 6.3a.31. CPWS11: (a) pixel intensity values averaged across the 10 mm cross section when dry (solid blue line) and wet (dotted green line); signal intensity values at depths of (b)  $\sim 400 \mu\text{m}$ , (c)  $\sim 700 \mu\text{m}$ , and (d)  $\sim 1000 \mu\text{m}$  across the lateral range of the scan over time. The OCT signals are in log scales.

The peak in figure 6.3a.31 (a) centered at approximately 400-450  $\mu\text{m}$  is due to scattering at the surface of the stone. The breadth of the peak is due to the rough sloped surface of the stone shown in figure 6.3a.30. Figure 6.3a.31. (b) – (d) sample the signal intensity at a specific depth of 400, 700 and 1000  $\mu\text{m}$  over the duration of the measurement. Water enters at 157 s, crossing the lateral range of the scan by 673 s. The 517 s time to cross the lateral range of 10mm gives a wetting front velocity of  $0.0019 \pm 0.0001 \text{ cm s}^{-1}$ . The hydraulic conductivity at this point is in the low middle range of semi-pervious.

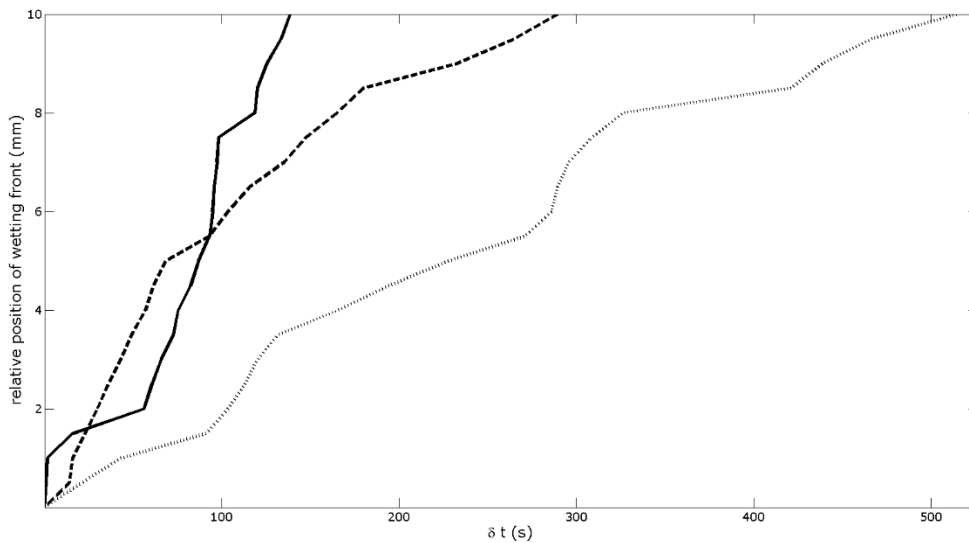


Figure 6.3a.23 Position of the wetting front over time for CPWS9 (black solid line), CPWS10 (black dashed line), CPWS11 (black dotted line).

The mostly intact “J” is carved to a depth of approximately 1 cm, exposing the interior of the stone, the hydraulic conductivity within the incised letter is significantly higher than the panel surface. The middle “W”, more rounded incision appears to have been carved less deeply ~5 mm and the hydraulic conductivity is within the high range of values recorded for the rest of the panel. The less precisely carved second “W” is imposed on a line of original rock art but does not appear to

have been cut through the modified surface, the hydraulic conductivity is consistent with the rest of the panel, the positions of the wetting front over time are shown in figure 6.3.a.23 for the three scans.

Within the small spatial scale of ~20 cm across the inscription there is a significant difference in hydraulic conductivity measured from the high to the low range of semi pervious with depth on incision. Where the top centimetre of the surface has been removed and the interior of the stone has been exposed by the inscription, the stone is in the high range of semi pervious. This may represent the initial surface of the panel before long term atmospheric exposure and weathering processes resulted in its current hydraulic conductivity in the low range of semi pervious, the consistency in the hydraulic conductivity across the weathered surface of the panel suggests that the effect of weathering processes has plateaued at the site.

### **6.3b. Roughting Linn**

The site is an elongated dome shaped outcrop approximately 20 m x 12 m, shown in figure 6.3b.1, with a large number of rock art motifs across its various faces. The outcrop is in a clearing surrounded by trees within a lowland basin.



Figure 6.3b.1. Roughting Linn decorated outcrop.

The site is surrounded by woodland and the outcrop has extensive growth of lichen and moss over motifs and panel and grass and small plants are growing in soil caught in niches in the rock. This plant growth across the outcrop is described as the principle vulnerability of the site in the Heritage at risk Register [15] listing for the outcrop.

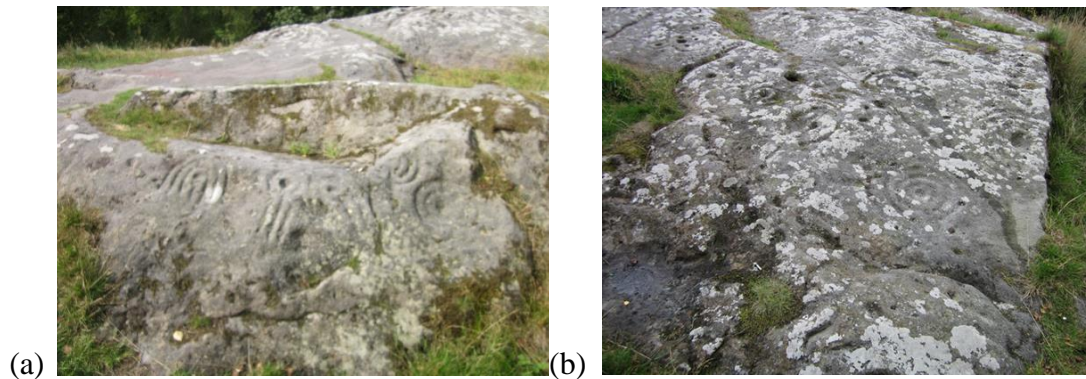


Figure 6.3b.2. Rock art panels showing plant growth (a) and lichen encrustation (b).

There are extensive solutional weathering features on the southern side of the outcrop, with intersecting karstic runnels, decantation flutings and solution pits, shown in figure 6.3.b.3. There does not appear to be any rock art motifs partially obscured by solutional weathering features, there is extensive growth of lichen and moss on the weathered slope of the outcrop.



Figure 6.3b.3. Karst runnel solution weathering features on the southern face of the outcrop.

The site has been damaged by the removal of stone by historic quarrying (pre - 1850 [9]) of the outcrop which cuts across several motifs. More recent damage to the site has been caused by the application of red paint to the surface of one of the most unique motifs on the outcrop. The appearance of the surface suggests that an attempt has been made to scrub the paint off the surface. Images of the anthropogenic damage are shown in figure 6.3.b.4.

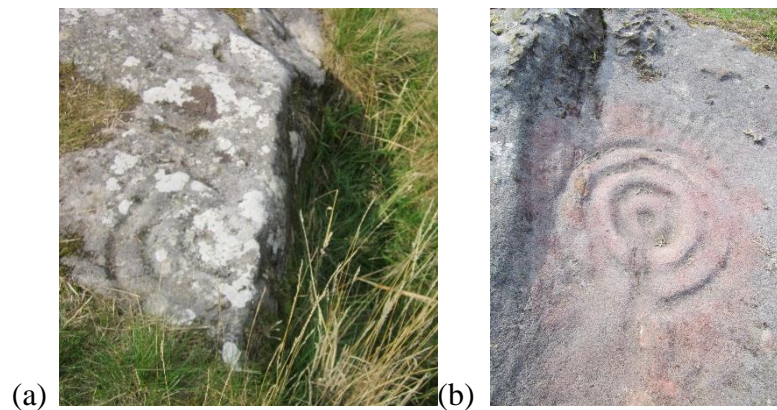


Figure 6.3b.4. Anthropogenic damage to the site: (a) quarry cut (b) paint residue.

The representative grain size distribution for the stone was determined from two OCT volume scans over different areas of  $6 \times 6$  mm using the imaging protocol described in chapter 2.



Figure 6.3b.5. Position of volume scan 1.

Volume scan 1 was performed on the host rock between two cup and ring motifs, shown in figure 6.3b.5. Within this volume 408 grains were identified, the size distribution of which is shown in figure 6.3b.

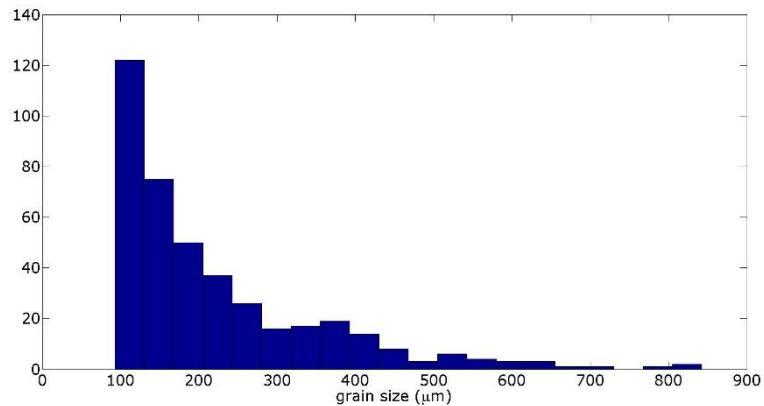


Figure 6.3b.6. Representative grain size distribution for Roughing Linn volume scan 1.

The minimum grain size detected was 93 μm, the maximum 842 μm with a mean of 221 μm and standard deviation of 135.



Figure 6.3b.7. Position of volume scan 2.

Volume scan 2 was performed in the cup of a motif with a residue of red paint, shown in figure 6.3b.7. Within this volume 535 grains were identified, the size distribution of which is shown in

figure 6.3b.8. The red paint residue does not appear to affect the OCT imaging of the subsurface structure.

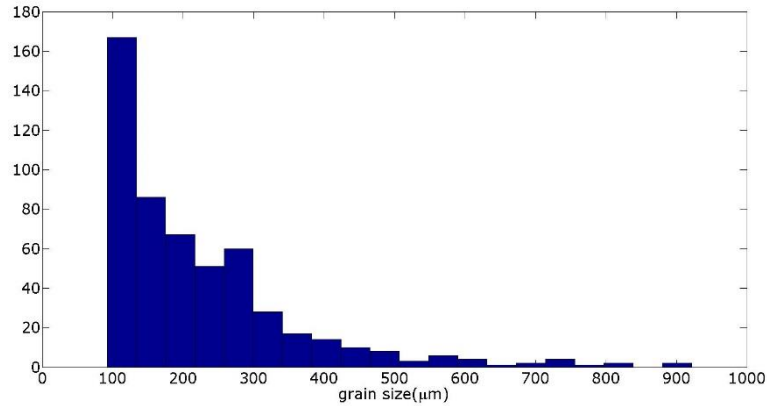


Figure 6.3b.8. Representative grain size distribution for Roughing Linn volume scan 2.

The minimum grain size detected was 92 μm, the maximum 922 μm with a mean of 223 μm and standard deviation of 138. The detected grain sizes from both scans are in the range of very fine to coarse sand, dominated by grains in the range of fine sand.



Figure 6.3b.9. Cup and concentric ring motifs on the north-west face on the outcrop.

In order to determine whether the hydraulic conductivity was affected by the modification of the stone by the formation of the motifs a control scan was performed on the unmodified outcrop in between two cup and ring motifs; Roughting Linn wetting scan 1 (RLWS1) at the same position as volume scan 1.

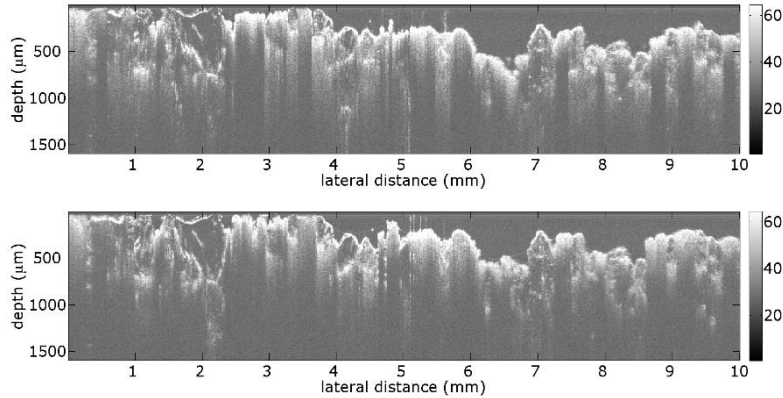


Figure 6.3b.10. OCT virtual cross sections of RLWS1 scan position when (a) dry and (b) wet.

Virtual cross sectional images of the scan position for RLWS1 are shown in figure 6.3b.10. when dry and wet. The presence of water in the sample reduces scattering as it reduces the refractive index mismatch, features can be seen to a greater depth within the stone.

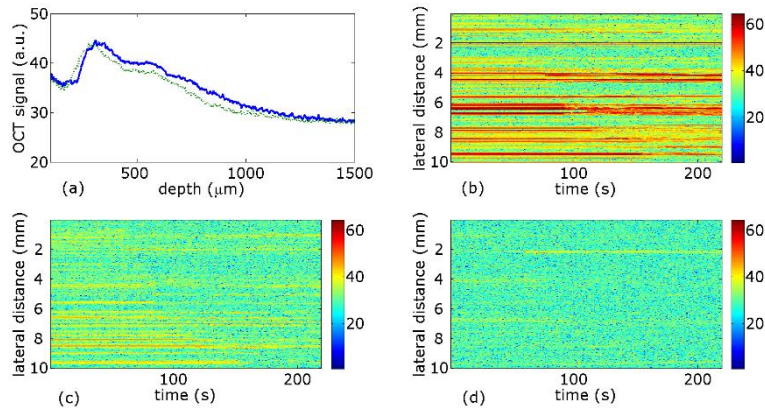


Figure 6.3b.11. RLWS1 : (a) pixel intensity values averaged across the 10 mm cross section when dry (solid blue line) and wet (dotted green line); signal intensity values at depths of (b)  $\sim 400 \mu\text{m}$ , (c)  $\sim 700 \mu\text{m}$ , and (d)  $\sim 1000 \mu\text{m}$  across the lateral range of the scan over time. The OCT signals are in log scales.

Figure 6.3b.11 (a) shows the decrease in pixel intensity values due to the reduction of scattering in the sandstone caused by the presence of water in the pore network. Depth scan intensity values were averaged across the 10 mm lateral range of the cross sections when both wet and dry. The peak centred at approximately  $500\text{--}550 \mu\text{m}$  is due to scattering at the surface of the stone, the breadth of the peak is due to the rough sloped surface of the stone, the shift is due to a slight movement of the probe towards the surface during the scan, no lateral movement occurred. Figure 6.3b.12 (b) – (d) sample the signal intensity at a specific depth of  $400$ ,  $700$  and  $1000 \mu\text{m}$  over the duration of the measurement. Water enters at  $55 \text{ s}$  crossing the lateral range of the scan by  $171 \text{ s}$ , showing little difference in water movement speed in the lateral direction between the different depths. The change in signal due to water cannot be detected below  $1 \text{ mm}$ . The  $115 \text{ s}$  time to cross the lateral range of the  $10 \text{ mm}$  gives a wetting front velocity of  $0.0087 \pm 0.0005 \text{ cm s}^{-1}$ . The hydraulic conductivity in the high middle range of semi-pervious.



Figure 6.3b.12 cup and concentric ring motif 1.

Motif 1 is formed of central cup surrounded by two concentric ring troughs pictured in figure 6.3b.12. There is encrustation of white lichen across the motif along with moss growth which is concentrated in the ring troughs. Roughting Linn wetting scan 2 (RLWS2) was performed with the OCT probe positioned on the peak surrounding the central cup of motif 1 in between areas of lichen encrustation.

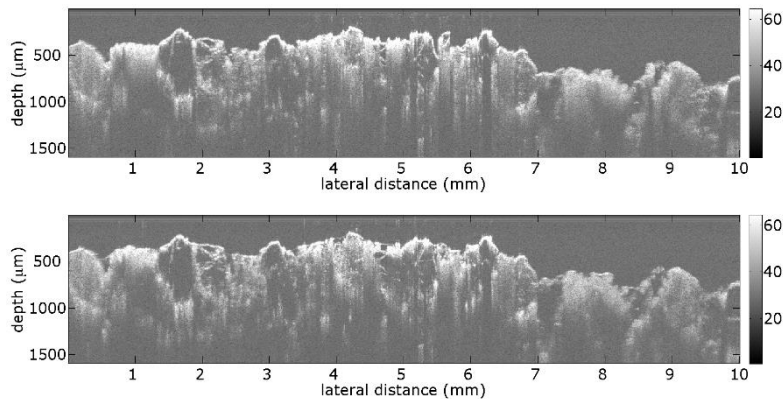


Figure 6.3b.13. OCT virtual cross sections of RLWS2 scan position when (a) dry and (b) wet.

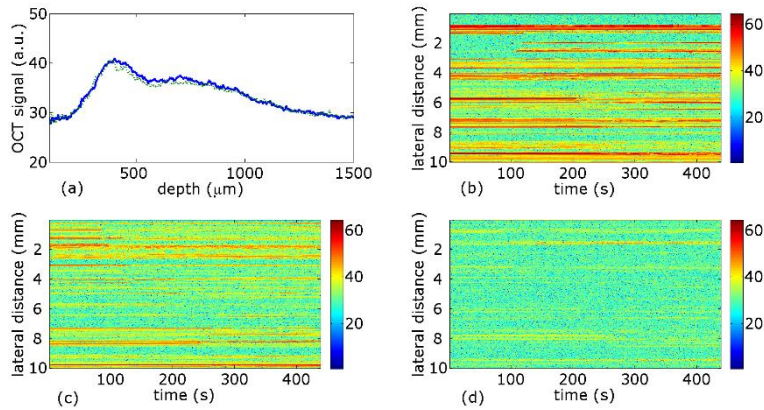


Figure 6.3b.14. RLWS2: (a) pixel intensity values averaged across the 10 mm cross section when dry (solid blue line) and wet (dotted green line); signal intensity values at depths of (b)  $\sim 400 \mu\text{m}$ , (c)  $\sim 700 \mu\text{m}$ , and (d)  $\sim 1000 \mu\text{m}$  across the lateral range of the scan over time. The OCT signals are in log scales.

The peak in figure 6.3b.14 (a) centered at approximately  $400\text{--}450 \mu\text{m}$  is due to scattering at the surface of the stone. The breadth of the peak is due to the rough sloped surface of the stone shown in figure 6.3b.13. Figure 6.3a.14. (b) – (d) sample the signal intensity at a specific depth of  $400$ ,  $700$  and  $1000 \mu\text{m}$  over the duration of the measurement. Water enters at  $69 \text{ s}$ , crossing the lateral range of the scan by  $268 \text{ s}$ . The  $199 \text{ s}$  time to cross the lateral range of  $10 \text{ mm}$  gives a wetting front velocity of  $0.005 \pm 0.0005 \text{ cm s}^{-1}$ . The hydraulic conductivity at this point is in the middle range of semi-pervious.

Roughing Linn wetting scan 3 (RLWS3) was performed with the OCT probe in the trough of inner ring of motif 1, between an area of moss and areas of lichen encrustation.

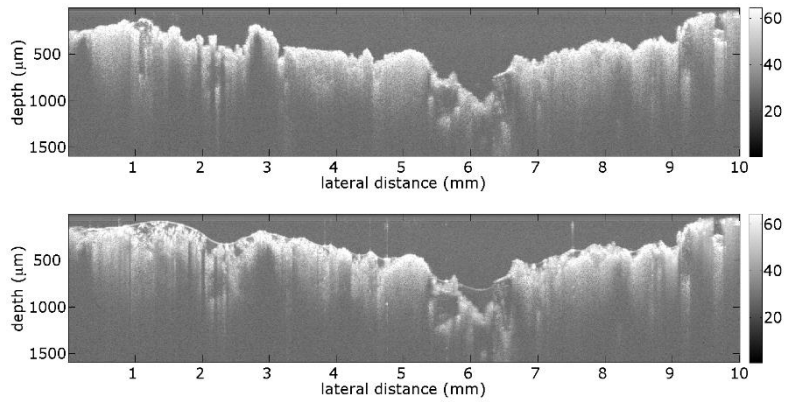


Figure 6.3b.15. OCT virtual cross sections of RLWS3 scan position when (a) dry and (b) wet.

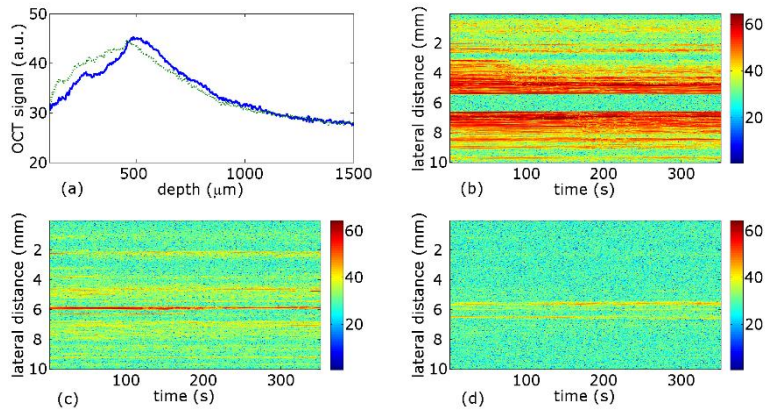


Figure 6.3b.16. RLWS3: (a) pixel intensity values averaged across the 10 mm cross section when dry (solid blue line) and wet (dotted green line); signal intensity values at depths of (b)  $\sim 400 \mu\text{m}$ , (c)  $\sim 700 \mu\text{m}$ , and (d)  $\sim 1000 \mu\text{m}$  across the lateral range of the scan over time. The OCT signals are in log scales.

The peak in figure 6.3b.16 (a) is centered at approximately  $500\text{-}550 \mu\text{m}$  is due to scattering at the surface of the stone. The breadth of the peak is due to the rough sloped surface of the stone shown in figure 6.3b.15. Figure 6.3a.16. (b) – (d) sample the signal intensity at a specific depth of  $400$ ,  $700$  and  $1000 \mu\text{m}$  over the duration of the measurement. Water enters at  $35 \text{ s}$ , crossing the lateral range of the scan by  $196 \text{ s}$ . The  $161 \text{ s}$  time to cross the lateral range of  $10 \text{ mm}$  gives a wetting

front velocity of  $0.0062 \pm 0.0005 \text{ cm s}^{-1}$ . The hydraulic conductivity at this point is in the middle range of semi-pervious.



Figure 6.3b.17 cup and concentric ring motif 2.

Motif 2 is formed of central cup surrounded by two concentric ring troughs pictured in figure 6.3b.17. There is encrustation of white lichen across the motif along with moss growth which is concentrated in the ring troughs. Roughting Linn wetting scan 4 (RLWS4) was performed with the OCT probe positioned in the central cup of motif 2.

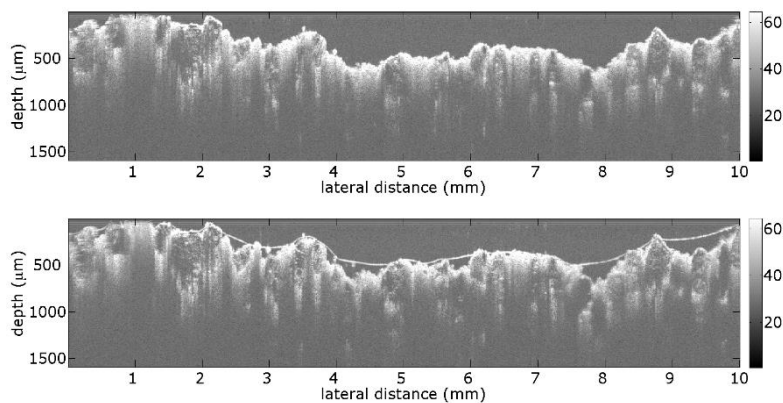


Figure 6.3b.18. OCT virtual cross sections of RLWS4 scan position when (a) dry and (b) wet.

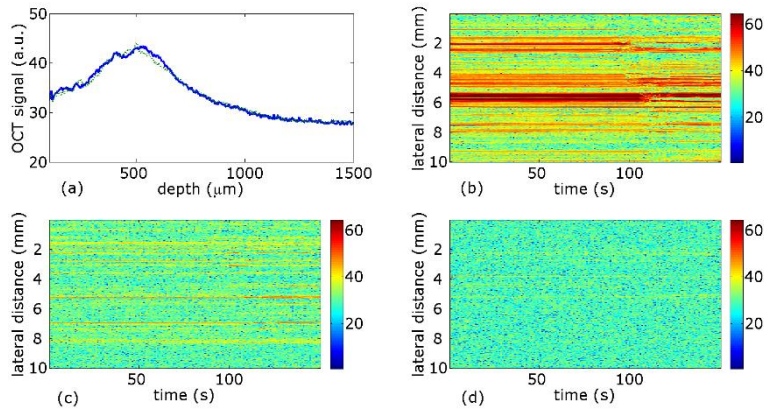


Figure 6.3b.19. RLWS4: (a) pixel intensity values averaged across the 10 mm cross section when dry (solid blue line) and wet (dotted green line); signal intensity values at depths of (b)  $\sim 400 \mu\text{m}$ , (c)  $\sim 700 \mu\text{m}$ , and (d)  $\sim 1000 \mu\text{m}$  across the lateral range of the scan over time. The OCT signals are in log scales.

The peak in figure 6.3b.19 (a) centered at approximately  $500\text{-}550 \mu\text{m}$  is due to scattering at the surface of the stone. The breadth of the peak is due to the rough sloped surface of the stone shown in figure 6.3b.18. Figure 6.3a.19. (b) – (d) sample the signal intensity at a specific depth of 400, 700 and  $1000 \mu\text{m}$  over the duration of the measurement. Water enters at 63 s, crossing the lateral range of the scan by 115 s. The 52 s time to cross the lateral range of 10 mm gives a wetting front velocity of  $0.019 \pm 0.001 \text{ cm s}^{-1}$ . The hydraulic conductivity at this point is in the high range of semi-pervious.

Roughting Linn wetting scan 5 (RLWS5) was performed with the OCT probe positioned on the peak surrounding the central cup of motif 2 between areas of lichen encrustation.

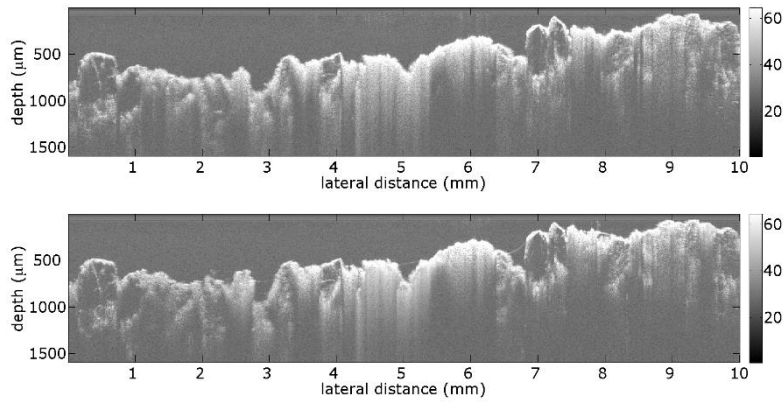


Figure 6.3b.20. OCT virtual cross sections of RLWS5 scan position when (a) dry and (b) wet.

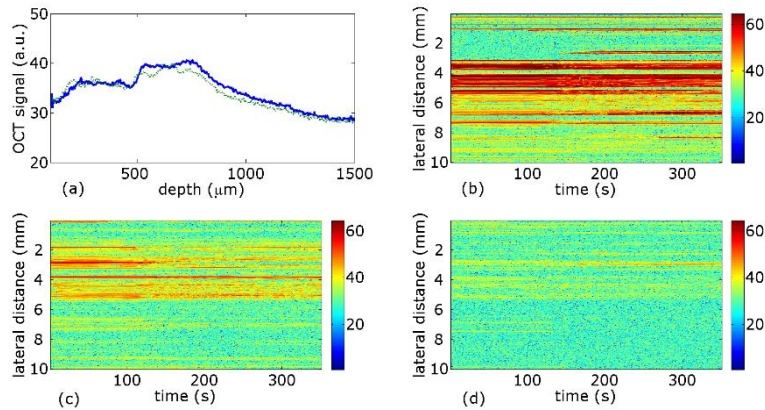


Figure 6.3b.21. RLWS5: (a) pixel intensity values averaged across the 10 mm cross section when dry (solid blue line) and wet (dotted green line); signal intensity values at depths of (b)  $\sim 400 \mu\text{m}$ , (c)  $\sim 700 \mu\text{m}$ , and (d)  $\sim 1000 \mu\text{m}$  across the lateral range of the scan over time. The OCT signals are in log scales.

The peak in figure 6.3b.21 (a) is centered at approximately  $500\text{-}550 \mu\text{m}$  is due to scattering at the surface of the stone. The breadth of the peak is due to the rough sloped surface of the stone shown in figure 6.3b.20. Figure 6.3a.21. (b) – (d) sample the signal intensity at a specific depth of 400, 700 and  $1000 \mu\text{m}$  over the duration of the measurement. Water enters at 77 s, crossing the lateral range of the scan by 177 s. The 99 s time to cross the lateral range of 10 mm gives a wetting front

velocity of  $0.010 \pm 0.001 \text{ cm s}^{-1}$ . The hydraulic conductivity at this point is in the high range of semi-pervious.

Roughing Linn wetting scan 6 (RLWS6) was performed with the OCT probe in the trough of the first ring surrounding the central cup of motif 2, between areas of lichen encrustation.

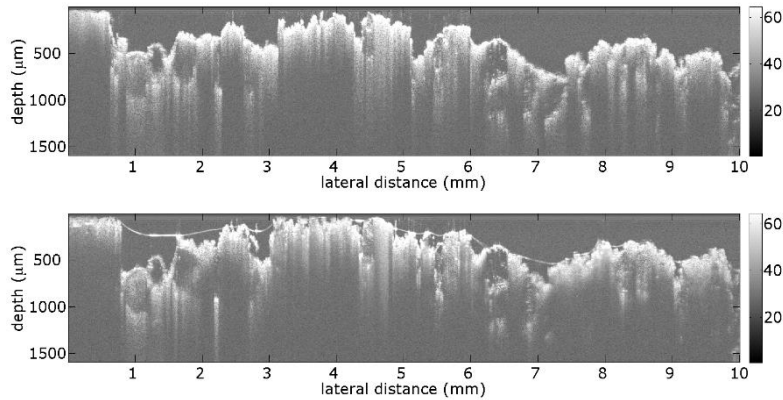


Figure 6.3b.22. OCT virtual cross sections of RLWS6 scan position when (a) dry and (b) wet.

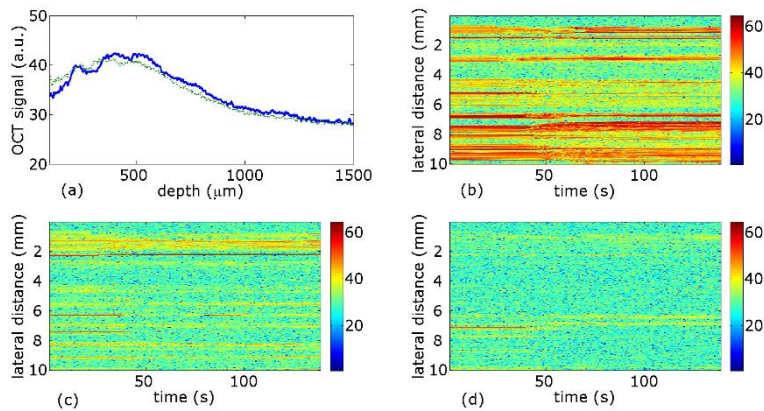


Figure 6.3b.23. RLWS6: (a) pixel intensity values averaged across the 10 mm cross section when dry (solid blue line) and wet (dotted green line); signal intensity values at depths of (b)  $\sim 400 \mu\text{m}$ , (c)  $\sim 700 \mu\text{m}$ , and (d)  $\sim 1000 \mu\text{m}$  across the lateral range of the scan over time. The OCT signals are in log scales.

The peak in figure 6.3b.23 (a) centered at approximately 500-550  $\mu\text{m}$  is due to scattering at the surface of the stone. The breadth of the peak is due to the rough sloped surface of the stone shown in figure 6.3b.22. Figure 6.3a.23. (b) – (d) sample the signal intensity at a specific depth of 400, 700 and 1000  $\mu\text{m}$  over the duration of the measurement. Water enters at 19 s, crossing the lateral range of the scan by 58 s. The 39 s time to cross the lateral range of 10 mm gives a wetting front velocity of  $0.026 \pm 0.001 \text{ cm s}^{-1}$ . The hydraulic conductivity at this point is in the high range of semi-pervious.

Roughing Linn wetting scan 7 (RLWS7) was performed with the OCT probe positioned on the peak between the inner and outer ring troughs of motif 2.

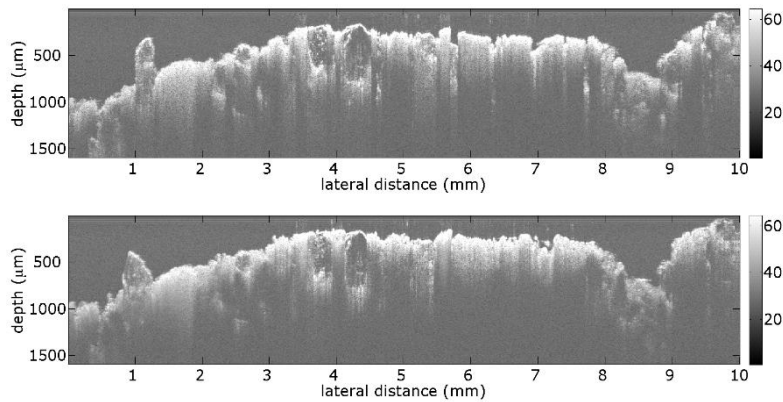


Figure 6.3b.24. OCT virtual cross sections of RLWS7 scan position when (a) dry and (b) wet.

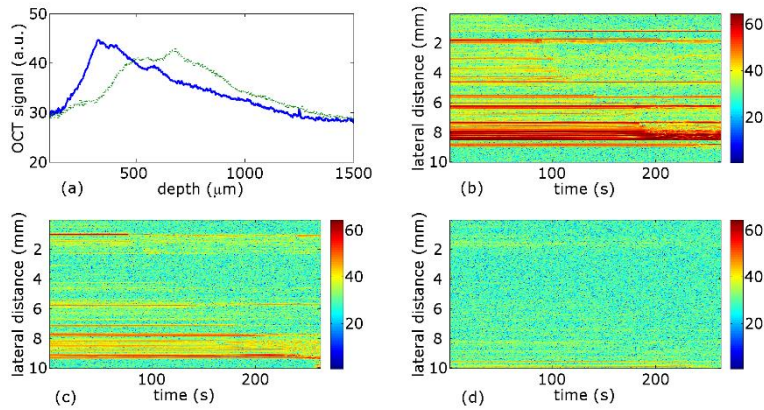


Figure 6.3b.25. RLWS7: (a) pixel intensity values averaged across the 10 mm cross section when dry (solid blue line) and wet (dotted green line); signal intensity values at depths of (b)  $\sim 400 \mu\text{m}$ , (c)  $\sim 700 \mu\text{m}$ , and (d)  $\sim 1000 \mu\text{m}$  across the lateral range of the scan over time. The OCT signals are in log scales.

The peak in figure 6.3b.25 (a) is centered at approximately  $300\text{-}350 \mu\text{m}$  is due to scattering at the surface of the stone. The breadth of the peak is due to the rough sloped surface of the stone shown in figure 6.3b.24. Figure 6.3a.25. (b) – (d) sample the signal intensity at a specific depth of 400, 700 and  $1000 \mu\text{m}$  over the duration of the measurement. Water enters at 58 s, crossing the lateral range of the scan by 259 s. The 199 s time to cross the lateral range of 10 mm gives a wetting front velocity of  $0.005 \pm 0.0005 \text{ cm s}^{-1}$ . The hydraulic conductivity at this point is in the middle range of semi-pervious.

Roughing Linn wetting scan 8 (RLWS8) was performed with the OCT probe positioned in the trough of the outer ring of motif 2.

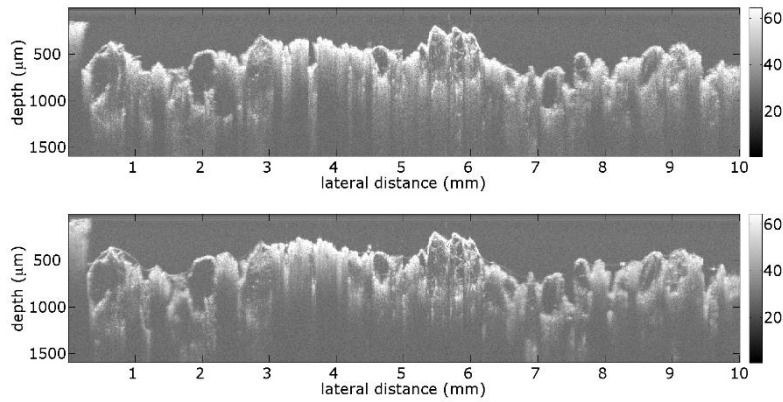


Figure 6.3b.26. OCT virtual cross sections of RLWS8 scan position when (a) dry and (b) wet.

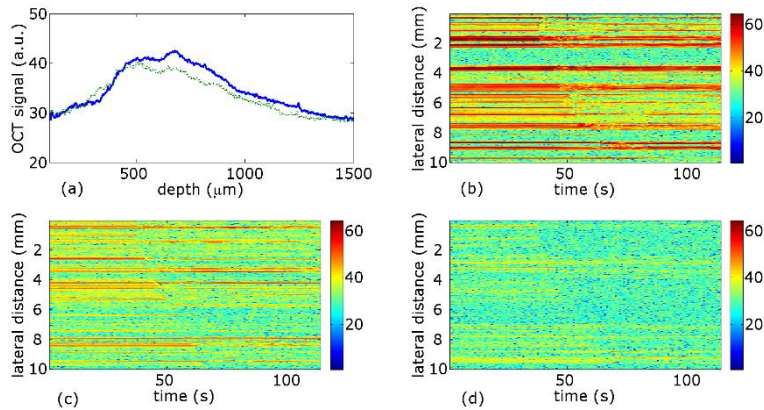


Figure 6.3b.27. RLWS8: (a) pixel intensity values averaged across the 10 mm cross section when dry (solid blue line) and wet (dotted green line); signal intensity values at depths of (b)  $\sim 400 \mu\text{m}$ , (c)  $\sim 700 \mu\text{m}$ , and (d)  $\sim 1000 \mu\text{m}$  across the lateral range of the scan over time. The OCT signals are in log scales.

The peak in figure 6.3b.27 (a) centered at approximately  $300\text{-}350 \mu\text{m}$  is due to scattering at the surface of the stone. The breadth of the peak is due to the rough sloped surface of the stone shown in figure 6.3b.26. Figure 6.3a.27. (b) – (d) sample the signal intensity at a specific depth of 400, 700 and  $1000 \mu\text{m}$  over the duration of the measurement. Water enters at 39 s, crossing the lateral range of the scan by 69 s. The 30 s time to cross the lateral range of 10 mm gives a wetting front

velocity of  $0.033 \pm 0.001 \text{ cm s}^{-1}$ . The hydraulic conductivity at this point is in the high range of semi-pervious.

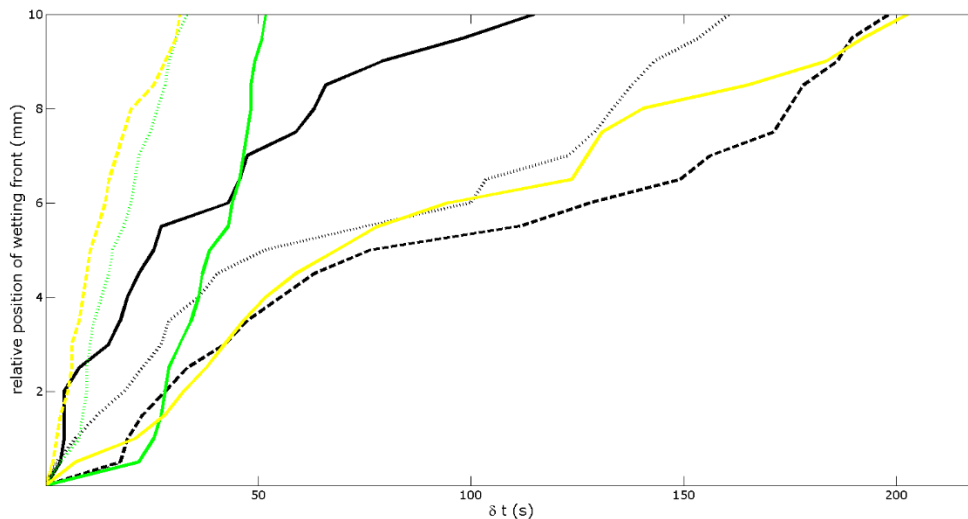


Figure 6.3b.28 Position of the wetting front over time for RLWS1 (black solid line), RLWS2 (black dashed line), RLWS3 (black dotted line), RLWS4 (green solid line), RLWS6 (green dotted line), RLWS7 (yellow solid line), RLWS8 (yellow dashed line).

The position of the wetting fronts for all scans are shown in figure 6.3b.28, the positions of these scans on the motifs are shown in the schematic diagram 6.3b.29, which also illustrates the extensive growth of lichens and moss across the rock art motifs. The results of the scans are summarised in table 6.3b.1.



Figure 6.3b.29 schematic of wetting scan positions and coverage of lichen (white infill) and mosses (hatched infill).

SCAN	POSITION	HYDRAULIC CONDUCTIVITY
RL1	unmodified outcrop	0.0087 cm s <sup>-1</sup>
RL2	Motif 1, 1 <sup>st</sup> ring peak	0.0050 cm s <sup>-1</sup>
RL3	Motif 1, 1 <sup>st</sup> ring trough	0.0062 cm s <sup>-1</sup>
RL4	Motif 2, central cup	0.019 cm s <sup>-1</sup>
RL5	Motif 2, 1 <sup>st</sup> ring peak	0.010 cm s <sup>-1</sup>
RL6	Motif 2, 1 <sup>st</sup> ring trough	0.026 cm s <sup>-1</sup>
RL7	Motif 2, 2 <sup>nd</sup> ring peak	0.005 cm s <sup>-1</sup>
RL8	Motif 2, 2 <sup>nd</sup> ring trough	0.033 cm s <sup>-1</sup>

Table 6.3a.1 Summary of wetting scan results

The measured hydraulic conductivities were consistently higher in the ring troughs compared to the peaks of the motif. The extensive surface coverage of lichen and moss indicate that the stone is bioreceptive [16], with hydraulic conductivities in the mid to high range of semi-pervious. The mean hydraulic conductivity is  $0.0099 \text{ cm s}^{-1}$ , in the high range of semi-pervious, the standard deviation of the measurements is  $0.0076$ , with a measurement uncertainty of  $0.001 \text{ cm s}^{-1}$ . There is significant variation in the measured hydraulic conductivity within a small spatial range across the outcrop, all of the measurements were performed in proximity to moss and lichen.

Roughing Linn wetting scan 9 (RLWS9) was performed with the OCT probe positioned in the cup of the red stained motif in the same position as volume scan 2. The OCT virtual cross-sections are shown in figure 6.3b.29, the surface of the stone appears to be more scattering at this point, presumably due to the presence of paint residue.

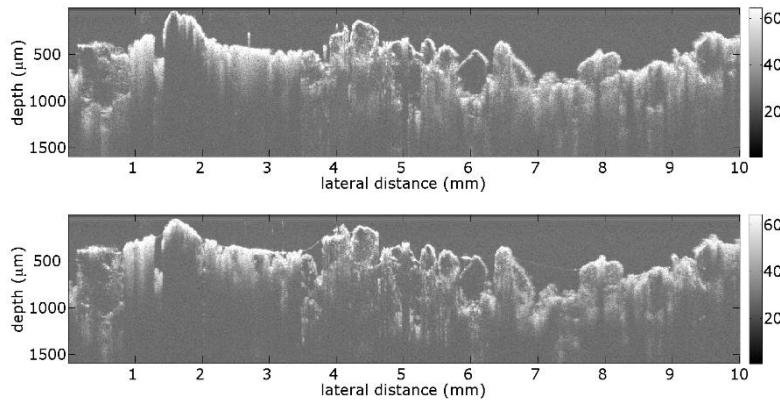


Figure 6.3b.29. OCT virtual cross sections of RLWS9 scan position when (a) dry and (b) wet.

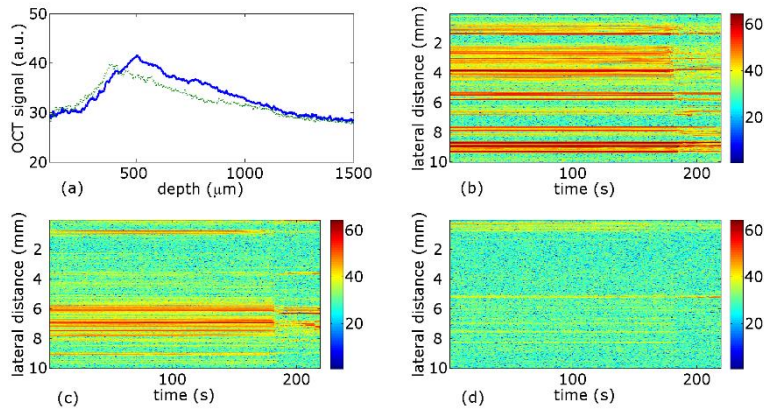


Figure 6.3b.30. RLWS9: (a) pixel intensity values averaged across the 10 mm cross section when dry (solid blue line) and wet (dotted green line); signal intensity values at depths of (b) ~400  $\mu\text{m}$ , (c) ~700  $\mu\text{m}$ , and (d) ~ 1000  $\mu\text{m}$  across the lateral range of the scan over time. The OCT signals are in log scales.

The peak in figure 6.3b.30 (a) centered at approximately 300-350  $\mu\text{m}$  is due to scattering at the surface of the stone. The relative sharpness of the peak may be due to paint residue on the surface of the stone shown in figure 6.3b.29. Figure 6.3a.30. (b) – (d) sample the signal intensity at a specific depth of 400, 700 and 1000  $\mu\text{m}$  over the duration of the measurement. Water enters at 179 s, crossing the lateral range of the scan by 187 s. The 8 s time to cross the lateral range of 10 mm gives a wetting front velocity of  $0.127 \pm 0.001 \text{ cm s}^{-1}$ , a significantly higher value than those measured for the rest of the outcrop. The hydraulic conductivity at this point is in the high range of pervious.

Roughing Linn wetting scan 10 (RLWS10) was performed on one of the most severely weathered motifs at the site, the rings have rounded uneven edges and extensive lichen encrustation predominately to the ring peaks of the motif.



Figure 6.3b.31 Weathered cup and ring motif.

The scan was performed with the OCT probe in the first ring trough around the central cup of the motif. The OCT virtual cross-sections of the scan are shown in figure 6.3b.32.

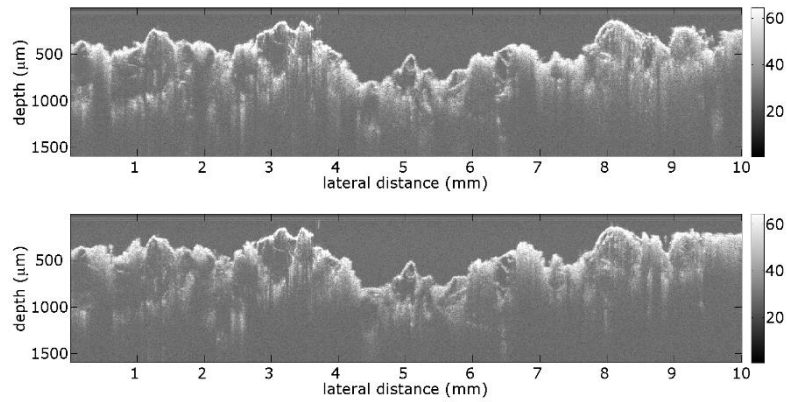


Figure 6.3b.32. OCT virtual cross sections of RLWS10 scan position when (a) dry and (b) wet.

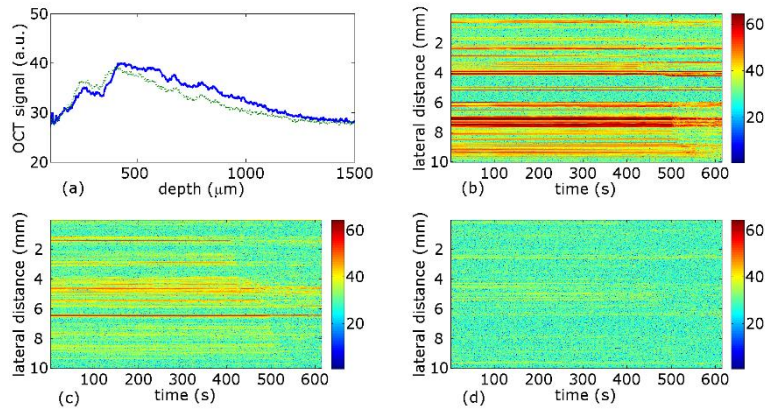


Figure 6.3b.33. RLWS10: (a) pixel intensity values averaged across the 10 mm cross section when dry (solid blue line) and wet (dotted green line); signal intensity values at depths of (b)  $\sim 400 \mu\text{m}$ , (c)  $\sim 700 \mu\text{m}$ , and (d)  $\sim 1000 \mu\text{m}$  across the lateral range of the scan over time. The OCT signals are in log scales.

The peak in figure 6.3b.33 (a) is centered at approximately  $300\text{--}350 \mu\text{m}$  is due to scattering at the surface of the stone. The breadth of the peak is due to the rough sloped surface of the stone shown in figure 6.3b.32. Figure 6.3a.33. (b) – (d) sample the signal intensity at a specific depth of  $400$ ,  $700$  and  $1000 \mu\text{m}$  over the duration of the measurement. Water enters at  $403 \text{ s}$ , crossing the lateral range of the scan by  $560 \text{ s}$ . The  $157 \text{ s}$  time to cross the lateral range of  $10 \text{ mm}$  gives a wetting front velocity of  $0.0064 \pm 0.0005 \text{ cm s}^{-1}$ . The hydraulic conductivity at this point is in the middle range of semi-pervious.

The wetting scan position for RLWS9 and 10 are shown in figure 6.3b.34. and the results are summarised in table 6.3b.2.

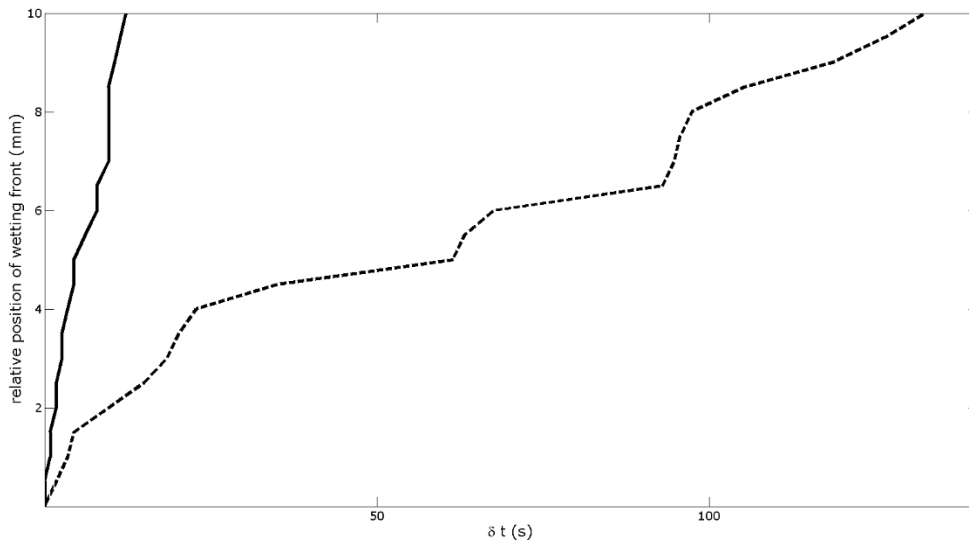


Figure 6.3b.34. Position of the wetting front over time for RLWS9 (black solid line), RLWS10 (black dashed line).

These results demonstrate the relative impact of natural weathering processes and anthropogenic intervention.

SCAN	SOURCE OF ALTERATION	HYDRAULIC CONDUCTIVITY
RL9	Anthropogenic; application and apparent attempted removal of paint to surface	0.12 cms <sup>-1</sup>
RL10	Natural; weathering processes and lichen encrustation	0.006 cms <sup>-1</sup>

The measurement performed on the motif where red paint had been applied showed a massive change in hydraulic conductivity compared to the host rock and all other measurements on the outcrop, whilst the severely but naturally weathered motif shows a hydraulic conductivity

consistent with the unmodified surface of the outcrop. The paint may have penetrated the subsurface of the stone affecting the surface tension of water within the stone.

### **6.3 Discussion**

A comparison between results found for the proxy sample and the rock art panel for Chatton Park demonstrates the importance of in-situ measurements of the rock art panels themselves, rather than reliance on proxy samples.

In the analysis of the proxy sample described in Chapter 3, the minimum grain size detected was 31  $\mu\text{m}$ , the maximum 359  $\mu\text{m}$  with a mean of 69  $\mu\text{m}$  and standard deviation of 45. Compared to the analysis of the rock art panel in-situ described in Chapter 6.3a where the minimum grain size detected was 93  $\mu\text{m}$ , the maximum 823  $\mu\text{m}$  with a mean of 211  $\mu\text{m}$  and standard deviation of 120. While visual inspection with a hand lens concluded that the cairn stone appeared representative at the time of collection, the grain size distributions measured for the proxy sample and in-situ are significantly different.

The proxy sample hydraulic conductivity described in Chapter 3, was measured for the un-weathered surface was obtained by slicing the samples using a diamond edged water cooled saw to access the interior un-weathered stone. The hydraulic conductivity for the proxy sample was  $0.024 \pm 0.001 \text{cm s}^{-1}$ , a value at the high range of semi pervious bordering on pervious.

The measurements of the rock art motif described in Chapter 6.3a show little variation in the hydraulic conductivity across the rock art panel or between the peaks and troughs of the motifs with a mean hydraulic conductivity of  $0.0018 \text{ cm s}^{-1}$  and a standard deviation of 0.0007, with a measurement uncertainty of  $0.001 \text{ cm s}^{-1}$ . This translates to an average value in the low middle range of semi-pervious. Where the relatively fresh surface (1860 carving) has been exposed to a

depth of 1cm the wetting front velocity of  $0.0071 \pm 0.0005$  cm s<sup>-1</sup>, the hydraulic conductivity is in the range of semi-pervious, the highest value recorded for the panel.

The proxy sample is clearly not representative of the rock art panel with respects to hydraulic conductivity or grain size distribution.

## References

1. A. Geike, Rock-weathering as illustrated in Edinburgh church yards: Proceedings, Royal Society, Edinburgh, v.10, p. 518-532 (1880)
2. G.F. Matthias, Weathering rates of Portland Arkose tombstones, Journal of Geological Education, 12 , 140-144 (1967)
3. T.C. Meierding, Marble tombstone weathering rates: a transect of the United States, Physical Geography, 2, 1-18, (1981)
4. R. U. Cooke, R. J. Inkpen, G. F. S. Wiggs, Using gravestones to assess changing rates of weathering in the United Kingdom. Earth Surface Process Landforms, 20, 531-46 (1995)
5. A.V. Turkington, T.R. Paradise, "Sandstone weathering: a century of research and innovation" Geomorphology 67, 229-253 (2005)
6. <http://www.derbyshireheritage.co.uk/Menu/Ancient/stonecircles/Barbrook-I.php>
7. <http://www.moorsforthefuture.org.uk/visiting-moors/audio-trails/gardoms-edge-roundhouse-rock-art>
8. Brown, D., A. Alder, and E. Bemand. A Possible Astronomically Aligned Monolith at Gardom's Edge. No. arXiv: 1203.0947. (2012)
9. Ancient Monuments and Archaeological Areas Act 1979  
<http://www.legislation.gov.uk/ukpga/1979/46>
10. <http://rockart.ncl.ac.uk/>

11. <http://archaeologydataservice.ac.uk/era/>
12. <http://www.megalithic.co.uk/>
13. S. Beckensall. British Prehistoric Rock Art. Tempus Publishing Ltd. (2002)
14. F.G. Bell. The physical and mechanical properties of the Fell Sandstones, Northumberland, England. Engineering Geology 12, 1-29, (1978)
15. <http://www.historicengland.org.uk/advice/heritage-at-risk/>
16. O. Guillitte. Bioreceptivity: a new concept for building ecology studies. The Science of the Total Environment. 167, 215-220. (1995)

## Chapter 7 Conclusions

The objective of this study was the development of techniques to apply non-destructive methods to replace current micro destructive techniques and to further enable the quantitative assessment of stone characteristics and vulnerability to weathering *in situ* without the need for sampling or reliance on proxy samples. The use of optical coherence tomography to produce virtual cross sections of the subsurface structure of sandstone as an “optical thin section” has been demonstrated, it is an effective non-invasive method to determine grain size distributions. The technique enables measurements over different areas of an outcrop removing the reliance on proxy samples to be representative. In Chapter 2 a protocol of spatial averaging of both cross sectional scans and depth profiles to create a composite image reducing noise features and improving the quality of the images is described. This optimisation of image acquisition enables the automatic detection of grain clasts to detect and characterise the grain size distribution. The depth range of imaging covers the subsurface structure of the stone at its interaction with the environment where the majority of weathering effects are likely to occur. The method can detect grain sizes from coarse silt (0.031-0.063 mm) to coarse sand (0.50-1.00 mm) determined by the resolution of the instrument and its depth range in the sample. The percentage of sandstone volume imaged as detectable grains varies with the sample but can be used to produce a representative grain size distribution.

The method was applied to the study of historic gravestones in Nottingham General Cemetery, the detected grain size distributions were similar for all stones. The grains size distributions were all dominated by grains in the range of medium to coarse silt, however only a small percentage of the material was identified as grain clast suggesting that the bulk of grains are smaller than the detection limit determined by the resolution of the technique.

The grain size distributions measured at the surface of rock art panels in Northumberland contained grains ranging from very fine to coarse sand, dominated by grains in the range of fine sand. Measurements were performed the rock art motifs themselves and determined that their formation had no impact on the grain size distributions found.

The use of OCT imaging to monitor the rounding and roughening of inscriptions and the detachment of surface flakes was also demonstrated in Chapter 6.1.b.

The capability of OCT to investigate water in porous materials was shown in Chapter 3. OCT can be used to register the movement of water through the porous network of dry samples to measure the depth resolved hydraulic conductivity of materials. Water acts as a clearing agent for OCT imaging of sandstone. The difference in pixel intensity values between dry and wet samples is shown to be an effective parameter with which to register the position of the wetting front. For this application, the image acquisition speed was set at 1.14 frames per second, enabling the technique to detect wetting front velocities from  $1\text{ cm s}^{-1}$  to  $10^{-6}\text{ cm s}^{-1}$  covering the full range of hydraulic conductivities likely to be found in natural sandstone, from pervious to impervious within a 2 hour observation time.

At Nottingham General Cemetery the measurements of hydraulic conductivities across the sandstones ranged from slightly pervious to the high end of semi- pervious and varied with the position and the intensity of weathering features for each stone. The change in hydraulic conductivity of the stones with the intensity of weathering features fell in three groups: three of the headstone showed an increase with increasing surface recession, two a decrease and two showed slightly pervious to impervious original surfaces with semi- pervious interiors. The stone

AF1850 presented a potential limitation to the technique, the presence of algal 'greening' on the surface may increase the humidity within the subsurface of the stone decreasing the effect of back-scattered intensity change as water moves through, as well as absorbing some of the incident light. In this case the approximate time of water ingress could be detected by the position of the wetting front across the range of the scan could not be discerned.

A measurement of the hydraulic conductivity of the primary stone of Barbrook I was performed giving a hydraulic conductivity  $0.0008 \pm 0.0001 \text{ cm s}^{-1}$ , in the low range of semi-pervious which is consistent with the expected value for the millstone grit lithology. The standing stone presents 5cm scale karst weathering features after an approximate 2000 year exposure. The low value for hydraulic conductivity may be a key factor in the durability of the stone.

The panel surface studied at Chatton Park is a bedding plane of the outcropping sandstone. The consistency in the weathering features observed at the surface is reflected by a consistency in the hydraulic conductivity across the rock art panel in the middle range of semi pervious. No difference was found for measurement between the peaks and troughs of the motifs. The presence of orange discolouration due to the deposition of iron minerals on the stone did not affect the hydraulic conductivity of the surface. An area of historic graffiti to the panel was investigated, where the top centimetre of the surface has been removed and the interior of the stone has been exposed by the inscription a significantly higher value for hydraulic conductivity was recorded. This value may represent the initial surface of the panel before long term atmospheric exposure and weathering processes caused the consistent lower values at the surface as the weathering plateaued at the site.

For the decorated outcrop at Roughing Linn the measured hydraulic conductivities show a greater variation and were consistently higher in the ring troughs compared to the peaks of the motif. The

hydraulic conductivities measured at Roughing Linn were higher than those at Chatton Park, in the mid to high range of semi- pervious, enabling the extensive surface coverage of lichen and moss at the site.

An investigation of modern graffiti at the Roughing Linn demonstrated the capability of OCT in quantifying the impact of anthropogenic damage to rock art panels. While there was no change to the subsurface structure due to the paint, there was a massive impact to the hydraulic conductivity. The massive increase in the hydraulic conductivity in this area may accelerate the weathering of one of the most unique motifs at the site.

OCT has been shown to be an effective technique to characterise and monitor the weathering and vulnerability of rock art panels in situ. Chapters 3 and 6 demonstrate the use of OCT imaging to determine the grain size distributions of sandstone. The measurement of hydraulic conductivity provides an indication of the vulnerability to weathering and a means of monitoring the effect of weathering processes over time. The non-invasive nature of the technique allows it to be used across the rock art panels and for long term monitoring of specific areas over time.

A comparison between results found for the proxy sample and the rock art panel for Chatton Park demonstrates the importance of in-situ measurements of the rock art panels themselves, rather than reliance on proxy samples. The proxy sample was found to be unrepresentative of the rock art panel with respects to hydraulic conductivity and grain size distribution.

The application of OCT to measure hydraulic conductivity has been demonstrated and its use in in-situ has been shown. The capability of the technique to investigate the application of stone treatments to sandstone and to monitor their performance was demonstrated in Chapter 3.5.

Two of the techniques investigated in this work were not implemented *in situ*, the use of hyperspectral imaging for remote moisture monitoring was investigated and found to be effective at determining water contents in sandstone and limestone. The technique would be effective where rock art is on the walls or ceilings of shelters or caves and inaccessible to other techniques but was not appropriate for the rock art panels studied.

Nuclear Magnetic resonance was investigated as a possible technique to determine the spatially resolved porosity of rock art monuments *in situ*. The long measurement times required and the susceptibility of the instrument to radio frequencies rendered the technique inappropriate for the study of rock art panels in an open air environment.

## **7.1 Further work**

### **Optical Coherence Tomography - monitoring of the application, impact and longevity of conservation treatments.**

The potential of optical coherence tomography to monitor the ingress and movement of fluid in porous media could have a range of application in the field of conservation of cultural heritage.

The technique has the potential to dynamically monitor the application and drying of conservation treatments in order to investigate penetration patterns, as well as to evaluate the effect on the hydraulic conductivity of the material at the time of treatment and for long term monitoring of its effectiveness *in situ*.

Preliminary experiments were performed, applying a solution of dilute titanium oxide pigment using the method described to investigate the potential of tracer particles to monitor the penetration of fluids into stone.

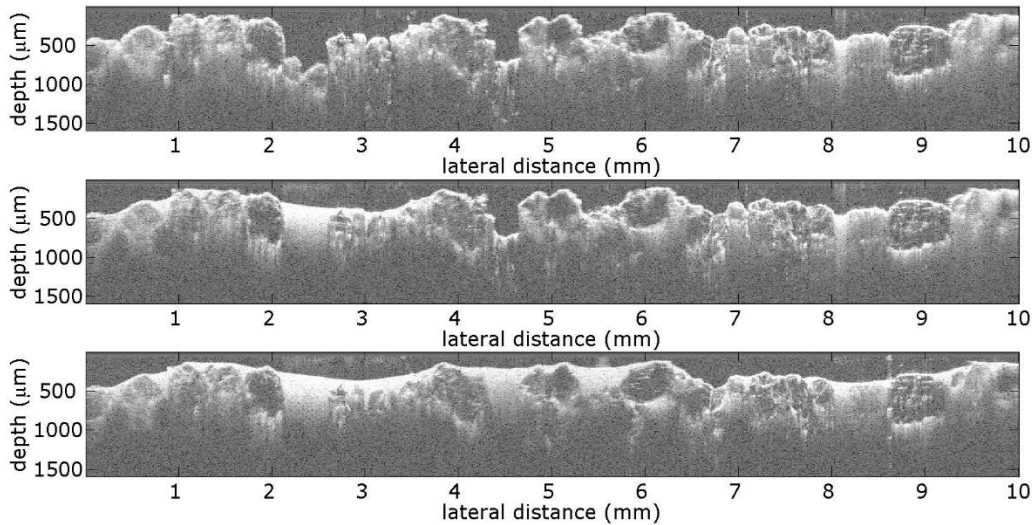


Figure 7.1 OCT ‘virtual’ cross-sections of sandstone (a) before application of pigmented solution (b) when solution has penetrated to 5 mm across from 0 (c) when solution has penetrated across full lateral range.

The wetting of coarse grained sandstone with a solution of titanium oxide pigment in water is shown in figure 7.1; before application, when the solution had penetrated halfway across the lateral range, and when fully wetted. The solution moved through the sandstone with a wetting front velocity of  $0.0071 \pm 0.001 \text{ cm s}^{-1}$ , compared to the hydraulic conductivity of  $0.0093 \pm 0.001 \text{ cm s}^{-1}$  for the same sample, the addition of the pigment solution to the water has presumably increased its viscosity, slowing its movement through the porous network. The presence of titanium oxide particles results in light scattering in the fluid making it appear bright in the OCT images, giving greater contrast to visualise the grain clasts. Areas that appear bright in the subsurface after the fluid has penetrated across may indicate the porous network of the stone.

A further test was carried out to monitor the penetration of the stone treatment IKO PRO Waterseal through sandstone, shown in figure 7.2; before application, when the solution had penetrated halfway across the lateral range, and when fully wetted. Waterseal is primarily composed of a mix of hydrocarbon liquids with a refractive index of around 1.50, closer to that of quartz (1.54) than water (1.33) enhancing the effect of optical clearing as it causes a greater reduction in the refractive index mismatch when it displaces air in the porous network of the stone.

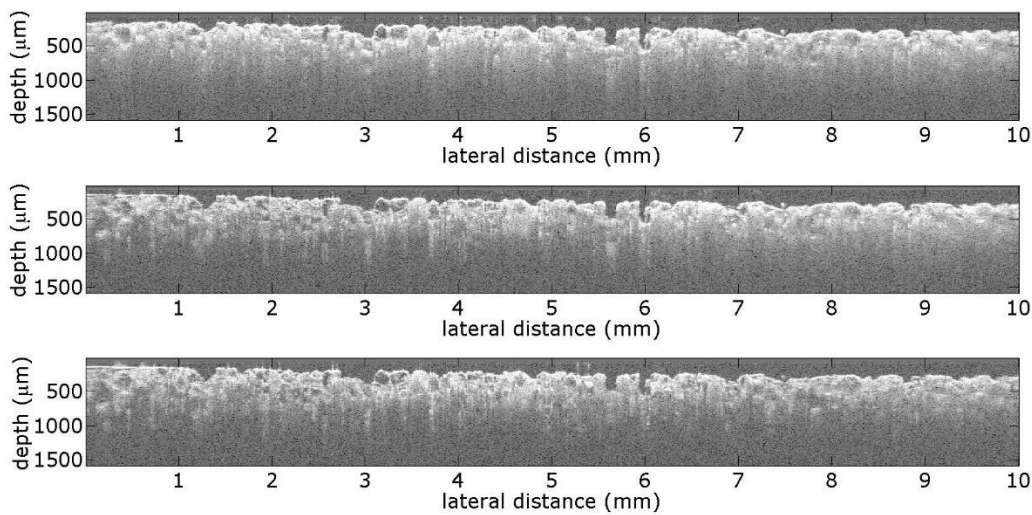


Figure 7.2 OCT ‘virtual’ cross-sections of sandstone (a) before application of stone treatment solution (b) when solution has penetrated to 5 mm across from 0 (c) when solution has penetrated across full lateral range.

The treatment penetrated through the sample quickly, with a wetting front velocity of  $0.054 \pm 0.001 \text{ cm s}^{-1}$ , compared to the hydraulic conductivity of  $0.0098 \pm 0.0005 \text{ cm s}^{-1}$  measured for the same sample. The mix of hydrocarbon fluids that form the solvent of the treatment have a lower density and viscosity than water, enabling it to move more rapidly through the porous network of the stone.

An attempt to measure the hydraulic conductivity of the stone once the treatment had dried found that the treatment had rendered the originally pervious sample impervious to water. Long term monitoring of treated surfaces with this method would enable the determination of longevity of stone conservation treatments *in situ*.

### **Hyperspectral imaging - application of the technique to painted caves and grottoes**

Hyperspectral imaging in the near infrared has been shown to be effective at determining the water content at the surface of limestone and sandstone samples in Chapter 4 of this thesis. For cultural heritage conservation purposes a greater application of the technique would be for the remote monitoring of moisture in surfaces which have been decorated such as painted grottoes and frescos.

Sandstone and limestone both have relatively flat spectra over the NIR region of interest with no spectral features that could overlap or distort the absorption feature due to water centred at 1450 nm. In order to determine the impact of surface pigments on the ability to detect water, model samples of a grotto wall and a wall painting were studied with a spectrometer when dry and after the application of water to the surface.

The model grotto wall was based on the grottoes of the Mogao near Dunhuang which were part of the Silk Road in China, it is composed of a sandstone substrate with a 3 cm layer of mud based plaster with a lime washed surface, shown in figure 4.9 (a). The lime wash surface was painted with test areas of the pigments; yellow ochre, red earth, indigo and azurite.

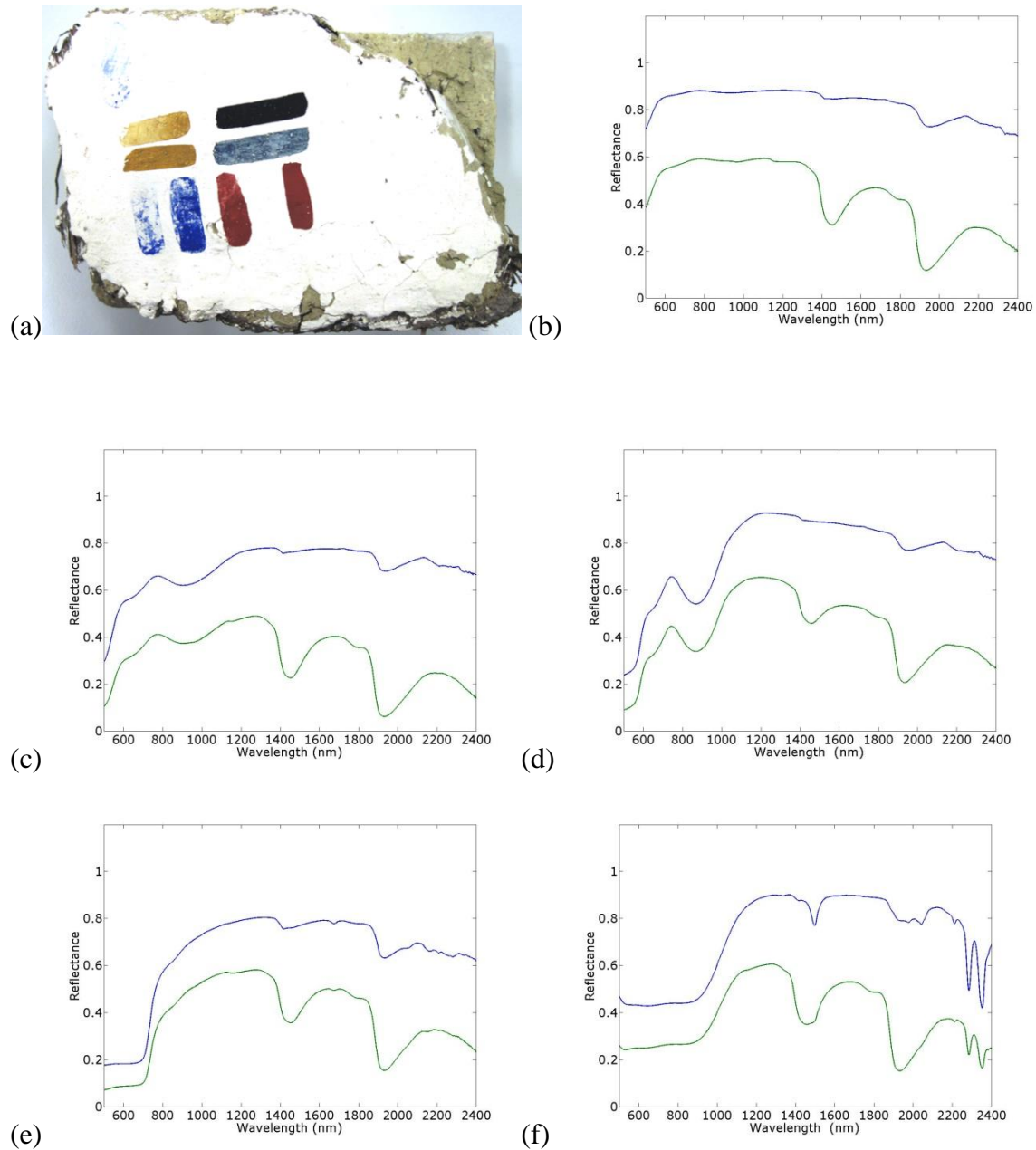


Figure 4.9 (a) mud wall with a  $\text{CaCO}_3$  preparation layer and painted with azurite, indigo, yellow ochre and red earth in animal glue; (b) spectra of the unpainted area with just the ground layer; (c) yellow ochre spectra (d) red earth spectra (e) indigo spectra (f) azurite spectra, when dry (blue line) and wet (green line).

As can be seen in figure 4.9(b) the unpainted lime washed surface of the model grotto has no significant features in the region of interest when dry, so the absorption feature centred at 1450 nm can be clearly seen in the spectra when wet. Figures 4.9 (b) and (d) show the spectra for the surface painted with yellow ochre and red earth respectively. Both these commonly used pigments have a relatively flat spectra in the region of interest and the water absorption feature can be clearly seen when wet. The spectra for indigo shown in figure 4.9(e) shows a small absorption feature when dry at 1400 nm, the pigment is very transparent in the infrared, so this may be due to the substrate. Figure 4.9 (f) shows the spectra for the surface painted with azurite when dry and wet. The spectra for azurite shows an absorption feature at 1500 nm, which is diagnostic for the identification of the pigment, the presence of the feature limits the ability to determine the presence of water on the surface from the water absorption feature centred at 1450 nm.

The model fresco wall painting is composed of a terracotta tile substrate with a 5 mm layer of 'fresco' prepared with a lime putty. The surface was painted with test areas of the pigments: yellow ochre, red earth, indigo and azurite.

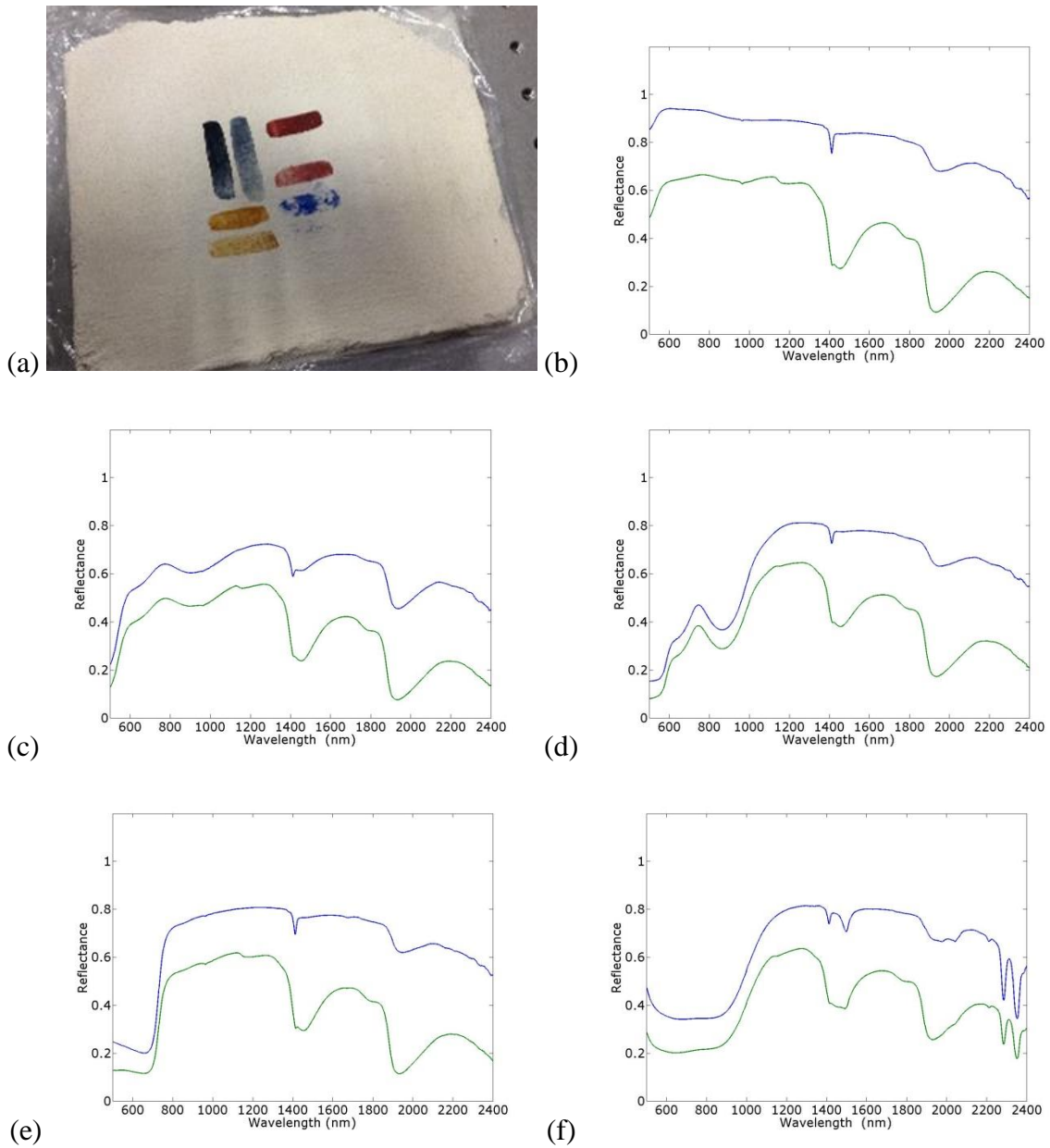


Figure 4.10 (a) ‘fresco’ prepared with a lime putty (b) plaster ground spectra (c) yellow ochre spectra (d) red earth spectra (e) indigo spectra (f) azurite spectra, when dry (blue line) and wet (green line)

As can be seen in the dry spectra of the fresco ground in figure 4.10(a) there is a sharp absorption feature centred at 1450 nm. This feature is due to the composition of the plaster, the feature can be seen in the dry spectra for each of the pigments studied 4.10 (b)-(e) and causes distortion to the water absorption feature in the wet spectra. This effect is pronounced in the azurite spectra in

figure 4.10(e) where the features due to both the plaster and azurite overlap the water absorption feature.

This technique has the potential to be applied to painted surfaces for remote moisture monitoring, but has limitations based on the composition of the surface. Prior knowledge of the substrate and the pigments applied to it are required to compensate for overlapping spectral features.

This may provide a useful and non-invasive technique with applications for *in situ* monitoring of dynamic changes in moisture content of historical and cultural artefacts at the surface and subsurface of porous media e.g. cave walls, buildings, and murals, for conservation purposes. It also has the potential to evaluate the effect and longevity of conservation treatments.

## PUBLICATIONS ARISING FROM THIS THESIS

### REFEREED JOURNAL PAPERS

E. Bemand, H. Liang. Optical coherence tomography for vulnerability assessment of sandstone, *Applied Optics*. 52, 3387-3393. (2013)

E. Bemand, H. Liang. Optical coherence tomography determination of representative grain size distributions in-situ. *Engineering Geology* (pending submission)

### CONFERENCE PROCEEDINGS

Brown, D., A. Alder, and E. Bemand. A Possible Astronomically Aligned Monolith at Gardom's Edge. No. arXiv: 1203.0947. (2012)

Bemand E., Bencsik M. and Liang H., OCT and NMR for non-invasive in-situ monitoring of the vulnerability of rock art monuments, *Proceedings of SPIE 8084*, 80840H (2011)

### BOOK

E. Bemand, H. Liang, M. Bencsik. Chapter 18: Non-invasive Methods for in-situ assessing and monitoring the vulnerability of Rock Art. *Open-Air Rock-Art Conservation and Management*. T. Darvill, A. P. Batarda Fernandes Eds. Routledge (2014)

### MEDIA

*Spotlight on Optics* May 21, 2013

A look inside rock art. *British Archaeology*. Issue 113, July/August 2010

